The Dissertation Committee for Edwin Yamid Ortega Certifies that this is the approved version of the following dissertation:

Inversion-Based Petrophysical Interpretation of Multi-Detector Logging-While-Drilling Sigma Measurements

Committee:

Carlos Torres-Verdín, Supervisor

William E. Preeg

Erich A. Schneider

Kamy Sepehrnoori

Hugh Daigle

Inversion-Based Petrophysical Interpretation of Multi-Detector Logging-While-Drilling Sigma Measurements

by

Edwin Yamid Ortega, B.S.; M.S.E.

Dissertation

Presented to the Faculty of the Graduate School of

The University of Texas at Austin

in Partial Fulfillment

of the Requirements

for the Degree of

Doctor of Philosophy

The University of Texas at Austin

May 2014

Dedication

A Rosita, en gratitud por todo su amor y apoyo, por enseñarme que la educación cambiaría mi mundo.

Acknowledgements

To many people I am indebted for their invaluable contributions to this project. To others, I am indebted for their gifts of courage, focus, and motivation to persevere in moments of hardship. First and foremost, I would like to express my most sincere gratitude to my supervisor, Dr. Carlos Torres-Verdín, for the opportunity of becoming part of his group, everything he taught me, his guidance, patience, and clever suggestions throughout this project. Never had I imagined, upon first joining his group, that working with him would change me so profoundly both professionally and personally. I indebt to him a large part of my education as a petrophysicist. The honor to have learned the practice of formation evaluation directly from the best is invaluable and unforgettable to me.

I would like to thank the following members of my committee: Dr. William Preeg, for his friendship and ample nuclear expertise in the co-supervision of my project; Dr. Eric Schneider, to whom I owe the understanding of nuclear physics that was the basis of important contributions presented in this dissertation; and to Dr. Kamy Sepehrnoori and Dr. Hugh Daigle for their time and technical guidance. During the course of my studies at The University of Texas at Austin, I was exposed to exceptional professors who fostered in me the passion for research and who contributed vastly to my professional development. I specifically wish to thank Dr. Buddie Mullins, Dr. Ekwere J. Peters, Dr. Kenneth Gray, Dr. Krishan Malik, Dr. Maša Prodanović, Dr. Quoc Nguyen, Dr. Robert Tatham, Dr. Stephen Ruppel, and Dr. William Fisher. I would like to express special gratitude for Dr. Ghislaine De Regge; whose lessons in technical English writing greatly facilitated the labor of composing my thoughts into written documents.

I fall short on words to express my gratitude for the support from several people in the oil and gas industry who helped me shape ideas into practical procedures, and who facilitated the testing of the algorithms presented in this dissertation on real field measurements acquired in multiple places around the globe. First, I thank Schlumberger-Doll Research for their collaborations on this project. Specifically, I would like to express deep gratitude for my friend Dr. Jeffrey Miles, with whom I spent several months in Cambridge, Massachusetts deciphering the challenges of multi-detector Sigma logging. His inspiration and suggestions played a vital role in consolidating the main contributions of this dissertation. While in Cambridge, I also had the privilege of being supervised by Dr. Darwin Ellis, who also contributed to this work and helped me develop ideas that came in use in the analysis of field measurements. My feeling of gratitude is no smaller toward John Ramus and Ed Stockhausen, who helped me in obtaining releases of field data that were fundamental in the development of this project. I also thank Dr. Marie-Laure Mauborgne because many of the ideas introduced in this dissertation stem from her previous work on Sigma logging, and to Dr. Brad Roscoe and Denis Heliot for making possible the collaborations between Schlumberger and The University of Texas at Austin. Second, I thank ConocoPhillips for multiple internships in which I was able to fully dedicate to the development of this study. I especially recognize the support I received from Mark Shannon.

The work reported in this dissertation was funded by The University of Texas at Austin's Research Consortium on Formation Evaluation, jointly sponsored by Afren, Anadarko, Apache, Aramco, Baker-Hughes, BG, BHP Billiton, BP, Chevron, ConocoPhillips, COSL, ENI, ExxonMobil, Halliburton, Hess, Maersk, Marathon Oil Corporation, Mexican Institute for Petroleum, Nexen, ONGC, OXY, Petrobras, PTT

Exploration and Production, Repsol, RWE, Schlumberger, Shell, Statoil, Total, Weatherford, Wintershall, and Woodside Petroleum Limited.

I am grateful to all my friends and fellow graduate students in the Formation Evaluation group at the Department of Petroleum and Geosystems Engineering for enriching my experience as a graduate student. Having the opportunity to share a diverse and multi-cultural environment with them transformed my vision on life and perception of the world in profound ways. I thank Oyinkansola Ajayi, Shaina Kelly, Marisa Jasso, David González, Juan Diego Escobar, Hamid Hadibeik, Essi Kwabi, Elton Ferreira, Haryanto Adiguna, Jordan Mimoun, Andy Popielski, Antoine Montaut, Philippe Marouby, Hyungjoo Lee, Siddarth Mishra, Olabode Ijasan, Zoya Heidari, Rohollah Abdollah-Pour, Chicheng Xu, Tatyana Torskaya, Vahid Shabro, Ankur Ghandi, Kanay Jerath, Abhishek Bansal, Amir Frooqnia, Shan Huang, Paul Sayar, Mathilde Luycx, Elsa Maalouf, Rebecca Gao, Dipo Olukitibi, and Eva Vinegar for their friendship. A special note of gratitude goes to my friend Marisa Jasso for taking the time to edit this document. I also thank the staff at the University of Texas at Austin who made this journey less stressful by facilitating administrative procedures. Specifically, thank you to Rey Casanova, Ben Voss, Frankie Hart, Cheryl Kruzie, and Roger Terzian. Likewise, I acknowledge the Texas Advanced Computing Center (TACC) for providing me with high-performance computational resources to complete the Monte Carlo simulations presented in this dissertation.

Above all, I want to express my loving gratitude to the most important people in my life. To *mamá* Rosita for her love and support during moments of joy and adversity, for celebrating with me every little victory, believing in me, and for being my inspiration always. Next, to the person who made this chapter of my life possible, my partner, best friend, and confidant, Reinel Solano, for motivating me to pursue graduate studies and supporting me throughout this journey. To his endearing support and advice, I owe much

of the man that I have become. Thanks to Angélica, Dana, Esperanza, Fredy, and everyone else in my family for believing in me, for being proud of me, and for their constant prayers. I especially want to thank my friends in Colombia for keeping long-lasting bonds that the distance could not break, and to all the great new friends that I have made in the United States, for giving me moments of joy that made this challenging experience easier.

Lastly, I thank God for all the great opportunities that He has given to me, and for taking care of the people I love while I have been away from home.

Thank you all.

Inversion-Based Petrophysical Interpretation of Multi-Detector Logging-While-Drilling Sigma Measurements

Edwin Yamid Ortega, Ph.D.

The University of Texas at Austin, 2014

Supervisor: Carlos Torres-Verdín

Pulsed-neutron borehole measurements involve a physical process in which a source emits energetic neutrons that lose energy upon collisions with formation nuclei, and are eventually captured by a nucleus to form a heavier, excited state. The excited nucleus decays to its ground state by the emission of gamma rays. Both thermal-neutron and gamma-ray populations decay with time at a rate defined by Sigma, which is a nuclear property that quantifies a material's ability to capture thermal neutrons. The large contrast in Sigma between hydrocarbon and salty connate water enables calculations of water saturation directly from pulsed-neutron measurements. Sigma logs have proven useful in the assessment of thinly bedded formations because they exhibit a small volume of investigation, and have been deemed superior to resistivity logs in the petrophysical evaluation of carbonate formations.

The recognized potential of Sigma logs in formation evaluation initiated the development of multi-detector Logging-While-Drilling (LWD) Sigma measurements. These measurements are acquired using one thermal-neutron and two gamma-ray detectors at different spacings from the source. Such a design is aimed at providing distinct radial depths of investigation to detect filtrate invasion in the near-wellbore zone. Despite their formation-evaluation potential, multi-detector time-decay measurements commonly

remain affected by invasion, shoulder-bed, and well-deviation effects. The purpose of this dissertation is to develop a fast-forward simulation method to reproduce multi-detector time decays and combine the method with inversion techniques to improve the petrophysical interpretation of LWD Sigma measurements.

First-order perturbation theory and a library of pre-calculated Monte Carlo detector-specific sensitivity functions and time decays are used to numerically simulate borehole Sigma measurements in realistic logging environments. The new simulation method is one hundred thousand times faster than rigorous Monte Carlo calculations and remains within two capture units of disparity. Next, the fast-forward simulation method is embedded within inversion algorithms to estimate layer-by-layer radial length of invasion and formation Sigma corrected for shallow invasion, shoulder-bed, and well-deviation effects. Both fast-forward and inverse modeling algorithms are benchmarked against laboratory and synthetic time decays.

The improvement of formation Sigma obtained with inversion-based interpretation leads to an improvement in the estimation of Sigma-derived water saturation. Likewise, the estimated radial length of invasion is combined with neutron and density measurements to correct the latter for invasion effects. Results indicate that the inversion-based interpretation method is well suited for the evaluation of high-porosity formations invaded by salty mud filtrate. Inversion-based interpretation of field LWD time decays enables the estimation of lower values of water saturation when compared to conventional Sigma interpretation or resistivity methods. Estimated values of water saturation are as much as fifty percent lower than predicted by conventional interpretation of Sigma logs in the case of measurements affected by shoulder-bed effects, and as much as one hundred percent lower than predicted by the conventional interpretation method for measurements additionally affected by salty filtrate invasion.

The key attributes of the combined petrophysical interpretation of multi-detector Sigma, neutron, and density measurements developed in this dissertation are that it explicitly enforces the physics of all nuclear measurements, honors the pressure and temperature dependency of reservoir fluid nuclear properties, and takes into account a-priori information such as mud-filtrate salinity, connate-water salinity, and bed-boundary locations.

Table of Contents

List of Tables xvii

List of Figures xxi

Chapter 1: Introduction 1

1.1 Background 1

1.2 Problem Statement 6

1.3 Research Objectives 7

1.4 Method Overview 9

1.5 Dissertation Outline 13

1.6. List Of Publications 15

1.6.1 Refereed Journal Publications 15

1.6.2 Conference Proceedings 16

Chapter 2: Multi-Detector Logging-While-Drilling Sigma Principles, Petrophysical Applications, and Environmental Effects 18

2.1 Introduction 19

2.2 Measurement Physics 22

2.3 Tool Operation 26

2.4 Signal Processing 28

2.5 Wireline Versus LWD Sigma 32

2.6 Detector Sensitivity 33

2.7 Environmental Effects 36

2.7.1 Diffusion Effects 36

2.7.2 Borehole Effects 38

2.8 Multi-Detector Sigma Interpretation 39

2.8.1 Mud-Filtrate Invasion Effects on LWD Measurements 39

2.8.2 Multi-Depth-of-Investigation, MDOI, Sigma 42

2.9 Conclusions 45

Chapter 3: Rapid Forward Modeling of Multi-Detector Logging-While-Drilling Sigma Measurements 63
3.1 Introduction 64
3.2 Rapid Numerical Simulation 67
3.2.1 Formulation 67
3.2.2 Time Decay Library 72
3.2.3 FSF Library 74
3.3 Numerical Results 76
3.3.1 Test-Pit Case I: Thick Homogeneous Formations 76
3.3.2 Test-Pit Case II: Piston-Like Invasion 77
3.3.3 Piston-Like Invasion Effects on MDOI Sigma Measurements 80
3.3.3.1 Invasion Into Oil-Bearing Formations 81
3.3.3.2 Invasion Into Gas-Bearing Formations 81
3.3.4 Effects of Smooth Invasion on MDOI Sigma Measurements 82
3.3.5 Shoulder-Bed Effects on MDOI Sigma Measurements 83
3.3.6 Combined Shoulder-Bed and Invasion Effects on MDOI Sigma Measurements 85
3.3.7 MDOI Sigma Logs Acquired in High-Angle/Horizontal (HA/HZ) Wells 85
3.4 Computational Speed 88
3.5 Discussion Speed 89
3.6 Conclusions 90

Chapter 4: One-Dimensional Radial Inversion of Multi-Detector Logging-While-Drilling Sigma Measurements 117
4.1 Introduction 117
4.2 One-Dimensional Inversion-Based Interpretation of Logging-While-Drilling Sigma Measurements 120
4.2.1 Formulation 120
4.2.2 Fast Jacobian Matrix Calculation 127
4.3 Interpretation of Synthetic Time Decays 130

4.3.1 Impact of Invasion-Zone Sigma, Σ_i, on Estimated Virgin-Zone Sigma and Radial Length of Invasion....131
4.3.2 Noise on Synthetic Multi-Detector Time Decays....133
4.3.3 Multiple Realization Study....134
4.4 Laboratory Results....138
4.5 Synthetic Results....139
4.5.1 Synthetic Case I....140
4.5.2 Synthetic Case II....143
4.6 Field Results....145
4.7 Discussion....147
4.8 Conclusions....148

Chapter 5: Two-Dimensional Inversion-Based Interpretation of Logging-While-Drilling Sigma Measurements....172
5.1 Introduction....173
5.2. Two-Dimensional Inversion of Multi-Detector Time Decays....177
5.2.1 Formulation....177
5.2.2 Jacobian Calculation....182
5.2.3 Assessment of Uncertainty....187
5.3 Synthetic Results....187
5.3.1 Synthetic Case I....188
5.3.2 Synthetic Case II....191
5.4 Field Results....194
5.4.1 Field Case I....194
5.4.2 Field Case II....199
5.5 Discussion....202
5.6. Conclusions....202

Chapter 6: New Analytical Method to Calculate Matrix- and Fluid-Corrected Total Porosity....219
6.1 Introduction....220
6.2. Method....226

6.2.1 Matrix-Corrected Neutron Porosity 226
6.2.2 Matrix-Corrected Density Porosity 234
6.2.3 Calculation of Total Porosity From Matrix- and Fluid-Corrected Nuclear Measurements 235
6.3 Synthetic Results 239
6.3.1 Synthetic Case I 239
6.3.2 Synthetic Case II 242
6.4 Field Results 243
6.4.1 Field Case I 244
6.4.2 Field Case II 246
6.4.3 Field Case III 247
6.4.4 Field Case IV 249
6.5 Discussion 251
6.6 Conclusions 252

Chapter 7: Joint Petrophysical Interpretation of Multi-Detector Nuclear Measurements Corrected for Invasion, Shoulder-Bed, and Well-Deviation Effects 270
7.1 Introduction 271
7.2 Multi-Detector LWD Nuclear Measurements 275
7.2.1 The Multi-Function LWD Tool 275
7.2.2 Nuclear Suite Sensitivity Functions 277
7.3 Two-Dimensional Inversion of Multi-Detector Measurements 279
7.3.1 Improved Estimation of Reference Invasion-Zone Sigma 279
7.3.2 Multi-Detector Thermal-Neutron and Density Porosity 280
7.4 Nuclear-Based Estimation of Fluid Type And Water Pore Volume 285
7.4.1 Nuclear Mixing Laws 285
7.4.2 PVT-Consistent Nuclear Interpretations 287
7.4.3 Nuclear-Based Petrophysical Solver 288
7.4.4 Estimation of Uncertainty 291
7.5 Multi-Nuclear Interpretation Workflow 291
7.6 Synthetic Results 293

7.6.1 Synthetic Case I 293
7.6.2 Synthetic Case II 295
7.7 Field Results 297
7.7.1 Field Case I 297
7.7.2 Field Case II 300
7.7.3 Field Case III 303
7.7.4 Field Case IV 306
7.7.5 Field Case V 309
7.8 Conclusions 311
Chapter 8: Summary, Conclusions, and Recommendations 331
8.1 Summary 331
8.2 Conclusions 334
8.2.1 Part One: Study of the Potential and Limitations of Multi-Detector LWD Sigma Measurements 335
8.2.2 Part Two: Rapid Forward Modeling of Multi-Detector Logging-While-Drilling Sigma Measurements 337
8.2.3 Part Three: Inversion-Based Interpretation of Multi-Detector LWD Sigma Measurements 339
8.2.4 Part Four: Integration of Multi-Detector LWD Sigma Measurements with Other Borehole Nuclear Measurements 342
8.3 Contributions 346
8.4 Recommendations for Best Practices 348
8.5 Recommendations for Future Work 351
Appendix A 354
List of Symbols 356
References 365
Vita 371

List of Tables

Table 2.1: Summary of drilling parameters assumed in simulations of mud-filtrate invasion. 47

Table 2.2: Summary of petrophysical properties assumed for different rock types. 48

Table 2.3: Summary of virgin- and invasion-zone properties for LWD Sigma and resistivity simulations. 49

Table 3.1: Summary of assumed lithology, porosity, water salinity (C_w), and intrinsic Sigma (Σ_{int}) for the blocks corresponding to test-pit measurements and simulations reported in **Figure 3.4**, and Monte Carlo (MC), Test-pit, and Fast-Forward (FF) modeled Sigmas. 92

Table 3.2: Summary of lithology, in-situ fluid type, porosity, filtrate salinity (C_{filt}), virgin- and invasion-zone migration length ($L_{m\,v}$, $L_{m\,i}$), and Sigma (Σ_v , Σ_i), and virgin-zone fluid Sigma (Σ_f) for test-pit measurements and simulations reported in **Figure 3.9** and **Figure 3.10**. 93

Table 3.3: Summary of assumed lithology, thickness, in-situ fluid, porosity, total water saturation (S_w), water salinity (C_w), migration length (L_m), and intrinsic Sigma (Σ_{int}) for formations corresponding to the simulations of Sigma logs affected by shoulder beds reported in **Figure 3.12**. 94

Table 3.4: Summary of assumed lithology, thickness, in-situ fluid type, porosity, total water saturation (S_w), water salinity (C_w), and intrinsic Sigma (Σ_{int}) for formations corresponding to the simulations of Sigma logs reported in **Figure 3.13**. 95

Table 3.5: Summary of assumed lithology, thickness, in-situ fluid type, porosity, total water saturation (S_w), water salinity (C_w), migration length (L_m), intrinsic Sigma (Σ_{int}), and radial length of invasion (r_i) for shale and sandstone intercalations corresponding to the simulations of Sigma logs simultaneously affected by shoulder beds and invasion reported in **Figure 3.14**. Filtrate salinity is 200 kppm [NaCl] and Σ_{filt} is 98 c.u. Shale matrix composition is 80% chlorite and 20% kaolinite. 96

Table 3.6: Summary of assumed lithology, thickness, in-situ fluid type, porosity, total water saturation (S_w), water salinity (C_w), migration length (L_m), and intrinsic Sigma (Σ_{int}) for shale and sandstone formations corresponding to the simulations of Sigma logs in the 85°-well reported in **Figure 3.15**. Shale matrix composition is 80% chlorite and 20% kaolinite.....97

Table 3.7: Summary of assumed porosity, mineral volumetric fractions, oil, gas, and water saturations (S_o ,S_g, S_w), virgin- and invasion-zone Sigma (Σ_v ,Σ_i) and radial length of invasion (r_i) for the formations corresponding to the simulations of Sigma logs in the 85°-well with asymmetric invasion reported in **Figure 3.16**. Filtrate salinity is 250 kppm [NaCl], Σ_{filt} = 120 c.u., connate water salinity is 180 kppm [NaCl], and Σ_w = 88.4 c.u. 98

Table 3.8: Comparison of Monte Carlo (MC) and Fast-Forward (FF) method CPU times required to model test-pit and synthetic cases reported in this chapter and average difference for each case. 100

Table 4.1: Summary of petrophysical properties assumed for the virgin and invasion zone materials corresponding to synthetic decays used for inversion in **Figure 4.13**. Filtrate salinity is 200 [NaCl] kppm and filtrate Sigma is 98 c.u. 150

Table 4.2: Summary of petrophysical properties assumed for the virgin- and invasion-zone materials corresponding to synthetic decays used for Synthetic Case I. Filtrate salinity is 200 [NaCl] kppm and filtrate Sigma is 98 c.u. 151

Table 4.3: Summary of petrophysical properties assumed for the virgin- and invasion-zone materials corresponding to layered formations in Synthetic Case II. Gas Sigma and density are 5.7 c.u. and 0.14 g/cm^3, respectively, at 150 ^{o}F and 24131.65 kPa (3500 psia). Oil (87% Carbon, 13% Hydrogen) Sigma and density are 21.26 c.u. and 0.82 g/cm^3, respectively. Drilling fluid is 123-kppm [NaCl] WBM, and filtrate Sigma, $\Sigma_{mf,}$ is 66.7 c.u. 152

Table 5.1: Summary of assumed lithology, thickness, porosity, water saturation (S_w), gas saturation (S_g), virgin-zone Sigma (Σ_v), invaded-zone Sigma (Σ_i), and matrix Sigma (Σ_m), and radial length of invasion ($\boldsymbol{r_i}$) for the formations corresponding to Synthetic Case I. Filtrate salinity is 200 kppm [NaCl], Σ_{mf} = 96.6 c.u., connate water salinity is 80 kppm [NaCl], and Σ_w = 50.3 c.u. 206

Table 5.2: Summary of assumed lithology, thickness, porosity, water saturation (S_w), gas saturation (S_g), virgin-zone Sigma (Σ_v), invaded-zone Sigma (Σ_i), and matrix Sigma (Σ_m), and radial length of invasion ($\boldsymbol{r_i}$) for the formations corresponding to Synthetic Case II. Filtrate salinity is 200 kppm [NaCl], Σ_{mf} = 96.6 c.u., connate water salinity is 80 kppm [NaCl], and Σ_w = 50.3 c.u. 207

Table 6.1: Density, inverse of migration length for an AmBe and a 14-MeV neutron source, Sigma, and hydrogen index for various minerals and water of different salinities.....254

Table 6.2: Assumed properties for the formations in Synthetic Case II. Gas properties calculated at 10342.14 kPa (1500 psia) and 150°F (0.07 g/cm^3). ξ_{sh} = 0.0801 cm^{-1} for wet chlorite and ξ_{ss} = 0.0276 cm^{-1} for quartz. 256

Table 7.1: Summary of assumed thickness, porosity, mineral volumetric fractions, in-situ fluid type, water saturation (S_w), invasion- and virgin-zone densities (ρ_i and ρ_v), inverse of migration lengths (ξ_i and ξ_v), Sigmas (Σ_i and Σ_v), and radial lengths of invasion (r_i) for Synthetic Case I. Filtrate salinity is 200 kppm [NaCl], Σ_{mf} = 96.6 c.u., and connate water salinity is 80 kppm [NaCl], Σ_w = 50.3 c.u.....313

Table 7.2: Summary of assumed thickness, porosity, mineral volumetric fractions, in-situ fluid type, water saturation (S_w), invasion- and virgin-zone densities (ρ_i and ρ_v), inverse of migration lengths (ξ_i and ξ_v), Sigmas (Σ_i and Σ_v), and radial lengths of invasion (r_i) for Synthetic Case II. Filtrate salinity is 230 kppm [NaCl], Σ_{mf} = 112 c.u., and connate water salinity is 80 kppm [NaCl], Σ_w = 50.3 c.u. 314

List of Figures

Figure 1.1: Comparison of radial geometrical factors (*J*) for a Compensated Dual Resistivity (CDR) LWD tool (Anderson, 2001) and the LWD Sigma tool under study in the case of conductive invasion. 17

Figure 2.1: The LWD tool with details about detectors used for Sigma logging.50

Figure 2.2: Three-detector signals for an LWD Sigma measurement in a 34-p.u. water-saturated sandstone. The inset at the bottom left compares the slope of decay signals at late times, where the difference in slopes is due to tool and borehole effects dependent upon detector position and measured particles.....51

Figure 2.3: Comparison of wireline (a) and LWD Sigma (b) tools and channels.52

Figure 2.4: Short-spaced gamma-ray detector time decays for the Longhorn wireline tool and the LWD tool under study.....53

Figure 2.5: Three-dimensional (a) and azimuthal (b) detector sensitivity maps for the LWD Sigma tool in a 34-p.u. fresh water-bearing sandstone formation. In the 3D map, bright areas indicate high sensitivity.....54

Figure 2.6: Synthetic Sigma logs of the (a) near thermal-neutron, (b) long-spaced gamma-ray, and (c) short-spaced gamma-ray detectors of the LWD tool. The yellow square lines identify the full-response apparent Sigma for each formation. Track (d) shows the volumetric composition of the rocks in the sequence. Blue, green, and red identify water, oil, and gas, respectively. The depth interval between points on these synthetic logs can be irregular because they are plotted at the true 50% axial response of the measurement, which varies at each depth.....55

Figure 2.7: Uncorrected apparent Sigma versus intrinsic Sigma, for MCNP simulations and for experimental test-pit measurements acquired with the LWD tool under study. 56

Figure 2.8: Apparent Sigma calculated from MCNP simulations as a function of borehole fluid Sigma and tool standoff, *S.O.* Sketches on top describe the two standoff configurations. Panel (a) describes standoff at the back of the tool (sector opposite to detector side), while panel (b) describes standoff at the front of the tool (detector side). 57

Figure 2.9: Invasion maps for a vertical well for (a) *TAB* equal to 360 seconds (0.1 hr) and, (b) *TAB* equal to 10800 seconds (3 hr). From left to right: simulations of mud-filtrate invasion in rock types I, II, and III. The dashed line identifies maximum sensitivity of LWD Sigma measurement for the tool under study. 58

Figure 2.10: Invasion maps for WBM at 3447.48-kPa (500 psi) overbalance pressure invading an oil-bearing sandstone formation for $K_v/K_h = 1$ (a) and $K_v/K_h = 2$ (b) after 10800 seconds (3 hr) of exposure. Formation type II. Notice the slight asymmetric shape of the invasion profile for the case of permeability anisotropy. 59

Figure 2.11: Radial geometrical factors for the three detectors of the LWD Sigma tool in a 34-p.u. freshwater-saturated sandstone formation. 60

Figure 2.12: Numerical simulations of LWD Sigma (b) and phase resistivity (c) in the case of piston-like invasion of 200-kppm [NaCl] brine in a 20-p.u. oil-bearing shaly sand formation. Track (a) displays the assumed petrophysical model. 61

Figure 2.13: Numerical simulations of LWD Sigma (b) and phase resistivity (c) in the case of piston-like invasion of 30-kppm [NaCl] brine in a 20-p.u. oil-bearing shaly sand formation. Track (a) displays the assumed petrophysical model. 62

Figure 3.1: Comparison of Monte Carlo simulated (red makers) and fast-forward simulated (solid dark orange line) multi-detector time decays corresponding to measurements in a 10-c.u. material. The green and blue solid lines describe pre-calculated Monte Carlo time decays for the three detectors of the LWD Sigma tool, which are used to approximate the tool response in the material of intermediate absorption cross section. 101

Figure 3.2: Multi-detector gamma-ray and thermal-neutron time decay library for the LWD Sigma tool under consideration. Time decays are the result of 2000-μs Monte Carlo calculated single-pulse decays superposed in time to follow the pulsing scheme of the actual multi-function LWD tool.102 102

Figure 3.3: Thermal-neutron absorption (SSn and LSn detectors) and thermal-neutron (Near detector) FSFs corresponding to materials of different absorption cross sections. (a) Shows radially and azimuthally integrated FSFs along the tool, whereas (b) shows vertically and azimuthally integrated FSFs as a function of radial distance into the formation. Note: the vertical axis on panel (a) cannot be shown because the position of the source and detectors of the commercial tool under study is confidential. 103

Figure 3.4: Comparison of multi-detector Monte Carlo simulated (blue solid lines), fast-forward simulated (green solid lines), and test-pit measured (red markers) time decays for two materials of low and high absorption cross section. The calculation of each Monte Carlo time decay takes approximately 10 hours of CPU time, while the calculation of each fast-forward modeled time decay takes approximately 0.25 seconds....104

Figure 3.5: Experimental facility used to emulate piston-like invasion. The concentric steel liners are used to physically separate virgin- and invasion-zone fluids. 105

Figure 3.6: Monte Carlo simulated multi-detector pulsed-source time decays for various piston-like radial lengths of invasion into a 34-p.u. sandstone formation. The rock is fresh water-saturated in the virgin zone, and 200-kppm [NaCl] brine saturated in the invasion zone.....106

Figure 3.7: Three-detector (from left to right) time decay measurements at various radial lengths of invasion (from top to bottom) for 200-kppm [NaCl] brine invading a fresh-water saturated 34-p.u. sandstone block. The black dashed line identifies MCNP-calculated time decays including the liners in the test pit, which is to be compared to the actual test-pit measurements shown in red markers. The blue solid line shows MCNP-calculated time decays without including the liners, which is to be compared to the fast-forward simulations shown in green solid lines.107

Figure 3.8: Apparent Sigma as a function of radial length of invasion derived from Monte Carlo (MC) and fast-forward (FF) simulated time decays shown in **Figure 3.7**. 108

Figure 3.9: Comparison of apparent Sigma from Monte Carlo and fast-forward modeled time decays corresponding to 200-kppm [NaCl] brine invading oil-bearing 34-p.u. (left panel) and 17-p.u. (right panel) sandstone formations. The contrast between invasion- and virgin-zone Sigma is 25 c.u. and 12 c.u. for the 34-p.u. and 17-p.u. cases, respectively. The blocky dark green shade and numbers in the middle describe the radial length of invasion at each depth level, ranging from no invasion at the top to 38.1 cm (15 in) at the bottom.....109

Figure 3.10: Comparison of apparent Sigma from Monte Carlo and fast-forward simulated time decays corresponding to 200-kppm [NaCl] brine invading 30-p.u. gas-bearing sandstone formations. The blocky light-colored shade and numbers on the right identify the radial length of invasion at each depth level, ranging from no invasion at the top to 38.1 cm (15 in) at the bottom.....110

Figure 3.11: (a) Sketch of 16 ramp-up radial invasion cases in the range of no invasion to a 38.1-cm maximum radial extent ramp-up invasion profile, and (b) Sigma logs calculated from Monte Carlo and fast-forward simulated time decays for each invasion profile. Dashed red lines describe the shapes of intermediate invasion profiles.....111

Figure 3.12: Multi-detector Sigma logs (a), (b), (c) calculated from Monte Carlo (white markers) and fast-forward (gray solid lines) simulated time decays for an alternating sequence of 15.24-cm (6-in) shale (33.9 c.u.) and oil-bearing sandstone (9.65 c.u.) formations. The blocky yellow line identifies the apparent Sigma values for each bed as if acquired in thick homogeneous formations. The panel on the right (d) shows volumetric rock compositions. Blue and green colors represent water and oil volumes, respectively.....112

Figure 3.13: Multi-detector Sigma logs (a), (b), (c) calculated from simulated Monte Carlo (white markers) and fast-forward (gray solid lines) time decays in sequence involving carbonate and siliciclastic formations, variable porosities, and oil, gas, and brine saturated formations. The blocky yellow line identifies the apparent Sigma values for each formation as if acquired in thick homogeneous formations. The panel on the right (d) shows volumetric rock compositions. Blue, red, and green colors represent water, gas, and oil volumes, respectively.....113

Figure 3.14: Multi-detector Sigma logs (a), (b), (c) calculated from simulated Monte Carlo (white markers) and fast-forward (gray solid lines) time decays in a sequence of 76.2-cm (2.5-ft) bedded shale and sandstone formations affected by invasion. Blocky green and blue solid lines indicate apparent virgin- and invasion-zone Sigma values for each formation, respectively. Radial length of invasion is represented by the light yellow blocks in each sandstone formation, which is 20.32 cm (8 in) at the top sand layers, and 10.16 cm (4 in) for the rest of the sand layers. The panel on the right (d) shows the volumetric rock composition. Red, green, and blue colors represent gas, oil, and water volumes, respectively. 114

Figure 3.15: Multi-detector Sigma logs (a), (b), (c) calculated from Monte Carlo (white markers) and fast-forward (gray solid lines) time decays for an 85^{o}-deviated well penetrating a sequence of 30.48-cm (true stratigraphic thickness, TST) sandstone-shale alternations. Blocky green lines identify apparent Sigma values for each bed as if measured in a thick homogeneous block of the material. The panel on the right (d) shows the volumetric rock composition of the sub-layers in the model.....115

Figure 3.16: (a) Sketch of 85^{o} deviated well penetrating the sequence of layered formations described in **Table 3.7**. The inset on the right shows the shape of the assumed asymmetric invasion front. (b) Forward-model simulated multi-detector apparent Sigma images and fast-forward (blue solid line) and Monte Carlo (red makers) calculated apparent Sigma log for the upper sector of the LWD tool. The maximum difference between the two results is observed at the thermal-neutron detector in high-Sigma shale thin layers because of higher statistical noise in both MC and FF models. Radial length of invasion is 20.32 cm at the bottom sector and 0 cm at the top sector for all the permeable formations in the sequence.116

Figure 4.1: (a) Synthetic decays for the 32 pulses of the pulsed-source LWD tool under study for the case of 34-p.u. fresh-water bearing sandstone invaded 12.7-cm (5-in) deep by 200-kppm [NaCl] WBM, and (b) portion of the actual time decays used for Sigma calculation and defined as the measurement vector, **d,** in this dissertation (corresponds to the portion of the signal inside the dashed square at the top). 154

Figure 4.2: Data vector, **d**, for one measurement of the multi-detector LWD Sigma tool (burnt-orange solid line) and corresponding relative (magenta solid line) and modified (red solid line) diagonals of the data weight matrix, $\mathbf{W}_d$. The dashed horizontal black line indicates the similar importance assigned to the late-time components of the three signals. 155

Figure 4.3: Simulated multi-detector signals for two different virgin rocks (Σ_v), invaded by fluids with different salinity (Σ_i) at two different radial lengths of invasion (r_i). This figure illustrates the possible non-uniqueness of the multi-detector decay measurements and the importance of using a reference value for invasion-zone Sigma (Σ_i) to limit the region of solution space.....156

Figure 4.4: One-dimensional radial inversion flowchart for multi-detector thermal-neutron and gamma-ray decays. Σ_i is calculated invasion-zone Sigma, Σ_{LSn} and Σ_{Near} are borehole- and diffusion-corrected LSn and Near detector Sigmas, respectively. $\mathbf{m}_R$ is model properties reference vector, $\mathbf{m}^o$ is an initial smart guess for the model properties, **d** is the numerically simulated set of multi-detector decays, $\mathbf{d^o}$ is the measured multi-detector set of decays, $\mathbf{m}^k$ is the set of model properties at iteration *k*. 157

Figure 4.5: Radial geometrical factors for the SSn (yellow solid line), LSn (blue solid line), and Near (red solid line) detectors, respectively, of the LWD tool under study in a 34-pu. Fresh water saturated sandstone formation calculated using the Monte Carlo N-Particle (MCNP, X-5 Monte Carlo Team, 2003) code.....158

Figure 4.6: Relative error on estimated virgin Sigma as a function of relative error on guessed invasion-zone Sigma, ($\Delta\Sigma_i / \Sigma_i$), and radial length of invasion for invasion- and virgin-zone Sigma contrast of 5 c.u. (a) and 25 c.u. (b), and relative error on radial length of invasion as a function of relative error on guessed invasion-zone Sigma, ($\Delta\Sigma_i / \Sigma_i$), and radial length of invasion for invasion- and virgin-zone Sigma contrast of 5 c.u. (c) and 25 c.u. (d). Colors indicate different radial lengths of invasion. 159

Figure 4.7: Relative error on virgin Sigma not corrected for invasion effects induced by piston-like invasion of salty filtrate as a function of radial length of invasion and invasion-virgin zone Sigma contrast. 160

Figure 4.8: (a) Multi-detector synthetic signal without noise (red solid line) and simulated noisy signal in a 10-c.u. material while drilling at *ROP* equal to 0.17 cm/s (blue markers) and 1.7 cm/s (green markers), and (b) fractional uncertainty $\mathbf{f} = \sqrt{N}/N$ for both penetration rates described in the top panel. 161

Figure 4.9: (a) Estimated Virgin Sigma and (b) radial length of invasion as a function of actual radial length of invasion and flushed/virgin Sigma contrast for the cases of brines of different salinities that are piston-like invading a 34-p.u. freshwater-bearing sandstone formation. The colors represent Sigma contrast between virgin and invasion zones. The vertical bars represent the standard deviation of the distribution of estimated properties after a multiple realization study on synthetic decays with noise corresponding to drilling at 0.255 cm/s (30 fph). The bar midpoints represent the mean of the properties' distribution. 162

Figure 4.10: (a) Virgin Sigma Confidence Index (*CI*) as a function of radial length of invasion and Sigma contrast, and (b) radial length of invasion Confidence Index (*CI*) as a function of radial length of invasion and Sigma contrast. The colors represent contrast between virgin- and invasion-zone Sigmas for brines of different salinities piston-like invading a 34-p.u. freshwater-bearing sandstone formation.....163

Figure 4.11: Laboratory formation used to simulate invasion of 200-kppm [NaCl] brine into a fresh water saturated 34-p.u. sandstone. The metallic cylinders in the center of the sandstone block are 1-mm thick steel liners used to physically separate virgin and invasion zones. These liners affect measured multi-detector time decays. 164

Figure 4.12: Reconstruction (red solid lines) of test-pit experimental measurements (colored markers). Insets at the top left of each diagram show the estimated virgin Sigma and radial length of invasion with standard deviations. Insets at the bottom right of each diagram describe the actual model properties at radial lengths of invasion corresponding to 0 cm (a), 5.08 cm (b), 10.16 cm (c), and full invasion (d) of 200-kppm [NaCl] brine into a 34-p.u. fresh-water saturated sandstone. Note: misfit between actual and inverted Sigma values are due to the presence of steel liners separating invaded and uninvaded zones in the experimental setup, which are not included in the inversion model.....165

Figure 4.13: (a) Diagram of layers and radial invasion, (b) measured and fitted multi-detector decays, (c) simulated porosity logs in sandstone units, and (d) borehole and diffusion corrected multi-detector Sigma logs for Synthetic Case I. Layer thickness is 2.43 m (8 ft). Each set of decays is simulated at the bed center to avoid shoulder-bed effects. 166

Figure 4.14: Inversion results for Synthetic Case I. (a), (b), and (c) synthetic (blue solid line) and fitted (red solid line) apparent Sigma for the SSn, LSn, and Near detectors, respectively, and true model (blue dashed line) and estimated (red dashed line) virgin formation Sigma with error bars, and reference invasion-zone Sigma (black dashed line), (d) Multi-detector diffusion- and borehole-corrected Sigma logs, and model virgin-zone (magenta dashed line) and invasion-zone (blue dashed line) Sigma, (e) Actual (blue dashed line) and estimated (red dashed line) radial length of invasion with error bars, (f) Diagram of borehole, invasion, and formation, (g) Actual (blue solid line), estimated (red solid line), and SSn-calculated (blue dashed line) water saturation. SSn-calculated water saturation represents the estimated water saturation calculated directly from the borehole- and diffusion-corrected SSn Sigma log without correction for invasion effects. 167

Figure 4.15: (a) Diagram of layers and radial invasion, (b) synthetic (blue solid lines) and fitted (red solid lines) multi-detector decays, (c) simulated LWD density (red solid line), neutron (blue solid line), squared averaged (green solid line), and actual porosity (green dashed line) logs in limestone units, (d) borehole- and diffusion-corrected multi-detector (SSn, LSn, and N) Sigma logs , calculated matrix Sigma log (orange solid line), and actual virgin- and invasion-zone Sigmas per layer (magenta and blue dashed lines, respectively), and (e) rock volumetric mineral and fluid compositions for Synthetic Case II. 168

Figure 4.16: Inversion results for Synthetic Case II. (a), (b), and (c) synthetic (blue solid line) and fitted (red solid line) apparent Sigma for the SSn, LSn, and Near detectors, respectively, and true model (blue dashed line) and estimated (red dashed line) virgin formation Sigma with error bars, and reference invasion-zone Sigma (black dashed line), (d) Multi-detector diffusion- and borehole-corrected Sigma logs, and model virgin-zone (magenta dashed line) and invasion-zone (blue dashed line) Sigma, (e) True (blue dashed line) and estimated (red dashed line) radial length of invasion with error bars, (f) Diagram of borehole, invasion, and formation, (g) True (blue solid line), estimated (red solid line), and SSn-calculated (blue dashed line) water saturation. The SSn-calculated water saturation represents the estimated water saturation calculated directly from the borehole- and diffusion-corrected SSn Sigma log without correction for invasion effects. 169

Figure 4.17: Field case multi-detector fitted (red solid line) and measured (black markers) time decays in the 3.048-m (10-ft) section corresponding to the gas-bearing formation penetrated by a 40^{o} deviated well. 170

Figure 4.18: One-dimensional inversion-based interpretation of multi-detector decay curves in a 10-ft gas-bearing formation. SBM filtrate salinity is 137 kppm [NaCl equivalent] and filtrate Sigma is 72.3 c.u. Gas Sigma calculated at reservoir and temperature pressure equals 2 c.u. (a) Borehole and diffusion corrected multi-detector Sigma logs (N, SSn, and LSn) and assumed invasion-zone Sigma, (b) estimated virgin Sigma (green squared log) with error bars, assumed invasion Sigma (black markers), and confidence index (*CI*), (c) estimated radial length of invasion with confidence index and error bars, (d) diagram of estimated radial length of invasion, borehole, and formation, (e) neutron (blue solid line), gamma-gamma density (red solid line), averaged squared (solid green line), and neutron-gamma density (magenta solid line) porosity logs in limestone units, (f) high-frequency phase resistivity logs, and (g) mineral composition from spectroscopy and calculated water saturation from SSn Sigma (light-blue solid line), resistivity (dark-blue solid line), and estimated after correcting formation Sigma for invasion effects with the 1D radial inversion (black dashed line). .171

Figure 5.1: Sketch of Near (green), SSn (blue), and LSn (red) detector spatial sensitivity projected on thinly bedded formations without invasion (a), and with shallow invasion in permeable layers (b). The figure illustrates the complexity of estimating layer-by-layer properties under an acquisition condition where actual formation properties are simultaneously masked by shoulder-bed and shallow-invasion effects. 208

Figure 5.2: Representation of intrinsic Sigmas of the assumed siliciclastic sequence of 0.1524-m (0.5 ft) thick formations with shallow invasion in the permeable layers for Synthetic Case I. Water-based mud filtrate of 150 kppm [NaCl] invades gas-bearing formations of different connate water saturation. High-Sigma (dark) uninvaded formations represent shales. 209

Figure 5.3: Inversion results for Synthetic Case I. (a), (b), and (c) Measured (blue solid line) and fitted (red solid line) apparent Sigma for the SSn, LSn, and Near detectors, respectively, and true model (blue dashed line) and estimated (red dashed line) virgin formation Sigma with error bars, and reference invasion-zone Sigma (black dashed line). (d) Multi-detector diffusion- and borehole-corrected Sigma logs, model virgin-zone (magenta dashed line) and invasion-zone (blue dashed line) Sigma, (e) actual (blue dashed line) and estimated (red dashed line) radial length of invasion with error bars, (f) diagram of borehole (brown), invasion (blue), and formation (yellow), and (g) actual (blue solid line), estimated (red solid line), and SSn-calculated (blue dashed line) water saturation. SSn-calculated water saturation represents the estimated water saturation calculated directly from the borehole- and diffusion-corrected SSn Sigma log at bed centers, without correcting for coupled shallow invasion and shoulder-bed effects.....210

Figure 5.4: Representation of intrinsic Sigmas of assumed 0.1524-m (0.5 ft) thick oil-bearing sandstone formations embedded within shale formations and penetrated by an 85^{o} deviated well for Synthetic Case II. Water-based mud of 200 kppm [NaCl] invades oil-bearing formations of different connate water saturation. The radial profile of invasion is assumed azimuthaly uniform in the three permeable layers.....211

Figure 5.5: (a) Upper sector apparent multi-detector LWD Sigma logs for univaded (solid lines) and invaded (dashed lines) oil-bearing sandstone formations in Synthetic Case II. (b) Multi-detector LWD Sigma images in virgin formations, and (c) Multi-detector LWD Sigma images assuming invasion of 5.08 cm, 10.16 cm, and 20.32 cm in the three oil-bearing sandstone formations. 212

Figure 5.6: Inversion results for Synthetic Case II. (a), (b), and (c) Measured (blue solid line) and fitted (red solid line) apparent Sigma for the SSn, LSn, and Near detectors, respectively, and true model (blue dashed line) and estimated (red dashed line) virgin formation Sigma with error bars, and reference invasion-zone Sigma (black dashed line). (d) Multi-detector diffusion- and borehole-corrected Sigma logs, model virgin-zone (magenta dashed line) and invasion-zone (blue dashed line) Sigma, (e) actual (blue dashed line) and estimated (red dashed line) radial length of invasion with error bars, (f) diagram of borehole (brown), invasion (blue), and formation (yellow), and (g) actual (blue solid line), estimated (red solid line), and SSn-calculated (blue dashed line) water saturation. SSn-calculated water saturation represents the estimated water saturation calculated directly from the borehole- and diffusion-corrected SSn Sigma log at bed centers, without correcting for coupled shallow invasion and shoulder-bed effects.....213

Figure 5.7: Well trajectory and borehole- and diffusion-corrected SSn Sigma log for Field Case I. The section of interest corresponds to the low-Sigma gas-bearing thinly bedded section penetrated at an angle of approximately 45^{o}. Multi-detector Sigma measurements are mostly affected by shoulder-bed and shallow-invasion effects, and to some extent also by well-deviation effects. 214

Figure 5.8: Set of LWD measurements corresponding to Field Case I. (a) Natural gamma-ray log, (b) compensated density image, (c) neutron and density porosity logs in limestone p.u., (d) high-frequency phase (PH) resistivity logs, (e) spectroscopy log, (f),(g), and (h) background-corrected field time-decays for the SSn, LSn, and Near detectors, respectively, (i) borehole- and diffusion-corrected multi-depth-of-investigation, MDOI, Sigma logs, and (j) time of exposure to mud filtrate before the acquisition of LWD measurements. 215

Figure 5.9: 2D inversion-based interpretation of multi-detector decay curves for Field Case I. SBM filtrate salinity is 137 kppm [NaCl equivalent] and filtrate Sigma is 72.3 c.u. Gas Sigma calculated at reservoir and temperature pressure equals 2 c.u. (a) Borehole and diffusion corrected multi-detector Sigma logs (Near, SSn, and LSn) and assumed invasion-zone Sigma, (b) estimated virgin-zone Sigma (green squared log) with error bars, assumed invasion-zone Sigma (black markers), and confidence index (*CI*), (c) estimated radial length of invasion with confidence index and error bars, (d) diagram of borehole (brown), invasion (blue), and formation (yellow), (e) neutron (blue solid line), gamma-gamma density (red solid line), averaged squared (solid green line), and neutron-gamma density (magenta solid line) porosity logs in limestone units, (f) high-frequency phase resistivity logs, (g) mineral composition from spectroscopy and calculated water saturation from SSn Sigma (light-blue solid line), resistivity (dark-blue solid line), and estimated after correcting formation Sigma for shallow-invasion, shoulder-bed, and well-deviation effects using the 2D inversion (black dashed line), and (h) comparison of the shallowest sensing phase resistivity log (P16H) and SSn Sigma log. 216

Figure 5.10: Well trajectory and borehole- and diffusion-corrected SSn Sigma log for Field Case II. The section of interest corresponds to the low-Sigma oil-bearing thinly bedded section penetrated at an angle of approximately 70^{o}. Multi-detector Sigma measurements are mostly affected by shoulder-bed and well-deviation effects. The effect of filtrate invasion is not strong in this field example due to the similar absorption cross section of low-salinity mud filtrate and oil-bearing formations with partial water saturations. 217

Figure 5.11: 2D inversion-based interpretation of multi-detector decay curves for Field Case II. SBM filtrate salinity is 46 kppm [NaCl equivalent] and filtrate Sigma is 38 c.u. (a) Borehole and diffusion corrected multi-detector Sigma logs (Near, SSn, and LSn) and assumed invasion-zone Sigma, (b) estimated virgin-zone Sigma (green squared log) with error bars, assumed invasion-zone Sigma (black markers), and confidence index (*CI*), (c) estimated radial length of invasion with confidence index and error bars, (d) diagram of borehole (brown), invasion (blue), and formation (yellow), (e) neutron (blue solid line), gamma-gamma density (red solid line), averaged squared (solid green line), and neutron-gamma density (magenta solid line) porosity logs in limestone units, (f) high-frequency phase resistivity logs, (g) mineral composition from spectroscopy and calculated water saturation from SSn Sigma (light-blue solid line), resistivity (dark-blue solid line), and estimated after correcting formation Sigma for shallow-invasion, shoulder-bed, and well-deviation effects using the 2D inversion (black dashed line), and (h) comparison of the shallowest sensing high-frequency, phase resistivity log (P16H) and SSn Sigma log. 218

Figure 6.1: SNUPAR-derived bulk inverse of migration length (ξ_{bulk}) as a function of limestone water-filled porosity. 257

Figure 6.2: Comparison of ξ calculated using SNUPAR, a linear mixing law, and the new mixing law in equation 6.4 for the case of a sandstone matrix fully saturated with (a) fresh water and (b) gas at 150 ^{o}F and 6894.75 kPa (1000 psia) as a function of total porosity. Gas density is 0.04 g/cm^3 in (b). 258

Figure 6.3: Inverse of migration length for hydrocarbons of different gas molar fractions, χ_g, (or lightness) in the range of dry gas to black oil and water of various electrolyte concentrations as a function of pressure and temperature. 259

Figure 6.4: Comparison of linear mixing approximation for the inverse of migration length of mixtures of solid components *A* and *B* to SNUPAR calculations. The minerals considered for components *A* and *B* are quartz, calcite, and wet chlorite. 260

Figure 6.5: Comparison of calculated ξ using the new mixing law (dashed lines), SNUPAR (solid lines), and a linear-mixing law (dotted lines) for (a) water-filled and (b) gas-filled rocks with various matrix compositions; using η as a function of C_{sh} enables the accurate reproduction of SNUPAR results, which deviate significantly from a linear mixing law. 261

Figure 6.6: SNUPAR calculated relationship between ξ_f and ρ_f for various hydrocarbon and water mixtures displaying a linear relationship between both nuclear properties.....262

Figure 6.7: Results for Synthetic Case I. Calculated porosity using the RMS method (left) and the new method to approximate total porosity (right) in clean sandstone formations saturated with (a) water, and with (b) gas....263

Figure 6.8: Results for Synthetic Case I. Calculated porosity using the RMS method (left) and the new equation for porosity (right) in (a) a 50% Chlorite-50% Quartz formation saturated with water, and in (b) a 100% wet Chlorite formation saturated with methane.....264

Figure 6.9: Results for Synthetic Case II. (a) Simulated gamma-ray spectroscopy log, (b) simulated thermal-neutron and density porosity logs in limestone p.u., and RMS averaged total porosity, (c) matrix-corrected neutron and density logs, and matrix- and fluid-corrected estimation of total porosity, (d) comparison of RMS averaged, matrix- and fluid-corrected, and actual model porosities, and (e) assumed mineral and fluid volumetric model.....265

Figure 6.10: Field Case I. (a) Calculated C_{sh} from gamma-ray logs compared to core C_{sh}, (b) induction resistivity logs, (c) neutron and density porosity logs in limestone p.u., (d) matrix-corrected neutron and porosity logs using the new method, (e) comparison of RMS average porosity, matrix- and fluid-corrected porosity using the new method to NMR and core porosity, and (f) calculated fluid density. 266

Figure 6.11: Field Case II. (a) Mineral composition from LWD gamma-ray spectroscopy measurements, (b) LWD high-frequency phase resistivity logs, (c) LWD neutron and density porosity logs in limestone p.u., (d) matrix-corrected neutron and porosity logs using the new method, (e) comparison of RMS average porosity, and matrix- and fluid-corrected porosity using the new method, and (f) calculated fluid density. ...267

Figure 6.12: Field Case III. (a) Mineral compositions from wireline gamma-ray spectroscopy compared to XRD mineral volume fractions, (b) resistivity logs, (c) neutron and density porosity logs in limestone p.u., (d) matrix-corrected neutron and density logs using the new method, (e) comparison of RMS porosity and matrix- and fluid-corrected total porosity using the new method compared to core measurements, (f) calculated fluid density, (g) calculated matrix density compared to core measurements, and (h) calculated water saturation. 268

Figure 6.13: Field Case IV. (a) Mineral compositions from wireline gamma-ray spectroscopy compared to XRD mineral volume fractions, (b) resistivity logs, (c) neutron and density porosity logs in limestone p.u., (d) matrix-corrected neutron and density logs using the new method, (e) comparison of RMS porosity and matrix- and fluid-corrected total porosity using the new method compared to core and NMR measurements, (f) calculated fluid density, (g) calculated matrix density compared to core measurements, and (h) calculated water saturation.269

Figure 7.1: LWD measurement suite in a highly deviated North Sea well. Sigma logs correlate with resistivity measurements but lack of artificial effects such as horns and separation at bed boundaries. Sigma logs show very good agreement with neutron, density porosity, gamma-ray, and gamma-ray spectroscopy logs. 315

Figure 7.2: Sketch of commercial LWD multi-function tool with emphasis on the nuclear measurement suite (Sigma, neutron, and density). 316

Figure 7.3: Comparison of radial and vertical sensitivity functions for multi-detector density, neutron, and Sigma measurements for the LWD tool under study in a 28 p.u. fresh water-saturated limestone formation. 317

Figure 7.4: Light hydrocarbon compound volume for various fluid types, χ_g, as a function of pressure and temperature. Results calculated from a simulated flash calculation considering mixtures of methane and decane of gas molar fractions in the range of 0 to 1. 318

Figure 7.5: Workflow to perform invasion, shoulder-bed, and well-deviation effect correction on multi-detector Sigma, density, and thermal neutron porosity measurements, and post-integration using a nuclear solver to estimate fluid type and water pore volume. 319

Figure 7.6: Inversion results for Synthetic Case I. (a) Simulated (blue) and reconstructed (red) multi-detector time decays, (b) borehole- and diffusion-corrected Sigma logs, (c) simulated and reconstructed Near and Far neutron inverse of migration length logs, (d) simulated and reconstructed short-spaced (SSg) and long-spaced (LSg) gamma density logs, (e) sketch of borehole, invasion profile, and virgin formation, corrected virgin- and invaded-zone (f) Sigma, (g) neutron, and (h) density logs, (i) virgin-zone volumetric model, and (j) comparison of model and estimated water saturation. On track (i): the color scale on bottom represents hydrocarbon type. Blue color represents water. Matrix minerals are chlorite (gray), limestone (light green), and quartz (orange). Well deviation is 80^o. 320

Figure 7.7: Inversion results for Synthetic Case II. (a) Simulated (blue) and reconstructed (red) multi-detector time decays, (b) borehole- and diffusion-corrected Sigma logs, (c) simulated and reconstructed Near and Far neutron inverse of migration length logs, (d) simulated and reconstructed short-spaced (SSg) and long-spaced (LSg) gamma density logs, (e) sketch of borehole, invasion profile, and virgin formation, corrected virgin- and invaded-zone (f) Sigma, (g) neutron, and (h) density logs, (i) virgin-zone volumetric model, and (j) comparison of model and estimated water saturation. On track (i): the color scale on bottom represents hydrocarbon type. Blue color represents water. Matrix minerals are chlorite (gray), limestone (light green), and quartz (orange). Well deviation is 0^{o}. 321

Figure 7.8: Reconstructed field measurements and corrected layer-by-layer nuclear properties for Field Case I. (a) Measured (blue) and reconstructed (red) multi-detector time decays, (b) borehole- and diffusion-corrected Sigma logs, (c) measured and reconstructed Near and Far neutron inverse of migration length logs, (d) measured and reconstructed short-spaced (SSg) and long-spaced (LSg) gamma density logs, (e) sketch of borehole, invasion profile, and virgin formation, corrected virgin- and invaded-zone (f) Sigma, (g) neutron, and (h) density logs, respectively, and (i) virgin-zone volumetric model. On track (i): the color scale on bottom represents hydrocarbon type. Blue color represents water. Matrix minerals are clay (gray), limestone (light green), and quartz (orange). 322

Figure 7.9: Inversion results for Field Case I. (a) Estimated radial length of invasion with error bars, (b) borehole- and diffusion-corrected measured Sigma logs, (c) matrix-corrected neutron and density porosity logs, and matrix- and fluid-corrected estimated total porosity, (d) comparison of water saturation estimated form resistivity logs and using the introduced workflow, (e) virgin-zone volumetric model, (f) field and simulated high-frequency resistivity logs and layer-by-layer resistivity, and confidence index on virgin-zone Sigma. 323

Figure 7.10: Reconstructed field measurements and corrected layer-by-layer nuclear properties for Field Case II. (a) Measured (blue) and reconstructed (red) multi-detector time decays, (b) borehole- and diffusion-corrected Sigma logs, (c) measured and reconstructed Near and Far neutron inverse of migration length logs, (d) measured and reconstructed short-spaced (SSg) and long-spaced (LSg) gamma density logs, (e) sketch of borehole, invasion profile, and virgin formation, corrected virgin- and invaded-zone (f) Sigma, (g) neutron, and (h) density logs, respectively, and (i) virgin-zone volumetric model. On track (i): the color scale on bottom represents hydrocarbon type. Blue color represents water. Matrix minerals are clay (gray), limestone (light green), and quartz (orange).324

Figure 7.11: Inversion results for Field Case II. (a) Estimated radial length of invasion with error bars, (b) borehole- and diffusion-corrected measured Sigma logs, (c) matrix-corrected neutron and density porosity logs, and matrix- and fluid-corrected estimated total porosity, (d) comparison of water saturation estimated form resistivity logs and using the introduced workflow, (e) virgin-zone volumetric model, (f) field and simulated high-frequency resistivity logs and layer-by-layer resistivity, and confidence index on virgin-zone Sigma. 325

Figure 7.12: Reconstructed field measurements and corrected layer-by-layer nuclear properties for Field Case III. (a) Measured (blue) and reconstructed (red) multi-detector time decays, (b) borehole- and diffusion-corrected Sigma logs, (c) measured and reconstructed Near and Far neutron inverse of migration length logs, (d) measured and reconstructed short-spaced (SSg) and long-spaced (LSg) gamma density logs, (e) sketch of borehole, invasion profile, and virgin formation, corrected virgin- and invaded-zone (f) Sigma, (g) neutron, and (h) density logs, respectively, and (i) virgin-zone volumetric model. On track (i): the color scale on bottom represents hydrocarbon type. Blue color represents water. Matrix minerals are clay (gray), limestone (light green), and quartz (orange).326

Figure 7.13: Inversion results for Field Case III. (a) Estimated radial length of invasion with error bars, (b) borehole- and diffusion-corrected measured Sigma logs, (c) matrix-corrected neutron and density porosity logs, and matrix- and fluid-corrected estimated total porosity, (d) comparison of water saturation estimated form resistivity logs and using the introduced workflow, (e) virgin-zone volumetric model, (f) field and simulated high-frequency resistivity logs and layer-by-layer resistivity, and confidence index on virgin-zone Sigma. 327

Figure 7.14: Reconstructed field measurements and corrected layer-by-layer nuclear properties for Field Case IV. (a) Measured (blue) and reconstructed (red) multi-detector time decays, (b) borehole- and diffusion-corrected Sigma logs, (c) measured and reconstructed Near and Far neutron inverse of migration length logs, (d) measured and reconstructed short-spaced (SSg) and long-spaced (LSg) gamma density logs, (e) sketch of borehole, invasion profile, and virgin formation, corrected virgin- and invaded-zone (f) Sigma, (g) neutron, and (h) density logs, respectively, and (i) virgin-zone volumetric model. On track (i): the color scale on bottom represents hydrocarbon type. Blue color represents water. Matrix minerals are clay (gray), limestone (light green), and quartz (orange).328

Figure 7.15: Inversion results for Field Case IV. (a) Density-derived caliper, (b) borehole- and diffusion-corrected measured Sigma logs, (c) azimuthal gamma-ray image and bed boundary locations, (d) matrix-corrected neutron and density porosity logs, and matrix- and fluid-corrected estimated total porosity, (e) comparison of water saturation estimated form resistivity logs and using our workflow, (f) virgin-zone volumetric model, (g) field and simulated high-frequency resistivity logs and layer-by-layer resistivity, and confidence index on virgin-zone Sigma...329

Figure 7.16: Inversion results for cased-hole Field Case V. (a) Mineral volumetric concentrations from gamma-ray spectroscopy logs, (b) natural gamma-ray log, (c) matrix-corrected neutron and density porosity logs, and matrix- and fluid-corrected estimated total porosity, (d) water saturation calculated form resistivity logs and using our nuclear solver, (e) a sketch of in-situ fluid distributions and fluid type; the color scale on bottom represents hydrocarbon type and blue represents water, (f) induction resistivity logs, and measured and reconstructed (g) Sigma, (h) compensated density, and (i) compensated neutron logs.....330

Chapter 1: Introduction

Estimation of water saturation is one of the most important tasks in formation evaluation because it has a direct impact on reserves calculation and reservoir performance. Typically, resistivity-based methods are used to calculate water saturation in porous media. The difficulty of acquiring resistivity measurements in cased holes led to the development of Pulsed Neutron Capture (PNC) measurements to estimate formation Sigma. Chlorine, a strong thermal-neutron absorber, is commonly found in connate water and yields large values of Sigma. The contrast between connate water and hydrocarbon Sigma permits the calculation of water saturation using a linear mixing law. Recently, LWD Sigma measurements were introduced into the oil and gas industry. This dissertation seeks to advance the field of Sigma logging by expanding the knowledge and improving the petrophysical interpretation of LWD Sigma measurements. In this chapter, I review relevant literature in the field of Sigma logging, and breakthroughs in interpretation methods of borehole nuclear measurements that will be used as a reference to advance the interpretation of Sigma logs. The objectives, methods, and outline of the dissertation are also detailed in this chapter.

1.1 BACKGROUND

Sigma, also referred to as *macroscopic thermal neutron capture cross section*, is a nuclear property of a material that determines its ability to absorb low-energy neutrons. Sigma measurements are important in formation evaluation because, in the presence of

saline water (significant concentrations of NaCl), Sigma can be used to calculate water saturation. These measurements have historically been utilized to evaluate water saturation in cased-hole formations (Morris and Quinlan, 2005). Sigma logs are especially useful for the evaluation of low-resistivity, low-contrast (LRLC) reservoirs (Simpson and Menke, 2010). Sigma is also ideal for the evaluation of carbonates because textural parameters, which are difficult to calculate in carbonates due to the heterogeneous nature of these formations, are not needed to calculate water saturation from Sigma logs (Gyllensten et al., 2009).

Sigma logs can be integrated with resistivity logs in conventional reservoirs to assess water saturation in the absence of connate water samples (Aqivlera, 1979), or be used to perform resistivity-independent quantitative analyses such as calculations of water saturation. Formation resistivity is customarily inversely proportional to formation Sigma. The correlation between both measurements makes Sigma useful for qualitative analysis, such as geosteering. The similarities notwithstanding, both measurements have disparate volumes of investigation. Resistivity measurements have a larger volume of investigation than Sigma measurements (Griffiths, 2010). It then follows that Sigma logs are better suited to detect and evaluate thinly bedded formations traversed by deviated wells.

The potential of conventional Sigma logs in formation evaluation spearheaded the development of LWD Sigma logging as part of the measurements acquired by a pulsed-neutron, multi-function LWD tool (Weller et al., 2005). Multi-detector Sigma extends the physical basis of conventional Sigma as a means to evaluate presence of invasion (Gyllensten et al., 2009). The multi-function LWD tool has one thermal-neutron detector,

and two gamma-ray detectors at different spacing from the source. Differences in source-detector spacing and types of particles measured provide the tool with three distinct radial lengths of investigation. **Figure 1.1** compares the radial geometrical factors of the multi-detector Sigma measurements acquired by the LWD tool under study and the radial geometrical factors of phase and amplitude resistivity for a propagation tool in the case of conductive invasion. Observe that LWD Sigma measurements display high sensitivity to the presence of invasion in the near wellbore zone, and that resistivity measurements are only slightly sensitivity or insensitive to perturbations in the shallow near-wellbore zone. Array resistivity measurements are better suited to detect deeper invasion typically encountered in wireline logging conditions.

Qualitative analysis of multi-depth-of-investigation (MDOI) Sigma measurements, analogous to array resistivity logs, indicates presence of invasion. This feature of LWD Sigma has the potential to enable the assessment of radial length of invasion and virgin-zone Sigma in the near-wellbore area. El-Din et al. (2012) introduced a method to estimate radial length of invasion and virgin-zone Sigma. Their method enabled the correction of invasion-affected Sigma logs and improved the integration of Sigma and resistivity measurements. Mauborgne et al. (2013) applied the same method to identify the water-oil contact in a reservoir drilled with oil-based mud (OBM), and to estimate radial length of invasion.

Regardless of the many benefits of Sigma logging, interpretation of multi-detector Sigma logs can be difficult. Sigma logs can be affected by multiple factors, such as filtrate invasion, tool standoff, thermal-neutron diffusion, well deviation, and/or geometrical

effects due to presence of thinly bedded formations, the latter of which is referred to as shoulder-bed effects. Interpretation of thermal-neutron and gamma-ray time decays in thinly bedded formations is significantly complicated because each detector senses different fractions of the virgin and invasion zones of each layer. Additionally, low connate water salinities, approximately below 25 NaCl kppm, preclude the use of Sigma logs to estimate water saturation (Vail et al., 1996). Sufficient salt concentration is necessary in connate water to generate enough contrast between hydrocarbon and water Sigma and enable their differentiation.

Shoulder-bed and well-deviation effects were early recognized in the interpretation of resistivity logs (Suau et al., 1973). Most of the observations made in the study of shoulder-bed effects on resistivity measurements also extend to nuclear measurements. Shoulder-bed effects produce false separation of array measurements in uninvaded formations (Xiao et al., 2003). The effects are additionally accentuated in the case of deviated wells crossing thinly bedded formations (Hardman et al., 1987). Adjacent shaly formations can lead to hydrocarbon-bearing thinly bedded formations being overlooked (Warrillow et al., 1995). Experimental measurements and analytical models (Chemali et al., 1983; Frenkel et al. 1997) were proposed to correct formation resistivity. It was recognized that the most complete manner to reduce shoulder-bed and deviation effects from borehole measurements is through inversion using a 3D forward simulation model that can rapidly and accurately reproduce the physics of the measurement (Lin et al., 1984).

Modeling multi-detector Sigma measurements is challenging because they involve complex thermal neutron and gamma ray transport phenomena (Lamarsh et al., 2001;

Stacey, 2007). The complete transport process can be accurately modeled by solving the coupled neutron and gamma-ray Boltzmann equation (Lewis, 1993). Solutions to the Boltzmann equation can be calculated with Monte Carlo techniques such as those implemented with the MCNP software (X-5 Monte Carlo Team, 2005), which can accurately model particle time decays under general formation/borehole configurations. Despite its robustness, the Monte Carlo method is computationally expensive and, consequently, not practical for inversion-based petrophysical interpretation.

Multiple methods have been proposed to rapidly simulate borehole nuclear measurements. Initial methods invoked the thermal-neutron diffusion equation (Locke and Smith, 1975; Henderson and Maynard, 1965) and time-dependent versions of the diffusion equation to approximate gamma-ray time decays (Allen et al., 1965; Henderson and Maynard, 1965; Jennings and Weber, 1995; Mikael, 1999). Yet, such models are unable to accurately reproduce the complexity of coupled neutron-gamma interactions in realistic logging conditions. The solution of Boltzmann's equation can also be approximated using a Taylor series expansion and the concept of flux perturbations (Greenspan, 1976; Watson 1984; Case and Watson, 1994). Flux perturbations are based on using a-priori known tool responses in background environments coupled with the spatial sensitivity of the detectors to rapidly determine tool responses in complex logging environments. This approximation method is reliable to rapidly correct shoulder-bed and well-deviation effects on neutron and density measurements and to improve the estimation of hydrocarbon pore volume (Mendoza et al., 2007; Ijasan et al., 2013a; Shetty et al., 2012.).

Few studies have addressed the numerical simulation of mud-filtrate invasion and shoulder-bed effects on Sigma logs. Allen et al. (1965) used a two-group diffusion approach to investigate the effect of piston-like invasion on Sigma logs. However, the study considered only thick horizontal formations and axis-symmetrical piston-like invasion profiles. Mimoun et al. (2011) used the first-order perturbation method to rapidly simulate behind-casing Sigma measurements acquired in thinly bedded layers of sand and shale accounting for thermal-neutron diffusion at interlayer boundaries. Haley (1995) developed a log response equation to interpret Sigma logs in sand-shale laminated systems. As of yet, no study has addressed the correction of Sigma logs for combined invasion, shoulder-bed, and well-deviation effects. The impact of these combined effects on multi-detector LWD Sigma has not been studied, as the measurement was recently introduced to the oil and gas industry and its petrophysical interpretation can be substantially complicated.

1.2 PROBLEM STATEMENT

Conventional interpretation of Sigma logs is based on a linear mixing law of the rock and fluid's Sigma. It is typically assumed that the measurement is acquired at a considerable time after drilling such that invasion is not present in the near-wellbore region. In LWD situations, however, that assumption does not hold true; the exposure of the formation to drilling mud and overbalance pressures in the period of time from the rock breakage until the measurement is acquired, suggests the presence of invasion that affects Sigma and other shallow-sensing borehole measurements.

Quantitative interpretation of Sigma logs affected by shallow salty-filtrate invasion leads to inaccurate estimations of water saturation. The presence of invasion may also mask

neutron-density crossovers that would otherwise help to qualitatively identify hydrocarbon-bearing formations. Additionally, LWD Sigma measurements are not only affected by invasion but also by borehole diffusion, shoulder-bed effects, and geometrical effects introduced by the orientation of the tool with respect to the formation bedding plane. These effects have a varying impact on each detector response and must be corrected to perform accurate petrophysical evaluations.

Previous advances in the interpretation of LWD measurements recommend the development of a rapid simulation model of multi-detector time decays that can be combined with inversion techniques to estimate layer-by-layer radial length of invasion and virgin-zone Sigma devoid of geometrical and environmental effects. The estimation of radial length of invasion may also be used to correct other shallow-sensing nuclear measurements, such as neutron and density, for invasion effects and improve petrophysical interpretations derived from borehole nuclear measurements.

1.3 RESEARCH OBJECTIVES

The main purpose of this dissertation is to advance the field of Sigma logging through the inversion-based interpretation of multi-detector, time-decay measurements acquired in realistic situations to identify in-situ fluids, evaluate water saturation, assess radial length of invasion, and integrate Sigma with other borehole measurements. The general purpose can be described by the following four sequential objectives:

1. To understand the benefits and limitations of multi-detector LWD Sigma measurements. This objective includes describing the physical basis of multi-detector LWD Sigma measurements, the differences between cased-hole and

openhole Sigma, petrophysical information that can be obtained by using different detectors, and environmental effects. Laboratory and Monte Carlo simulations will be used to achieve this objective.

2. To develop a rapid and accurate method to numerically simulate LWD multi-detector time decays in realistic logging environments. The method should take into account specific tool configuration and pulsing scheme of the commercial LWD tool under study, and should be benchmarked against laboratory and Monte Carlo simulated multi-detector time decays.

3. To develop inversion algorithms to reduce invasion and other environmental and geometrical effects present in measured multi-detector time decays while assessing uncertainty in estimated formation properties. This objective will include the development of 1D-radial and 2D inversion algorithms to estimate layer-by-layer virgin-zone Sigma and radial length of invasion. The inversion algorithms will be validated using laboratory measurements, as well as synthetic and field measured multi-detector decays. Interpretation of results will include comparisons to resistivity measurements and uncorrected Sigma logs to establish the advantages and disadvantages of using the inversion methods developed in this dissertation.

4. To integrate multi-detector LWD Sigma measurements with other borehole nuclear measurements to improve nuclear-based petrophysical interpretations. This objective is twofold. For one, it includes the development of a new and simple analytical expression for total porosity, which separates both matrix and fluid effects on neutron and density porosity logs, as all nuclear interpretations presented

in this dissertation rely largely on accurate estimations of porosity. Secondly, this objective includes the development of a workflow to perform joint interpretation of multi-detector neutron, density, and Sigma logs to reduce invasion, shoulder-bed, and well-deviation effects when invasion is shallow. Pressure, temperature, and salinity dependency of fluid nuclear properties will be considered in petrophysical interpretations.

1.4 METHOD OVERVIEW

This dissertation begins studying the physical basis, acquisition, processing, and interpretation of multi-detector Sigma logging. The purpose of the first part of the dissertation is to provide the reader with an understanding of the limitations and benefits of the measurement, as well as recommendations that must be considered during planning, acquisition, and interpretation of LWD Sigma logs. The equations of thermal-neutron and gamma-ray transport, and assumptions that are used to calculate formation Sigma from time decays are described. I then explain tool operation and processing of time decays to calculate apparent Sigma, as well as a comparison of LWD and wireline Sigma measurements. Subsequently, the use of three detectors is explained in terms of its impact on petrophysical interpretation. Monte Carlo N-Particle (MCNP) calculated and laboratory measurements are used to study borehole and diffusion effects. To assess the potential of the multi-detector Sigma measurement, I calculate invasion profiles across formations under typical drilling conditions for the LWD multi-function tool under study. Comparisons of multi-detector Sigma and propagation resistivity are made based on simulations for various fluid types and radial lengths of invasion to define cases in which

each measurement has the greatest potential to assess radial length of invasion. Additionally, I discuss the significant effect of tool standoff on Sigma measurements based on Monte Carlo simulations.

The second part of the dissertation describes the most significant technical contribution of the dissertation. I introduce a novel, fast and accurate method to numerically simulate LWD multi-detector time decays in realistic borehole environments. The method relies on first-order approximations using Monte Carlo pre-calculated and detector-specific libraries of particle time decays and flux sensitivity functions (FSF), while accounting for detector-specific borehole and diffusion effects. Simulations are benchmarked against laboratory measurements and MCNP calculations. The novelty of the method is that it simulates time decays rather than Sigma itself. This enables a direct relationship between actual rock Sigma and multi-detector diffusion-affected time decays, thereby removing intermediate correction steps often used to convert apparent Sigma into intrinsic formation Sigma. The following sections of the dissertation use this rapid simulation model and inversion techniques to correct multi-detector time decays for various environmental and geometrical effects in a sequentially increasing degree of complexity.

In the third part of the dissertation, the forward simulation model is coupled with nonlinear inversion techniques to interpret laboratory, synthetic, and field measured multi-detector time decays. First, I formulate a 1D-radial, nonlinear inversion algorithm of multi-detector decays to correct LWD Sigma measurements across thick formations for invasion effects, and examine the stability of the problem. A multiple realization study in synthetic

decays with realistic noise, multiple Sigma contrasts, and multiple radial lengths of invasion is performed to quantify the stability and uncertainty of the estimations. A Confidence Index (*CI*) that is used together with covariance-derived error bars is determined from the multiple-realization study. Laboratory measurements, along with synthetic and field measured multi-detector decays, are used to benchmark the algorithm. The ideas introduced in this part of the dissertation are innovative because the estimation of radial length of invasion from nuclear measurements is a novel concept in formation evaluation, and rapid calculation of the components of the Jacobian matrix in the 1D-radial inversion had not been published before. This section only studies the isolation of invasion effects from LWD Sigma measurements, and does not consider the effect of adjacent formations and/or the effect of the relative angle between the well and formation plane.

Subsequently, I present a 2D multi-detector time-decay inversion algorithm to correct multi-detector nuclear measurements in thin and invaded formations affected not only by invasion, but also by shoulder-bed and well-deviation effects. I begin by introducing the formulation of the 2D inversion algorithm. Then, a method to rapidly calculate the Jacobian matrix necessary to perform the nonlinear inversion of multi-detector decays is described. Synthetic and field examples are used to illustrate the potential of the multi-detector thermal-neutron and gamma-ray decay inversion compared to using conventional Sigma and resistivity logs to estimate water saturation.

The final part of this dissertation consists of the integration of Sigma and other borehole nuclear measurements. I introduce a new and intelligible analytical expression for total porosity that effectively separates both matrix and fluid effects on neutron and density

porosity logs to improve the estimation of total porosity. The expression stems from a new nonlinear mixing law for neutron migration length that is combined with a linear density mixing law to calculate total porosity. The new expression is benchmarked against Schlumberger's Nuclear Parameter program (SNUPAR, McKeon et al., 1989) calculations and is tested on two conventional and two shale-gas field examples.

Lastly, I develop a workflow to integrate LWD Sigma measurements with neutron and density measurements, i.e., fluid-sensitive nuclear measurements. The procedure begins with the correction for matrix and fluid effects to neutron and density logs to estimate porosity as described in the previous paragraph. Multi-detector time decays are then used to assess radial length of invasion and estimate virgin-zone Sigma, while simultaneously correcting Sigma measurements for shoulder-bed and well-deviation effects. A 2D inversion algorithm is used to correct two-detector neutron and density logs for invasion and shoulder-bed effects. The latter algorithm relies on the output of the time-decay (Sigma) inversion to correct neutron and density logs for invasion effects. The final step invokes a nuclear-based solver to estimate water saturation and fluid type. This solver is based on linear mixing laws for Sigma and density, and the new mixing law for migration length introduced in this dissertation. In addition, flash calculations and SNUPAR are used to calculate fluid nuclear properties as a function of pressure, temperature, and salinity. Synthetic and field examples are used to test the workflow and elaborate on the advantages and limitations of the method.

1.5 DISSERTATION OUTLINE

This dissertation consists of four parts and eight chapters. The introductory chapter presents the motivations behind LWD Sigma logging and its importance in formation evaluation. Relevant literature regarding the study of Sigma measurements and environmental and geometrical effects on borehole measurements is cited. Subsequently, I describe the main objectives of the dissertation and methods used to enable inversion-based interpretation of multi-detector time decays.

The first part of the dissertation is presented in Chapter 2. This section outlines the principles of LWD Sigma logging. I present the physical basis behind multi-detector Sigma logging, as well as assumptions, corrections, and processing of the measurement. I study the importance of assessing radial length of invasion in LWD situations by simulating filtrate invasion in the range of possible exposure times to mud filtrate for the LWD tool under study. Additionally, a comparison of simulated Sigma and resistivity logs is presented to understand the impact of shallow invasion on both measurements.

Chapter 3 chronicles the second part of the dissertation. This chapter is the core of the dissertation and introduces a new method to rapidly simulate multi-detector time decays in 3D geometries. The method relies on Monte Carlo calculated libraries of time decays and sensitivity functions specific for each detector. Complex thermal-neutron and gamma-ray interactions are accurately taken into account by using first-order perturbation theory. The purpose of the model is to enable the rapid inversion of measured multi-detector decays to decouple various geometrical and borehole effects. I validate the model using

laboratory measurements, as well as MCNP calculations for the pulsed-source LWD tool under study.

The third part of the dissertation comprises the use of the rapid simulation model to invert measured multi-detector time decays and is presented in Chapters 4 and 5. Chapter 4 introduces a 1D-radial inversion algorithm to correct Sigma measurements for invasion in thick formations and vertical or slightly deviated wells. Chapter 5 presents a 2D inversion algorithm to simultaneously correct Sigma measurements for invasion, shoulder-bed, and well deviation effects. In both chapters, inversion algorithms are validated using synthetic and field examples. Comparisons of water saturation calculated using corrected layer-by-layer Sigma and resistivity logs are also described. In Chapter 5, I highlight the benefits and shortcomings of using Sigma logs rather than resistivity logs in the case of thinly bedded formations and/or highly deviated wells.

The fourth and final part of the dissertation encompasses the integration of multi-detector LWD Sigma measurements with other nuclear borehole measurements, and is presented in Chapters 6 and 7. Chapter 6 introduces a new equation to calculate total porosity from matrix- and fluid-corrected neutron and density logs. The improved estimation of total porosity is aimed to enhance the estimation of a reference value for invasion-zone Sigma needed in the inversion algorithms to reduce non-uniqueness. Calculated porosity using the new equation is benchmarked against core and Nuclear-Magnetic-Resonance (NMR) porosity.

Chapter 7 integrates the 2D Sigma inversion algorithm, the new equation for porosity and forward-simulation models of multi-detector density, and neutron

measurements for the LWD multi-function tool under study. I show that estimations of radial length of invasion can be used qualitatively to correct neutron and density logs for invasion effects. Additionally, Sigma, neutron, and density logs are simultaneously corrected for shoulder-bed and well-deviation effects. I propose a workflow that relies on corrected nuclear measurements and invokes a flash calculation to estimate water pore volume and the hydrocarbon type that best reproduces corrected nuclear properties. Two synthetic and five field examples are used to test the method.

Finally, Chapter 8 summarizes the contributions, conclusions, and recommendations originating from this dissertation.

1.6. List Of Publications

Several of the research studies described in this dissertation have been published, or submitted for peer review to various journals and conferences. The list of publications is presented below.

1.6.1 Refereed Journal Publications

Ortega, E., C. Torres-Verdín, and W.E. Preeg, 2014, Fast-forward modeling of multi-detector logging-while-drilling Sigma measurements: Geophysics *(accepted for publication).*

Ortega, E., C. Torres-Verdín, W.E. Preeg, and J. Miles, 2014, 1D radial inversion of multi-detector logging-while-drilling Sigma measurements: Geophysics *(submitted for publication).*

Ortega, E., C. Torres-Verdín, and W.E. Preeg, 2014, 2D inversion of LWD thermal-neutron and gamma-ray time decays affected by shoulder-bed, well-deviation, and shallow-invasion effects: Geophysics *(submitted for publication).*

Ortega, E., C. Torres-Verdín, and W.E. Preeg, 2014, Joint petrophysical interpretation of multi-detector nuclear measurements corrected for invasion, shoulder-bed, and well-deviation effects: Geophysics *(submitted for publication).*

1.6.2 Conference Proceedings

Ortega, E., C. Torres-Verdín, W.E. Preeg, and J. Miles, 2013, Multi-detector LWD Sigma logging principles, petrophysical applications, and environmental effects: Transactions of the Society of Petrophysicists and Well Log Analysts, 54th Annual Logging Symposium, paper NNN.

Ortega, E., and C. Torres-Verdín, 2014, New analytical method to calculate matrix- and fluid-corrected total porosity in organic shale: Society of Petroleum Engineers Annual Technical Conference and Exhibition Proceedings, SPE 170909.

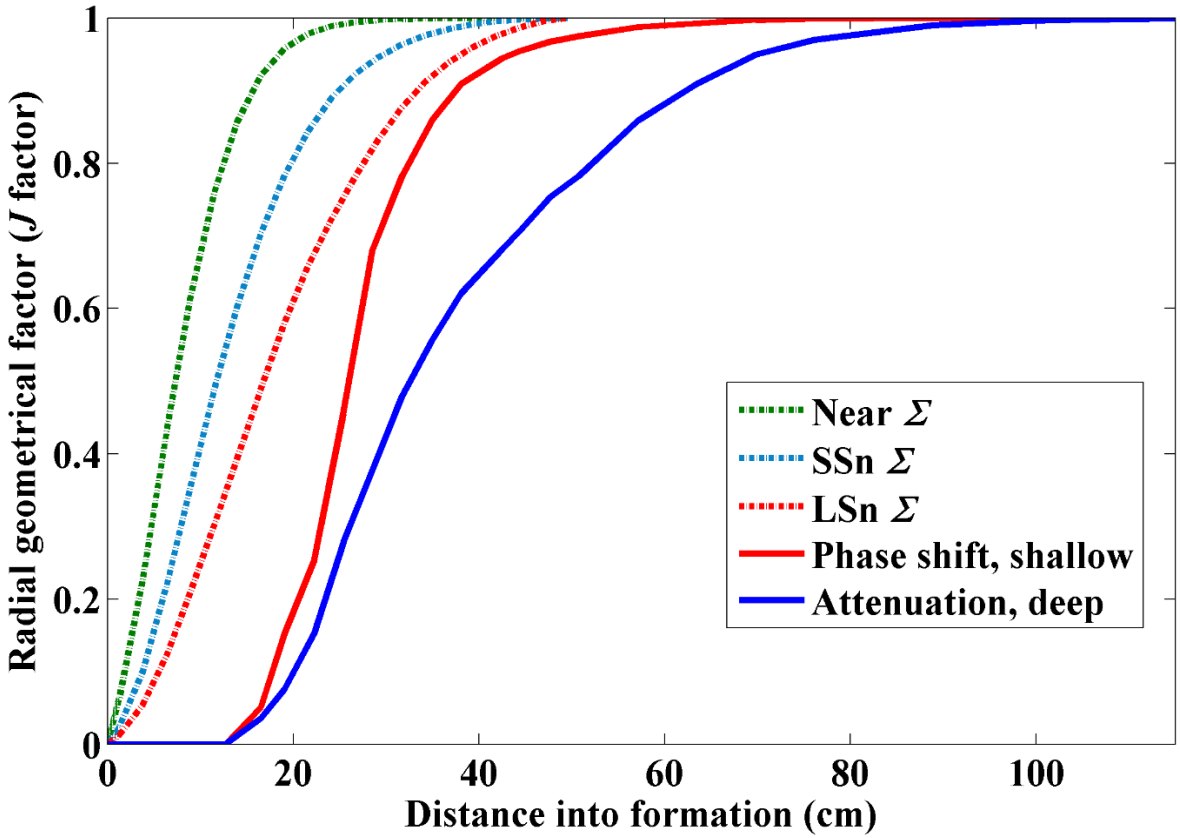

Figure 1.1: Comparison of radial geometrical factors (*J*) for a Compensated Dual Resistivity (CDR) LWD tool (Anderson, 2001) and the LWD Sigma tool under study in the case of conductive invasion.

Chapter 2: Multi-Detector Logging-While-Drilling Sigma Principles, Petrophysical Applications, and Environmental Effects

The potential of LWD Sigma logs compared to cased-hole Sigma logs notwithstanding, there is limited literature addressing the specifics of openhole Sigma logging such as tool operation, environmental effects, limitations, and interpretation because the tool was only recently introduced into the oil and gas industry. The overall objective of this chapter is to describe the physical basis of multi-detector LWD Sigma measurements, the differences between cased-hole and openhole Sigma measurements, petrophysical information that can be obtained by using different detectors, environmental effects, and best practices.

I analyze Monte Carlo simulations and test-pit data to appraise environmental effects related to diffusion, tool standoff, borehole fluid, and borehole size. To assess the potential of multi-detector Sigma logs, I compute radial invasion profiles for a wide range of formations under typical LWD drilling conditions. Finally, a comparison is made of LWD Sigma and resistivity responses to define cases in which each measurement has the best potential to assess radial length of invasion.

Results show that the different sensitivities of the LWD Sigma tool detectors have implications in thin-bed and invasion detection, and are affected by environmental effects to different degrees. The near neutron detector has good vertical resolution and is strongly affected by environmental effects, while the long-spaced gamma-ray detector is stable to

environmental effects, but is more affected by statistical noise. Borehole effects can be important in the case of significant washouts. I also show that at shallow radial lengths of invasion, LWD Sigma outperforms LWD resistivity to diagnose presence of invasion. However, LWD resistivity is better suited to detect invasion beyond 35 cm (14 in). Moreover, I show that multi-detector Sigma should be targeted to high-porosity, hydrocarbon-bearing formations invaded by salty filtrate.

2.1 INTRODUCTION

Sigma is the macroscopic thermal neutron capture cross section of the formation, which can be used in the presence of saline water to measure water saturation. Sigma logs have historically been used for time-lapse interpretation of water saturation to overcome the difficulties of resistivity logging in cased holes (Morris and Quinlan, 2005). Sigma logs can be run in open holes for fluid identification in low-resistivity, low-contrast (LRLC) reservoirs (Simpson and Menke, 2010). They can also be integrated with resistivity logs in conventional reservoirs to assess water saturation in the absence of connate water samples (Aqivlera, 1979), and be used to evaluate water saturation in carbonate reservoirs.

The potential of conventional Sigma logs in formation evaluation spearheaded the development of LWD Sigma logging. Accordingly, the physical basis of conventional Sigma was extended to multi-detector Sigma as a means to evaluate presence of invasion (Gyllensten et al., 2009). LWD Sigma measurements are affected by invasion because the formation is exposed to drilling fluid at overbalance pressures from the time that the rock is drilled until measurement acquisition. Typical distances between the drill bit and Sigma

detectors are between approximately 7.6 and 15 m (25 and 50 ft), depending on the placement of the LWD collar. Standard drilling rates in formations where Sigma logs are acquired range from 0.085 to 2.5 cm/s (10 to 300 ft/hr). The formation is exposed to mud filtrate for a time period between about six minutes to a few hours; this is enough to cause at least shallow invasion. Allen et al. (1965) studied invasion effects on Sigma measurements and reported that shallow invasion is sufficient to mask the formation response because of the shallow nature of the measurement.

Analogous to resistivity logs, qualitative analysis of multi-depth-of-investigation curves indicates presence of invasion. This feature of LWD Sigma has the potential to enable the quantification of radial length of invasion and virgin Sigma in the near-wellbore area by using forward and inverse modeling of measurement responses. A method to quantify radial length of invasion and virgin Sigma was successfully applied in an Abu Dhabi field. This method allows correcting invasion-affected Sigma logs and improves the integration of Sigma and resistivity measurements (El-Din et al., 2012).

Interpretation of LWD Sigma logs must be preceded by detector-specific environmental corrections for the presence of the borehole and tool housing. The Sigma value estimated directly from a time decay curve differs from its intrinsic or real material Sigma value (Murdoch et al., 1990). A common method used to estimate Sigma from decay curves considers that the rate of decay is proportional only to the total absorption cross section of the material, Σ_a^N , and the average thermal neutron velocity, v (Mickael, 1999). However, the number of particles in the detector location decays not only due to absorption,

but also due to diffusion of the particle cloud away from the detector (Hilchie et al., 1969). As a consequence, the absorption cross section obtained from decay curves is overestimated, and hence requires correction to yield reliable values of Sigma. Diffusion effects depend upon position from the source, borehole fluid, borehole size, and tool standoff.

Important applications of Sigma logging in LRLC reservoirs, carbonates, and resistivity measurements have triggered the development of different wireline tools with specific tool design, operation, and environmental corrections. Nonetheless, the study of the specifics of LWD Sigma is fairly new, and the impact of invasion on Sigma logs is now gaining attention. This chapter provides a guide to understand the operation, potential, and limitations of multi-detector LWD Sigma logs.

First, I explain the physics behind thermal-neutron and gamma-ray time-dependent measurements and the main assumptions behind basic petrophysical interpretation. Second, I describe the LWD Sigma tool operation, multi-detector sensitivity, and signal processing, and establish comparisons against conventional wireline pulsed-neutron-capture tools. Third, I study invasion phenomena in the case of small filtrate-exposure times typical of LWD measurements for different types of rocks and drilling conditions. Lastly, I describe the multi-depth-of-investigation capability of the LWD Sigma tool for invasion assessment and make comparisons against resistivity measurements for invasion of water-based mud (WBM) of different salinities into oil-bearing shaly sandstone.

2.2 MEASUREMENT PHYSICS

Formation evaluation relies on measurements of physical properties of rocks to identify mineral and fluid components and quantify their volumetric proportions. In the case of nuclear logging, differences in radiation transport in different minerals and fluids enable the estimation of bulk density, bulk hydrogen index, mineral composition, and total thermal-neutron absorption cross section, otherwise known as Sigma.

Time-dependent nuclear measurements rely on the physics of neutron and gamma-ray transport in porous media. Thermal-neutron transport as a function of time can be described by the integral time-dependent Boltzmann equation, namely

$$\frac{1}{v_N}\frac{\partial \psi_N}{\partial t} = -\Sigma_t^N \psi_N - \nabla \cdot \psi_N \hat{\Omega} + \int_0^\infty dE' \int_{4\pi} d\hat{\Omega} \psi_N(E', \hat{\Omega}') \Sigma_s^N(E' \to E, \hat{\Omega}' \to \hat{\Omega}) + S_N, \quad (2.1)$$

where $\psi_N = \psi_N(\mathbf{r}, E, \hat{\Omega}, t)$ is thermal-neutron angular flux at position $\mathbf{r}$, energy E, and direction $\hat{\Omega}$ at time t, $v_N = v_N(E)$ is neutron velocity at average thermal energies, $\Sigma_t^N = \Sigma_t^N(\mathbf{r})$ is total interaction cross section of the materials at position $\mathbf{r}$ for neutrons in the thermal range of energy. $\Sigma_t^N = \Sigma_a^N(\mathbf{r}) + \Sigma_s^N(\mathbf{r})$, where $\Sigma_a^N(\mathbf{r})$ and $\Sigma_s^N(\mathbf{r})$ are the thermal-neutron absorption and scattering cross sections, respectively; $S_N = S_N(\mathbf{r}, E, \hat{\Omega}, t)$ is the time-dependent volumetric source of thermal neutrons, where S_N is given by the spatial distribution of fast neutrons and the fast-neutron scattering cross section.

In the case of thermal neutrons, the source term $S_N = 0$ after neutrons originating from the last pulse reach their thermal state. Additionally, under the assumption that the main component of thermal-neutron decay is absorption, rather than scattering, i.e., $\Sigma_s^N << \Sigma_a^N$, equation 2.1 becomes

$$\frac{1}{v_N}\frac{\partial \boldsymbol{\psi}_N}{\partial t} = -\Sigma_a^N \boldsymbol{\psi}_N - \nabla \cdot \boldsymbol{\psi}_N \hat{\boldsymbol{\Omega}}. \tag{2.2}$$

Equation 2.2 describes the time-dependent behavior of a population of thermal neutrons after the last pulse of a high-energy neutron source.

Interpretation of thermal-neutron decays in formation evaluation assumes that at the detector position, the term $\nabla \cdot \boldsymbol{\psi}_N \hat{\boldsymbol{\Omega}}$ in the right-hand side of equation 2.2 is negligible. The assumption is based on considering only the time-dependent behavior of the thermal-neutron population, while neglecting the position dependency of the flux. Neglecting the position terms in equation 2.2 results in

$$\frac{1}{v_N}\frac{\partial \boldsymbol{\psi}_N}{\partial t} = -\Sigma_a^N \boldsymbol{\psi}_N . \tag{2.3}$$

The solution to equation 2.3 is

$$\boldsymbol{\psi}_N = \boldsymbol{\psi}_N^o e^{-v_N \Sigma_a^N t} \quad , \tag{2.4}$$

where $\boldsymbol{\psi}_N^o$ is the thermal-neutron angular flux at the time when all fast neutrons reach thermal energies, about 10 μs after the last pulse for a 14-MeV neutron source. Equation

2.4 is the basis of pulsed-neutron capture, or Sigma, logs. The slope of log (ψ_N), the log of the counts in a thermal-neutron detector, versus time enables the estimation of the thermal-neutron absorption cross section, Σ_a^N .

The assumptions of negligible spatial flux dependency and small scattering cross section result in apparent values of Σ_a^N that deviate from actual values of material cross section. Therefore, detector-dependent corrections are necessary before attempting any interpretation of thermal-neutron decay curves. Such corrections will be explained in the environmental correction section of this chapter.

The LWD tool counts not only thermal neutrons but also gamma rays with respect to time. Boltzmann's equation describes the transport of any type of radiation. Therefore, equation 2.1 with gamma-ray interaction cross sections fully describes gamma-ray transport. The source of gamma rays is given by absorption interactions of thermal neutrons as a function of time, energy, and position, namely

$$S_\gamma = \psi_N \Sigma_a^N \ , \tag{2.5}$$

while the time-dependent transport of gamma rays is given by the modified Boltzmann equation

$$\frac{1}{v_\gamma}\frac{\partial \psi_\gamma}{\partial t} = -\Sigma_t^\gamma \psi_\gamma - \nabla \cdot \psi_\gamma \hat{\Omega} + \int_0^\infty dE' \int_{4\pi} d\hat{\Omega} \psi_\gamma (E', \hat{\Omega}') \Sigma_s^\gamma (E' \to E, \hat{\Omega}' \to \hat{\Omega}) + S_\gamma \ . \tag{2.6}$$

Assuming negligible gamma-ray scattering cross section, Σ_s^γ, equation 2.6 becomes

$$\frac{1}{v_\gamma}\frac{\partial \boldsymbol{\psi}_\gamma}{\partial t} = -\Sigma_a^\gamma \boldsymbol{\psi}_\gamma - \nabla \cdot \boldsymbol{\psi}_\gamma \hat{\boldsymbol{\Omega}} + \boldsymbol{\psi}_N \Sigma_a^N . \tag{2.7}$$

Because gamma rays move at speeds 10^5 times faster than thermal neutrons, the leftmost term of equation 2.7 can be neglected, whereby

$$0 = -\Sigma_a^\gamma \boldsymbol{\psi}_\gamma - \nabla \cdot \boldsymbol{\psi}_\gamma \hat{\boldsymbol{\Omega}} + \boldsymbol{\psi}_N \Sigma_a^N . \tag{2.8}$$

Similarly to thermal-neutron analysis, the spatial dependency of the flux is negligible. Then,

$$\boldsymbol{\psi}_\gamma = \frac{\boldsymbol{\psi}_N \Sigma_a^N}{\Sigma_a^\gamma} . \tag{2.9}$$

By replacing $\boldsymbol{\psi}_N$ in equation 2.9 with the solution from equation 2.4, equation 2.9 becomes

$$\boldsymbol{\psi}_\gamma = \boldsymbol{\psi}_N^o e^{-v_N \Sigma_a^N t} \frac{\Sigma_a^N}{\Sigma_a^\gamma} . \tag{2.10}$$

Equation 2.10 can be rewritten as

$$\log \boldsymbol{\psi}_\gamma = -v_N \Sigma_a^N t + \log \boldsymbol{\psi}_N^o \frac{\Sigma_a^N}{\Sigma_a^\gamma} . \tag{2.11}$$

Equation 2.11 indicates that gamma rays preserve the time dependency of the thermal-neutron population, and therefore the slope of the log of the gamma counts versus time also allows for the estimation of the thermal neutron absorption cross section, Σ_a^N.

The use of both neutron and gamma-ray detectors is advantageous since their measurements have different quality depending upon the environment in which the measurement is performed. Environments with high-absorption cross sections yield high gamma ray production, and therefore the gamma ray statistics are generally better than the thermal-neutron statistics. However, late time counts are suppressed by highly absorbing media depleting the neutron population. Environments that favor scattering rather than absorption, such as gas-bearing formations, will have lower rates of gamma-ray generation, and therefore the statistics in the neutron detectors will be superior.

I have shown that detecting neutrons or gamma rays as a function of time allows one to infer apparent values of Σ_a^N .The conversion from apparent Σ_a^N to the best measurement of true formation value is achieved by environmental corrections which account for variations in radiation transport. The conversion will be discussed in section 2.7.

2.3 TOOL OPERATION

Pulsed neutron measurements combine a switchable electronic neutron generator with appropriate gamma-ray or neutron detectors. A typical pulsed neutron generator device creates deuterium-tritium fusion reactions to emit energetic neutrons at 14.1 MeV. This pulsed fast-neutron source builds up a cloud of neutrons that undergo multiple collisions with nuclei in the formation and borehole, losing energy with each scattering. Once a fast neutron has reached thermal equilibrium with the environment, at energy about

0.025 eV, it is absorbed by a nucleus to form a heavier, excited state. The excited nucleus decays to its ground state by the emission of gamma rays.

This dissertation is focused on a commercial multi-function LWD tool that combines traditional triple-combo formation evaluation with advanced nuclear measurements such as Sigma and neutron capture spectroscopy (Weller et al., 2005). The pulsed-neutron section of the tool contains multiple neutron and gamma-ray detectors that are used variously for the measurements of neutron porosity, Sigma, and spectroscopy. The Sigma measurement is derived from three of the detectors: a near thermal-neutron detector (Near), a short-spaced gamma-ray detector (SSn), and a long-spaced gamma ray detector (LSn). **Figure 2.1** shows a sketch of the tool with detail on the detectors used for Sigma logging. The near thermal-neutron detector is a helium-3 tube which is primarily sensitive to thermal neutrons. The short and long gamma-ray detectors use NaI crystal scintillators. Both gamma rays and thermal neutrons are counted as a function of time to produce three decay curves for each logged depth level.

The neutron generator uses a repeating pulsing scheme to build up the neutron population and reduce statistical noise in the Sigma decay measurement. Since Sigma logs measure a time-dependent exponential decay, the statistical quality of the measurement decreases at late decay times because the population of thermal neutrons is depleted. The statistics of the decay measurement are improved by bursting a series of pulses that build up the thermal-neutron and gamma-ray populations at late times. The multiple signals

superpose with time, preserving the late-time decay rate while allowing for the detection of a higher number of particles and thereby reducing the statistical noise.

A simplified pulsing scheme for the LWD tool is shown at the top of **Figure 2.2**. The measurement starts with a fast-neutron burst of 10 μs duration, followed by a 25-μs window for spectroscopy measurements. The pulse-and-wait sequence is repeated 32 times and is followed by a 380-μs interval to measure the time-dependent decay from which Sigma is calculated. This cycle is repeated 62 times, after which background gamma rays are measured to account for any natural radioactivity or formation activation.

Figure 2.2 also shows 32-pulse multi-detector signals for a 34-p.u. sandstone formation computed using MCNP. Observe the buildup in the neutron and gamma-ray populations at early times. The section of the curves used to calculate Sigma is shown by the blue bar at the top. The inset at the bottom left of the figure illustrates a side-by-side comparison of the late-time parts of the pulsed signal. Though the measurement is acquired across the same homogeneous formation, the late-time slope for each detector is different. The difference in the slope is caused by diffusion and borehole effects resulting from different source-detector spacing and the nature of thermal-neutron and gamma-ray transport.

2.4 SIGNAL PROCESSING

Ignoring diffusion, the decay signal in a multi-component system can be described as

$$\mathbf{n}(t)_{bulk} = \sum_{i=1}^{n} A_i e^{-v_N t\left(\Sigma_a^N\right)_i}, \tag{2.12}$$

where A_i is the amplitude, and $\left(\Sigma_a^N\right)_i$ is the thermal-neutron absorption cross section of component *i*. The term $v_N \Sigma_a^N$ is equal to the slope of the late-time signal. The inverse of the term is called the thermal-neutron decay lifetime, τ. $\mathbf{n}(t)$ is defined as $\mathbf{n}(t) = \left[N(t_1) \quad N(t_2) \quad \cdots \quad N(t_{tb})\right]^T$, $N(t)$ are the counts at a specific time bin *t*, and t_1, t_2 ,… t_{tb}, are the irregular time bins of the pulsed-neutron commercial tool under study from 0 μs to 415 μs, where time 0 μs is the time at which the last pulse is generated for a total number of *tb* time bins (Ortega et al., 2013).

Several techniques can be used to estimate formation Sigma out of decay curves, e.g., fitting two exponentials or *n*-number of exponentials analogous to nuclear magnetic resonance, (NMR), signal interpretation, or the moments method. Theoretically, NMR-like inversion can be used to find a distribution of Sigma values that combine to generate the bulk decay signal, which, in principle, is the sum of contributions from the formation, borehole fluids, and the strong neutron-absorbing material of the tool itself. However, the signals of the materials in the formation can be similar and only distinguish from the borehole signal. Therefore, NMR-like inversion or fitting of more than two exponential forms is rendered impractical.

Least squares minimization of two exponential components is a practical technique to separate borehole and formation responses. In the typical logging environment, the

logarithmic slope of the early-time signal is equal to the inverse of the borehole thermal decay time, $1/\tau_{BH}$. The slope of the late-time signal is equal to the inverse of the formation thermal decay time, $1/\tau_F$. The velocity term, v_N, is about 0.22 cm/μs for thermal neutrons. Hence, the thermal neutron absorption cross section, given in units of total area available for absorption interactions per volume of material, is defined as

$$\Sigma_a^N \left[\frac{\text{cm}^2}{\text{cm}^3}\right] = \frac{1/\tau_F}{v_N}\left[\frac{1/\mu\text{s}}{\text{cm}/\mu\text{s}}\right] = \frac{1/\tau_F\,[1/\mu\text{s}]}{0.22\ \text{cm}/\mu\text{s}}\,. \tag{2.13}$$

To avoid the manipulation of small numbers, in formation evaluation Σ_a^N is multiplied by 10^3. One capture unit, c.u., is defined as 10^{-3} cm^2/cm^3, as follows

$$\Sigma_a^N \left[\text{c.u.}\right] = 10^3 \cdot \Sigma_a^N \left[\frac{\text{cm}^2}{\text{cm}^3}\right]. \tag{2.14}$$

The moments method (Crámer, 1946) is another useful technique to calculate the formation thermal-decay time out of decay signals. The method is based on the determination of the first and zero moments of a decay curve, rather than fitting an exponential form of the type shown in equation 2.12. The use of the first moment assumes that the decay follows a single exponential distribution, so it is most appropriate for late-time measurements that are relatively free of borehole effects. The calculation consists of

$$\tau_F = \frac{\sum_{i=0}^{n} t(i)\cdot CR_i}{\sum_{i=0}^{n} CR_i}\,, \tag{2.15}$$

where $t(i)$ is center of time bin *i*, and CR_i is count rate at time bin *i*. A numerical correction is necessary to account for the fact that the sum is performed within a finite time window. The method is advantageous for its robustness in computing τ_F from statistically noisy signals. The processing of the LWD tool under study uses the two-exponential fit method to process Sigma from the thermal-neutron detector (Near), and the moments method to process Sigma from the gamma-ray detectors (SSn and LSn).

Sigma is a nuclear property of interest in formation evaluation because it exhibits significantly different values in formations saturated by gas, oil and salty brine and in formations with different clay volumes. Chlorine is a notably strong absorber of thermal neutrons. The absorption cross section of water ranges from about 22 c.u. for completely fresh water to about 125 c.u. for NaCl-saturated brine. By contrast, oil has Sigma of about 20 c.u. Since most connate waters contain salt, the response of a Sigma log can show the transition from an oil-bearing to a brine-bearing formation. The lack of chlorine in fresh water (22 c.u.), however, makes it nearly impossible to distinguish it from oil (20 c.u.) with Sigma logs. Other good absorbers of thermal neutrons in the formation include hydrogen and elements present in clay minerals such as iron, potassium, and trace amounts of rare earth elements like gadolinium. Clay-rich formations (20 to 60 c.u.) exhibit values of Sigma much higher than clean siliciclastic (4.5 c.u.) or carbonate formations (4.5 to 7 c.u.). Because of the contrast in Sigma for different earth materials, Sigma is used as a fluid discriminator and normally correlates with lithology and resistivity logs.

2.5 WIRELINE VERSUS LWD SIGMA

Conventional pulsed-neutron capture logging was developed as a means to estimate water saturation in cased holes. Wireline tools are slim because of the mechanical restrictions within producing wells. The tools are equipped with a fast-neutron source, and a set of short-spaced and long-spaced gamma-ray scintillators. Different versions of the tool include single-pulse, dual-pulse, and multi-pulse source burst schemes. The use of two detectors is intended for compensation of diffusion and borehole effects. Wireline Sigma measurements produce several apparent Sigmas and one environmentally corrected Sigma log. The early-time response is dominated by the presence of neutron-absorbing steel casing and cement. **Figure 2.3a** shows a sketch of a wireline Sigma tool that has two gamma-ray detectors. The slim tool does not fill up the borehole, and therefore the presence of fluids in the borehole can have an important effect on wireline Sigma measurements. The measurement is acquired after enough filtrate cleanup time is allowed, and therefore interpretation assumes the tool is sensing only invasion-free formation.

Responses from LWD and wireline Sigma tools are different because of differences in both tool architecture and environmental conditions. LWD tools are built into a large collar that nearly fills up the borehole. **Figure 2.3b** shows a side-by-side comparison of the LWD tool against the wireline tool. Notice that the LWD Sigma detectors may not be fully flush against the formation because of the presence of the stabilizer containing the density section of the tool. The LWD tool produces three independent Sigma measurements, from one thermal-neutron detector and two gamma-ray detectors. Moreover, interpretations of

LWD Sigma tools cannot discard the effect of invasion because the formation is logged right after exposing it to drilling fluid at overbalance pressures. The invasion phenomenon is discussed in section 2.8.

Measurements of LWD Sigma are made in an open hole without casing and cement; however, due to the larger tool size there is a larger fast response from the tool itself. Consequently, differences between wireline and LWD tools in the borehole portion of decay signals can be expected. **Figure 2.4** shows decay curves for the short-spaced gamma-ray detectors of the wireline Longhorn tool, an in-house tool designed at The University of Texas at Austin, and the LWD tool under study. The LWD signal shows better differentiation between borehole and formation signals mainly due to the presence of the thick steel collar of the tool. Thermal neutrons within the LWD tool die away quickly and thus the signal at late times is less affected by the presence of the borehole fluid. Notice from the early-time decay slopes that the absorption cross section of the LWD tool is higher than the volumetric average over the borehole fluid, casing, and cement. The rapid fall of the borehole signal in the LWD tool is advantageous from the point of view that it provides a relatively clean formation response in the later time window from which Sigma is calculated.

2.6 DETECTOR SENSITIVITY

The three detectors of the LWD Sigma measurement possess different spatial sensitivities that are inherent to source-detector spacing and to neutron and gamma-ray physics. Regardless of spacing, thermal neutrons and gamma rays exhibit different spatial

distributions in the porous media. Thermal neutrons spreading away from the near-wellbore zone are most likely to be absorbed on their way back to the detector and not be counted as neutrons. However, those absorbed neutrons can generate gamma rays that have a good chance of being counted in the gamma-ray detectors. Hence, thermal-neutron detectors have a smaller volume of investigation than gamma-ray detectors.

Figure 2.5 shows tridimensional detector sensitivity maps computed using MCNP for the three detectors of the LWD tool under study. I use an MCNP model of the tool and the weight windows functionality of MCNP to generate thermal-neutron maps for the neutron detector and thermal-neutron absorption maps for the gamma detectors. The detectors' spatial sensitivity is variable and depends on the nuclear properties of the material where the measurement is acquired. **Figure 2.5** shows the sensitivity of the tool in a 34-p.u. sandstone formation fully saturated with fresh water.

One advantage LWD Sigma has over wireline Sigma is that it is possible to use three detectors with different vertical and radial resolution. The near thermal-neutron detector has better vertical resolution as compared to conventional one- or two-detector wireline gamma-ray decay tools. **Figure 2.5a** shows how the vertical resolution of the near neutron detector permits the sensing of layers about half or a quarter the thickness of what the short-spaced gamma-ray and long-spaced gamma-ray detectors can resolve, respectively. The thermal-neutron detector is, indeed, especially useful for thin-bed detection. However, there is a tradeoff between improved vertical resolution and shallow depth of investigation. The thermal-neutron detector measurement is generally statistically

stable, but it is the most affected by environmental effects such as standoff and invasion because of its small volume of investigation.

The long-spaced gamma-ray detector has the largest volume of investigation out of the three detectors because of its spacing from the fast neutron source and the greater distance of transport for a coupled neutron-gamma measurement versus a neutron-neutron measurement. Normally, the long-spaced detector can sense up to 35 cm into the formation at the expense of rather poor vertical resolution. The long-spaced gamma-ray detector is less affected by environmental effects such as significant standoff, but because of its large spacing from the source, and thereby fewer counts, its signals can be noisier. The short-spaced gamma-ray detector provides intermediate vertical and radial resolution compared to the other detectors and also a balance between signal noise and stability to environmental effects. **Figure 2.5b** shows the azimuthal sensitivity for each of the three detectors of the LWD tool. The gamma-ray detectors have similar azimuthal sensitivities, and are affected by the materials located opposite to the detector side of the tool. The thermal-neutron detector is highly focused. I will show in the following section how the differences in azimuthal sensitivity have important implications in the effect of borehole fluid, borehole size, and tool standoff in the measurement.

I use MCNP to generate multi-detector signals for the LWD tool in a siliciclastic sequence to illustrate the effect of detector sensitivity on Sigma logs. **Figure 2.6** shows the calculated multi-detector Sigma logs computed from MCNP decay signals (dots), as well as the full response of apparent Sigma that would be achieved in each formation if it were

infinitely thick (yellow square lines). Notice that the thermal-neutron detector can read close to the apparent bed Sigma in the thin shale layer at 1.5 m and the sand layer underneath. The response of the long-spaced detector is smoother. Interpretation of only the long-spaced detector Sigma would be misleading, resulting in the identification of only one thick layer with intermediate value of Sigma. The long-spaced gamma-ray detector is highly affected by shoulder beds because of its large volume of investigation. The short-spaced gamma-ray detector, with intermediate vertical resolution and depth of investigation, allows the detection of three different layers but does not sense the true formation Sigma values of the thin layers.

2.7 Environmental Effects

Pulsed neutron capture measurements can be affected by several factors that mask the true formation response. The main environmental effects are diffusion and borehole effects.

2.7.1 Diffusion Effects

The assumptions implicit in the analysis of time decays, such as negligible scattering compared to absorption and negligible spatial dependence of the particle flux, have implications in the Sigma values that are calculated from decay curves. Sigma estimated from late-time decays is an apparent value of Sigma, Σ_{app}, that differs from the real material or intrinsic Sigma, Σ_{int}. Since the deviation is due to the particle movement driven by concentration gradients, the phenomenon is often referred to as diffusion effects.

Close to the source, diffusion gradients are high and thus the decay of particles is strongly affected not only by neutron absorption but also by scattering or diffusion. As a consequence, the apparent thermal-neutron detector Sigma deviates significantly from the real material Sigma. Away from the source, the particle concentration gradients are low, causing fewer diffusion effects in the long-spaced gamma detector and Sigma values closer to intrinsic Sigma. Additionally, a naïve interpretation of decay curves would assume that at late times the bulk response is dominated only by the formation. In fact, at late times there is diffusion of neutrons from the formation into the borehole where few particles would otherwise remain unabsorbed; tool and borehole effects are constantly present in the measurement.

Apparent Sigma must be converted to intrinsic Sigma via corrections derived from calibration of the tool in a wide range of formation materials, borehole fluids, and borehole sizes. It is only intrinsic Sigma that follows a linear volumetric mixing of the Sigma of the components of the formation, and thus intrinsic Sigma is required to perform interpretation of Sigma logs.

Figure 2.7 shows uncorrected apparent Sigma plotted against true intrinsic Sigma values for experimental and MCNP data over a wide range of Sigma. The experimental data are from the three Sigma detectors of the LWD tool in various test pits. Simulated MCNP and experimentally measured decay curves are processed with the moments method for the gamma-ray detectors and with a two-exponential fit for the neutron detector. The measurements are made with a 20-cm (7 7/8-in) LWD tool without standoff. The colored

lines show polynomial fits to the simulated data. The polynomials allow for the correction of borehole and diffusion effects in the case where no standoff is present. Additional calibration is performed by service companies to account for diffusion effects related to borehole fluid and size.

2.7.2 Borehole Effects

Borehole effects are highly dependent on tool standoff and the azimuthal sector where standoff occurs. **Figure 2.8** shows apparent Sigma values for MCNP simulations of the 20-cm (7 7/8-in) LWD tool in the case of different types of fluids filling the borehole. **Figure 2.8a** and **Figure 2.8b** illustrate the case of standoff in the azimuthal sector opposite to detector orientation, and on the detector side of the tool, respectively. The fluids in the borehole span the range from gas to saturated brine. The drilling fluid fills both the borehole and the internal mud channel of the tool.

Borehole fluid effects are smaller when the detector side of the tool is against the formation (or, specifically, there is only the slight standoff introduced by the presence of a stabilizer). **Figure 2.8a** shows that the effect of the fluid inside the mud channel is small because the tool housing steel dominates the borehole response. The neutron detector, which has small azimuthal sensitivity, is less affected by standoff at the back of the tool. The long-spaced gamma-ray detector, with its large azimuthal sensitivity, is the most affected.

Borehole fluid effects are important when the detector is not in contact with the formation. **Figure 2.8b** shows that the neutron detector is the most affected by standoff at

the front sector because its sensitivity is focused on that side of the tool. Standoff in the range of only 2 to 5 cm (1 to 2 in) in front of the neutron detector can mask the formation response. The gamma-ray detectors are less affected by small standoff at the front sector. However, 7 cm (3 in) of standoff can significantly alter the detector response. These observations are important in LWD Sigma interpretation because tool standoff might generate separation of the three Sigma logs and be erroneously interpreted as invasion. Interpretation of multi-detector Sigma logs should be preceded by borehole quality check.

2.8 MULTI-DETECTOR SIGMA INTERPRETATION

2.8.1 Mud-Filtrate Invasion Effects on LWD Measurements

LWD Sigma measurements use multiple detectors to assess invasion in the shallow near-wellbore zone, i.e., 0 to 35 cm (0 to 14 in). To understand why interpretation of LWD Sigma logs can have added value over interpretation of only LWD resistivity logs, I study invasion phenomena in typical LWD scenarios.

Mud-filtrate invasion can be present at the time of LWD borehole measurements; even though it is a common assumption that the duration of exposure to pressurized drilling fluid is too brief for invasion to take place. Radial length of invasion is dependent upon the overbalance pressure, the petrophysical properties of the formation, rheological properties of the drilling fluid, and time-after-bit (*TAB*). *TAB* is the period of time between the passage of the bit through a formation until the LWD measurement is made. The time of exposure is given by

$$TAB = \frac{h_{bit}}{ROP}, \tag{2.16}$$

where h_{bit} is the spacing between the bit and the LWD measurement point, and *ROP* is the rate of penetration.

Typically, the LWD tool is mounted above the drilling motor, at about 9 m (30 ft) from the bit. The rate of penetration varies depending on the formation type, drilling fluid, and operational conditions. However, a range of *ROP* between 0.085 and 2.5 cm/s (10 and 300 ft/hr) can be considered extreme limits within the wide range of possible conditions. At an average h_{bit} of 9 m, and *ROP* between 0.085 and 2.5 cm/s, the range of typical *TAB* is between 360 and 10800 seconds (0.1 and 3 hr). Measurements acquired 3600 seconds (1 hr) after bit passage are typical.

The purpose of this section is to identify a range of expected radial lengths of invasion in LWD conditions that allows to understand the potential of multi-detector Sigma. I compute invasion maps for the case of WBM invading an oil-bearing sandstone rock under the drilling and logging conditions presented in **Table 2.1** for the three different rock types presented in **Table 2.2**. I use the reservoir simulation module (Abdollah-Pour, 2011) in UTAPWeLS, a formation evaluation platform developed at The University of Texas at Austin to model mud-filtrate invasion.

First, I investigate the range of possible radial lengths of invasion that can be expected under regular LWD conditions. **Figure 2.9** shows invasion maps for drilling conditions 1 and 2 (from top to bottom) and the three rock types defined in **Table 2.2** (from

left to right). Invasion profiles are not piston-like, but rather smooth due to capillary forces in the porous media. However, the midpoint of the smooth invasion profile is a good approximation of radial length of invasion. The insets in each panel indicate the radial length of invasion for each case. The dashed lines indicate the maximum sensitivity of the LWD Sigma tool (35 cm). Invasion deeper than the dashed lines results in the overlay of the three curves of the MDOI Sigma logs. Notice that only LWD Sigma measured under drilling conditions 1, i.e., small *TAB*, would yield separation in LWD Sigma curves. The important detail in **Figure 2.9** is that shallow-sensing LWD measurements under regular drilling conditions can be completely masked by the presence of mud filtrate. A lack of separation of the Sigma curves indicates either no invasion or full invasion, while separation indicates radial length of invasion within 35 cm from the wellbore.

Filtrate invasion results indicate that any radial length of invasion in the range of sensitivity of LWD Sigma, and even beyond 35 cm can be expected under regular LWD conditions. Now, I investigate the possibility of tear-drop invasion profiles in short exposure times typical of LWD logging conditions in an oil-bearing formation. The reasons for the asymmetric shape of the invasion profile are mainly gravity and permeability anisotropy. **Figure 2.10** shows the invasion profile for a horizontal well in rock type II for *TAB* equal to 10800 seconds (3 hr) for cases of equivalent horizontal and vertical permeability, $K_v/K_h = 1$ (top), and $K_v/K_h = 2$ (bottom). **Figure 2.10a** shows that for long LWD times such as 10800 seconds the effect of gravity is minimal, and the invasion profile is symmetric if there is no permeability anisotropy. **Figure 2.10b** shows that in the case of

K_v/K_h equal to 2 there is asymmetry in the invasion profile. Nonetheless, the shape of the invasion front is just a slight deviation from the symmetric profile and is far from having a tear-drop shape. Highly asymmetric profiles are unlikely to develop under short exposure times to drilling fluid.

During LWD Sigma processing, the time decay signals from different azimuthal sectors are averaged and combined into one signal to improve the statistics at each depth level. The symmetric nature of the invasion profile for short exposure times typical in LWD operations suggest that the averaging is apposite and does not introduce artifices in tool response. Should asymmetric invasion occur, the sector averaging would blur the actual formation response by combining all the sector signals into one average invasion measurement.

Simulations of filtrate invasion indicate that invasion is possible within the shallow near-wellbore zone, in addition to invasion deeper than the sensitivity of the LWD Sigma detectors. Results also show that due to short times of exposure to drilling fluid, the shape of the invasion front is fairly symmetric, even in the case of permeability anisotropy in the formation. At the next stage of the study, I analyze the response of the Sigma and resistivity measurements across the wide range of radial lengths of invasion that these reservoir simulations suggest in the LWD environment.

2.8.2 Multi-Depth-of-Investigation, MDOI, Sigma

An important feature of LWD Sigma logging is the capability to provide three radial depths of investigation in the shallow near-wellbore zone. Analogous to resistivity tools,

as previously mentioned, the multiple depths of investigations can be used to assess the presence of invasion. **Figure 2.11** shows the radial cumulative sensitivity functions, known as *J* factors, for the LWD Sigma tool in 34-p.u. sandstone fully saturated with fresh water. The *J* factors suggest that radial lengths of invasion within the range of maximum sensitivity of the long-spaced detector, about 35 cm, yield separation in the LWD Sigma curves. Hence, separation in the three Sigma logs is a tool for qualitative and quantitative assessment of invasion. The separation is analogous to the separation that could be expected in different channels of a resistivity measurement. The question at this point is how different are the responses of LWD Sigma and resistivity to invasion.

LWD propagation resistivity measurements typically produce amplitude and phase resistivity logs from low and high frequencies. The tools have transmitters and receivers with different spacing that provide the measurement with multiple depths of investigation to assess the presence of invasion and evaluate virgin-zone resistivity even in the presence of invasion. This section compares the responses of MDOI resistivity and Sigma measurements in the presence of invasion of WBM of different salinities. The main purpose of this phase of the study is to define when separation in the resistivity and Sigma logs can be an indication of invasion and to know whether one measurement outperforms the other one under certain conditions.

I generate LWD Sigma and resistivity logs in a sequence of 61-m (200 ft) shaly sandstone layers being piston-like invaded by 200-kppm [NaCl] brine (**Figure 2.12**) in case 1 and 30-kppm [NaCl] brine (**Figure 2.13**) in case 2. The Sigma logs are generated using

MCNP-computed decay curves and applying detector-specific diffusion corrections shown in **Figure 2.7**. The resistivity log simulations are performed using a forward model for LWD resistivity (Zaslavsky et al., 2006); I only show simulations for the high-frequency phase channels because they have the shallowest depth of investigation in the propagation measurement. **Table 2.3** describes the properties of the virgin and flushed zones for invasion cases 1 and 2.

Figure 2.12 compares LWD Sigma and resistivity for case 1, the case of high-salinity brine invading oil-bearing shaly sandstone. Track (a) shows the earth model. Full invasion exists at the top layer and no invasion exists at the bottom layer. The high salinity of the mud filtrate, 200-kppm [NaCl], and 20 p.u. generate a contrast in the nuclear properties of the virgin and invasion zones. The contrast between virgin- and invasion-zone Sigma and resistivity is big enough to cause separation in both sets of curves. Separation in multi-detector Sigma logs allows detection of invasion in the zone within 12 cm (5 in) from the borehole. However, in this shallow near-wellbore zone, the resistivity logs overlay and therefore are not suitable to assess shallow invasion. Invasion deeper than 35 cm does not cause separation in Sigma curves, but it does produce separation in phase resistivity curves. This behavior is a consequence of the shallow nature of pulsed neutron capture measurements compared to resistivity measurements.

Figure 2.13 compares LWD Sigma and resistivity for case 2, the case of low-salinity brine invading oil-bearing shaly sandstone. Notice how in this case the resistivity measurements provide a better way to detect invasion than Sigma logs. The presence of

invasion almost does not perturb the response in the Sigma log because the difference between virgin and flushed Sigma is only 2 c.u. Decreasing the mud-filtrate salinity from 200 kppm [NaCl] to 30 kppm [NaCl] generates only a very low contrast between virgin-zone and invasion-zone Sigma; the contrast in resistivity, however, is still significant.

One of the main limitations of the MDOI Sigma logging is evidenced in the lack of separation of the multi-detector curves in **Figure 2.13**. It is necessary that there be enough contrast between Sigma in the virgin and invasion zones to detect the presence of shallow near-wellbore invasion. The contrast is only possible in the case of salty mud filtrate invading a high-porosity hydrocarbon-bearing formation, or conversely a fresh oil-based mud invading into salty connate water.

2.9 CONCLUSIONS

The commercial LWD Sigma tool uses a 14.1-MeV pulsed neutron generator and three detectors to extract three independent Sigma logs: one from a thermal-neutron detector (Near) and two from gamma-ray detectors (SSn and LSn), all at different spacings to provide different radial lengths of investigation. There exists a tradeoff between signal noise and stability to environmental effects unique to each detector. The thermal-neutron Sigma measurement of the LWD tool is suited to recognize thin layers. However, the caliper log should be checked for washouts because the near detector is highly affected by tool standoff. The long-spaced gamma-ray detector is less affected by invasion and tool standoff, but LSn measurements generally display less statistical quality.

Calculation of Sigma from time-decay curves produces an apparent Sigma which must be corrected for detector-specific diffusion and borehole effects. The environmental correction is larger in the thermal-neutron detector than in the long-spaced gamma-ray detector. Additionally, the effect of fluid in the borehole is especially important if there is standoff at the detector side of the tool.

An important feature of LWD Sigma tools is that the different radial lengths of investigation of the three Sigma measurements permit the assessment of invasion in the shallow near-wellbore zone. Separation of the three Sigma curves indicates presence of invasion in the zone within 35 cm from the borehole wall. Invasion in LWD conditions can be in the range of a few inches to even several feet into the formation, and tear-drop invasion profiles are unlikely to develop by the time LWD measurements are acquired.

In the case of brine invading a high-porosity rock, multi-detector Sigma is useful to assess invasion in the shallow near-wellbore zone and outperforms the resistivity measurement. However, if there is only a small difference between the salinity of the drilling fluid and formation fluid, and/or if the rock has low porosity, the contrast in Sigma between virgin and invaded zones is not sufficient to assess invasion. Salt should be added to drilling fluid whenever MDOI Sigma is intended for assessment of shallow invasion. The MDOI Sigma method is especially well-suited to the evaluation of hydrocarbon-bearing, high-porosity formations invaded by high-salinity filtrate.

Table 2.1: Summary of drilling parameters assumed in simulations of mud-filtrate invasion.

Drilling Condition	h_{bit} **(m)**	***ROP*** **(cm/s)**	***TAB*** **(seconds)**	**Overbalance pressure (kPa)**
1	9.14	2.54	360	3447.38 (500 psi)
2	9.14	0.085	10800	3447.38

Table 2.2: Summary of petrophysical properties assumed for different rock types.

Rock Type	**Porosity (p.u.)**	***K* (md)**	S_{wirr}	K_{ro} **at** S_{wirr}	P_c **at** S_{wirr} **(kPa)**
I	10	1	0.1	0.9	138
II	15	5	0.1	0.9	74
III	20	50	0.1	0.9	28

Table 2.3: Summary of virgin- and invasion-zone properties for LWD Sigma and resistivity simulations.

Invasion Case	C_{mf} **(kppm)**	S_{wirr}	C_{sh}	R_{mf} **at 170°F (ohm-m)**	Σ_{mf} **(c.u.)**	R_{xo} **(ohm-m)**	R_t **(ohm-m)**	Σ_i **(c.u.)**	Σ_v **(c.u.)**
1	200	0.1	0.2	0.025	98	0.73	20	26	12.5
2	30	0.1	0.2	0.085	32	2.61	20	14	12.5

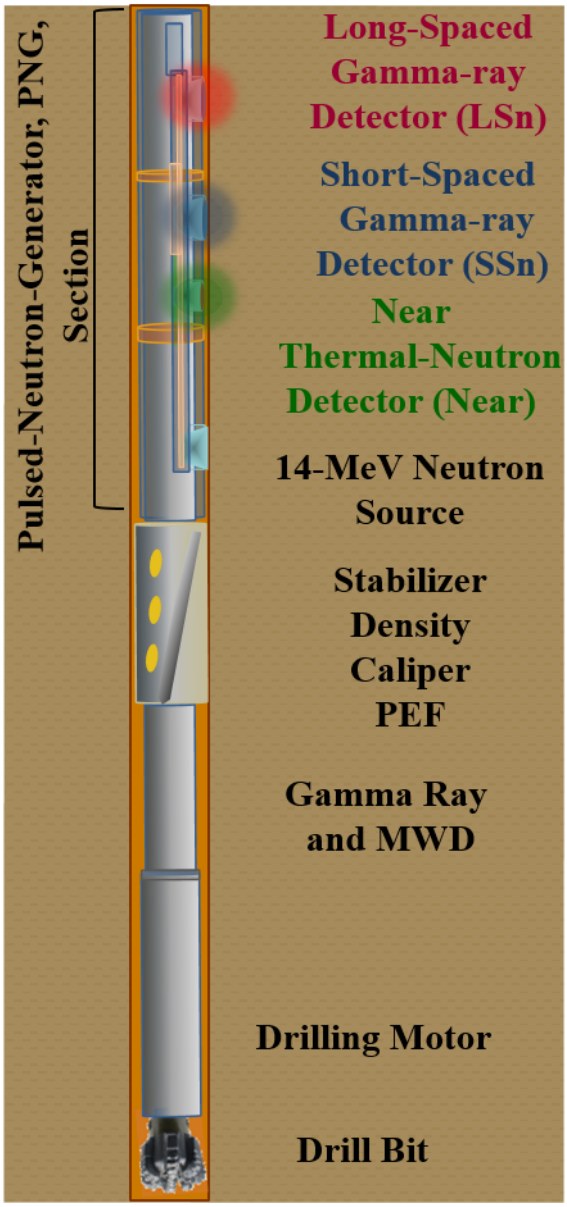

Figure 2.1: The LWD tool with details about detectors used for Sigma logging.

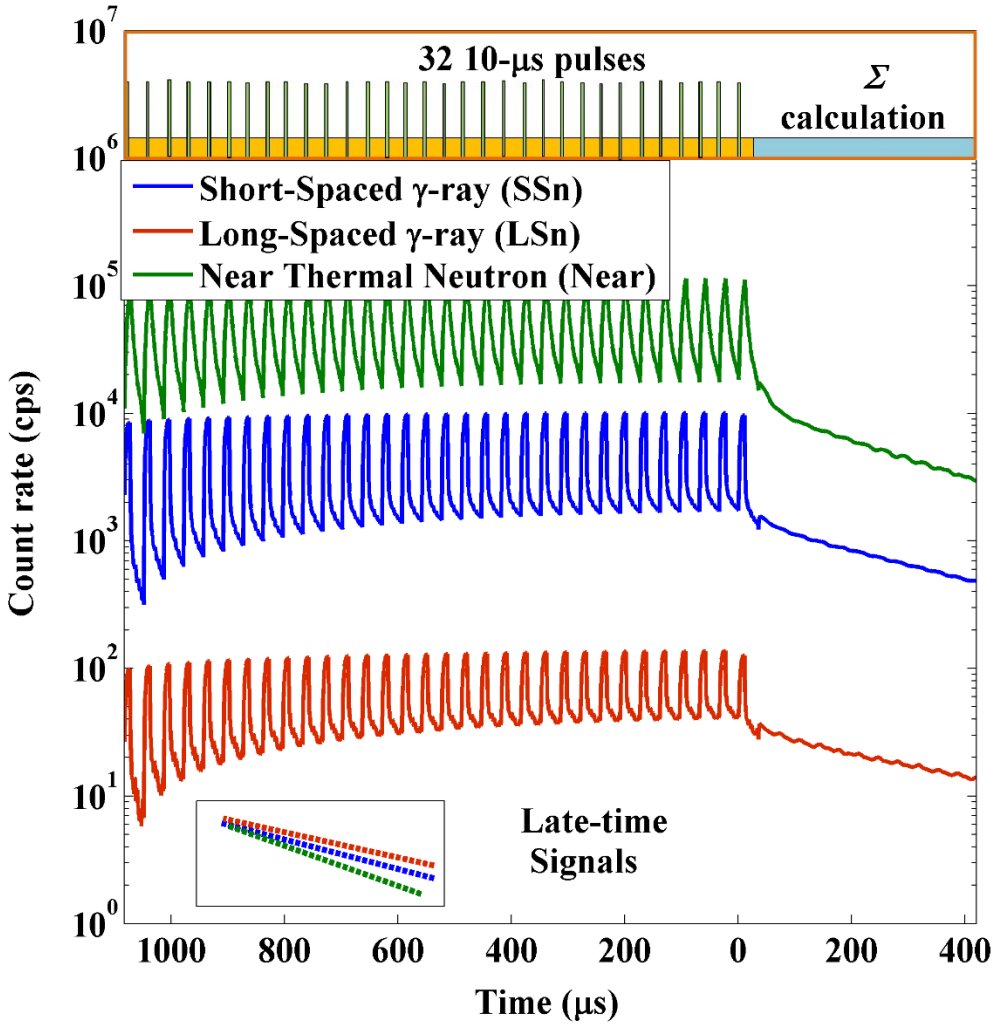

Figure 2.2: Three-detector signals for an LWD Sigma measurement in a 34-p.u. water-saturated sandstone. The inset at the bottom left compares the slope of decay signals at late times, where the difference in slopes is due to tool and borehole effects dependent upon detector position and measured particles.

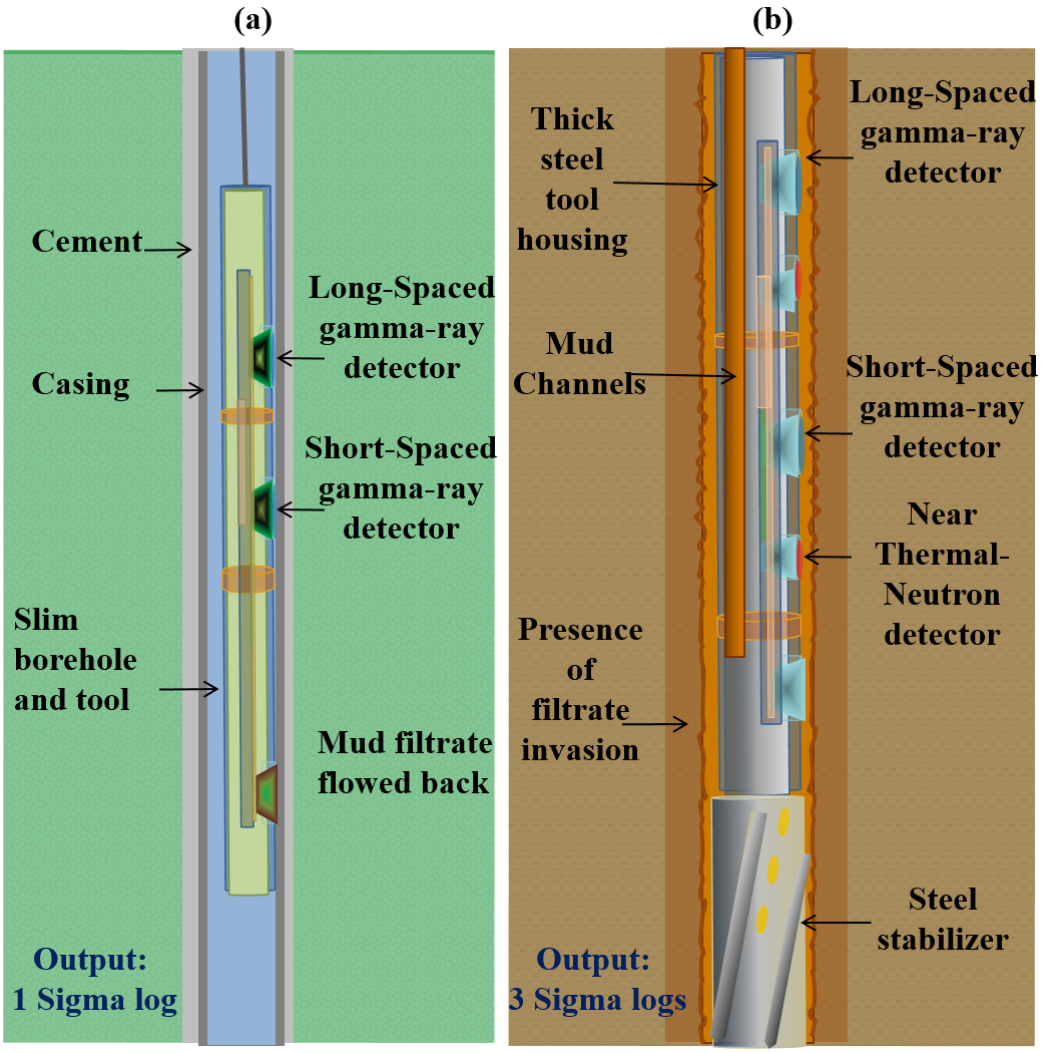

Figure 2.3: Comparison of wireline (a) and LWD Sigma (b) tools and channels.

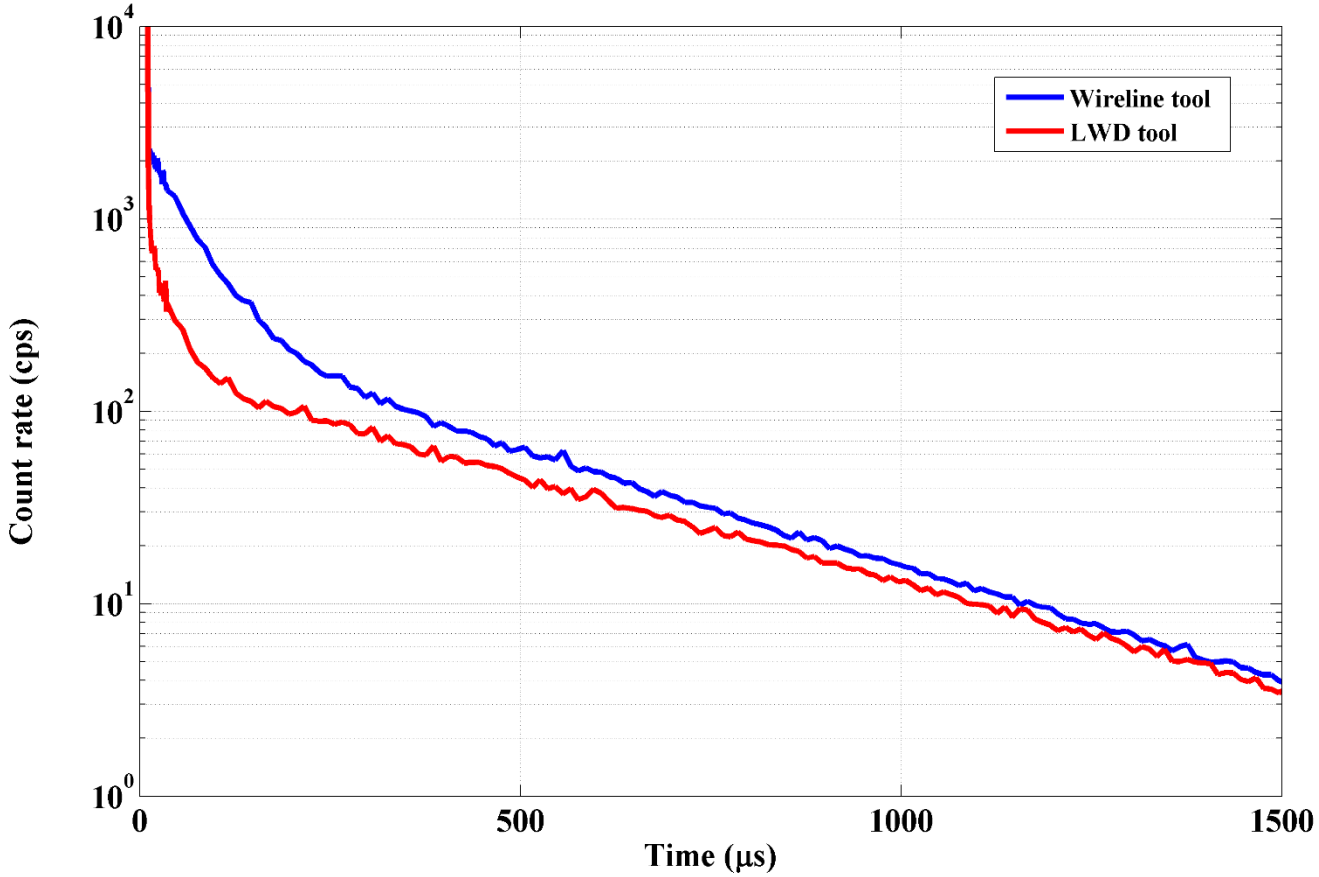

Figure 2.4: Short-spaced gamma-ray detector time decays for the Longhorn wireline tool and the LWD tool under study.

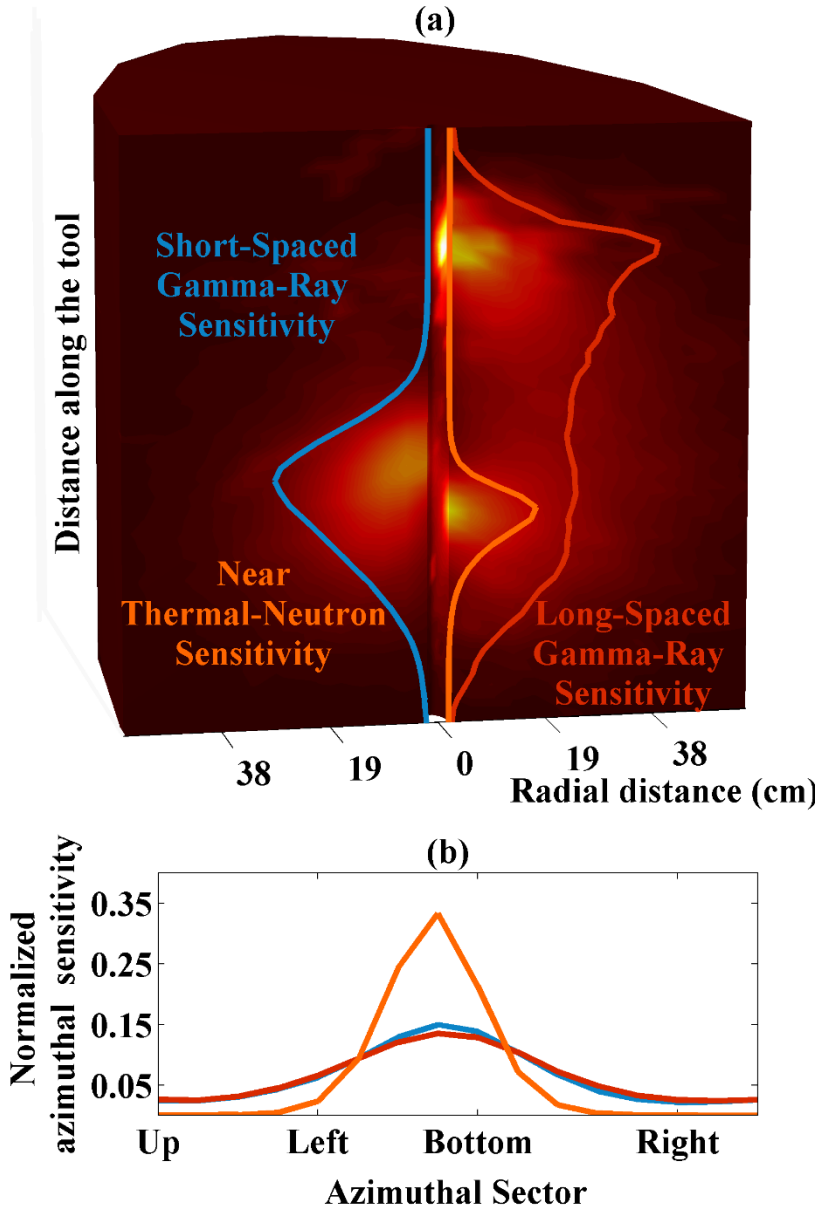

Figure 2.5: Three-dimensional (a) and azimuthal (b) detector sensitivity maps for the LWD Sigma tool in a 34-p.u. fresh water-bearing sandstone formation. In the 3D map, bright areas indicate high sensitivity.

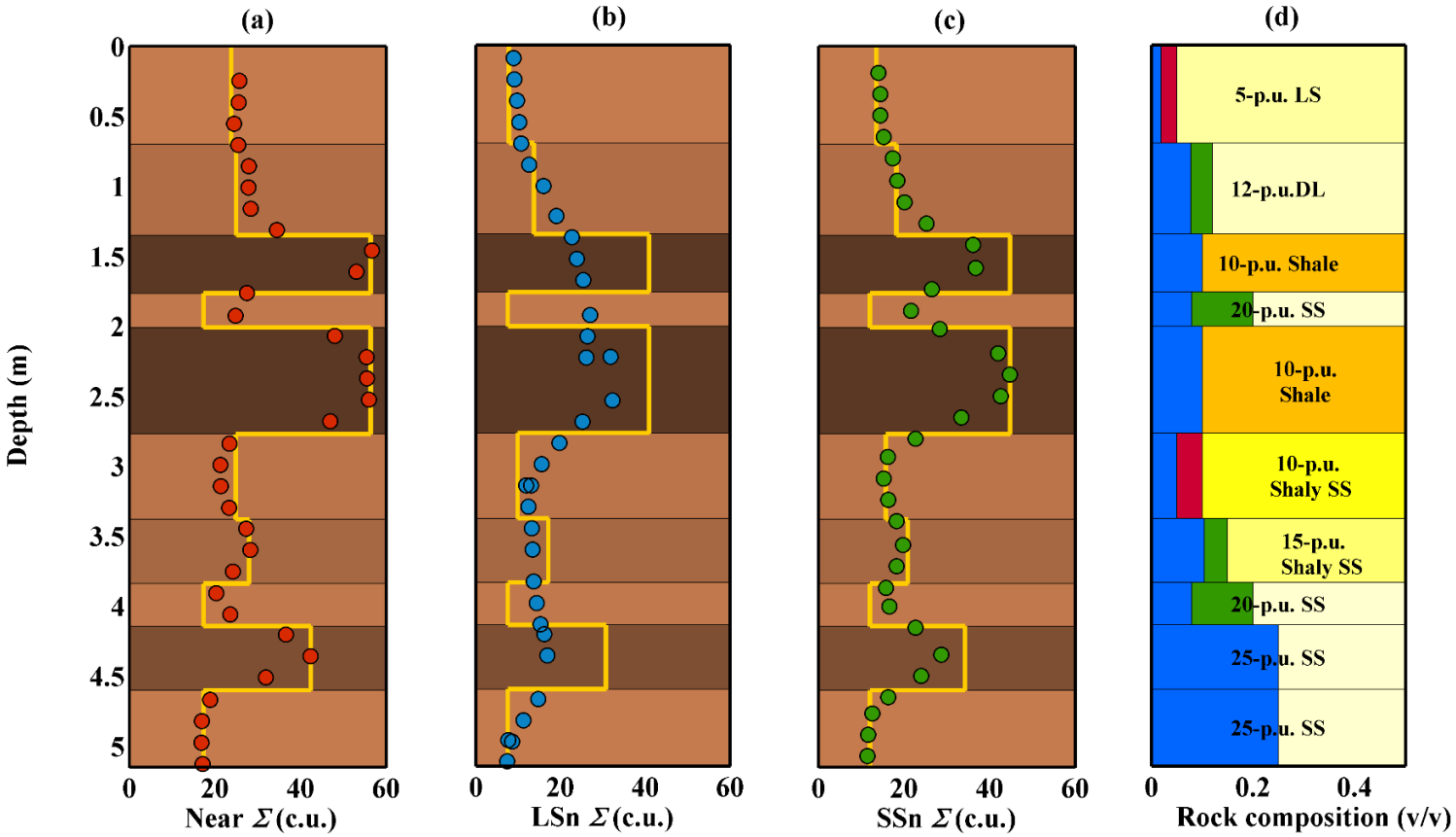

Figure 2.6: Synthetic Sigma logs of the (a) near thermal-neutron, (b) long-spaced gamma-ray, and (c) short-spaced gamma-ray detectors of the LWD tool. The yellow square lines identify the full-response apparent Sigma for each formation. Track (d) shows the volumetric composition of the rocks in the sequence. Blue, green, and red identify water, oil, and gas, respectively. The depth interval between points on these synthetic logs can be irregular because they are plotted at the true 50% axial response of the measurement, which varies at each depth.

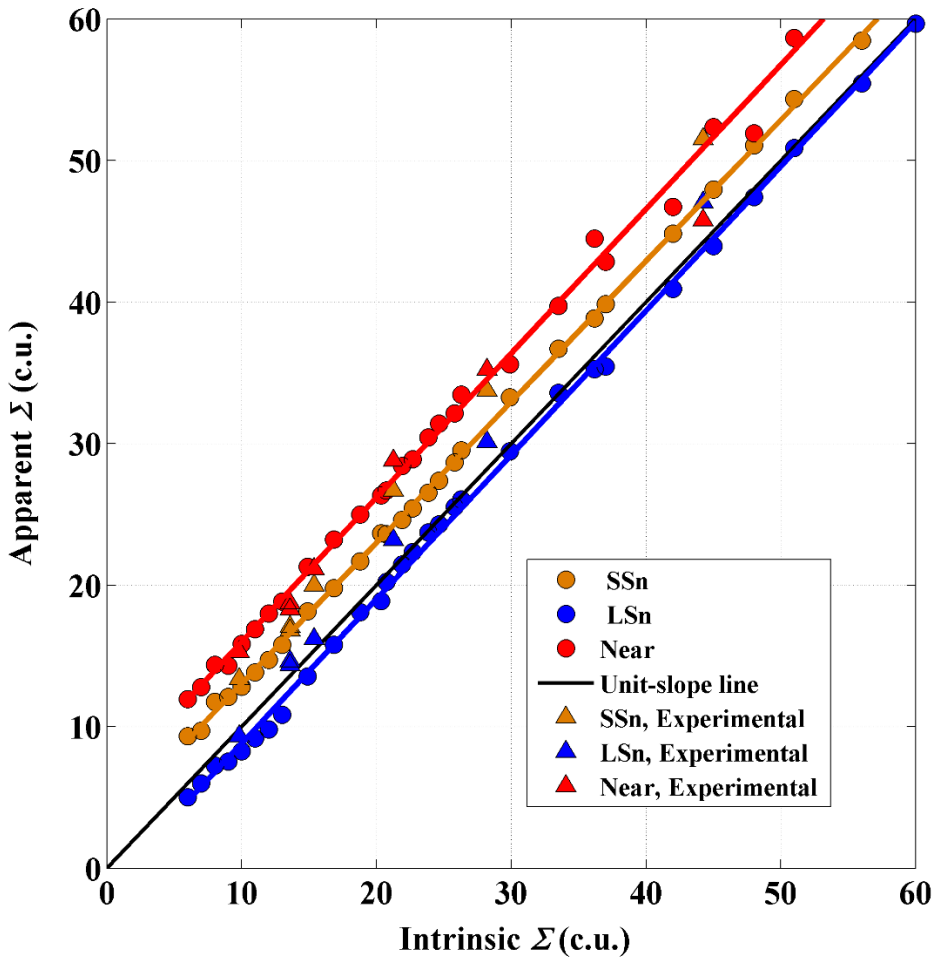

Figure 2.7: Uncorrected apparent Sigma versus intrinsic Sigma, for MCNP simulations and for experimental test-pit measurements acquired with the LWD tool under study.

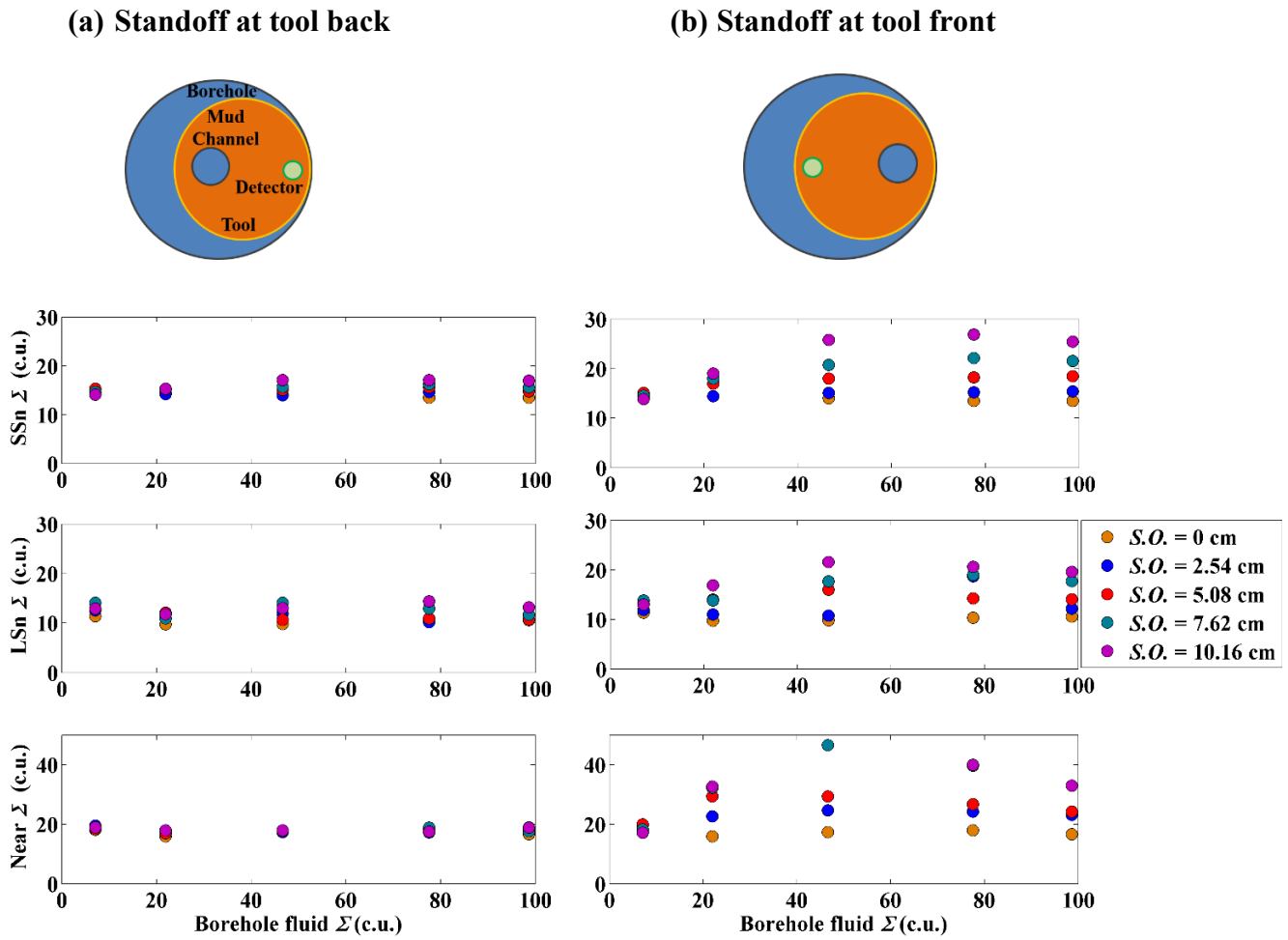

Figure 2.8: Apparent Sigma calculated from MCNP simulations as a function of borehole fluid Sigma and tool standoff, *S.O.* Sketches on top describe the two standoff configurations. Panel (a) describes standoff at the back of the tool (sector opposite to detector side), while panel (b) describes standoff at the front of the tool (detector side).

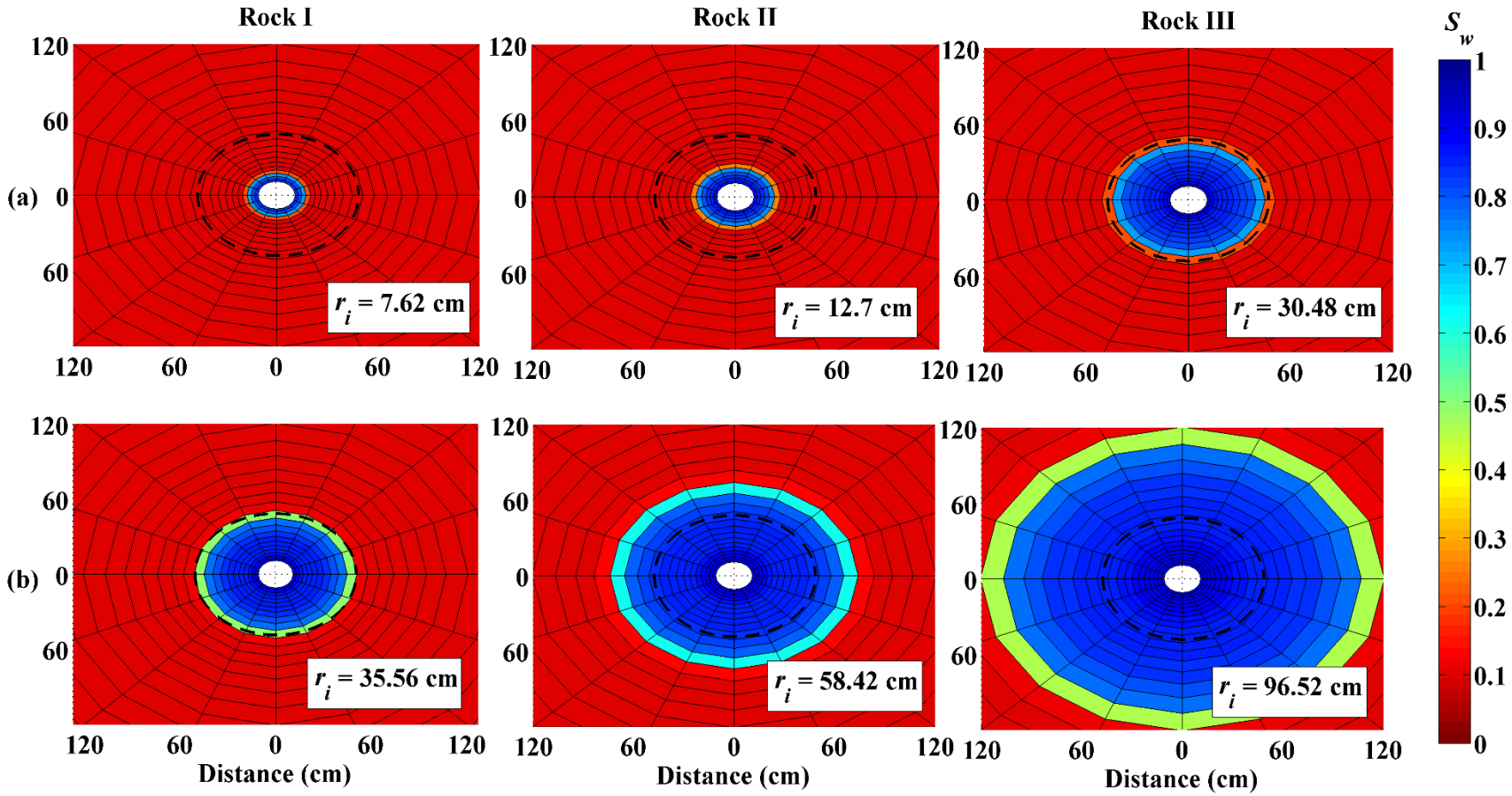

Figure 2.9: Invasion maps for a vertical well for (a) *TAB* equal to 360 seconds (0.1 hr) and, (b) *TAB* equal to 10800 seconds (3 hr). From left to right: simulations of mud-filtrate invasion in rock types I, II, and III. The dashed line identifies maximum sensitivity of LWD Sigma measurement for the tool under study.

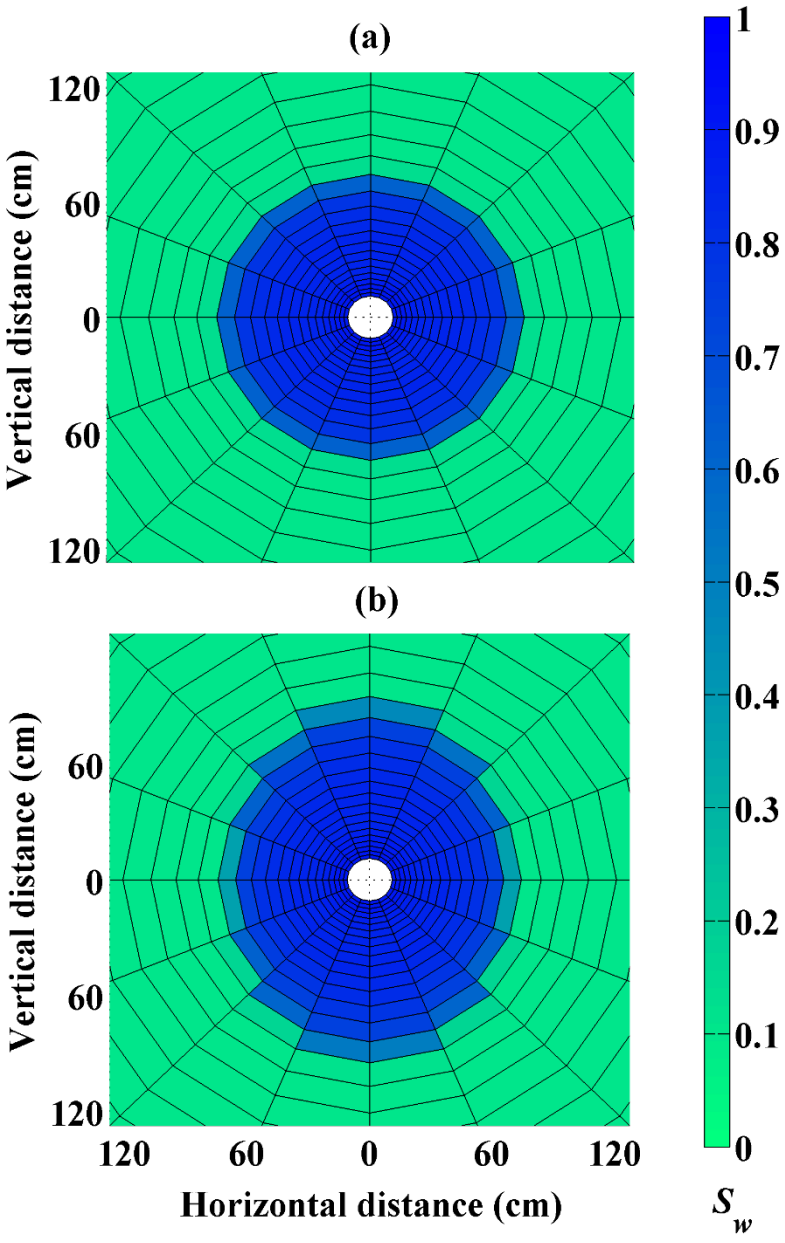

Figure 2.10: Invasion maps for WBM at 3447.48-kPa (500 psi) overbalance pressure invading an oil-bearing sandstone formation for $K_v/K_h = 1$ (a) and $K_v/K_h = 2$ (b) after 10800 seconds (3 hr) of exposure. Formation type II. Notice the slight asymmetric shape of the invasion profile for the case of permeability anisotropy.

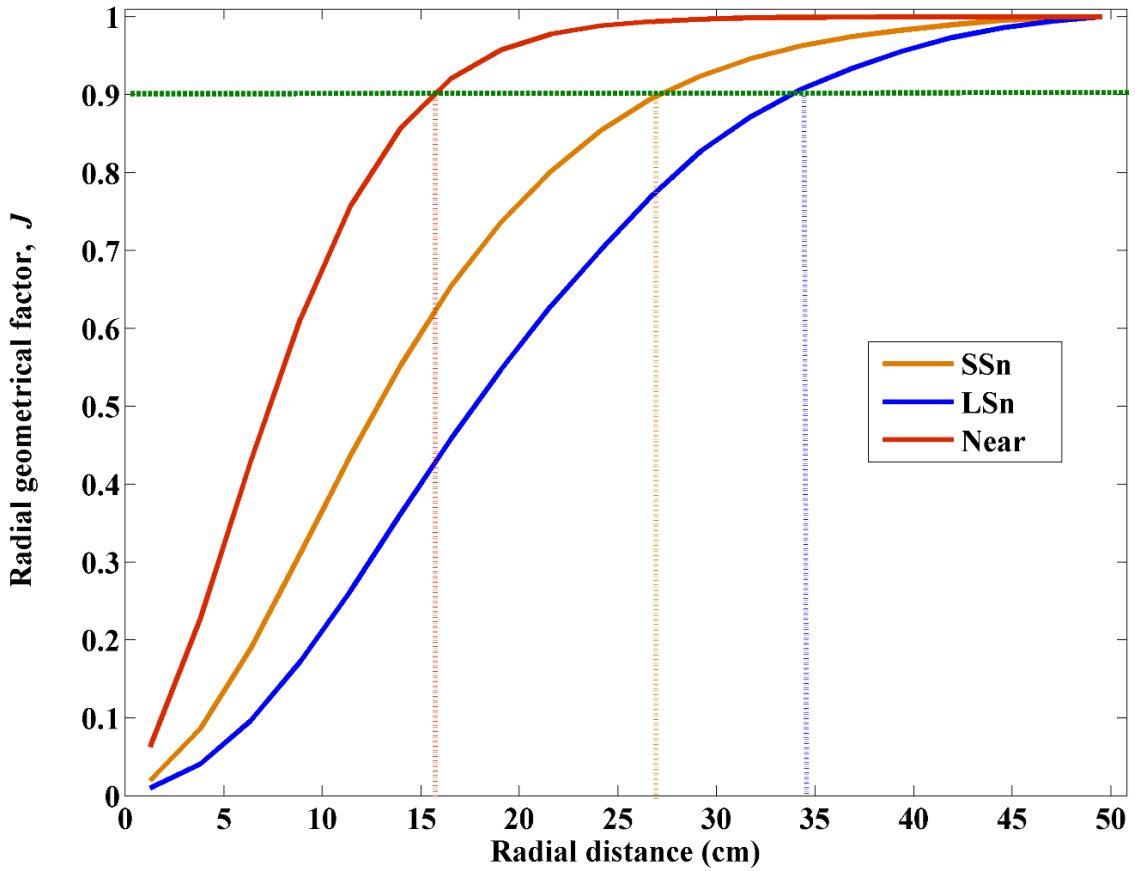

Figure 2.11: Radial geometrical factors for the three detectors of the LWD Sigma tool in a 34-p.u. freshwater-saturated sandstone formation.

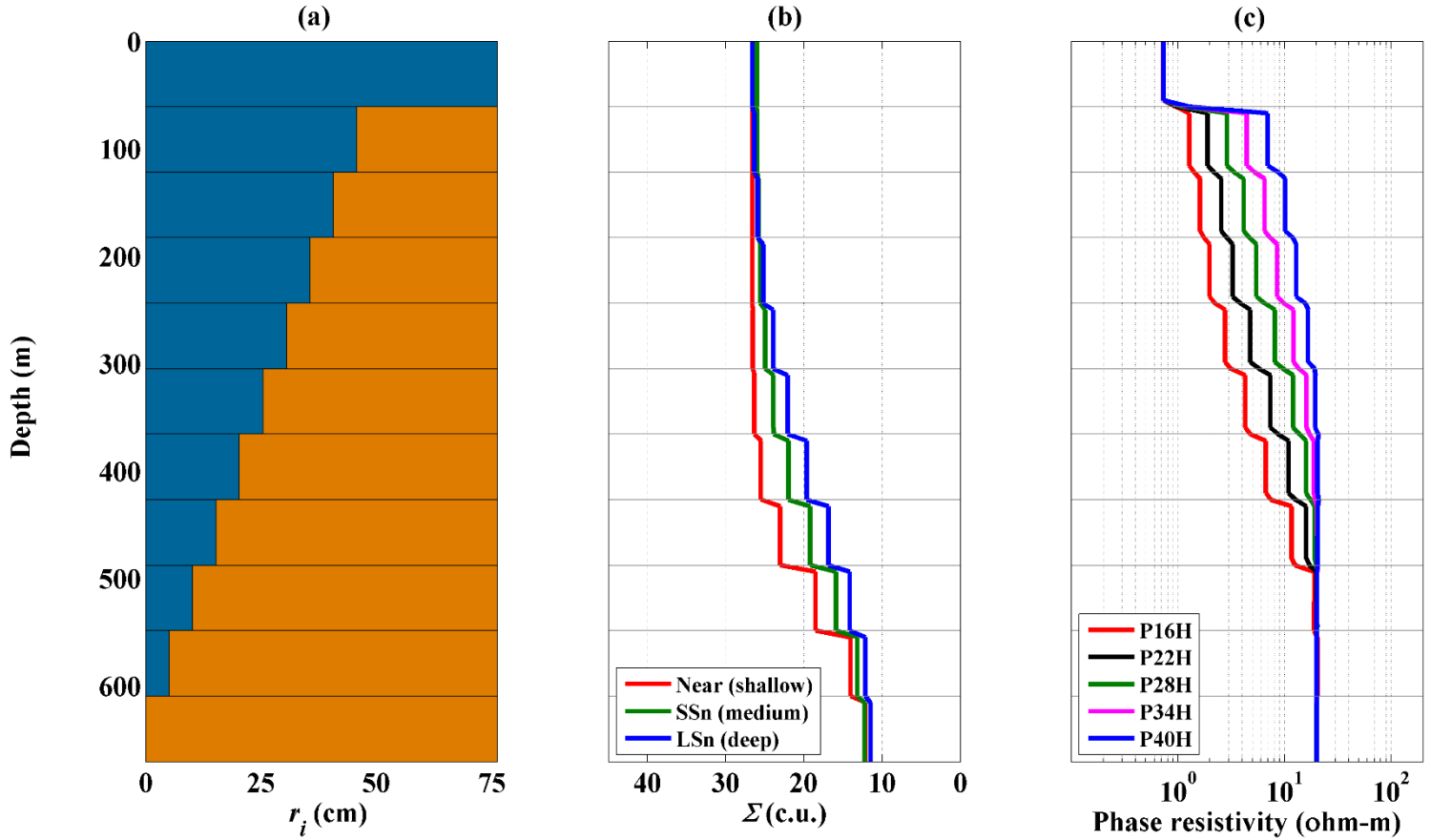

Figure 2.12: Numerical simulations of LWD Sigma (b) and phase resistivity (c) in the case of piston-like invasion of 200-kppm [NaCl] brine in a 20-p.u. oil-bearing shaly sand formation. Track (a) displays the assumed petrophysical model.

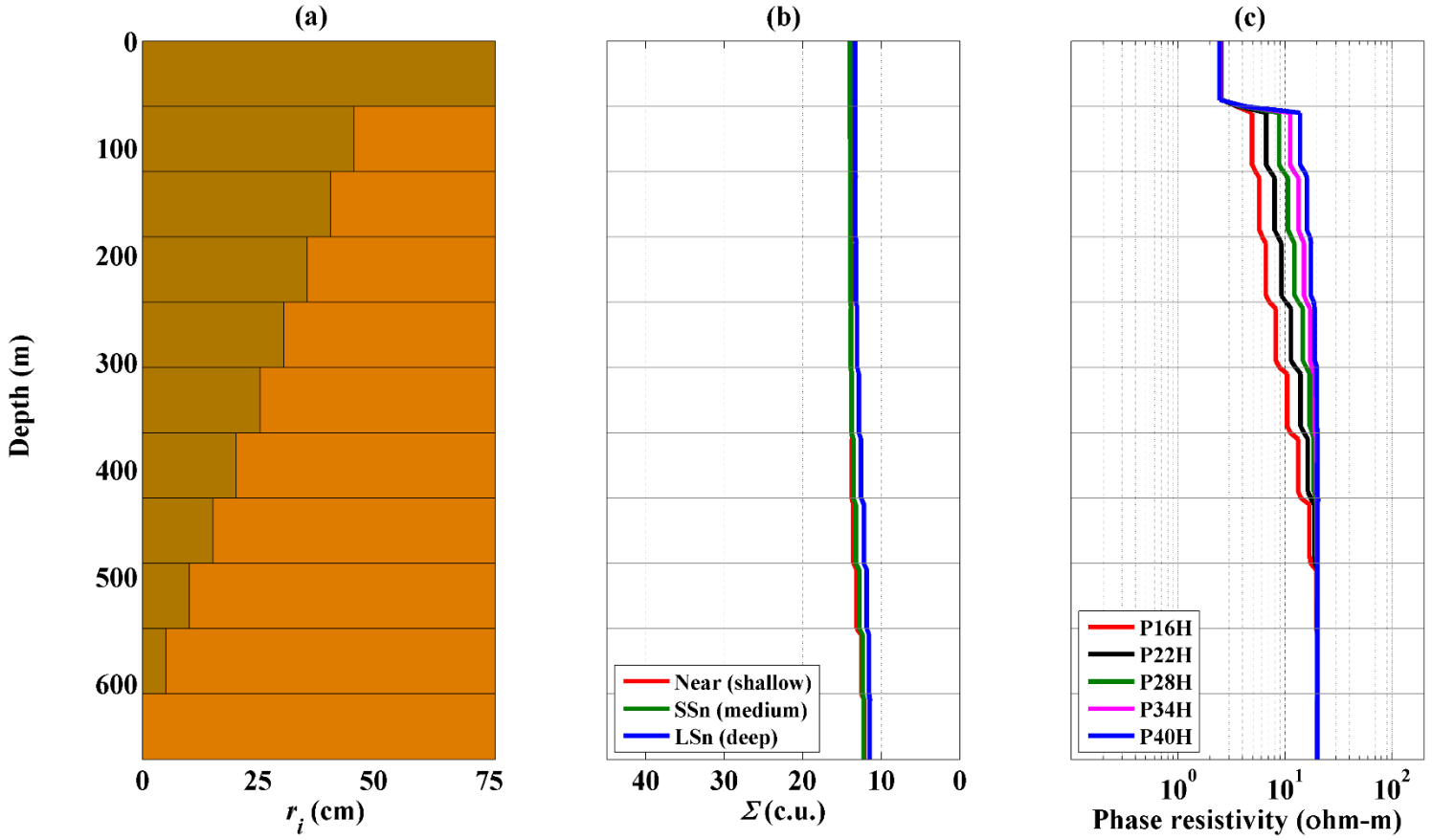

Figure 2.13: Numerical simulations of LWD Sigma (b) and phase resistivity (c) in the case of piston-like invasion of 30-kppm [NaCl] brine in a 20-p.u. oil-bearing shaly sand formation. Track (a) displays the assumed petrophysical model.

Chapter 3: Rapid Forward Modeling of Multi-Detector Logging-While-Drilling Sigma Measurements

Interpretation of LWD Sigma logs is often affected by several environmental and/or geometrical effects which can mask the formation response. A fast numerical simulation method embedded with inversion-based techniques can be used to estimate intrinsic formation Sigma from borehole measurements affected by shoulder-bed, invasion, and/or environmental effects. In this chapter, I develop a fast and accurate method to numerically simulate LWD multi-detector time decays in realistic borehole environments. The method relies on Monte Carlo pre-calculated libraries of particle time decays and detector–specific flux sensitivity functions (FSF), while accounting for detector-specific borehole and diffusion effects. Simulations are benchmarked against laboratory measurements and Monte Carlo N-Particle (MCNP) transport code calculations. Results indicate that multi-detector time decays acquired under complex geometrical conditions can be numerically simulated with average absolute disparities within 2 capture units (c.u.) in a hundred thousandth of the computer time required by MCNP. The simulation of time decays, rather than Sigma itself enables a direct relationship between actual rock Sigma and multi-detector diffusion-affected time decays, thereby removing intermediate correction steps often used to convert apparent into intrinsic formation Sigma.

3.1 INTRODUCTION

The best way to correct environmental and geometrical effects on Sigma logs is to combine fast numerical simulations with inversion to explicitly estimate the formation Sigma. Development of a forward model for Sigma logs can, however, be challenging due to the complexity of nuclear transport phenomena that govern time-dependent nuclear measurements. Modeling Sigma measurements is not trivial because they involve complex thermal neutron and gamma ray transport phenomena (Lamarsh et al., 2001; Stacey, 2007). Main particle interactions are in the form of multi-energy neutron scattering in any direction and within energy levels, absorption, generation of gamma rays of multiple energies, and gamma ray attenuation.

The complete transport process involved in Sigma measurements can be accurately modeled by solving the coupled neutron and gamma-ray Boltzmann equation (Lewis, 1993), for instance, using numerical methods such as discrete ordinates, but they are often extremely slow (Michael, 1999). Solutions can also be approximated with Monte Carlo techniques such as those implemented with the MCNP software (X-5 Monte Carlo Team, 2005), which can accurately model population time decays under general formation/borehole configurations. However, despite its flexibility, the Monte Carlo method is time-consuming and therefore not suitable for inversion methods needed to estimate formation Sigma from Sigma logs affected by complex borehole and formation conditions.

Several approaches have been proposed to rapidly simulate borehole nuclear measurements. Rapid pulsed-neutron-capture modeling was motivated by the need to calculate departure curves to correct Sigma estimated from time decays for diffusion effects (Preeg et al., 1986), rather than for inversion applications. The first fast simulation methods invoked the diffusion equation to model isotropic scattering undergone by thermal neutrons (Locke and Smith, 1975; Henderson and Maynard, 1965). A combination of diffusion-approximated thermal-neutron fluxes convolved with gamma-ray attenuation kernels enabled the calculation of gamma-ray responses to model density and PEF logs (Tittman, 1964; Tittle, 1961). Two-group diffusion approaches have proved valuable to model diffusion effects in thick homogeneous formations (Mickael, 1992). Analogous to neutron/gamma-ray measurement modeling, several authors have used the time-dependent version of the diffusion equation to approximate gamma-ray time decays (Allen et al., 1965; Henderson and Maynard, 1965; Jennings and Weber, 1995; Mikael, 1999). Yet, such models can not accurately approach the complexity of coupled neutron-gamma interactions in realistic logging conditions that involve multiple materials and three-dimensional (3D) configurations, and do not have the computer speed necessary for inversion applications.

The solution of the Boltzmann equation can also be approximated with a Taylor series expansion (Watson, 1984; Case and Watson, 1994) and the concept of flux perturbations (Greenspan, 1976), wherein the order of the expansion defines the degree of accuracy of the solution. Watson (1992) proposed a first-order perturbation method to calculate tool responses using an a-priori known tool response in a homogeneous material

of known cross section together with the spatial sensitivity of the detector. The spatial sensitivity, known as the Flux Sensitivity Function (FSF), determines the relative change in detector response resulting from relative changes in the nuclear properties of the materials within the volume of investigation of the detector, known as perturbations. Mendoza et al. (2007) showed that the first-order perturbation method is reliable to rapidly simulate time-independent tool responses in challenging logging conditions, such as those of invasion of water-based mud into gas-bearing sands, thin beds, and measurements affected by tool standoff. However, first-order perturbations may not be sufficiently accurate to model highly nonlinear effects present in nuclear measurements. Second-order approximations (Zhou et al., 2009) and diffusion-flux difference methods (Ijasan et al., 2013a) have been advanced to improve modeling of nonlinear effects such as those due to tool standoff.

There exist no published studies that address fast modeling of Sigma logs in realistic situations including presence of thin layers, invasion, well deviation, and/or standoff. Modeling of Sigma measurements has generally fallen into studies that address correction of diffusion effects across thick homogeneous formations. Few studies have entertained the numerical simulation of invasion and shoulder-bed effects on Sigma logs. Allen et al. (1965) used a two-group diffusion approach to investigate the effect of piston-like invasion on Sigma logs, but the study only considered thick horizontal formations and axis-symmetrical piston-like invasion profiles. Mimoun et al. (2011) used the first-order perturbation method to rapidly simulate behind-casing Sigma measurements acquired in

thinly bedded intercalations of sand and shale accounting for thermal-neutron diffusion at interlayer boundaries. The study is a remarkable first step toward the rapid simulation of Sigma logs, but does not reproduce time decays and relies on diffusion corrections to relate apparent Sigma to intrinsic formation Sigma.

The primary focus of this chapter is to develop a numerical algorithm to rapidly and accurately simulate thermal-neutron and gamma-ray time decays for the three Sigma detectors present in a multi-function LWD tool, by reproducing borehole and diffusion effects under complex conditions of formation and well geometries.

The outline for this chapter is as follows: First, I describe the multi-detector Sigma tool and processing; next, I introduce the method to simulate detector-dependent particle time decays from a library of FSFs and time decays. Finally, I benchmark modeling results against two sets of laboratory measurements and several sets of Monte Carlo simulations of increasing complexity. Results show that the new simulation method provides accurate multi-detector time decays under complex logging conditions and reproduces Sigma logs within average 2 c.u. of disparity in approximately 1e-5 the CPU time required to perform full Monte Carlo simulations, i.e. 1 second versus 27 hours.

3.2 Rapid Numerical Simulation

3.2.1 Formulation

The most advanced code available to model nuclear radiation phenomena is MCNP. The code's accuracy and flexibility enables the modeling of complex geometrical

configurations, sensor, sources, and physical tool properties. However, modeling with MCNP is time consuming and therefore it is not efficient for inversion-based interpretation of borehole nuclear measurements. Fast and accurate modeling of nuclear measurements can be performed by approximating the full Boltzmann transport equation introduced in Chapter 2.

Time-independent nuclear responses can be expressed in the form of a Taylor series expansion as a function of the nuclear interaction cross section that controls a specific type of measurement (Watson, 1984; Case and Watson, 1994). If the total number of counts at the detector position $\mathbf{r}_R$ in a material of interaction cross section α_B is known to be $N_B(\mathbf{r}_R)$ (for instance, from full Monte Carlo simulations in that material), the new number of counts when the material is replaced by a material of interaction cross section $\alpha_B + \Delta\alpha(\mathbf{r})$, can be approximated as (Watson, 1984; X-5 Monte Carlo Team, 2005)

$$N^m(\mathbf{r}_R) = N_B(\mathbf{r}_R) + N_B(\mathbf{r}_R)\sum_{m=1}^{\infty}\int d\mathbf{r}\,\frac{1}{m!}\frac{d^m N}{d\alpha^m}(\mathbf{r}_R,\mathbf{r})\left(\frac{\Delta\alpha(\mathbf{r})}{\alpha_B(\mathbf{r})}\right)^m, \qquad (3.1)$$

where the term $\frac{1}{m!}\frac{d^m N}{d\alpha^m}(\mathbf{r}_R,\mathbf{r})$ is a normalized sensitivity coefficient known as Flux Sensitivity Function (FSF), and the approximation $N^m(\mathbf{r}_R)$ is the m^{th} degree Taylor polynomial of $N(\mathbf{r}_R)$. The FSF is a function of the known material cross section and includes borehole and tool properties. Equation 3.1 describes the approximation of the

effective response based on a-priori knowledge about the detector response in a background material, $N_B(\mathbf{r}_R)$, and the change in detector response as a function of multiple perturbations, $d^m N / d\alpha^m$. The integral in equation 3.1 describes the addition of all the partial perturbations in the space of sensitivity of the detector, $\Delta\alpha(\mathbf{r})^m$, weighted by the partial sensitivity of the detector at the location where each perturbation occurs.

Even though nuclear detector responses are nonlinearly dependent on the interaction cross section, α, the higher-order terms in equation 3.1 can be neglected in the case of small perturbations to the background material, i.e., nonlinear detector responses can be locally approximated in the form of first-order Taylor series if the perturbation is small. Neglecting the higher-order terms in equation 3.1, the first-order approximation of time-independent nuclear measurements can be expressed as

$$N^m(\mathbf{r}_R) = N_B(\mathbf{r}_R) + \Delta N(\mathbf{r}_R), \tag{3.2}$$

whereupon

$$N(\mathbf{r}_R) = N_B(\mathbf{r}_R) + N_B(\mathbf{r}_R)\int d\mathbf{r}\,\mathrm{FSF}(\mathbf{r}_R,\mathbf{r},\alpha_B)\left(\frac{\Delta\alpha(\mathbf{r})}{\alpha_B(\mathbf{r})}\right). \tag{3.3}$$

The perturbation parameter, or interaction cross section, in equation 3.3 is the cross section that mostly controls the nuclear measurement being approximated, e.g., density in bulk density measurements, and the inverse of migration length ($1/L_m$) in neutron porosity measurements. In the case of pulsed neutron capture measurements, I define the perturbation parameter as the thermal-neutron absorption cross section, Σ_a, because it is

the nuclear property of the formation that predominantly affects the time evolution of the population decay and is also the nuclear property that I intend to model. Equation 3.3 can be written for one time bin of a pulsed-neutron decay measurement as

$$N(\mathbf{r}_R) = N_B(\mathbf{r}_R) + N_B(\mathbf{r}_R)\int d\mathbf{r}\mathrm{FSF}\left(\mathbf{r}_R,\mathbf{r},\Sigma_{a_B}\right)\left(\frac{\Delta\Sigma_a(\mathbf{r})}{\Sigma_{a_B}(\mathbf{r})}\right). \tag{3.4}$$

The concept of linear perturbations to approximate detector counts can be extended to reproduce time decays for certain materials of cross section Σ_a if the time decay for a background material Σ_{a_B} is known. I apply the first-order perturbation to each time bin in a time decay as follows

$$\mathbf{n}(\mathbf{r}_R,t) = \mathbf{n}_B(\mathbf{r}_R,t) + \mathbf{n}_B(\mathbf{r}_R,t)\int d\mathbf{r}\mathrm{FSF}\left(\mathbf{r}_R,\mathbf{r},\Sigma_{a_B},t\right)\left(\frac{\Delta\Sigma_a(\mathbf{r})}{\Sigma_{a_B}(\mathbf{r})}\right), \tag{3.5}$$

where $\mathrm{FSF}\left(\mathbf{r}_R,\mathbf{r},\Sigma_{a_B},t\right)$ is the time- and detector-dependent FSF and $\mathbf{n}(\mathbf{r}_R,t)$ is the particle time decay for a given detector. . In Chapter 2, $\mathbf{n}(\mathbf{r}_R,t)$ was defined as a detector-specific time decay for the irregular time bins of the pulsed-neutron commercial tool under study from 0 μs to 415 μs, where time 0 μs is the time at which the last pulse is generated.

The time dependency in the sensitivity function is not practical for fast simulation purposes because it requires having a different sensitivity map for each of the multiple time bins of the time decay measurement. Additionally, FSFs specific for the late-time components of the time decay would be difficult to accurately calculate because of the significant statistical noise resulting from the reduced amount of particles at late times. Instead, I use

a time-integrated $\mathrm{FSF}\left(\mathbf{r}_R,\mathbf{r},\Sigma_{a_B}\right)$ calculated in the late-time interval that is dedicated to calculate formation Sigma. Equation 3.5 can be rewritten as

$$\mathbf{n}\left(\mathbf{r}_R,t\right)=\mathbf{n}_B\left(\mathbf{r}_R,t\right)+\mathbf{n}_B\left(\mathbf{r}_R,t\right)\int d\mathbf{r}\mathrm{FSF}\left(\mathbf{r}_R,\mathbf{r},\Sigma_{a_B}\right)\left(\frac{\Delta\Sigma_a\left(\mathbf{r}\right)}{\Sigma_{a_B}\left(\mathbf{r}\right)}\right). \tag{3.6}$$

Equation 3.6 indicates that a-priori knowledge of the three time decays of the LWD tool detectors in a material of absorption cross section Σ_{a_B} and the detector-dependent FSFs in that material can be used to approximate three new time decays. The FSFs account for the effect of multiple perturbations in Sigma, $\Sigma_{a_B}\left(\mathbf{r}\right)+\Delta\Sigma_a\left(\mathbf{r}\right)$, induced at several locations within the volume of sensitivity of each detector.

The three panels in **Figure 3.1** describe the first-order time decay approximation method for the SSn, LSn, and Near detectors of the LWD tool. Blue and green solid lines identify MCNP-calculated time decays for materials of 6 and 14 c.u and red markers describe the time decay calculated using MCNP in a 10-c.u. material, while the dark orange line identifies the simulated time decay for the 10-c.u. material using the first-order approximation described by equation 3.6. Notice the good agreement between simulated and Monte Carlo time decays, and also how the shape of the early- and late-time parts of the decay are reproduced for each detector. The characteristic borehole decay section and bump at 35-μs are characteristics of time decays associated with the pulsing scheme used by the pulsed-neutron generator of the LWD tool. These features can be reproduced by the

fast-forward method because the pre-calculated signals are superimposed in time to reproduce the actual pulsing scheme enforced by the LWD tool.

The simulation of particle time decays using first-order approximations is accurate for small changes in absorption cross section. Nevertheless, simulation of actual LWD Sigma measurements frequently involves high contrasts in absorption cross sections. These changes are common when logging across siliciclastic sequences because of the high contrast between the Sigma of the pure end members of the sequence, and also in cases involving invasion of high-salinity mud filtrate into hydrocarbon-bearing formations. Because the latter are the most important conditions of applicability of MDOI Sigma measurements (Ortega et al., 2013), it is imperative to adjust the first-order perturbation method to approach significant changes in material cross section. I propose the construction of a Monte Carlo pre-computed library of time decays and late-time FSFs, specific to each detector of the LWD tool, to be used together with the first-order perturbation method. Such an approach has the potential to enable the fast and accurate calculation of time decays in cases that involve complicated geometries with high variations in absorption cross section within the specific range of the sensitivity of each detector.

3.2.2 *Time Decay Library*

The fast-forward algorithm is aimed at reproducing tool measurements in a wide range of materials that may be encountered under practical logging conditions. Because first-order approximations are more accurate whenever the perturbation is small, I pre-compute single-pulse time decays using MCNP for a wide range of homogeneous materials

spanning the range of 6 to 120 c.u. Most formation materials have Sigma values in the range of 6 to 60 c.u., but I include higher Sigma decays in order to simulate borehole effects due to salty brine in the mud. The construction of the library consists of two steps: first, the computation of single-pulse 2000-μs time decays; second, the superposition in time of the single-pulse time decays using the pulsed-source protocol of the tool under study to emulate actual features in the shape of the time decays associated with the pulsing scheme. The library is calculated for each detector to account for borehole and diffusion effects that depend upon detector position and type of measured particles.

The decay of particles at late times is not only dominated by absorption in the formation but also by borehole and diffusion effects, as mentioned in Chapter 2. Service companies perform laboratory and numerical experiments under a wide range of borehole conditions and materials of known Sigma to develop correction factors that enable the calculation of intrinsic Sigma from apparent Sigma. However, the correction is not always perfect and it is an intermediate step between the fundamental physical measurement and intrinsic Sigma.

The simulation procedure advanced in this chapter has the advantage of providing a direct relationship between intrinsic Sigma and borehole/diffusion-affected time decays at each detector. Consequently, no borehole/diffusion correction factors are needed because all the borehole and diffusion effects are carried out from computationally expensive Monte Carlo calculations into the library of time decays. **Figure 3.2** shows the library of time decays for materials in the range between 6 and 120 c.u. for the three

detectors of the LWD Sigma tool. The library can be pre-calculated with MCNP using any tool configuration to adapt the fast-forward modeling method to other detection systems.

3.2.3 *FSF Library*

The use of Monte Carlo calculated FSFs in the fast-forward simulation algorithm accounts for all the intricate transport phenomena that determine the multi-detector response, including nuclear interactions in the formation, the borehole, and the tool. I pre-calculate a library of FSFs to account for changes in detector sensitivity as a function of absorption cross section, Σ_a, of the logging environment. In the case of the thermal neutron detector, I use MCNP to calculate the 3D spatial importance of thermal neutrons, which takes into account the generation of fast neutrons, scattering in energy and space, and subsequent thermal-neutron absorption. In the case of the gamma-ray detectors, I use MCNP to calculate the 3D spatial importance of thermal-neutrons that undertake absorption and whose generated gamma rays are able to reach the scintillators of the LWD tool. In addition to the processes affecting the thermal-neutron FSFs, the gamma-ray FSFs take into account the attenuation of gamma rays due to Compton scattering and photoelectric absorption.

To summarize the previous two sections, the fast-forward model reproduces all the detector-specific particle transport complexity by using a pre-calculated library of time decays which combine detector-specific diffusion and borehole/tool effects, and the

following two sensitivity functions pre-calculated for each detector of the LWD tool under study:

- Thermal-neutron FSFs for the thermal-neutron detector, and
- Thermal-neutron absorption FSFs for the gamma-ray detectors,

where both the FSF and time decay library are calculated as a function of Σ_a of the logging environment.

Figure 3.3 describes the variation of the 3D sensitivity maps across materials of different absorption cross section for the SSn, LSn, and Near detectors of the LWD tool as a function of absorption cross section. Notice that increasing Sigma "shrinks" the thermal-neutron FSF and "stretches" the gamma-ray FSF. The FSFs reflect the fact that high absorption cross section results in thermal neutrons away from the borehole not being capable to be scattered toward the detector without suffering absorption. Therefore, high-Sigma environments give rise to fewer thermal-neutron and more gamma-ray counts from regions located far from the detector. This indicates that realistic logging environments imply a change in the 3D sensitivity of each detector at every depth as a function of the absorption cross section of the environment. The logging environment affects not only the shape of the FSFs, but also the uncertainty of the measurement because the uncertainty of nuclear measurements is inversely proportional to the square root of the total number of counts registered at the detectors (Ellis and Singer, 2007). Accordingly, the noise in Sigma measurements increases as the absorption cross section of the materials increases.

3.3 NUMERICAL RESULTS

In this section I benchmark the fast-forward (FF) model against Monte Carlo (MC) simulations and available test-pit data to appraise the reliability and speed of the developed numerical simulation method. For the sake of conciseness, I only benchmark the results in time-decay space for the test-pit examples, and in Sigma space in both test-pit and synthetic examples. Sigma will be calculated from gamma-ray time decays (SSn, LSn) using the moments method, and from thermal-neutron time decays (Near) using the two-exponential method (explained in Chapter 2, section 2.4). I generate and benchmark synthetic examples of increasing level of complexity; including thick homogeneous formations, invasion, thin layers, and deviated wells.

3.3.1 Test-Pit Case I: Thick Homogeneous Formations

This synthetic case is designed to compare the tool response acquired in a test-pit thick homogeneous formation block to Monte Carlo and fast-forward simulated decays. The measurement was acquired with a 20-cm (7 7/8-in) LWD tool in a cylindrical test pit containing a 41.7-p.u. sandstone block that mimics the actual tool measurement across a massive layer. I simulate two cases; first, a block saturated with fresh water, and second, a block saturated with 196-kppm [NaCl] brine. The fresh-water and brine saturated blocks have intrinsic Sigma values typical of a hydrocarbon-saturated sandstone and a shale formation, respectively. **Figure 3.4** shows Monte Carlo, fast-forward simulated, and test-pit measured time decays for the two laboratory blocks and the three detectors of the LWD tool under study. **Table 3.1** shows the properties of the homogeneous blocks and calculated

Sigma from multi-detector decays across both blocks. Nuclear properties in the table were calculated using SNUPAR.

Comparison of the signals in **Figure 3.4** indicates that the forward model is efficient in reproducing Monte Carlo simulated signals. I reproduce each time decay in 0.3 seconds, compared to 10 hours using MCNP. The maximum difference between laboratory and Monte Carlo derived Sigmas is 4 c.u. and occurs at the thermal-neutron detector in the brine saturated block, which suggests that the test-pit signal could be affected by noise. However, the average difference between Monte Carlo and fast-forward derived Sigmas are 0.5 c.u. (SSn), 0.6 c.u. (LSn), and 1.1 c.u. (Near). Both sets of time decays were reproduced in 4.07 seconds using the fast-forward model, compared to a 2.5-day CPU time period using MCNP. The match between the measured signal and both Monte Carlo and fast-forward simulated signals indicates that the nuclear modeling implemented is an accurate representation of the radiation physics taking place in the test-pit measurement.

3.3.2 Test-Pit Case II: Piston-Like Invasion

The three different radial lengths of investigation of the detectors of the LWD Sigma tool allow sensing the presence of invasion in the shallow near-wellbore zone if there is significant contrast between virgin- and invasion-zone Sigmas (Ortega et al., 2013). The measurement is useful in formation evaluation because other nuclear measurements used to characterize the formation are shallow sensing, hence highly affected by shallow invasion. Recognizing the presence of invasion in the near-wellbore zone can help to

accurately characterize in-situ formation fluid, and improve the accuracy of nuclear measurement interpretations.

I compare Monte Carlo and fast-forward simulated time decays against test-pit measurements at piston-like radial lengths of invasion of 0 cm, 5.08 cm, 10.16 cm, and 38.1 cm (0 in, 2 in, 4 in, and 15 in). Piston-like invasion is not necessarily the best description of the radial invasion profile in a formation because capillary forces can generate smooth radial profiles. Nonetheless, modeling of piston-like invasion is a good approximation of the average radial length of invasion disregarding the actual shape of the invasion profile. Piston-like invasion is modeled in the laboratory using the experimental facility shown in **Figure 3.5**, which has 1-mm steel liners arranged at different radii. The purpose of the liners is to separate the fluids in the virgin- and invasion-zone porous media. The pit has a 34-p.u. sandstone block that is saturated with fresh water in the virgin zone. The liners interspace is saturated with 200-kppm [NaCl] brine. The measurement is a good example of an experimental setting to mimic piston-like invasion; even so, nuclear measurements acquired in this pit are affected by the presence of the high-absorbing steel of the liners. Formation Sigma from the thermal-neutron and gamma-ray decays in this laboratory setting is expected to be higher than the actual Sigma from the sandstone block alone.

Figure 3.6 illustrates three-detector Monte Carlo simulated decays at the four radial lengths of invasion. Note the effect of radial length of investigation on the late-time parts of the pulsed-source decay. The 0-cm, 5.08-cm (2 in), and 10.16-cm (4 in) invasion signals

in the LSn detector have similar slopes because the LSn detector is not significantly affected by shallow invasion. Still, the Near-detector slopes differ significantly from one another due to the high impact of shallow invasion on the short-spaced thermal-neutron measurement.

Presence of steel liners in the test-pit measurement increases the slope of the measured signals when compared to the fast-forward signals that do not include the liners. The thin steel sheets cannot be simulated using the forward model because of the coarse nature of the grid that the model relies on (2.54-cm radial spacing). However, the liners can be modeled using MCNP. **Figure 3.7** describes Monte Carlo simulations with and without the steel liners. Monte Carlo simulations with the liner are compared to test-pit measurements to verify the reliability of the Monte Carlo computations and processing to replicate the real tool response. Monte Carlo simulations without the liner are compared to fast-forward simulations. Note the good agreement with both pairs of time decays.

Thus far fast-forward modeling results have been verified against Monte Carlo calculations in the form of time decays because time decays are the fundamental measurement that bears the physics of pulsed-neutron-capture measurements. Yet, as previously mentioned, for the sake of conciseness the next benchmarking exercises are displayed in apparent Sigma space, which is Sigma calculated from the late-time section of time decays. I compute both Monte Carlo and fast-forward time decays and then estimate formation Sigma using the moments method for the gamma-ray detectors and the two-exponential method for the thermal-neutron detector. **Figure 3.8** shows Sigma from the

Monte Carlo and fast-forward simulated time decays in **Figure 3.7**. Note that the good match between the Monte Carlo and fast-forward simulated decays cascades down to a good match in apparent Sigma values. Maximum difference between Monte Carlo and fast-forward derived Sigmas is 2.6 c.u. (SSn), 1.9 c.u. (LSn), and 3.8 c.u. (Near), and average difference is 1 c.u. (SSn), 1.1 c.u. (LSn), and 1.7 c.u.(Near). Time decays for this test-pit example were reproduced in 4.58 seconds, compared to a 5-day CPU time period using MCNP.

3.3.3 Piston-Like Invasion Effects on MDOI Sigma Measurements

The three synthetic examples in **Figure 3.9** and **Figure 3.10** verify the ability of the forward model to reproduce Monte Carlo simulated multi-detector time decays in cases involving different Sigma contrasts between virgin and invasion zones, and various piston-like radial lengths of invasion. I simulate multi-detector time decays throughout a set of layered and thick hydrocarbon-bearing sandstone formations invaded with 200-kppm [NaCl] WBM. Formations are oil-bearing in **Figure 3.9** and gas-bearing in **Figure 3.10**. Radial lengths of invasion are in the range of no invasion at the top of the sequence up to 35.56-cm (14 in) deep invasion at the bottom, which is equivalent to full invasion for Sigma measurements. The time decays at each depth level are not affected by shoulder beds because each sublayer is thicker than the vertical resolution of all the detectors of the LWD Sigma tool.

3.3.3.1 *Invasion Into Oil-Bearing Formations*

Table 3.2 describes the properties of the virgin- and invasion-zone formations in the three cases of piston-like invasion. **Figure 3.9** compares Sigma logs calculated from Monte Carlo and fast-forward simulated decays on 34-p.u. (left, Case 1) and 17-p.u. (right, Case 2) formations to display the performance of the forward model at different virgin- and invasion-zone Sigma contrasts. The fast-forward method accurately reproduces not only the radial Sigma profile for each detector, but also the magnitude of the response, which is associated with borehole/diffusion effects. Maximum differences between Monte Carlo and fast-forward derived Sigmas are 1.4 c.u. (SSn), 2.3 c.u. (LSn), and 3.3 c.u. (Near), and average difference is 0.8 c.u. (SSn), 1.2 c.u. (LSn), and 1.2 c.u.(Near) in the 34-p.u. formation case (left panel in **Figure 3.9**). Maximum differences between Monte Carlo and fast-forward derived Sigmas are 1 c.u. (SSn), 0.7 c.u. (LSn), and 2.39 c.u. (Near), and average difference is 0.5 c.u. (SSn), 0.4 c.u. (LSn), and 1 c.u.(Near) in the 17-p.u. formation case (right panel in **Figure 3.9**). Three-detector time decays at 16 radial lengths of invasion were simulated in 9.39 seconds with the fast forward method and in 20-days of CPU time with MCNP.

3.3.3.2 *Invasion Into Gas-Bearing Formations*

Simulation of nuclear measurements in environments containing gas is challenging due to the high contrast in migration length between gas-bearing rocks (because of low hydrogen index), and other common subsurface materials. The contrast typically involves nonlinear effects that result in significant errors in first-order approximations. The shape

of the sensitivity functions in gas-bearing rocks is also different from that of water-bearing formations due to significant differences in radiation transport in such environments (Mimoun et al., 2011). However, the detector-specific library of FSFs and decays upon which the fast forward method is based comprises a wide range of subsurface materials, including low-Sigma gas-bearing formations. This allows one to perform small perturbations to pre-calculated gas cases to model challenging configurations such as invasion on gas-bearing rocks. **Figure 3.10** compares Sigma derived from Monte Carlo and fast-forward simulated decays for 200-kppm [NaCl] filtrate invading a 30-p.u. gas-bearing sandstone formation. The nuclear properties of the formation are described in **Table 3.2** (Case 3). Maximum differences between Monte Carlo and fast-forward derived Sigmas are 2.9 c.u. (SSn), 1 c.u. (LSn), and 3.3 c.u. (Near), and average difference is 1.6 c.u. (SSn), 0.5 c.u. (LSn), and 1.6 c.u. (Near). However, the agreement is not as good as in the oil-bearing cases probably because of late-time diffusion effects between virgin and invasion zones not accounted for in the fast-forward method. Each of the three sets of piston-like invasion results was reproduced in 9.39 seconds using the fast forward method, compared to 20 days of CPU time using MCNP.

3.3.4 Effects of Smooth Invasion on MDOI Sigma Measurements

The objective of this synthetic example is to appraise the accuracy of the fast-forward model to simulate ramp-up radial invasion profiles resulting from capillary forces in porous media and/or different times of exposure to filtrate (time-after-bit, *TAB*). Generally, LWD measurements are acquired such that the top section of the formation is

invaded deeper than the bottom because of longer *TAB*. I simulate several cases of ramp-up invasion starting from no invasion until reaching a 38.1-cm (15-in) deep ramp-up invasion profile, with 14 intermediate invasion cases. The ramp-up invasion profiles are described on **Figure 3.11a**; the x-axis identifies the maximum radial extent of each invasion front.

Multi-detector Sigma logs derived from Monte Carlo and fast-forward simulations for all these cases are shown on **Figure 3.11b**. This case illustrates the effectiveness of the method to reproduce changes in Sigma as the asymmetric invasion profile begins to affect the LSn detector first, and increasingly affects the response in the SSn and Near detectors. Maximum differences between Monte Carlo and fast-forward derived Sigmas are 2.7 c.u. (SSn), 1.9 c.u. (LSn), and 1.3 c.u. (Near), and average difference is 0.8 c.u. (SSn), 0.7 c.u. (LSn), and 0.8 c.u. (Near). FF Sigma logs were reproduced in 9.39 seconds compared to 20 days of CPU time with MCNP.

3.3.5 Shoulder-Bed Effects on MDOI Sigma Measurements

Differences in the vertical resolution of the three LWD detectors cause the measurements to be affected by shoulder beds in different ways. In this section I simulate time decays for two sequences of formations with thickness much lower than the vertical resolution of the LWD Sigma detectors. First, I describe simulations of multi-detector Sigma logs across 15.24-cm (6-in) layered siliciclastic formations in **Figure 3.12**. **Table 3.3** describes the properties of the sand and shale layers. Nuclear properties in the table were calculated using SNUPAR. Observe that the Near detector measurement acquired

across 15.24-cm layers exhibits deflections that enable layer identification. However, not even the thermal-neutron detector Sigma log shows true apparent Sigma values, while the gamma-ray detectors show one average Sigma value throughout the sequence. Maximum differences between Monte Carlo and fast-forward derived Sigmas are 2.2 c.u. (SSn), 3.3 c.u. (LSn), and 3.3 c.u. (Near), while average difference is 1.3 c.u. (SSn), 0.9 c.u. (LSn), and 1.4 c.u. (Near). Multi-detector time decays in this case were simulated in 14.2 seconds, compared to 37.5 days of CPU time with MCNP.

Second, **Figure 3.13** describes simulations across layers with different thickness, porosity, and fluid saturation described in **Table 3.4**. Nuclear properties in the table were calculated using SNUPAR. Notice how in this case the forward method reproduces the deflections present in Monte Carlo-simulated logs even at depths where various layers of contrasting Sigma affect all the detectors. Maximum differences between Monte Carlo and fast-forward derived Sigmas are 4.8 c.u. (SSn), 5 c.u. (LSn), and 6.8 c.u. (Near), while average difference is 1.1 c.u. (SSn), 1 c.u. (LSn), and 1.8 c.u. (Near). The linear-perturbation FF predictions deviate more from Monte Carlo simulations than in previous synthetic examples due to highly nonlinear diffusion-dominated effects induced at the boundary of thinly bedded shale and sand alternations. In both previous examples, measurements simulated across the sand formations are highly affected by shoulder beds. The ability of the fast-forward method to reproduce shoulder-bed effects enables the estimation of true formation Sigmas when there is another borehole measurement available, e.g., density images, to detect interlayer boundaries.

3.3.6 Combined Shoulder-Bed and Invasion Effects on MDOI Sigma Measurements

Presence of invasion in thinly bedded formations is a challenging case to simulate because of the presence of different materials with contrasting absorption cross section within the volume of investigation of the detectors. Even though challenging to simulate and interpret, it is common to encounter such configurations when penetrating a thinly bedded sequence of layers exposed to mud at overbalance pressure. **Figure 3.14** compares Sigma logs derived from Monte Carlo and fast-forward simulations in a 76.2-cm (2.5-ft) thick layered sequence invaded by 200-kppm [NaCl] WBM. **Table 3.5** describes the properties of the layers in the sequence. Nuclear properties in the table were calculated using SNUPAR. In this case, I simulate invasion of 20.32 cm (8 in) in the two upper sand formations and 10.16 cm (4 in) in the four lower sand formations. Notice how the fast-forward model reproduces the strong effect of invasion and improved vertical resolution in the Near detector, together with the slighter effect of invasion and poor vertical resolution in the LSn detector. Time decays for this complicated configuration were simulated with maximum differences between Monte Carlo and fast-forward derived Sigmas of 3.2 c.u. (SSn), 5 c.u. (LSn), and 3.8 c.u. (Near), and average difference of 1.1 c.u. (SSn), 1.1 c.u. (LSn), and 1.4 c.u.(Near). FF time decays were simulated in 19.4 seconds, compared to 53.75 days of CPU time with MCNP.

3.3.7 MDOI Sigma Logs Acquired in High-Angle/Horizontal (HA/HZ) Wells

Interpretation of logs acquired in HA/HZ wells is non-trivial because the angular sectors of the tool sense layered formations in different relative proportions at each

measurement location. These geometrical effects mask the true properties of the layered formations and give rise to errors in petrophysical estimations. The best way to interpret logs acquired in HA/HZ wells is to get rid of the geometrical effects by performing inversion-based interpretation. Because the forward modeling of geometrical effects is a fundamental part of any inversion approach, in this section I aim to show the ability of the fast forward method to reproduce measurement effects on multi-detector time decays due to the relative angle between layered formations and the well.

Figure 3.15 shows multi-detector Sigma logs obtained with Monte Carlo and fast-forward simulations in an 85-degree well penetrating a sequence of 30.48-cm sand formations interbedded with shale formations. **Table 3.6** summarizes the properties of the layers in the sequence. Nuclear properties in the table were calculated using SNUPAR. The configuration is significantly challenging to simulate because of the high contrast between layers and the high variability of the measurement configuration at different sectors. Results show that the 3D sensitivity maps used in the fast-forward model accurately reproduce the geometrical effects present in highly deviated wells penetrating layers thinner than the vertical resolution of the LWD Sigma tool detectors. I simulated these logs in 12.6 seconds using the fast forward method and 31.25 days of CPU with MCNP, yielding maximum differences between Monte Carlo and fast-forward derived Sigmas of 2 c.u. (SSn), 4.5 c.u. (LSn), and 3.8 c.u. (Near), and average absolute differences of 0.6 c.u. (SSn), 2.1 c.u. (LSn), and 1.3 c.u.(Near).

Asymmetric invasion profiles have been reported in wireline logging due to gravitational and permeability anisotropy effects, or at the boundary between layers of contrasting permeability in deviated wells (Passey et al., 2005). In the case of LWD logging, reservoir simulations of WBM invasion into oil-bearing formations shown in Chapter 2 indicated that asymmetric invasion effects are negligible due to small times of exposure to drilling mud. However, I am interested in testing the versatility of the method to simulate time decays in cases where asymmetric invasion is present due to prolonged exposure to filtrate, e.g. during drillstring trippings. In this example, I also show the capability of the method to produce 360^{o} Sigma images. **Figure 3.16** shows Sigma images derived from multisector fast-forward simulations in an 85^{o} well penetrating the complex sequence of layers described in **Table 3.7**. Nuclear properties in the table were calculated using SNUPAR.

The configuration shown at the top of **Figure 3.16** describes a realistic and challenging environment to simulate multi-detector Sigma logs because the measurements are affected simultaneously by multiple environmental and geometrical effects, including shoulder beds, asymmetrical invasion (i.e., the top sector is almost not affected by invasion, while the bottom sector measurements sense mostly invasion), and by geometrical effects due to the relative angle between the well and layers. I compare upper sector Sigma logs derived from Monte Carlo and fast-forward simulated decays. Maximum differences between Monte Carlo and fast-forward derived Sigmas are 5 c.u. (SSn), 3.2 c.u. (LSn), and 7 c.u. (Near), and average absolute differences are 1 c.u. (SSn), 1.1 c.u. (LSn), and 2.3 c.u.

(Near). The large difference in Near detector logs occurs in the thinly bedded shale intercalations, where both MCNP and pre-calculated time decays for high-Sigma materials used by the FF model are subject to increased statistical errors due to the low number of counts in such strong absorbers. In other sections, the maximum difference in Near detector Sigma is approximately 3 c.u. I calculated 16-sector, three-detector decays at 71 measurement points in 28 seconds compared to 4 years of CPU time that would be required with MNCP. The fast-forward modeling method reproduces the measurements 5 million times faster than MCNP, thereby opening the possibility of its use with inversion-based interpretation methods to explicitly account for all the environmental and geometrical factors that affect LWD measurements when inferring petrophysical properties derived from Sigma.

3.4 COMPUTATIONAL SPEED

The fast-forward simulation results documented in this chapter were obtained with an Intel(R) Pentium(R) 4-CPU, 3.20-GHz computer. Monte Carlo simulations were performed using a parallelized version of MCNP5 in Stampede, a Linux cluster in the Texas Advanced Computing Center. Stampede has a Dell PowerEdge C8220 Cluster with Intel Xeon Phi coprocessors. **Table 3.8** summarizes the CPU time required to simulate multi-detector time decays for all the examples documented in this chapter. On average, the fast-forward model reproduces multi-detector time decays approximately 1e5 faster than MCNP.

3.5 DISCUSSION SPEED

Multiple methods can be used to simulate LWD Sigma measurements. However, not all of them are suitable for inversion-based petrophysical interpretation. Speed and accuracy are key components of simulation models meant to be used for inversion. Initial stages of the development of the model introduced in this chapter included using (a) finite differences and diffusion approximations, and also (b) first-order perturbations to calculate directly Sigma logs, rather than time decays. Even though the finite difference method can be used to accurately approximate the solution of the Boltzmann equation or the thermal-neutron diffusion equation, its implementation in realistic logging environments that include multiple formations and/or a deviated wells is time consuming and not suitable for petrophysical applications. Attempts to simulate Sigma logs directly were unsuccessful to describe detector responses in the presence of invasion and/or thinly bedded formations. The reason is most likely that the effect of such perturbations in detector responses is more linear in count-rate space than in Sigma space; the latter one contains nonlinear borehole and diffusion effects. Watson's method (1984) is best applied to time-dependent nuclear measurements by reproducing the effect of perturbations in absorption cross section on detector count rates, rather than on formation properties derived from such count rates, e.g. Sigma. It was not only until I applied the perturbation on the count rates, instead of Sigma directly, that the use of sensitivity functions and first-order perturbation theory allowed to accurately calculate detector responses in the multiple challenging environments described in this chapter.

3.6 CONCLUSIONS

I developed a fast and accurate algorithm to numerically simulate 3D multi-detector thermal-neutron and gamma-ray time decays. The algorithm relies on a Monte Carlo pre-calculated library of detector-dependent 3D FSFs and time decays that take into account the actual pulsing protocol of the LWD tool under consideration. I implemented the library of FSFs with first-order perturbations to rapidly simulate time decays in complex geometries, including thin layers, invasion and/or HA/HZ wells. Simulated time decays include all pertinent detector-dependent borehole and diffusion effects.

I benchmarked the algorithm against Monte Carlo simulated time decays, and against laboratory measurements. Results show that the fast-forward algorithm accurately reproduces all the environmental and geometrical effects observed in Monte Carlo calculated time decays under complex measurement conditions, with average absolute differences within 2 c.u. and in 1e-5 the computer time required by MCNP. However, larger differences can be expected, especially in the Near detector time decays, when simulating measurements acquired in environments with uncommonly high Sigma values. Nonetheless, the accuracy of the simulation algorithm provides the level of reliability necessary to approximate the measurements under realistic and practical conditions that depart from the assumed geometry of sharp transition boundaries, piston-like invasion, and constant-angle well sections.

The main contribution of the work presented in this chapter is the development of a method to numerically simulate the fundamental pulsed neutron capture measurement,

i.e. time decays, rather than Sigma. Simulation of time decays provides several advantages such as (a) the use of all the information contained in the time decay, rather than a portion of it, (b) the reproduction of all the detector-specific diffusion and borehole effects, and (c) the elimination of correction factors stemming from tool calibration and used to convert apparent Sigma to intrinsic Sigma. One of the most important advantages of the simulation method is its versatility. It can be used in association with any pre-calculated FSF and time decay library for any tool using any pulsing scheme, and to calculate Sigma logs using any method of choice (two-exponentials, moments, NMR-like, etc.).

Table 3.1: Summary of assumed lithology, porosity, water salinity (C_w), and intrinsic Sigma (Σ_{int}) for the blocks corresponding to test-pit measurements and simulations reported in **Figure 3.4**, and Monte Carlo (MC), Test-pit, and Fast-Forward (FF) modeled Sigmas.

					SSn Σ (c.u.)			**LSn Σ (c.u.)**			**Near Σ (c.u.)**		
Material	**Porosity (p.u.)**	**Lithology**	**C_w (NaCl kppm)**	**Σ_{int} (c.u.)**	MC	Test pit	FF	MC	Test pit	FF	MC	Test pit	FF
1	41.7	Sands-tone	0	13.5	15.6	15.8	16.4	12.3	13.9	11.6	18.1	19.22	19.23
2	41.7	Sands-tone	196	43.7	46.7	47.2	46.6	43.1	44.3	42.7	51.2	54.32	50.02

Table 3.2: Summary of lithology, in-situ fluid type, porosity, filtrate salinity (C_{filt}), virgin- and invasion-zone migration length ($L_{m\,v}$, $L_{m\,i}$), and Sigma (Σ_v , Σ_i), and virgin-zone fluid Sigma (Σ_f) for test-pit measurements and simulations reported in **Figure 3.9** and **Figure 3.10**.

Piston-like Invasion Case	**Lithology**	**In-situ fluid**	**Porosity (p.u.)**	C_{filt} **(NaCl kppm)**	$L_{m\,v}$ **(cm)**	$L_{m\,i}$ **(cm)**	Σ_v **(c.u.)**	Σ_i **(c.u.)**	Σ_f **(c.u.)**
1	Sandstone	Oil	34	200	12.5	11.5	10.36	36.17	21.6
2	Sandstone	Oil	17	200	16.6	15.0	7.45	20.36	21.6
3	Sandstone	Gas	30	200	26.8	15.3	5.29	30.1	7.04*

*Gas Sigma calculated at 24131.65 kPa (3500 psia) and 150 ^{o}F.

Table 3.3: Summary of assumed lithology, thickness, in-situ fluid, porosity, total water saturation (S_w), water salinity (C_w), migration length (L_m), and intrinsic Sigma (Σ_{int}) for formations corresponding to the simulations of Sigma logs affected by shoulder beds reported in **Figure 3.12**.

Layer	**Lithology**	**Thickness (cm)**	**In-situ fluid**	**Porosity (p.u.)**	S_w	C_w **(NaCl kppm)**	L_m **(cm)**	Σ_{int} **(c.u.)**
1	Sandstone	15.24	Oil	10	0.45	200	20.48	9.65
2	80% (v/v) Chlorite 20 (v/v) % Kaolinite	15.24	Water	10	1	200	13.93	33.9

Table 3.4: Summary of assumed lithology, thickness, in-situ fluid type, porosity, total water saturation (S_w), water salinity (C_w), and intrinsic Sigma (Σ_{int}) for formations corresponding to the simulations of Sigma logs reported in **Figure 3.13**.

Layer	Lithology	Thickness (cm)	In-situ Fluid	Porosity (p.u.)	S_w	C_w (NaCl kppm)	Σ_{int} (c.u.)
1	Limestone	70.10	Gas	5	0.4	150	9.3
2	Dolomite	67.06	Oil	12	0.65	250	14.60
3	Shale	39.62	Water	10	1	200	41.86
4	Sandstone	24.38	Oil	20	0.4	50	9.38
5	Shale	76.20	Water	10	1	200	41.86
6	Shaly Sand	60.96	Gas	10	0.5	100	11.99
7	Shaly Sand	45.72	Oil	15	0.7	150	17.75
8	Sandstone	30.48	Oil	20	0.4	50	9.38
9	Sandstone	45.72	Water	25	1	220	30.63
10	Sandstone	54.86	Water	25	1	0	8.96

Table 3.5: Summary of assumed lithology, thickness, in-situ fluid type, porosity, total water saturation (S_w), water salinity (C_w), migration length (L_m), intrinsic Sigma (Σ_{int}), and radial length of invasion (r_i) for shale and sandstone intercalations corresponding to the simulations of Sigma logs simultaneously affected by shoulder beds and invasion reported in **Figure 3.14**. Filtrate salinity is 200 kppm [NaCl] and Σ_{filt} is 98 c.u. Shale matrix composition is 80% chlorite and 20% kaolinite.

Layer	**Lithology**	**Thickness (cm)**	**In-situ Fluid**	**Porosity (p.u.)**	S_w	C_w **(NaCl kppm)**	L_m **(cm)**	Σ_{int} **(c.u.)**	r_i **(cm)**
1	Shale	15.24	Water	10	1	200	13.93	33.9	0
2	Sandstone	15.24	Gas	20	0.1	200	24.8	6.83	20.32
3	Shale	15.24	Water	10	1	200	13.93	33.9	0
4	Sandstone	15.24	Gas	15	0.2	200	24.4	7.62	20.32
5	Shale	15.24	Water	10	1	200	13.93	33.9	0
6	Sandstone	15.24	Oil	13	0.25	200	19.3	9.20	10.16
7	Shale	15.24	Water	10	1	200	13.93	33.9	0
8	Sandstone	15.24	Oil	11	0.35	200	20.0	9.32	10.16
9	Shale	15.24	Water	10	1	200	13.93	33.9	0
10	Sandstone	15.24	Oil	10	0.45	200	20.48	9.65	10.16
11	Shale	15.24	Water	10	1	200	13.93	33.9	0
12	Sandstone	15.24	Water	10	1	200	20.0	13.85	10.16
13	Shale	15.24	Water	10	1	200	13.93	33.9	0

Table 3.6: Summary of assumed lithology, thickness, in-situ fluid type, porosity, total water saturation (S_w), water salinity (C_w), migration length (L_m), and intrinsic Sigma (Σ_{int}) for shale and sandstone formations corresponding to the simulations of Sigma logs in the 85°-well reported in **Figure 3.15**. Shale matrix composition is 80% chlorite and 20% kaolinite.

Layer	**Lithology**	**Thickness (cm)**	**In-situ Fluid**	**Porosity (p.u.)**	S_w	C_w **(NaCl kppm)**	L_m **(cm)**	Σ_{int} **(c.u.)**
1	Shale	30.48	Water	10	1	200	13.93	33.9
2	Sandstone	30.48	Oil	10	0.45	200	20.48	9.65
3	Shale	30.48	Water	10	1	200	13.93	33.9
4	Sandstone	30.48	Water	10	1	200	20.0	13.85
5	Shale	30.48	Water	10	1	200	13.93	33.9
6	Sandstone	30.48	Water	20	1	200	16.44	27.68
7	Shale	30.48	Water	10	1	200	13.93	33.9

Table 3.7: Summary of assumed porosity, mineral volumetric fractions, oil, gas, and water saturations (S_o ,S_g, S_w), virgin- and invasion-zone Sigma (Σ_v ,Σ_i) and radial length of invasion (r_i) for the formations corresponding to the simulations of Sigma logs in the 85°-well with asymmetric invasion reported in **Figure 3.16**. Filtrate salinity is 250 kppm [NaCl], Σ_{filt} = 120 c.u., connate water salinity is 180 kppm [NaCl], and Σ_w = 88.4 c.u.

Layer	Thickness (cm)	Porosity (p.u.)	Calcite fraction	Dolomite fraction	Clay fraction	S_o	S_g	S_w	Σ_v (c.u.)	Σ_i (c.u.)	r_i, (cm)
1	30.48	25	0.75	0	0	0.1	0	0.15	20.69	35.3	18
2	60.96	15	0.85	0	0	0.05	0	0.1	15.92	24.0	8
3	15.24	25	0.75	0	0	0.05	0	0.2	24.05	35.3	18
4	30.48	25	0.75	0	0	0.1	0	0.15	20.69	35.3	10
5	30.48	25	0.75	0	0	0.1	0	0.15	20.69	35.3	18
6	15.24	20	0.8	0	0	0.1	0	0.1	16.63	29.7	13
7	15.24	22	0.78	0	0	0.17	0	0.05	13.55	31.9	15
8	60.96	25	0.75	0	0	0.22	0	0.03	12.63	35.3	18
9	60.96	25	0.75	0	0	0.2	0	0.05	13.98	35.3	18
10	30.48	10	0.9	0	0	0.06	0	0.04	11.18	18.4	5
11	60.96	25	0.75	0	0	0.2	0	0.05	13.98	35.3	18
12	30.48	30	0.3	0.4	0	0.15	0	0.15	21.31	40.9	23
13	60.96	30	0.1	0.5	0.1	0.2	0	0.1	20.29	43.2	20
14	15.24	0.3	0	0	0.7	0	0	0.3	48.00	57.5	0
15	30.48	0.3	0.1	0.5	0.1	0.1	0	0.2	27.00	43.2	23
16	15.24	0.3	0	0	0.7	0	0	0.3	48.00	57.5	0

Table 3.7 (continued):

17	30.48	0.15	0.15	0.6	0.1	0.1	0	0.05	14.77	26.2	8
18	60.96	0.3	0	0	0.7	0	0	0.3	48.00	57.5	0
19	15.24	0.3	0.1	0.5	0.1	0.1	0	0.2	27.00	43.2	5
20	30.48	0.3	0	0	0.7	0	0	0.3	48.00	57.5	0
21	60.96	0.25	0.15	0.6	0	0	0.25	0	6.58	35.2	18
22	15.24	0.2	0.2	0.6	0	0	0.1	0.1	14.93	29.5	13
23	15.24	0.25	0.25	0.5	0	0	0.05	0.2	23.16	35.2	18
24	30.48	0.2	0.3	0.5	0	0	0.1	0.1	14.95	29.5	13
25	30.48	0.25	0.35	0.4	0	0	0.25	0	6.63	35.2	18
26	15.24	0.25	0.45	0.3	0	0	0.2	0.05	10.79	35.2	18
27	60.96	0.3	0.4	0.2	0.1	0.1	0.2	0	10.53	43.3	23
28	30.48	0.25	0.35	0.25	0.15	0.2	0.05	0	13.32	38.8	18
29	30.48	0.3	0.3	0.3	0.1	0	0	0.3	33.77	43.2	23
30	60.96	0.3	0.25	0.4	0.05	0	0	0.3	32.57	42.0	23

Table 3.8: Comparison of Monte Carlo (MC) and Fast-Forward (FF) method CPU times required to model test-pit and synthetic cases reported in this chapter and average difference for each case.

		CPU time		Average absolute error (c.u.)		
Case	**Measurement points**	**MC (days)**	**FF (seconds)**	**SSn**	**LSn**	**Near**
Test-pit homogeneous	2	2.5	7.07	0.5	0.6	1.1
Test-pit invasion	4	5	4.58	1.0	1.1	1.7
Piston-like invasion	16	20	9.39	0.8	1.2	1.2
Smooth invasion	16	20	9.39	0.8	0.7	0.8
Shoulder beds	30	37.5	14.2	1.1	1.0	1.8
Shoulder beds and invasion	43	53.75	19.4	1.1	1.1	1.4
High-angle well	25	31.25	12.6	0.6	2.1	1.3
High-angle well and asymmetric invasion	71 (x1 sector)	88.75	28	1.0	1.1	2.3

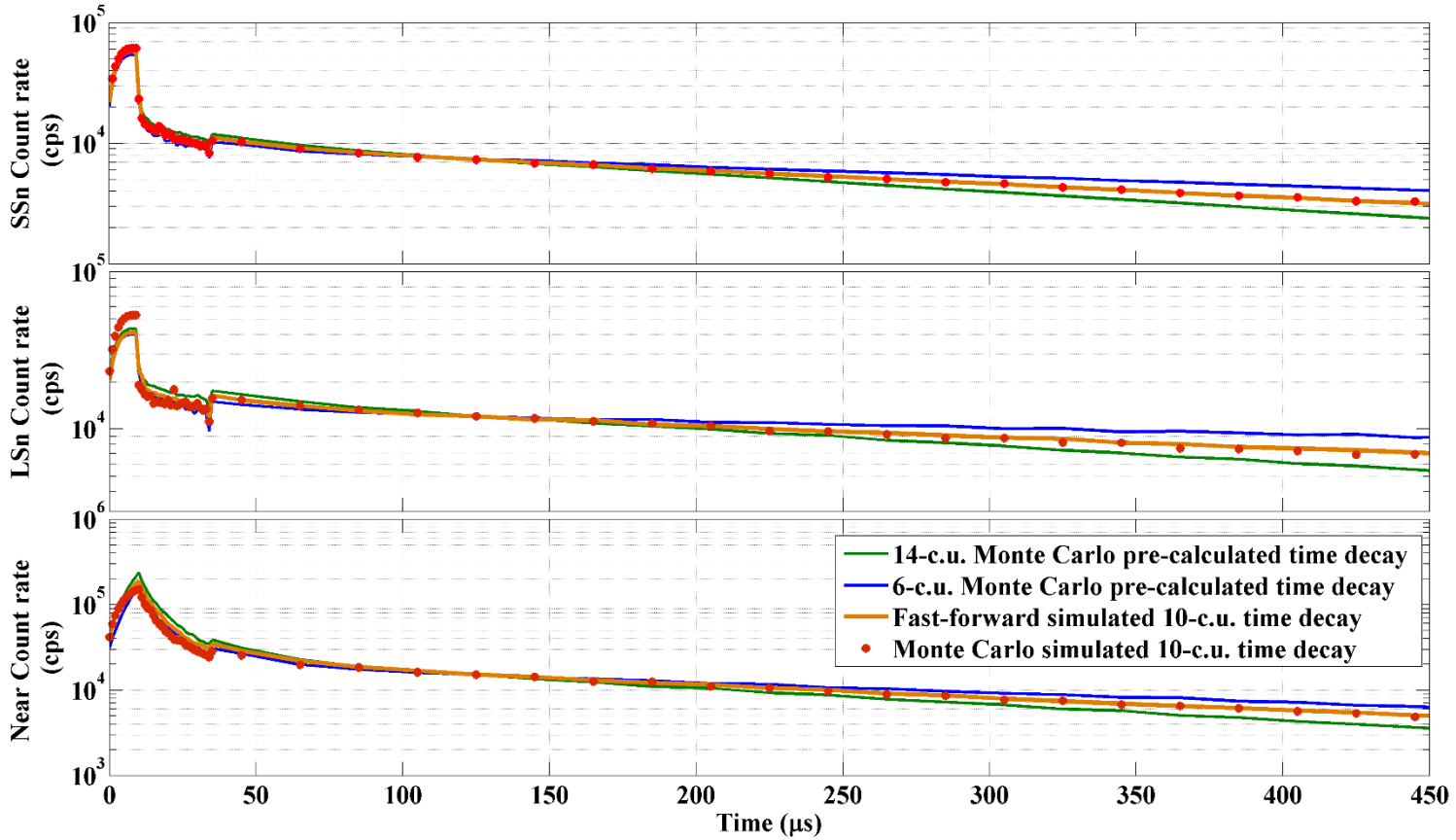

Figure 3.1: Comparison of Monte Carlo simulated (red makers) and fast-forward simulated (solid dark orange line) multi-detector time decays corresponding to measurements in a 10-c.u. material. The green and blue solid lines describe pre-calculated Monte Carlo time decays for the three detectors of the LWD Sigma tool, which are used to approximate the tool response in the material of intermediate absorption cross section.

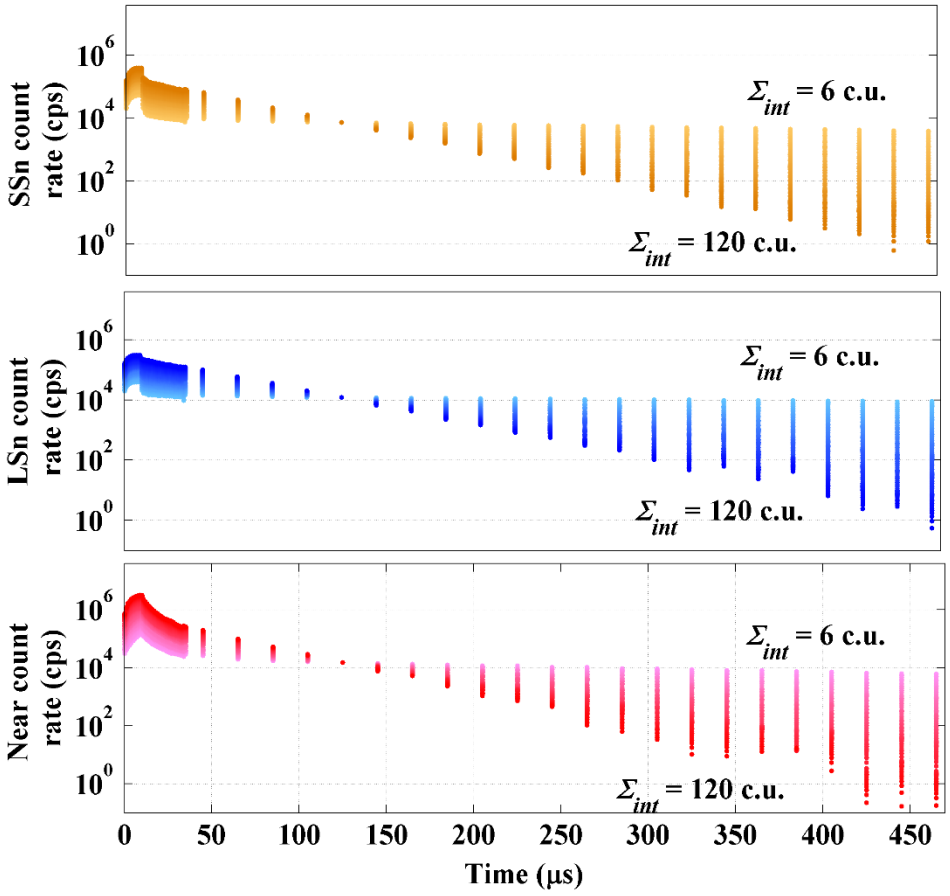

Figure 3.2: Multi-detector gamma-ray and thermal-neutron time decay library for the LWD Sigma tool under consideration. Time decays are the result of 2000-µs Monte Carlo calculated single-pulse decays superposed in time to follow the pulsing scheme of the actual multi-function LWD tool.

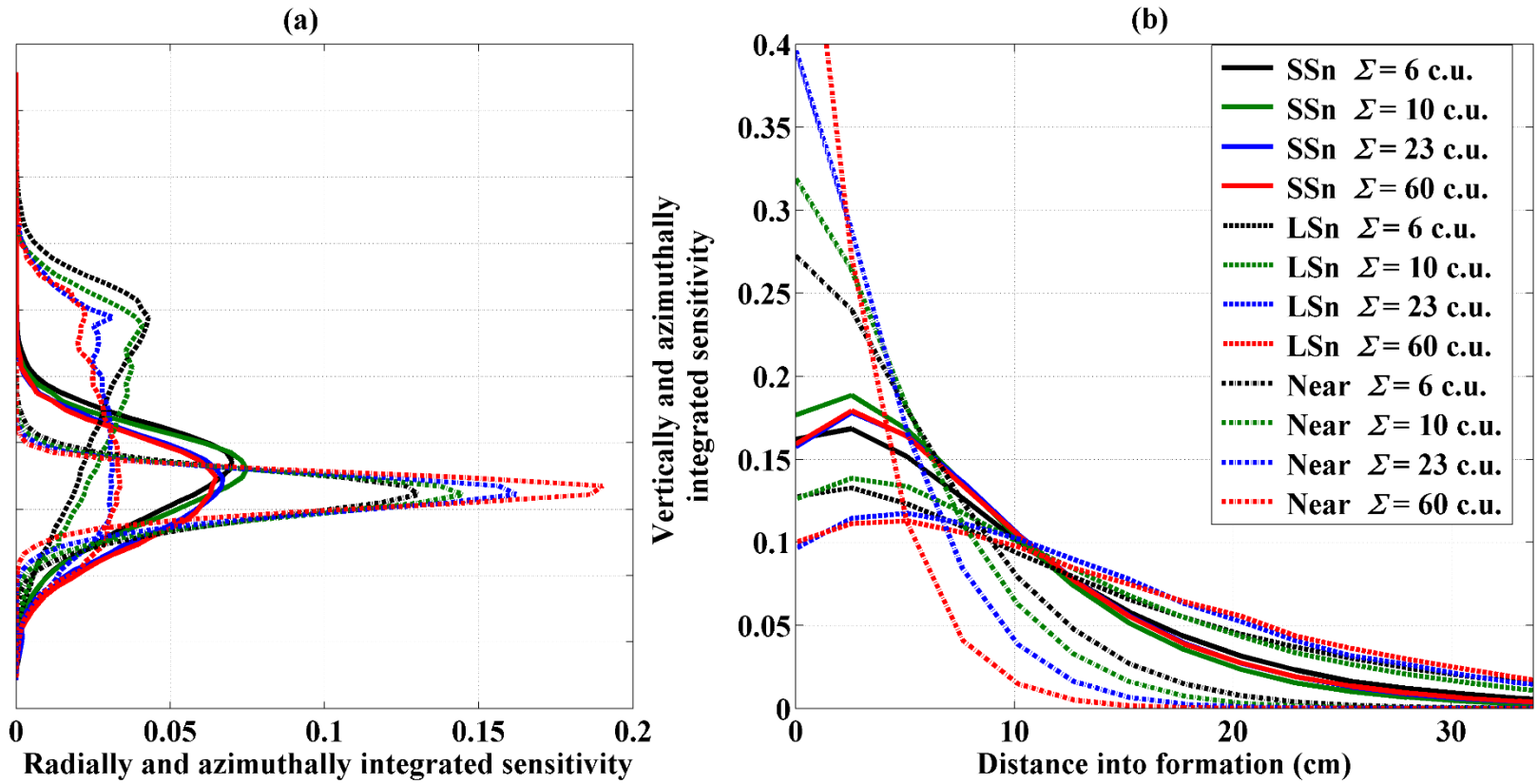

Figure 3.3: Thermal-neutron absorption (SSn and LSn detectors) and thermal-neutron (Near detector) FSFs corresponding to materials of different absorption cross sections. (a) Shows radially and azimuthally integrated FSFs along the tool, whereas (b) shows vertically and azimuthally integrated FSFs as a function of radial distance into the formation. Note: the vertical axis on panel (a) cannot be shown because the position of the source and detectors of the commercial tool under study is confidential.

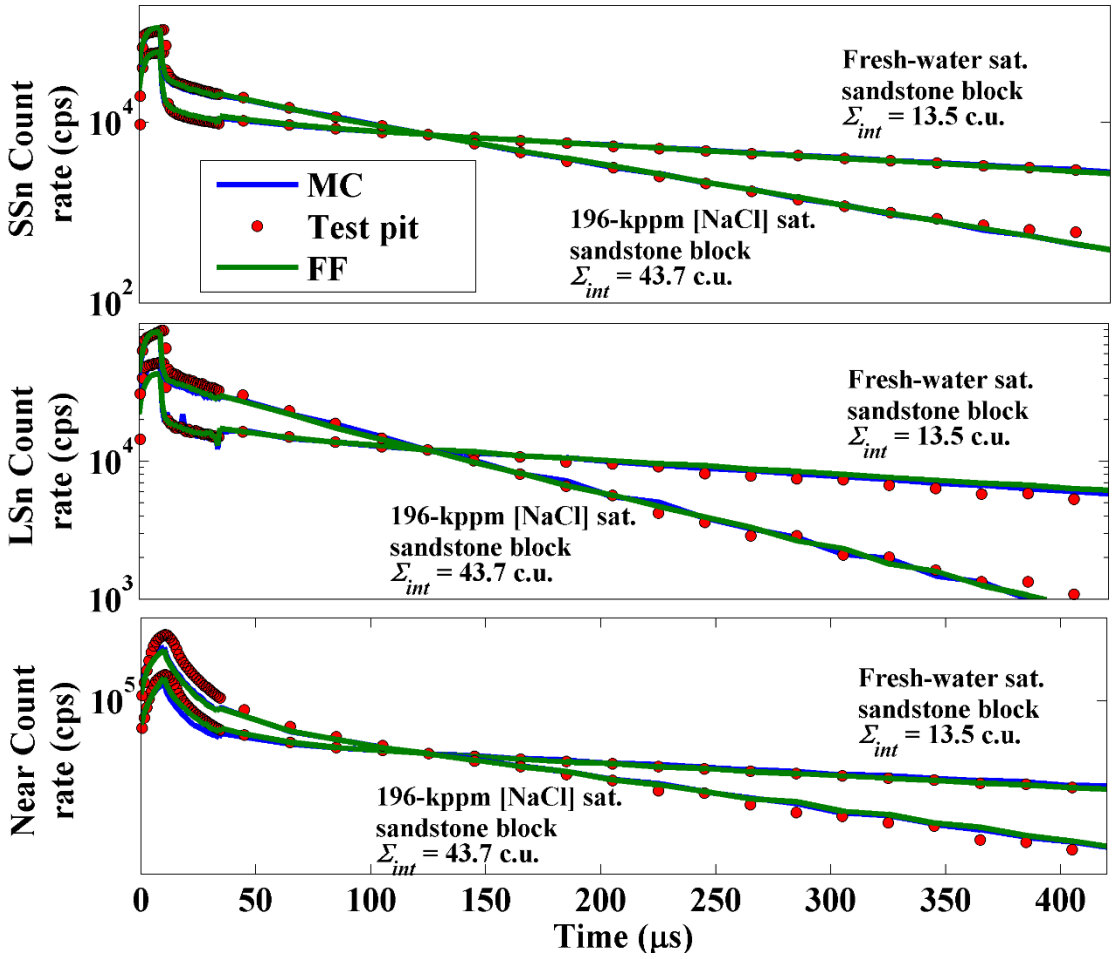

Figure 3.4: Comparison of multi-detector Monte Carlo simulated (blue solid lines), fast-forward simulated (green solid lines), and test-pit measured (red markers) time decays for two materials of low and high absorption cross section. The calculation of each Monte Carlo time decay takes approximately 10 hours of CPU time, while the calculation of each fast-forward modeled time decay takes approximately 0.25 seconds.

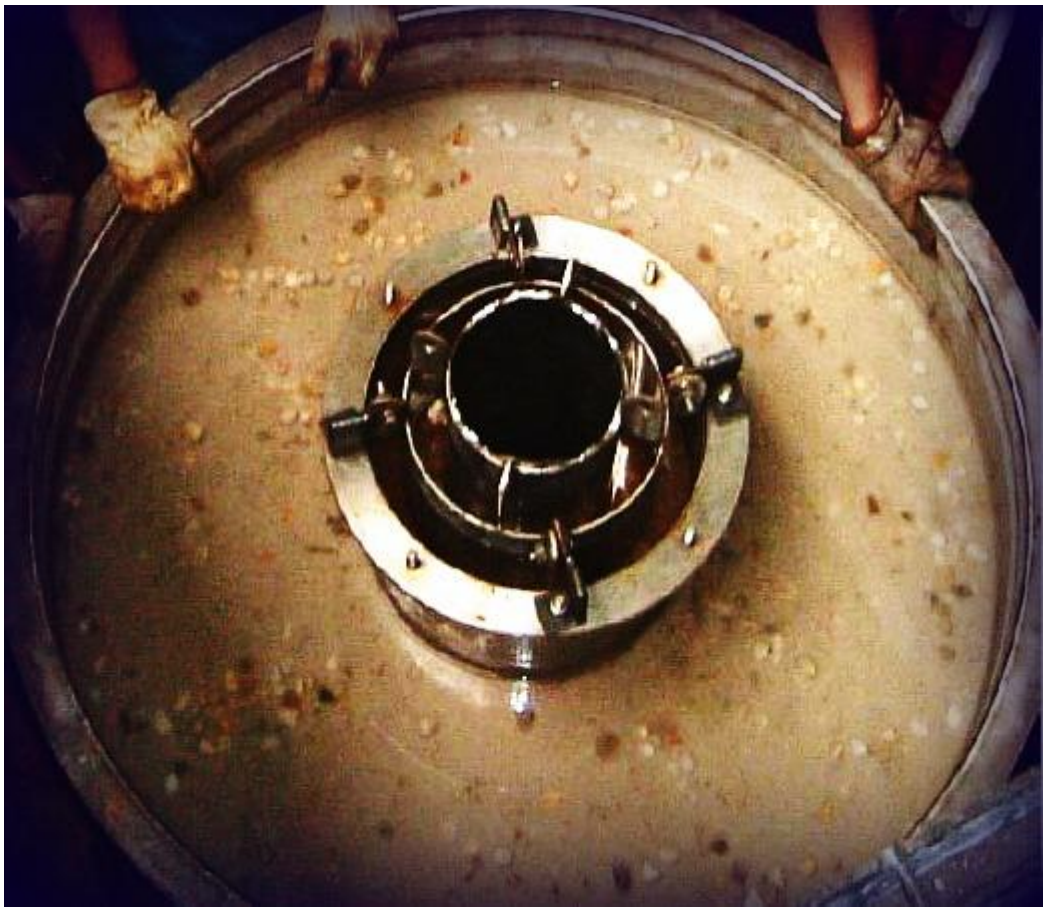

Figure 3.5: Experimental facility used to emulate piston-like invasion. The concentric steel liners are used to physically separate virgin- and invasion-zone fluids.

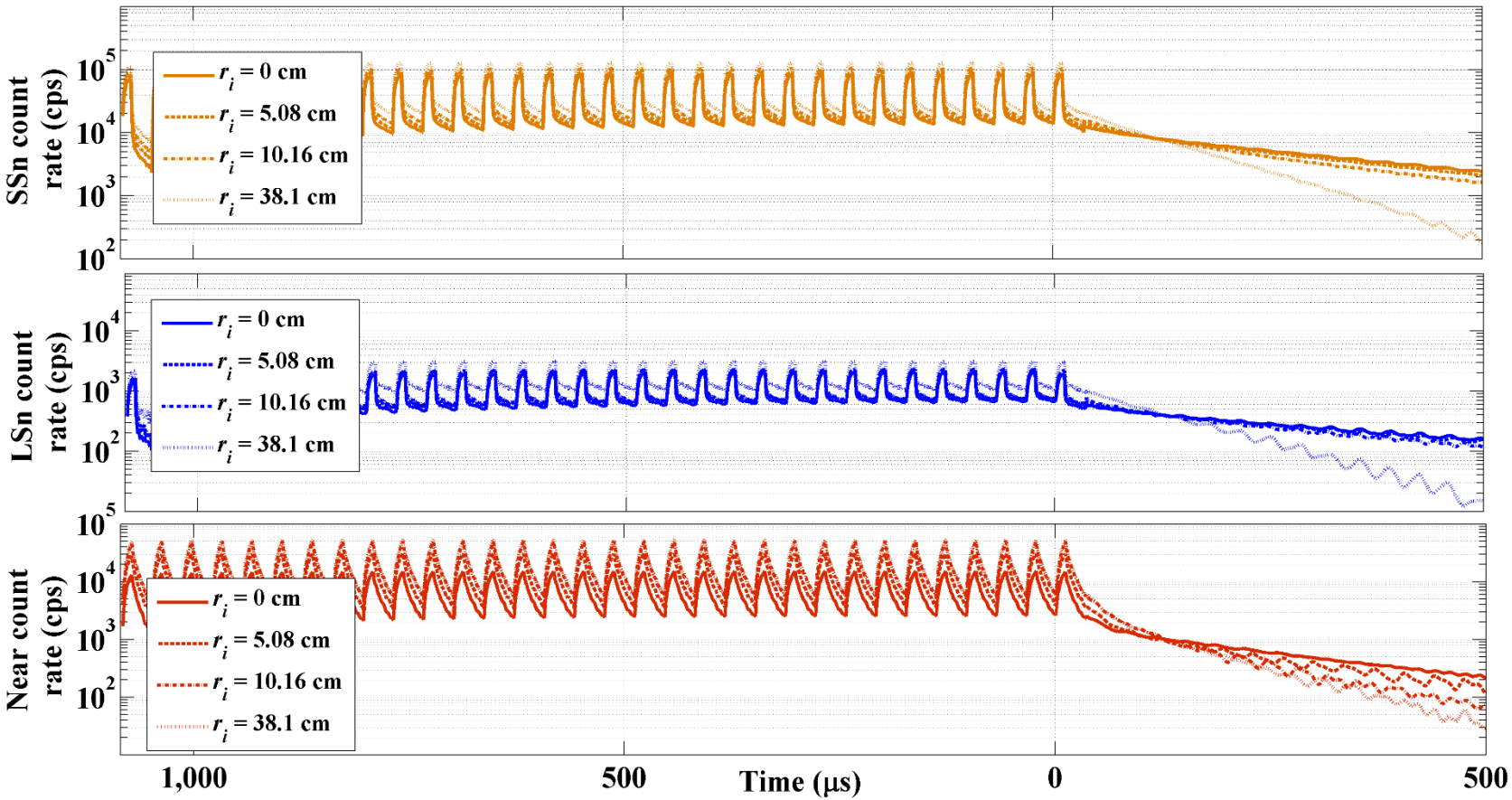

Figure 3.6: Monte Carlo simulated multi-detector pulsed-source time decays for various piston-like radial lengths of invasion into a 34-p.u. sandstone formation. The rock is fresh water-saturated in the virgin zone, and 200-kppm [NaCl] brine saturated in the invasion zone.

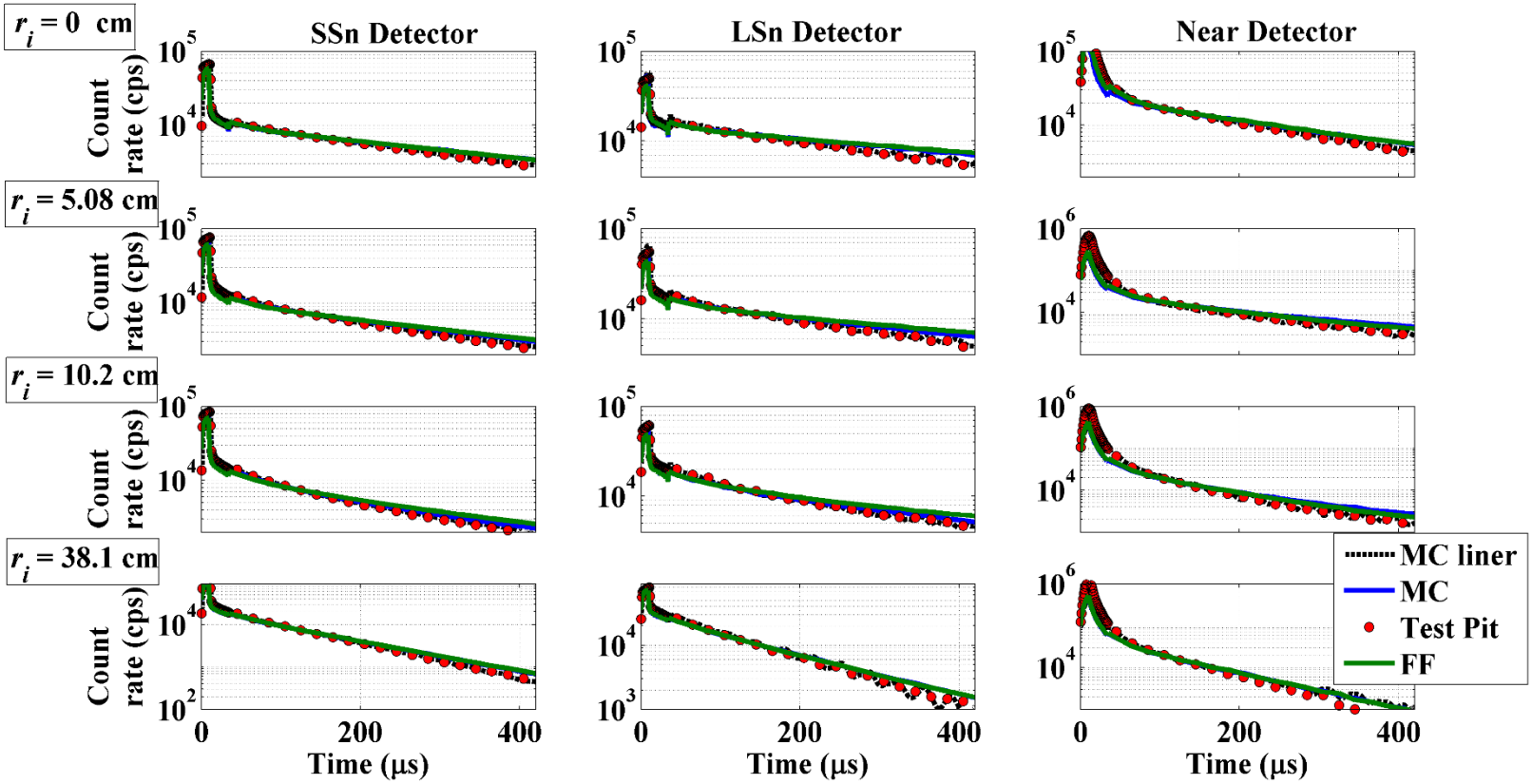

Figure 3.7: Three-detector (from left to right) time decay measurements at various radial lengths of invasion (from top to bottom) for 200-kppm [NaCl] brine invading a fresh-water saturated 34-p.u. sandstone block. The black dashed line identifies MCNP-calculated time decays including the liners in the test pit, which is to be compared to the actual test-pit measurements shown in red markers. The blue solid line shows MCNP-calculated time decays without including the liners, which is to be compared to the fast-forward simulations shown in green solid lines.

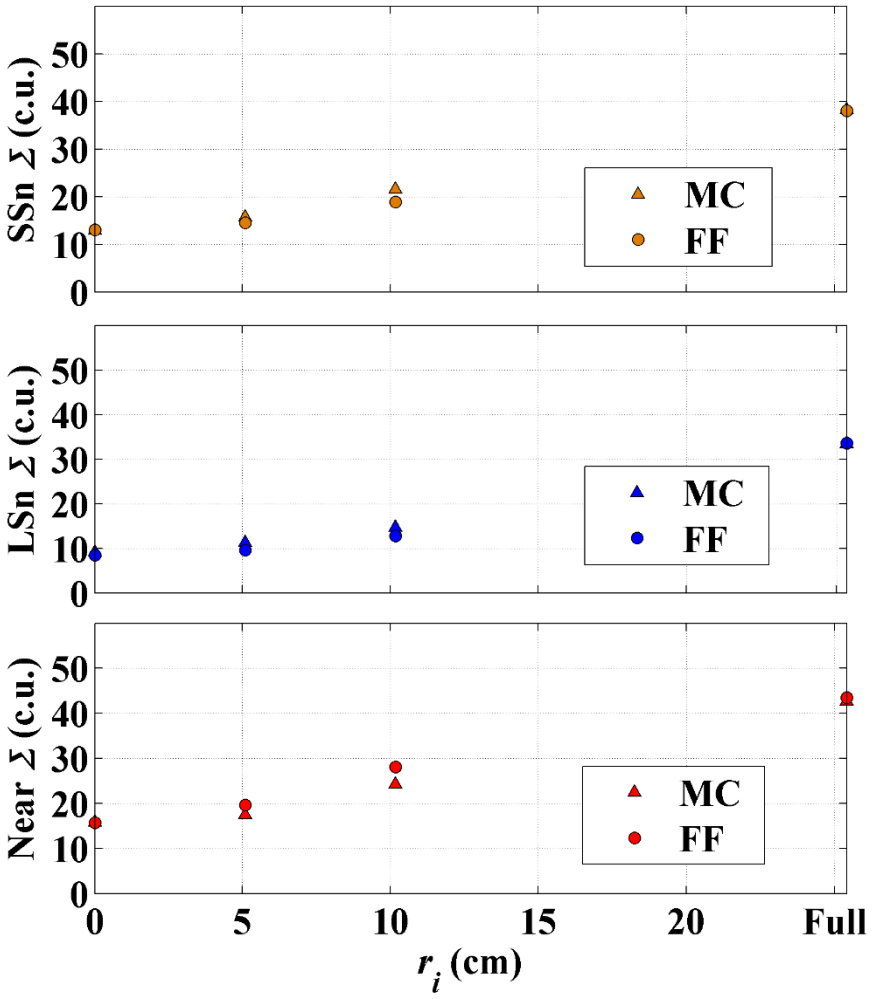

Figure 3.8: Apparent Sigma as a function of radial length of invasion derived from Monte Carlo (MC) and fast-forward (FF) simulated time decays shown in **Figure 3.7**.

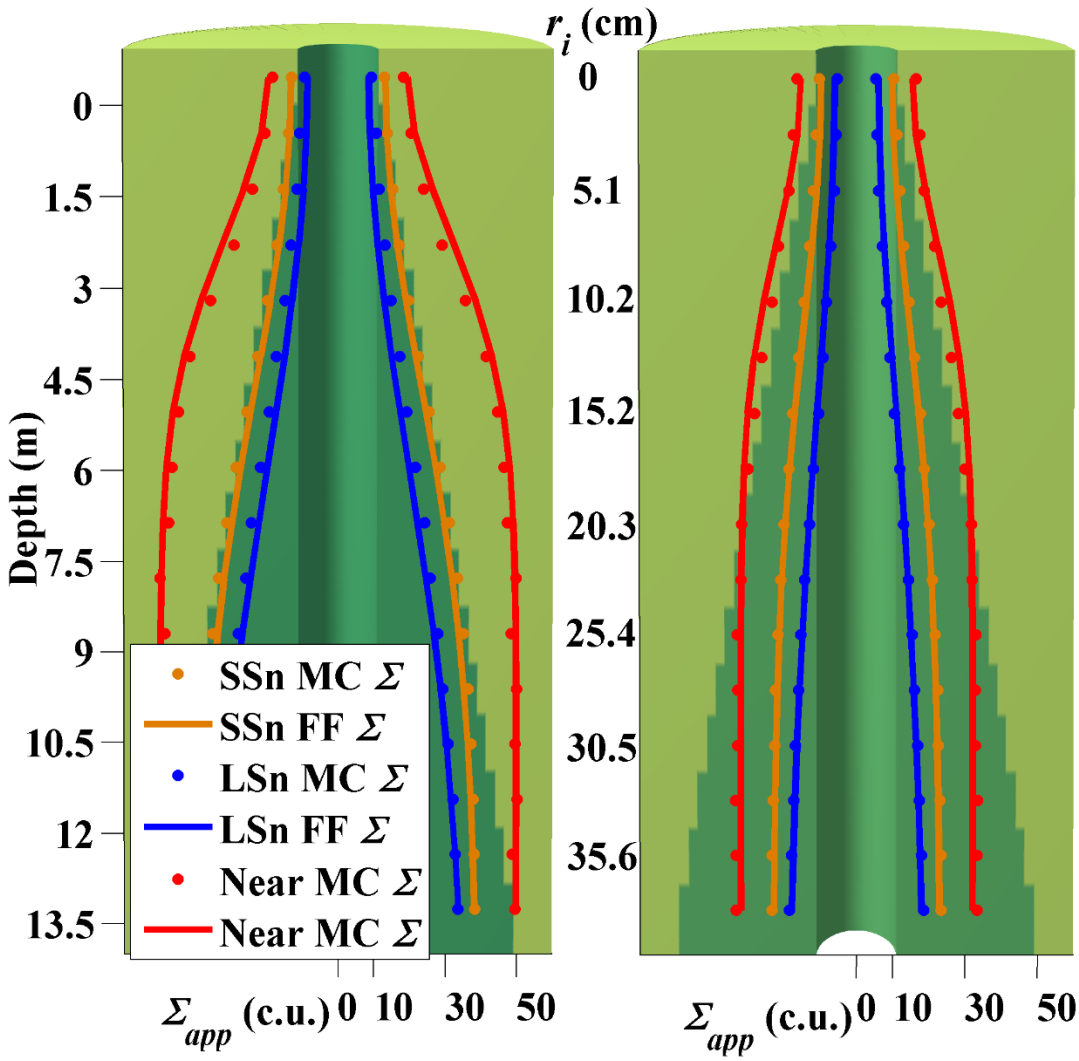

Figure 3.9: Comparison of apparent Sigma from Monte Carlo and fast-forward modeled time decays corresponding to 200-kppm [NaCl] brine invading oil-bearing 34-p.u. (left panel) and 17-p.u. (right panel) sandstone formations. The contrast between invasion- and virgin-zone Sigma is 25 c.u. and 12 c.u. for the 34-p.u. and 17-p.u. cases, respectively. The blocky dark green shade and numbers in the middle describe the radial length of invasion at each depth level, ranging from no invasion at the top to 38.1 cm (15 in) at the bottom.

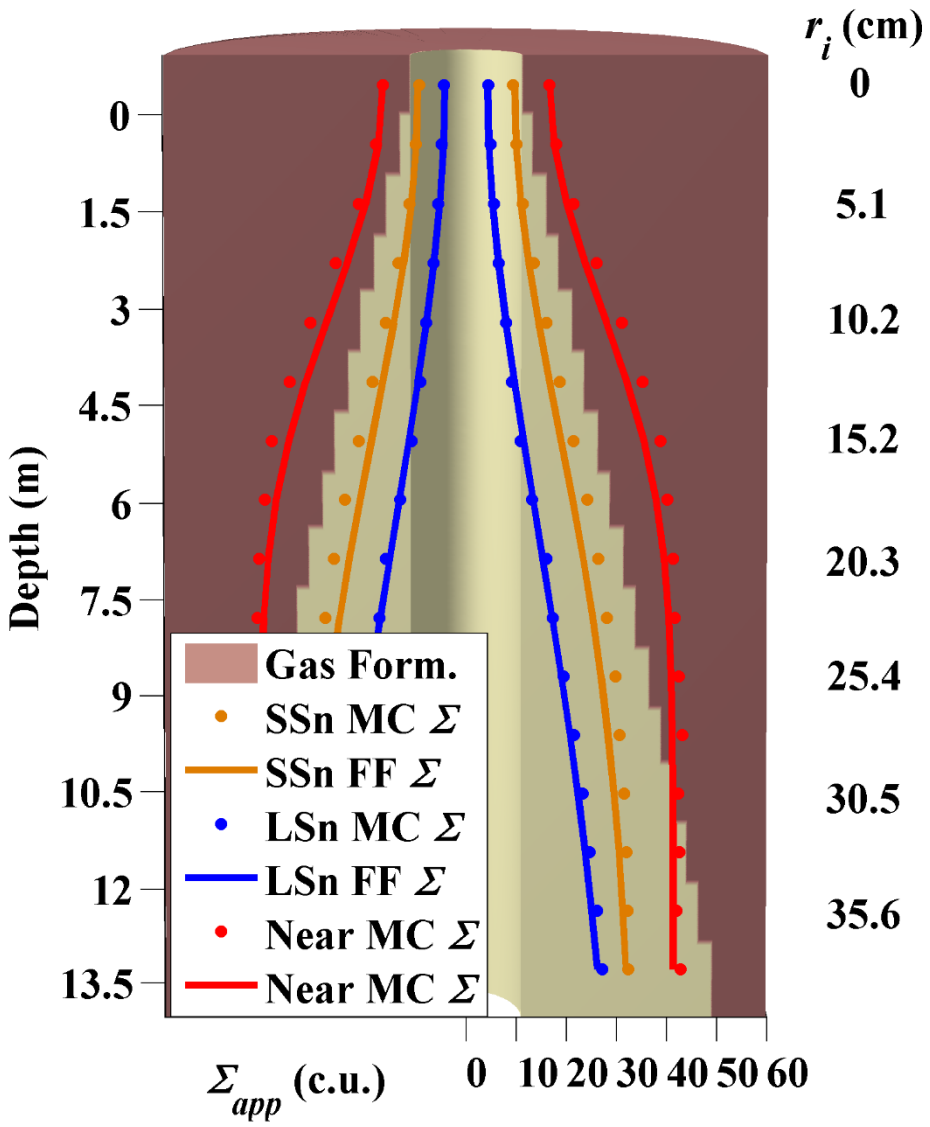

Figure 3.10: Comparison of apparent Sigma from Monte Carlo and fast-forward simulated time decays corresponding to 200-kppm [NaCl] brine invading 30-p.u. gas-bearing sandstone formations. The blocky light-colored shade and numbers on the right identify the radial length of invasion at each depth level, ranging from no invasion at the top to 38.1 cm (15 in) at the bottom.

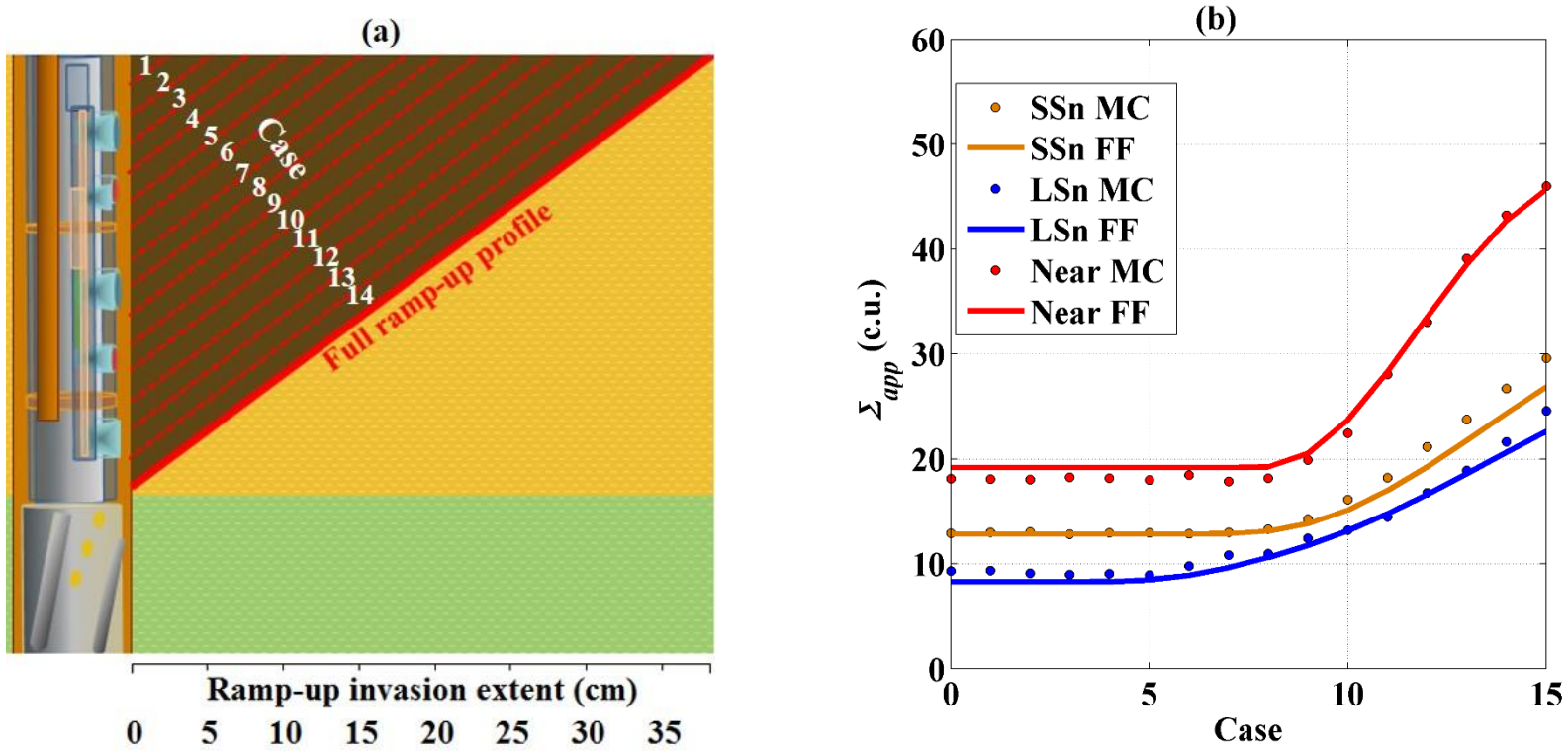

Figure 3.11: (a) Sketch of 16 ramp-up radial invasion cases in the range of no invasion to a 38.1-cm maximum radial extent ramp-up invasion profile, and (b) Sigma logs calculated from Monte Carlo and fast-forward simulated time decays for each invasion profile. Dashed red lines describe the shapes of intermediate invasion profiles.

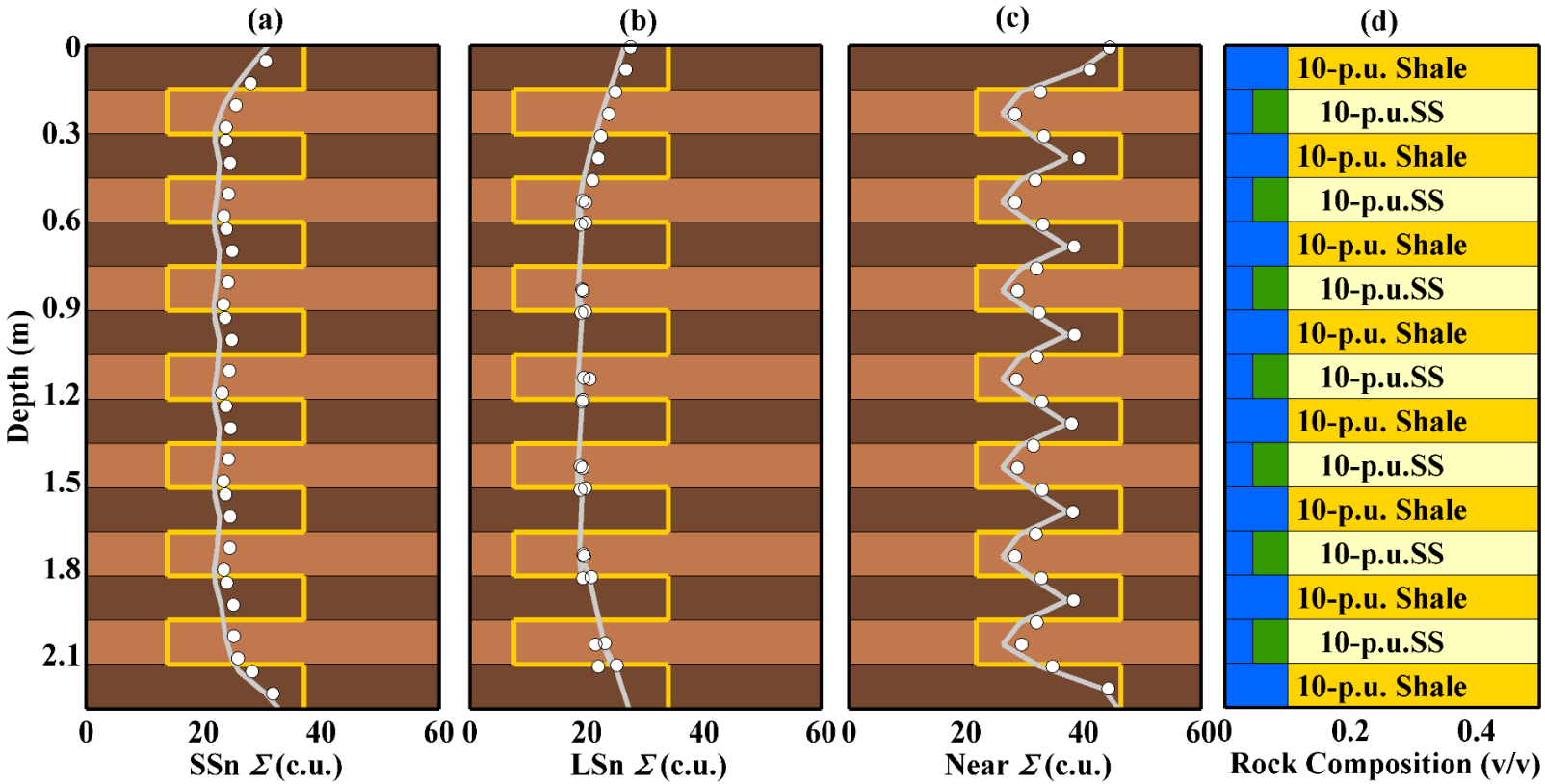

Figure 3.12: Multi-detector Sigma logs (a), (b), (c) calculated from Monte Carlo (white markers) and fast-forward (gray solid lines) simulated time decays for an alternating sequence of 15.24-cm (6-in) shale (33.9 c.u.) and oil-bearing sandstone (9.65 c.u.) formations. The blocky yellow line identifies the apparent Sigma values for each bed as if acquired in thick homogeneous formations. The panel on the right (d) shows volumetric rock compositions. Blue and green colors represent water and oil volumes, respectively

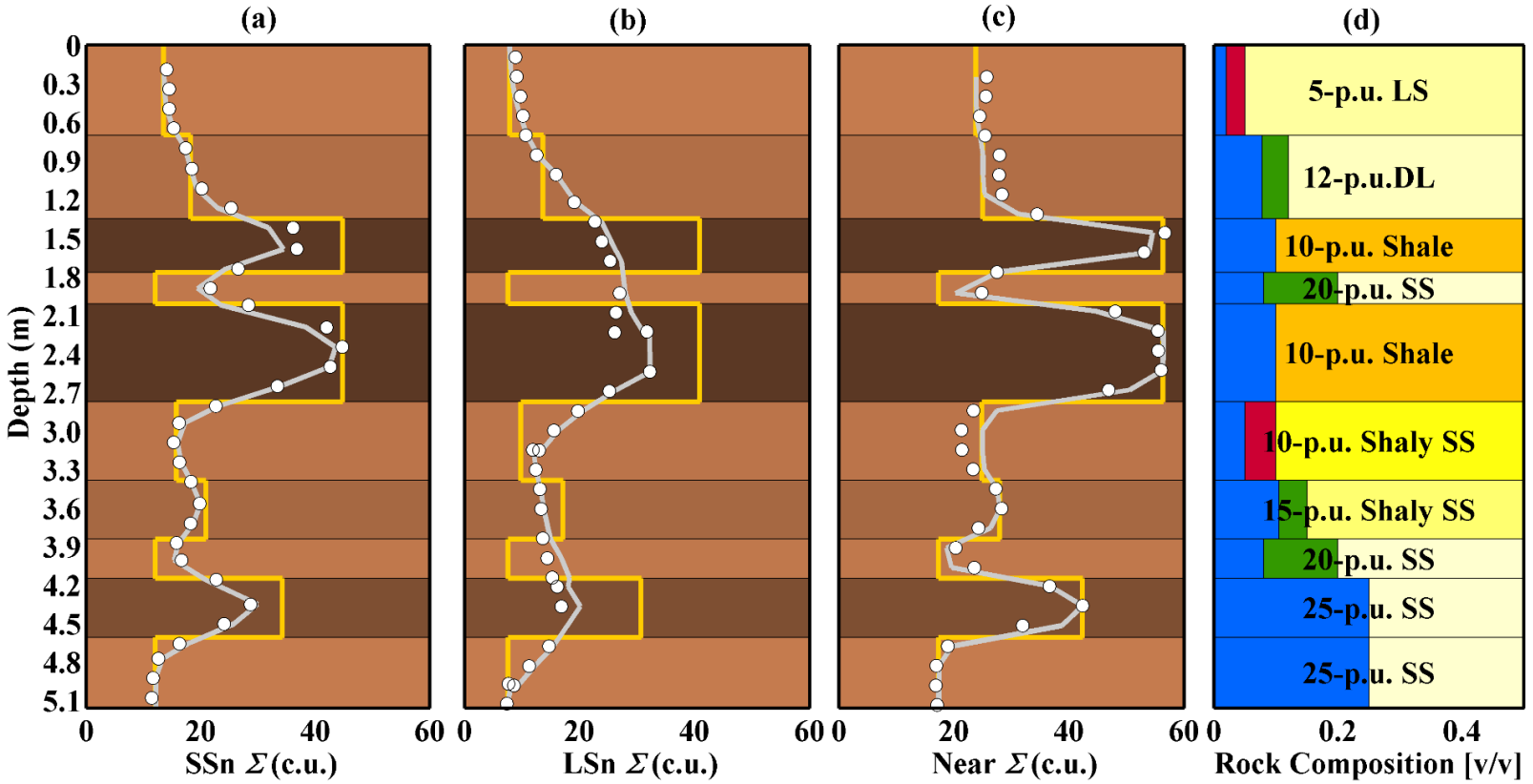

Figure 3.13: Multi-detector Sigma logs (a), (b), (c) calculated from simulated Monte Carlo (white markers) and fast-forward (gray solid lines) time decays in sequence involving carbonate and siliciclastic formations, variable porosities, and oil, gas, and brine saturated formations. The blocky yellow line identifies the apparent Sigma values for each formation as if acquired in thick homogeneous formations. The panel on the right (d) shows volumetric rock compositions. Blue, red, and green colors represent water, gas, and oil volumes, respectively.

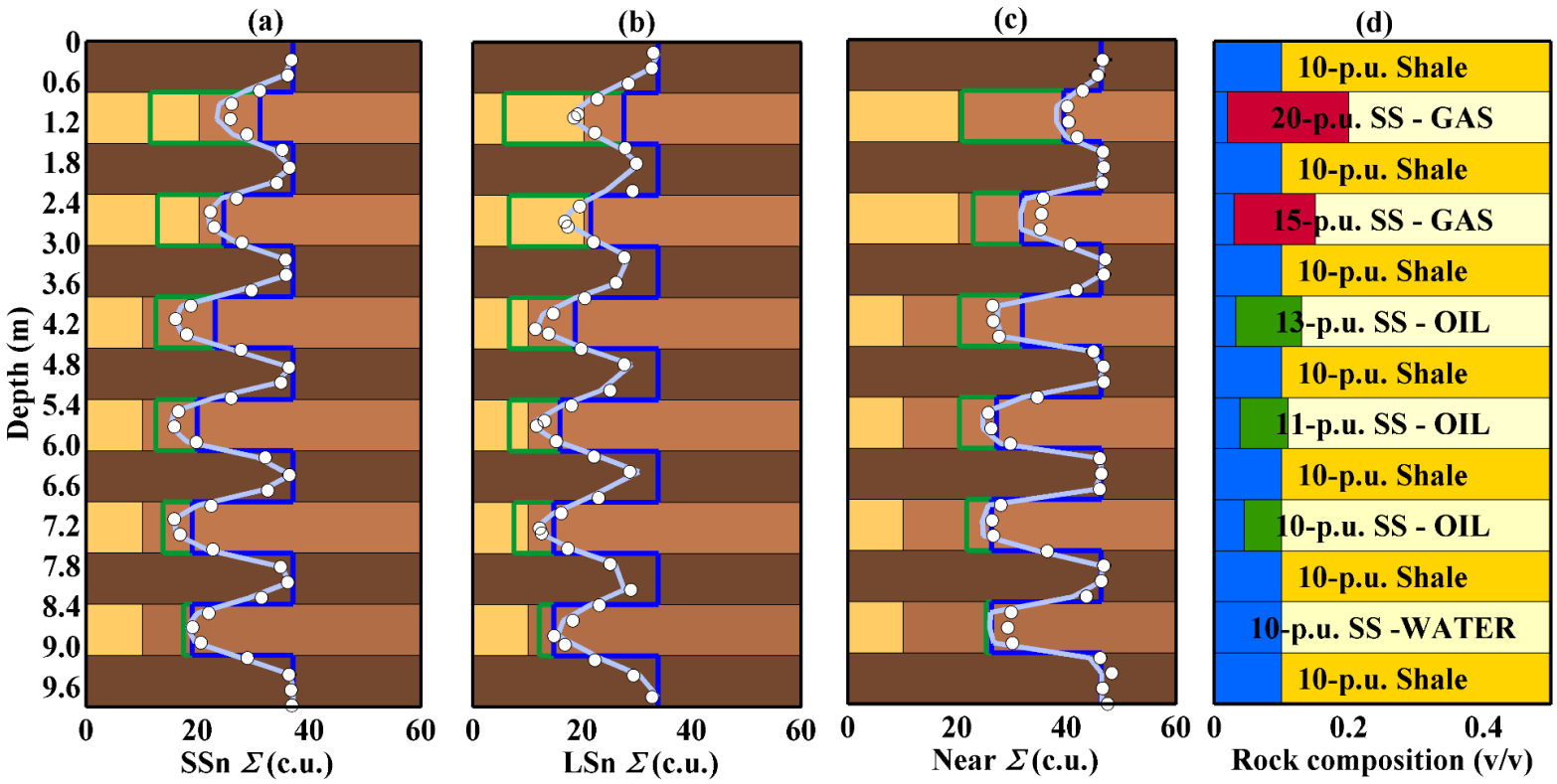

Figure 3.14: Multi-detector Sigma logs (a), (b), (c) calculated from simulated Monte Carlo (white markers) and fast-forward (gray solid lines) time decays in a sequence of 76.2-cm (2.5-ft) bedded shale and sandstone formations affected by invasion. Blocky green and blue solid lines indicate apparent virgin- and invasion-zone Sigma values for each formation, respectively. Radial length of invasion is represented by the light yellow blocks in each sandstone formation, which is 20.32 cm (8 in) at the top sand layers, and 10.16 cm (4 in) for the rest of the sand layers. The panel on the right (d) shows the volumetric rock composition. Red, green, and blue colors represent gas, oil, and water volumes, respectively.

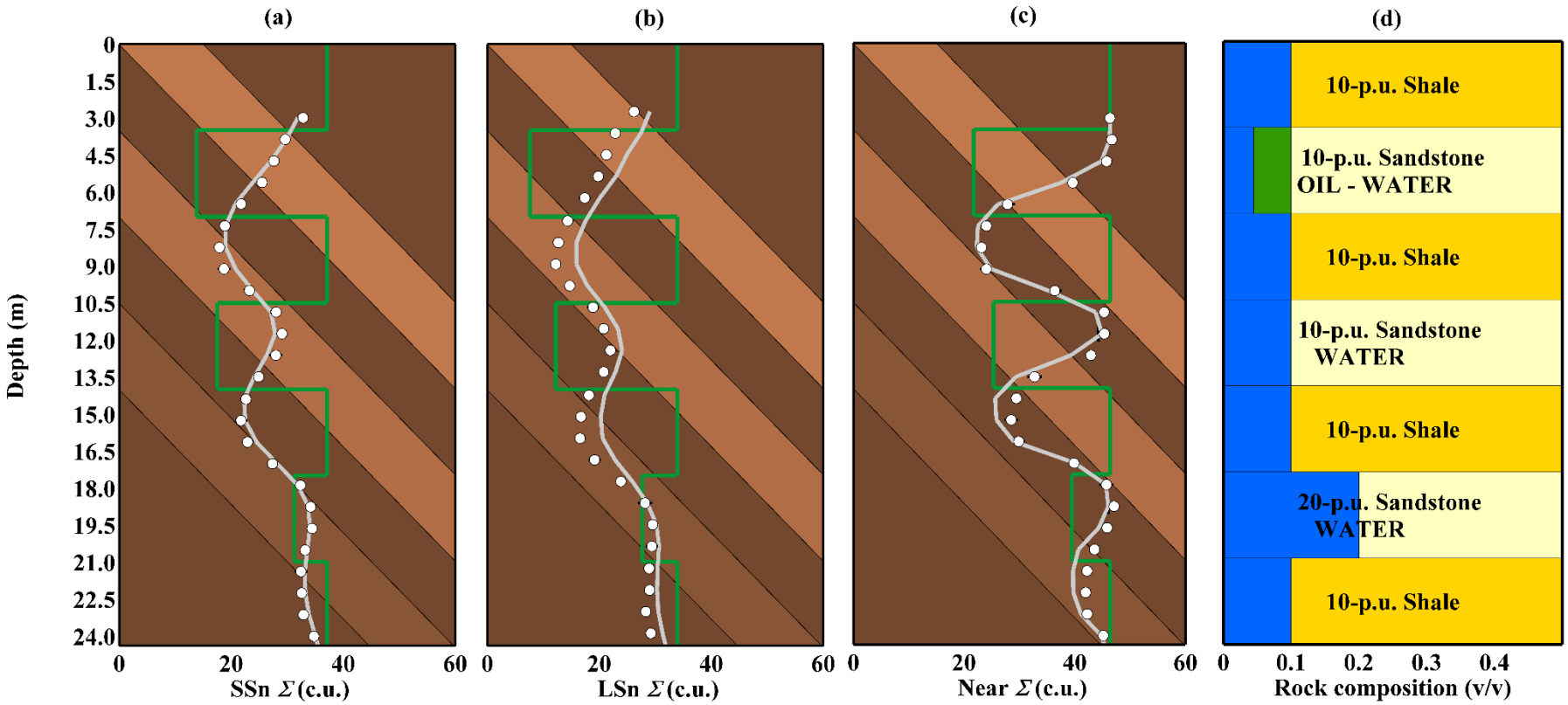

Figure 3.15: Multi-detector Sigma logs (a), (b), (c) calculated from Monte Carlo (white markers) and fast-forward (gray solid lines) time decays for an 85°-deviated well penetrating a sequence of 30.48-cm (true stratigraphic thickness, TST) sandstone-shale alternations. Blocky green lines identify apparent Sigma values for each bed as if measured in a thick homogeneous block of the material. The panel on the right (d) shows the volumetric rock composition of the sub-layers in the model.

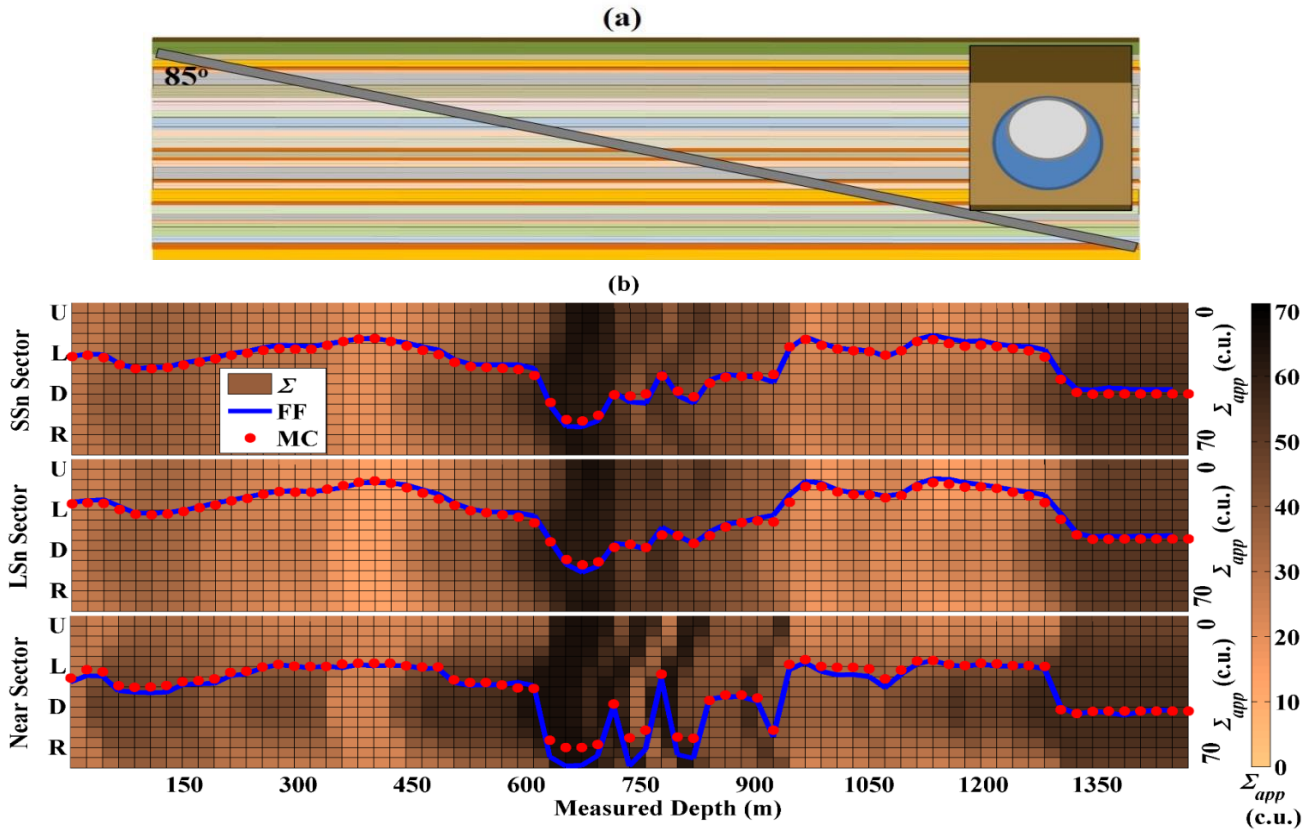

Figure 3.16: (a) Sketch of 85° deviated well penetrating the sequence of layered formations described in **Table 3.7**. The inset on the right shows the shape of the assumed asymmetric invasion front. (b) Forward-model simulated multi-detector apparent Sigma images and fast-forward (blue solid line) and Monte Carlo (red makers) calculated apparent Sigma log for the upper sector of the LWD tool. The maximum difference between the two results is observed at the thermal-neutron detector in high-Sigma shale thin layers because of higher statistical noise in both MC and FF models. Radial length of invasion is 20.32 cm at the bottom sector and 0 cm at the top sector for all the permeable formations in the sequence.

Chapter 4: One-Dimensional Radial Inversion of Multi-Detector Logging-While-Drilling Sigma Measurements

This chapter introduces a nonlinear gradient-based fast inversion method that uses the measured three-detector decays and a reference value for invasion-zone Sigma to estimate radial length of invasion and virgin formation Sigma. Synthetic logs are generated with realistic noise for numerous realizations, which are then used to study the stability of the inversion routine and the estimation of error bars. I propose the use of a Confidence Index (*CI)* derived from the multiple-realization study to define the conditions under which the multi-detector time-decay problem is not stable; finally, the reliability of the Sigma inversion method is verified in a set of test-pit measurements, two synthetic examples, and a field case. Synthetic results indicate that the inversion of multi-detector decays enables the correction of LWD Sigma measurements for invasion effects and improves the calculation of water saturation whenever there is contrast between invasion- and virgin-zone Sigma of more than 5 c.u. Field example results suggest that the inversion can accurately reproduce three-detector time decays honoring invasion effects evidenced in neutron-density porosity logs while managing the presence of noise.

4.1 INTRODUCTION

Interpretation of LWD measurements has typically been carried out under the assumption that invasion can be neglected because the time of exposure to drilling fluid is significantly small compared to wireline conditions. However, it was reported in Chapter

2 the significant impact of invasion in LWD Sigma logs because of the exposure of the formation to overbalanced drilling fluid from the time the bit breaks the rock until the measurement is actually acquired. Allen et al. (1965) studied the effect of shallow invasion on wireline Sigma measurements, reporting the dependence of detector spatial sensitivity on the absorption properties of the logging environment. Their study recognizes the importance of assessing invasion effects on Sigma log interpretation because of the shallow nature of the measurement. El Din et al. (2012) proposed the 1D inversion of virgin-zone Sigma, invasion-zone Sigma, and radial length of invasion based on pre-calculated Sigmas as a function of radial length of invasion. In this work they used Sigma logs which are subject to corrections for thermal neutron diffusion and borehole effects prior to inversion. Mauborgne et al. (2013) applied the same method to identify the water-oil contact in a reservoir drilled by oil-based mud (OBM) and to estimate radial length of invasion. The method reported in both studies is a simple and fast approach to correct Sigma logs for invasion effects. However, it is not an optimal solution for real logging conditions because it assumes that any separation between environmentally corrected Sigma logs is only due to invasion, without quantifying the impact of noise in the decays, and disregarding the uncertainty that the diffusion correction imposes on environmentally corrected Sigma logs. It also stops short of addressing the non-uniqueness of the problem and the estimation of error bars to formally assess the reliability of the multi-detector decay interpretation.

I introduce an approach for multi-detector decay interpretation based on the inversion of raw three-detector time decays. I invoke the fast-forward model developed in

Chapter 3 to minimize the misfit between noisy measurements and fast-forward simulated time decays. Minimizing the underlying time decays, rather than the derived Sigma log, has the advantage that there exists as few intermediate processing steps as possible between the raw measurements and the estimation of formation properties. The only corrections that are made to the raw decay curve count rates are: a fundamental correction for the characteristic dead-time of each detector; and the subtraction of background gamma-ray counts that arise from induced neutron activation and natural radioactivity. The method is not preconditioned by other environmental corrections to the data. Nonetheless, the method depends upon a reference value for invasion-zone Sigma, which is a function of porosity, matrix composition, and filtrate salinity. In addition, I study the stability of the proposed inversion for an extensive range of Sigma contrast between the virgin and invasion zones and radial lengths of invasion to quantify the uncertainty of the model. I use the results of this study to generate visual flags that provide a warning about conditions in which the multi-detector inversion might not be stable.

The structure of this chapter is as follows: first, I formulate the 1D inversion of multi-detector decays and examine the stability of the problem. Second, I test the algorithm on synthetic cases that include different Sigma contrasts, radial lengths of invasion, and inclusion of noise as a function of the logging environment Sigma and penetration rate, *ROP*. Then, I introduce a Confidence Index (*CI*) that is used together with covariance-derived error bars to ascertain the uncertainty of model outputs. I perform inversion of time decays acquired in a laboratory facility designed for the modeling of piston-like invasion,

and two synthetic cases that exhibit the effects of Sigma contrast, radial length of invasion, matrix Sigma, and porosity on the results. Finally, the method is applied to field data to evaluate the radial invasion profile and to correct Sigma for shallow-invasion effects in a thick gas-bearing formation. Results confirm that inversion of gamma-ray and thermal-neutron time decays acquired in thick shallow-invaded measurements enables the estimation of virgin Sigma and radial length of invasion, and that this method significantly improves the calculation of resistivity-independent water saturation in high-porosity formations that display virgin- and invasion-zone Sigma contrast larger than 5 c.u.

4.2 One-Dimensional Inversion-Based Interpretation of Logging-While-Drilling Sigma Measurements

4.2.1 Formulation

In this section it is desired to relate physical properties characterizing the multi-detector forward model, **m**, to the set of observations in three measured signals, **d**. This can be written in a generic form as a forward problem of the form

$$G(\mathbf{m}) = \mathbf{d}, \tag{4.1}$$

where G is a model used to numerically simulate $\mathbf{d}$ as a function of **m**.

The LWD Sigma tool measures three time decays at each depth level that in the case of thick homogeneous formations and no tool standoff are only a function of virgin formation Sigma, Σ_v, invaded-zone Sigma, Σ_i, and radial length of invasion, r_i. The fast-forward model to simulate multi-detector signals can be expressed as

$$G\begin{bmatrix}\Sigma_v\\ \Sigma_i\\ r_i\end{bmatrix}=\begin{bmatrix}\mathbf{n}_1(t)\\ \mathbf{n}_2(t)\\ \mathbf{n}_3(t)\end{bmatrix}, \tag{4.2}$$

where $\mathbf{n}_1(t)$ and $\mathbf{n}_2(t)$, are the gamma-ray time decays and $\mathbf{n}_3(t)$ is the thermal-neutron time decay for the SSn, LSn, and Near detectors of the LWD tool, respectively, and G is the non-linear multi-detector Sigma numerical simulator presented in Chapter 3. In Chapter 2, $\mathbf{n}(t)$ was defined as a detector-specific time decay for the irregular time bins of the pulsed-neutron commercial tool under study from 0 μs to 415 μs, where time 0 μs is the time at which the last pulse is generated.

The main purpose of the inversion is to estimate the values of Σ_v, Σ_i and r_i that best reconstruct a set of multi-detector Sigma measurements, $\mathbf{d}$. I seek to minimize the residual form $\|G(\mathbf{m})-\mathbf{d}\|_2^2$. The problem is non-unique because the detectors' response can be similar for different combinations of virgin- and invasion-zone Sigmas and radial lengths of invasion. To lend stability to the possibly ill-posed multi-detector decay problem, I seek to minimize the damped least squares problem of the form

$$F(\mathbf{m})=\|G(\mathbf{m})-\mathbf{d}\|_2^2+\alpha^2\|\mathbf{m}\|_2^2, \tag{4.3}$$

where α is the regularization parameter (Aster et al., 2013).

The simulation of multi-detector LWD decays is a nonlinear problem because of the nonlinear change of the detectors' sensitivity as a function of the logging environment absorption properties and the different shape of the radial sensitivity of the detectors. I

select Occam's method to perform the minimization and dynamically adjust the regularization parameter, α, to avoid exceeding the value of the misfit so that the effect of the regularization is progressively diminished as the algorithm reaches convergence. The most basic form of Occam's inversion algorithm can be written as (Aster et al., 2013)

$$\left[\mathbf{J}(\mathbf{m}^k)^T \cdot \mathbf{J}(\mathbf{m}^k) + \alpha^2 \mathbf{I}\right]\mathbf{m}^{k+1} = \mathbf{J}(\mathbf{m}^k)^T \left[\mathbf{d} - G(\mathbf{m}^k) + \mathbf{J}(\mathbf{m}^k)\mathbf{m}^k\right], \tag{4.4}$$

where $\mathbf{m}^k$ is the vector of model properties at iteration *k*, $\mathbf{m}^{k+1}$ is the updated trial model at iteration *k+1*, $\mathbf{J}(\mathbf{m}^k)$ is the Jacobian matrix, which invokes the first-order derivatives of the measurement vector with respect to the model properties, $G(\mathbf{m}^k)$ is the numerically modeled set of time decays for the trial $\mathbf{m}^k$, α is the updated regularization parameter, and $\mathbf{d}$ is the measurement vector consisting of measured multi-detector decays.

Next, I adjust Occam's inversion method for the nature of the multi-detector Sigma measurement problem. **Figure 4.1** shows the signals of the LWD tool under study for the case of 34-p.u. fresh-water bearing sandstone invaded 12.7-cm (5-in) deep by 200-kppm [NaCl] water-based mud (WBM). In Chapter 2, it was described that decays of the pulsed-source tool under study originate from 32 bursts of 14-MeV neutrons, each lasting 10-μs. The early part of the signal is only slightly sensitive to changes in the absorption cross section of the materials in the formation. Therefore, I focus on inversion-based interpretation of the late-time part of the signal shown in **Figure 4.1b** (inside the dashed square at the top panel), which corresponds to the last pulse of the pulsed source and the time-window dedicated to the Sigma measurement.

The measurement vector on the right-hand side of equation 4.1 considers the three late-time decays. The exponential nature of the three components of the data vector suggests the use of a data-weighting matrix in the inversion formulation to assign equal importance to all the time bins of each decay curve.

Occam's inversion algorithm modified to include a data-weighting matrix can be re-written as

$$\left[\left(\mathbf{W}_d \cdot \mathbf{J}(\mathbf{m}^k)\right)^T \cdot \left(\mathbf{W}_d \cdot \mathbf{J}(\mathbf{m}^k)\right) + \alpha^2 \mathbf{I}\right]\mathbf{m}^{k+1} = \mathbf{J}(\mathbf{m}^k)^T \left[\left(\mathbf{W}_d{}^T \cdot \mathbf{W}_d\right) \cdot \left(\mathbf{d} - G(\mathbf{m}^k) + \mathbf{J}(\mathbf{m}^k)\mathbf{m}^k\right)\right], \tag{4.5}$$

where $\mathbf{W}_d$ is a data-weighting matrix that is defined as a diagonal matrix, whose nonzero elements are given by $1/\mathbf{d}$, to minimize the relative misfit of the multi-detector time decay. However, at late times the response at different detectors varies within several orders of magnitude, which would result in assigning more weight to the detector whose decay presents the lowest magnitude. The statistical noise of nuclear measurements is inversely proportional to the square root of the counts; minimizing the relative misfit would assign high importance to low-magnitude noisy data points. To avoid this situation, and to evenly emphasize the response of the three late-time responses, I propose the use of a modified data-weighting matrix given by

$$\mathbf{W}_d = \begin{bmatrix} 1/\mathbf{n}_1^{\beta_{SSn}}(t) & 0 & 0 \\ 0 & 1/\mathbf{n}_2^{\beta_{LSn}}(t) & 0 \\ 0 & 0 & 1/\mathbf{n}_3^{\beta_{Near}}(t) \end{bmatrix} \tag{4.6}$$

where β_{SSn}, β_{LSn}, and β_{Near} are a set of coefficients that emphasize the response at the late time portion of the decay curves. Typically, detector count rate is highest at the Near detector, and lowest at the LSn detector. However, whether the SSn or Near detector count rate is higher varies according to the logging environment. I adjust β for different synthetic cases and find that $\beta_{SSn} = 1$, $\beta_{LSn} = 1.6$, and, $\beta_{Near} = 1.5$, allow one to assign each detector approximately the same importance in typical logging environments and work well to reconstruct the late-time part of the signals. **Figure 4.2** shows the shape of the data-weighting matrix to minimize the relative error, $1/\mathbf{d}$, and the modified relative error, $1/\mathbf{d}^{\beta}$. Notice that the modified version assigns similar weight to the three signals of the LWD tool and gives more importance to the late-time bins.

Ideally, the three time decay from the LWD tool are sufficient to estimate three unknown properties, i.e., Σ_v, Σ_i, and r_i. However, the tool response can be quite similar for different combinations of model properties, which leads to non-uniqueness in the inversion problem. **Figure 4.3** compares the multi-detector decays for two different configurations. One configuration corresponds to oil-bearing 30 p.u. sandstone invaded 12.7-cm deep by 200-kppm [NaCl] WBM. The second configuration corresponds to a gas-bearing 30-p.u. sandstone invaded 17.8-cm deep by 120-kppm [NaCl] WBM. The figure emphasizes the non-uniqueness of the problem. Different configurations of virgin- and invasion-zone Sigmas and radial lengths of invasion can generate similar decays in the

three detectors of the LWD Sigma tool. Additional information about the problem is helpful to limit the range of possible solutions that are consistent with the measured signal.

Multi-detector Sigma is not meant to be a standalone measurement, but rather to be combined with other borehole measurements. Because Sigma is a volumetric property, knowledge of the porosity, matrix composition, and mud filtrate permits the estimation of intrinsic Sigma in the invasion zone, i.e.,

$$\Sigma_i = \phi\Sigma_{mf} + (1-\phi)\Sigma_m \ , \tag{4.7}$$

where Σ_{mf} is mud filtrate Sigma, which is a function of filtrate salinity, composition, pressure, and temperature. Σ_m is the matrix Sigma, and ϕ is total porosity. Σ_{mf} can be calculated using SNUPAR, or other nuclear parameter software packages if filtrate salinity is known from mud reports. Σ_m can be calculated from the volumetric matrix composition derived from the spectroscopy log and a database of Sigma for common formation minerals. ϕ can be calculated from available neutron and density logs. Equation 4.7 assumes piston-like invasion and neglects the presence of residual hydrocarbon saturation in the invasion zone.

I introduce the use of a reference vector to address the non-unique nature of the multi-detector Sigma measurement, namely,

$$\mathbf{m}_R = \begin{bmatrix} \Sigma_{v_R} \\ \Sigma_{i_R} \\ r_{i_R} \end{bmatrix}. \tag{4.8}$$

However, I assume that there is no insight about virgin Sigma and radial length of invasion and set Σ_{v_R} and r_{i_R} equal to zero, i.e.,

$$\mathbf{m}_R = \begin{bmatrix} 0 \\ \phi\Sigma_{mf} + (1-\phi)\Sigma_m \\ 0 \end{bmatrix}. \tag{4.9}$$

Occam's inversion procedure including the modified data-weighting matrix and reference vector can be written as

$$\left[\left(\mathbf{W}_d \cdot \mathbf{J}(\mathbf{m}^k)\right)^T \cdot \left(\mathbf{W}_d \cdot \mathbf{J}(\mathbf{m}^k)\right) + \alpha^2 \mathbf{I}\right]\mathbf{m}^{k+1} = \mathbf{J}(\mathbf{m}^k)^T \left[\left(\mathbf{W}_d{}^T \cdot \mathbf{W}_d\right) \cdot \left(\mathbf{d} - G(\mathbf{m}^k) + \mathbf{J}(\mathbf{m}^k)\mathbf{m}^k\right)\right] + \alpha^2 \mathbf{m}_R^T. \tag{4.10}$$

Figure 4.4 shows the workflow used to estimate invasion-zone Sigma, virgin-zone Sigma, and radial length of invasion by iteratively calculating $\mathbf{m}^{k+1}$ and using a regularization parameter. I use the reference value for invasion-zone Sigma, Σ_{i_R}, and borehole- and diffusion-corrected Sigma logs from each detector time decay, i.e., Σ_{SSn}, Σ_{LSn}, and Σ_{Near}, to construct an initial guess for unknown model properties and to direct the solution of the inversion into the most probable region of solution space from a-priori knowledge.

The regularization parameter is chosen as a function of the unregularized cost function $F(\mathbf{m})$, i.e.,

$$\alpha = 0.01\chi^2, \text{ for } \chi^2 = \|F(\mathbf{m})\|_2^2 = \left[\mathbf{W}_d \cdot (G(\mathbf{m}) - \mathbf{d})^T\right] \cdot \left[\mathbf{W}_d \cdot (G(\mathbf{m}) - \mathbf{d})\right], \tag{4.11}$$

so that the regularization parameter is dynamically adjusted as the cost function is minimized. The impact of α on the estimation diminishes progressively as the algorithm achieves convergence.

4.2.2 Fast Jacobian Matrix Calculation

The calculation of the first-order derivatives of each of the three decays with respect to the model properties is a crucial step in the inversion algorithm. The speed of the inversion is largely dependent not only on the efficiency of the forward model, but also on the speed upon which the derivatives can be calculated. The Jacobian matrix for the multi-detector Sigma measurement in a thick piston-like invaded formation can be written as

$$\mathbf{J} = \begin{bmatrix} \dfrac{\partial \mathbf{n}_1(t)}{\partial \Sigma_v} & \dfrac{\partial \mathbf{n}_1(t)}{\partial \Sigma_i} & \dfrac{\partial \mathbf{n}_1(t)}{\partial r_i} \\ \dfrac{\partial \mathbf{n}_2(t)}{\partial \Sigma_v} & \dfrac{\partial \mathbf{n}_2(t)}{\partial \Sigma_i} & \dfrac{\partial \mathbf{n}_2(t)}{\partial r_i} \\ \dfrac{\partial \mathbf{n}_3(t)}{\partial \Sigma_v} & \dfrac{\partial \mathbf{n}_3(t)}{\partial \Sigma_i} & \dfrac{\partial \mathbf{n}_3(t)}{\partial r_i} \end{bmatrix}. \tag{4.12}$$

The easiest and fastest way to calculate the derivatives in the Jacobian matrix is to compute them from an analytical expression of the forward model. In Chapter 3, it was described that the rapid simulation model of multi-detector time decays relies on the use of a pre-calculated library of Flux-Sensitivity-Functions (FSF) and decay curves in a wide

range of materials. Chapter 3 explained that first-order perturbation theory is used to rapidly calculate detector responses to complex and realistic 3D configurations, namely

$$\mathbf{n}\left(\mathbf{r}_R,t\right)=\mathbf{n}_B\left(\mathbf{r}_R,t\right)+\mathbf{n}_B\left(\mathbf{r}_R,t\right)\int d\mathbf{r}\mathrm{FSF}\left(\mathbf{r}_R,\mathbf{r},\Sigma_{a_B}\right)\left(\frac{\Delta\Sigma_a\left(\mathbf{r}\right)}{\Sigma_{a_B}\left(\mathbf{r}\right)}\right), \tag{4.13}$$

where $\mathrm{FSF}\left(\mathbf{r}_R,\mathbf{r},\Sigma_{a_B}\right)$ is the detector-dependent FSF value at spatial location **r** integrated over the late-time interval that is used to calculate formation Sigma in a material of cross section $\Sigma_{a_B}\left(\mathbf{r}\right)$, $\mathbf{n}_B\left(\mathbf{r}_R,t\right)$ is the pre-calculated time decay in the background material, and $\mathbf{n}\left(\mathbf{r}_R,t\right)$ is the time-decay curve for a certain detector at position $\mathbf{r}_R$ after a perturbation $\Delta\Sigma_a\left(\mathbf{r}\right)$ is introduced in the material of known cross section within the volume of investigation of the detector.

In the case of piston-like invasion in a thick formation, multi-detector bulk time decays can be expressed as the weighted average of virgin and invasion-zone decays, namely,

$$\mathbf{n}\left(\mathbf{r}_R,t\right)=\left[\int_0^{r_i}\mathrm{FSF}\left(\mathbf{r}_R,\mathbf{r},\Sigma_{a_B}\right)d\mathbf{r}\right]\mathbf{n}_i\left(\mathbf{r}_R,t\right)+\left[\int_{r_i}^{\infty}\mathrm{FSF}\left(\mathbf{r}_R,\mathbf{r},\Sigma_{a_B}\right)d\mathbf{r}\right]\mathbf{n}_v\left(\mathbf{r}_R,t\right), \tag{4.14}$$

where the weight of each decay depends upon detector-specific sensitivity functions (FSFs) and on radial length of invasion. Equation 4.14 can be expressed in terms of detector-specific radial geometrical factors, *J*, defined as

$$J(r_i,\mathbf{r}_R)=\int_0^{r_i}\mathrm{FSF}\left(\mathbf{r}_R,\mathbf{r},\Sigma_{a_B}\right)d\mathbf{r}, \tag{4.15}$$

and

$$J(r_i,\mathbf{r}_R)=1-\int_{r_i}^{\infty}\mathrm{FSF}\left(\mathbf{r}_R,\mathbf{r},\Sigma_{a_B}\right)d\mathbf{r}\,. \tag{4.16}$$

Therefore,

$$\mathbf{n}\left(\mathbf{r}_\mathrm{R},t\right)=J(r_i,\mathbf{r}_R)\cdot\mathbf{n}_i\left(\mathbf{r}_R,t\right)+\left[1-J(r_i,\mathbf{r}_R)\right]\cdot\mathbf{n}_v\left(\mathbf{r}_R,t\right). \tag{4.17}$$

Figure 4.5 shows the radial geometrical factors for the LWD tool under study in a 34-p.u. freshwater saturated sandstone formation. The J factor describes the sensitivity of the bulk detector response to virgin- and invasion-zone Sigma at a given radial length of invasion. The Near detector, being shallow-sensing, is highly affected by invasion within the 15 cm closest to the borehole wall. The LSn detector, being deeper-sensing, is less affected by shallow invasion. Equation 4.17 is the analytic form of the fast-forward model used to simulate multi-detector decays in piston-like invaded, thick formations. However, the analytical form requires radial length of invasion, r_i, explicitly expressed to calculate the partial derivatives necessary for the calculation of the Jacobian matrix. I approximate the radial geometrical factor in terms of a fitted third-degree polynomial specific for each detector, i.e.,

$$J(r_i,\mathbf{r}_R)=a(\mathbf{r}_R)r_i^3+b(\mathbf{r}_R)r_i^2+c(\mathbf{r}_R)r_i+d(\mathbf{r}_R), \tag{4.18}$$

where $a(\mathbf{r}_R)$, $b(\mathbf{r}_R)$, $c(\mathbf{r}_R)$, and $d(\mathbf{r}_R)$ are detector-specific constants that need to be updated at each iteration as a consequence of the FSFs' dependency on the model properties, **m**. The fast-forward model can then be expressed as

$$\begin{aligned}\mathbf{n}\left(\mathbf{r}_R,t\right)=&\left[a(\mathbf{r}_R)r_i^3+b(\mathbf{r}_R)r_i^2+c(\mathbf{r}_R)r_i+d(\mathbf{r}_R)\right]\cdot\mathbf{n}_i\left(\mathbf{r}_R,t\right)+\\&\left(1-a(\mathbf{r}_R)r_i^3-b(\mathbf{r}_R)r_i^2-c(\mathbf{r}_R)r_i-d(\mathbf{r}_R)\right)\cdot\mathbf{n}_v\left(\mathbf{r}_R,t\right)\end{aligned}, \tag{4.19}$$

Equation 4.19 enables the analytical calculation of the first-order derivatives in the Jacobian matrix. The derivatives for each detector response as a function of the model properties Σ_v, Σ_i, and r_i, are given by

$$\frac{\partial \mathbf{n}(\mathbf{r}_R,t)}{\partial \Sigma_v} = \left(1 - a(\mathbf{r}_R) r_i^3 - b(\mathbf{r}_R) r_i^2 - c(\mathbf{r}_R) r_i - d(\mathbf{r}_R)\right) \cdot \left. \frac{\partial \mathbf{n}(\mathbf{r}_R,t)}{\partial \Sigma} \right|_{\Sigma_v}, \tag{4.20}$$

$$\frac{\partial \mathbf{n}(\mathbf{r}_R,t)}{\partial \Sigma_i} = \left[a(\mathbf{r}_R) r_i^3 + b(\mathbf{r}_R) r_i^2 + c(\mathbf{r}_R) r_i + d(\mathbf{r}_R) \right] \cdot \left. \frac{\partial \mathbf{n}(\mathbf{r}_R,t)}{\partial \Sigma} \right|_{\Sigma_i}, \tag{4.21}$$

and

$$\frac{\partial \mathbf{n}(\mathbf{r}_R,t)}{\partial r_i} = \left[3a(\mathbf{r}_R) r_i^2 + 2b(\mathbf{r}_R) r_i + c(\mathbf{r}_R) \right] \cdot \left(\mathbf{n}_i(\mathbf{r}_R,t) - \mathbf{n}_v(\mathbf{r}_R,t) \right). \tag{4.22}$$

4.3 Interpretation of Synthetic Time Decays

It is useful to generate synthetic data with known properties and realistic noise to study the reliability and accuracy of the inversion before applying it to real field data. In this section, I first study the inversion solution's sensitivity to the reference value for invasion-zone Sigma. I then develop a framework for applying realistic statistical noise to synthetic data, and I use multiple realizations of identical synthetic cases to evaluate the stability of the inversion and its uncertainties.

4.3.1 Impact of Invasion-Zone Sigma, Σ_i, on Estimated Virgin-Zone Sigma and Radial Length of Invasion

The impact of the initial guessed invasion-zone Sigma on virgin-zone Sigma varies according to the contrast between invasion-zone and virgin-zone Sigma and the radial length of invasion. **Figure 4.6** describes how a relative error on the reference value for invasion-zone Sigma, $\Delta\Sigma_i / \Sigma_i$, affects the relative error on the solution for virgin-zone Sigma, $\Delta\Sigma_v / \Sigma_v$, as determined by applying relative perturbations to Σ_i in the range of 0 to 40 % to cases including several radial lengths of invasion in the range of 0 to 25.4 cm and looking at the relative difference between estimated and actual virgin-zone Sigma Σ_v. To completely isolate the impact of the guessed Σ_i value, I did not add noise to these synthetic examples.

High Sigma contrast is desirable to estimate radial length of invasion; however, comparison of panels (a) and (b) in **Figure 4.6** suggests that the smaller the difference in salinity between original formation fluid and mud filtrate, the smaller the impact of the presence of filtrate in the near-wellbore zone. Note in panels (c) and (d) in **Figure 4.6** that the impact of the guessed invasion-zone Sigma is higher on estimated radial length of invasion that on estimated virgin-zone Sigma. This situation is desirable because the most important objective of the inversion is to correct formation Sigma for invasion effects to calculate water saturation in the most accurate manner.

Errors on radial length of invasion are smaller at intermediate depths because in this region the radial sensitivities of the detectors differ the most and, therefore, the three measurements are highly independent and can tolerate better the presence of noise and errors on guessed Σ_i. Note that the impact of the perturbation at deep radial lengths of invasion shows high variability and does not necessarily increase as the perturbation increases. The reason is that even without perturbing Σ_i, it is harder to define Σ_v and r_i as radial length of invasion increases. Additionally, for small perturbations on Σ_i, it can be more difficult for the algorithm to distinguish between actual and perturbed values, resulting in high errors on the estimations. If the perturbation is significantly off the actual Σ_i, at deep radial lengths of invasion, the algorithm is forced to adjust Σ_i to achieve convergence.

Figure 4.6 underscores the importance of having an accurate estimate for invasion-zone Sigma to use as a reference value. Even though the guess on invasion-zone Sigma can have a significant impact on the inversion, not correcting for invasion effects at all can lead to highly inaccurate estimations of virgin-zone Sigma. **Figure 4.7** shows the impact of piston-like invasion of mud filtrate on one-detector (SSn) formation Sigma at various Sigma contrasts and radial lengths of invasion. The figure describes the relative error on virgin Sigma induced by using one-detector Sigma and not correcting the measurement for shallow invasion effects. Notice that errors within 10% in virgin Sigma are expected for shallow radial lengths of invasion and also that the error increases up to 40% for invasion

up to 15-cm deep; the error is slightly sensitive to filtrate salinity in this region. However, the impact of invasion deeper than 15 cm on virgin Sigma is strongly dependent on filtrate salinity.

4.3.2 Noise on Synthetic Multi-Detector Time Decays

The counting of random nuclear events follows a Poisson distribution and is characterized by mean value, μ, and standard deviation, $\sigma_{realizations} = \sqrt{\mu}$. Accordingly, if N counts are expected within a certain time bin in a decay measurement, the standard deviation of the actual counts measured in an ensemble of realizations or experiments will be $\sqrt{N}$ (Lyons, 1986). The expected counts in the decay curves at each depth depend on the logging environment and the speed at which they are measured, and therefore so do their statistical noise. I apply Poisson counting statistics to generate realistic noise on the expected count rates as follows:

$$CR_i = CR_i^0 + \delta CR_i \ , \tag{4.23}$$

where $\delta CR_i = \lambda \cdot \frac{CR_i^0}{\sqrt{CR_i^0 \cdot AT \cdot DF}}$, and $AT = \frac{SD \cdot N_{filter}}{ROP}$.

CR_i^0 is the expected decay signal without noise in time bin i, δCR_i is the signal noise for one realization, λ is a random number from a standard normal distribution, AT is acquisition time (s), DF is duty factor for each time-bin (the fraction of the total acquisition time that the detector spends counting in a given time bin), SD is the sampling

interval (typically 15.24 cm), ROP is penetration rate (cm/s), and N_{filter} is the number of sampling intervals that are averaged to improve decay statistics. **Figure 4.8** shows random generated noise and fractional uncertainty, **f**, on time decays simulated in a 10-c.u. material for *ROP* of 0.17 cm/s (20 fph) and 1.7 cm/s (200 fph). Notice that the LSn gamma-ray detector and the late time component of the thermal-neutron Near detector are the sectors of the multi-detector signal that are more affected by statistical noise because of lower count rates.

4.3.3 Multiple Realization Study

In this section I evaluate the performance of the 1D inversion model in configurations with virgin- and invasion-zone Sigma contrasts in the range of 5 to 25 c.u., and various radial lengths of invasion for conductive invasion profiles ($\Sigma_v < \Sigma_i$). First, I generate 200 synthetic multi-detector decays for various fixed values of invasion into the formation, where the formation properties are listed in **Table 4.1**. In each new realization, the decays receive randomly generated noise as described by equation 4.23 and corresponding to *ROP* = 0.254 cm/s (30 fph). The nuclear properties in **Table 4.1** were generated using SNUPAR. Next, I perform 1D multi-detector decay inversions to obtain distributions of estimated properties and assess the repeatability of the results.

Figure 4.9 shows the mean values of virgin Sigma and radial length of invasion solved in the 200 realizations of each invasion length as a function of true radial length of invasion. The error bars indicate the standard deviation of the 200 realizations for each

point. Notice that the performance of the inversion routine is better for shallow radial lengths of invasion and reflects the shallow nature of the Sigma measurement. As radial length of invasion increases, the three detectors of the LWD tool lose sensitivity to the virgin zone and the error bars on virgin-zone Sigma increase. Simultaneously, the statistical noise in the decays increases as radial length of invasion increases because the tool progressively senses more the high-Sigma fluid in the invasion zone and less the low-Sigma fluid in the virgin-zone, i.e., the total number of counts in the time bins decreases with increased radial length of invasion. Therefore, the error bars on radial length of invasion also increase as salty mud filtrate invades deeper into the formation.

Low Sigma contrast makes the multi-detector inversion problem non-unique, i.e., the shape of decays can be considerably similar regardless of radial length of invasion. This is evidenced in **Figure 4.9** by the large size of the error bars in the 5-c.u. Sigma contrast case. The performance of the inversion in solving for radial length of invasion is particularly poor in cases where virgin- and invasion-zone Sigma contrast is low. Luckily, as shown in **Figure 4.6**, the effect of mud-filtrate invasion on virgin Sigma in this case is small and therefore; the inversion to correct for invasion effects is not necessary.

Quantification of uncertainty and stability is a crucial part of the inversion problem. As previously mentioned, the error bars in **Figure 4.9** are computed from the standard deviation of multiple realizations of an identical synthetic case with statistical noise. However, another method to estimate error bars is necessary for the inversion of field data in order to indicate the precision of the results. I use a modification of the so-called

covariance approach to evaluate error bars in nonlinear inverse problems. The weighted misfit vector can be expressed as

$$\boldsymbol{\zeta} = \mathbf{W}_d \cdot \left[\mathbf{d} - G(\mathbf{m}) \right], \tag{4.24}$$

and the standard deviation of the weighted noise is

$$s = \frac{\left\| \boldsymbol{\zeta} \right\|_2}{\sqrt{\nu}}, \tag{4.25}$$

where ν is the number of degrees of freedom.

The covariance matrix is modified to include the data-weighting matrix, $\mathbf{W}_d$, to account for the higher importance at the late time part of the signals in the measurement vector, namely

$$\mathbf{Cov(m)} = s^2 \cdot \left[\left(\mathbf{W}_d \cdot \mathbf{J} \right)^T \cdot \left(\mathbf{W}_d \cdot \mathbf{J} \right) \right]^{-1}, \tag{4.26}$$

and the standard deviation of the estimations can be written as

$$\boldsymbol{\sigma} = diag(\mathbf{Cov}(\mathbf{m}))^{1/2}. \tag{4.27}$$

Calculation of error bars using the method just described is only reliable when the distribution of the estimated properties follows a normal distribution. In the multiple realization study I noted that the multi-detector decay problem can be rendered unstable under certain conditions, such as deep invasion and/or low Sigma contrast. To ascertain when the estimations for an invasion problem do fall within the standard deviation given by equation 4.27, I propose the use of an index to set red flags in cases where the problem lacks stability. I introduce a “Confidence Index” defined as

$$CI = \frac{w}{1.96\sigma_{realizations}}, \tag{4.28}$$

where w is the test statistic in the Shapiro-Wilk normality test (Shapiro and Wilk, 1965), and $1.96\sigma_{realizations}$ is the 95% confidence interval in the estimated properties. **Figure 4.10** shows *CI* as a function of radial length of invasion and virgin- and invasion-zone Sigma contrasts in the range between 5 c.u. and 25 c.u. calculated from the distribution of estimated Σ_v and r_i in the multiple realization study described in the previous section.

The confidence index is meant to be used as an additional appraisal tool to the rigorous covariance-based method for error bar calculation. The calculation of error bars using the covariance matrix is only appropriate when the problem is stable and the solution converges to a normal distribution around a mean value. However, cases such as low virgin- and invasion-zone Sigma contrast are non-unique for multi-detector decay inversions, even though the size of the estimated error bar can be small for a particular realization. The confidence index, then, becomes a red flag to the novice user in those cases where uncertainty should be expected due to non-uniqueness in the estimation.

In the following sections I test the inversion algorithm on several synthetic and test pit examples and on field measured multi-detector time decays to assess the reliability of the multi-detector decay inversion, and also to evaluate the limitations of the method in realistic conditions of formation evaluation.

4.4 LABORATORY RESULTS

The inversion algorithm is tested in measurements acquired in the laboratory test pit described in Chapter 3 at piston-like radial lengths of invasion of 0 cm, 5.08 cm, 10.16 cm, and 38.1 cm (0 in, 2 in, 4 in, and 15 in). Piston-like invasion is emulated in the laboratory by using the formation shown in **Figure 4.11**, which has 1-mm steel liners arranged at different radii to separate invasion and virgin zones. In this example, the virgin zone is fresh water saturated (Σ_v = 10.4 c.u.) sandstone, and the invasion zone is 200-kppm [NaCl] saturated (Σ_i = 36.2 c.u.) sandstone. The measurement is a good example of an experimental setting to mimic piston-like invasion; even so, nuclear measurements acquired in this pit are affected by the presence of the high-absorbing steel of the liners.

The presence of steel liners in the test pit increases the slope of the measured time decay when compared to the fast-forward decay curves that do not include the liners. The thin steel sheets cannot be simulated using the forward model because of the coarse nature of the spatial grid in the model (2.54-cm radial spacing). Therefore, virgin Sigma estimated from the inversion algorithm is expected to be a few capture units above the real virgin intrinsic Sigma. **Figure 4.12** shows reconstructed time decays and estimated virgin Sigma and radial length of invasion for measurements acquired at the four radial lengths of invasion mentioned above. Estimated properties and actual test-pit properties are shown at the top left and bottom right of each panel, respectively. Uncertainties for the estimated properties were calculated using the covariance method in equation 4.27.

Figure 4.12 shows that the inversion algorithm reconstructs fairly well the signals and accurately estimates radial length of invasion. However, virgin-zone Sigma is significantly biased with respect to the actual value. The reason is, as previously mentioned, that the presence of steel liners affects the estimated value of virgin Sigma. On the other hand, the estimated radial length of invasion is close to the position of the liner in the test pit. The objective of this example is to assess whether the fast-forward model embedded within the inversion routine reliably reproduces the shape of the actual tool measured decays, which is largely determined by complex detector-specific borehole and diffusion effects.

4.5 SYNTHETIC RESULTS

In this section I use two synthetic examples to demonstrate time decay fits and inverted solutions for virgin Sigma and radial length of invasion. The synthetic examples include high-salinity mud filtrate invading a hydrocarbon saturated formation, known as conductive invasion, which is the ideal case for application of multi-detector Sigma. They also include the case of oil-based mud invading a brine-bearing formation, known as resistive invasion, and a low Sigma contrast case to display the limitations of the model. Simulated LWD neutron and density logs are displayed in both examples for the Longhorn LWD tool (Mendoza et al., 2010a ; Ijasan et al., 2013a).

4.5.1 Synthetic Case I

Synthetic Case I considers the inversion of multi-detector decays across a sequence of thick homogeneous 30-p.u. gas-bearing sandstone formations invaded by 200-kppm [NaCl] brine with noise corresponding to logging at 0.25 cm/s (30 fph). **Table 4.2** shows the properties of the invasion and virgin zones in the sequence, which were generated using SNUPAR. The top layer is not invaded and piston-like invasion progressively increases downwards 2.54-cm at a time. The bottom layer is fully invaded, while the virgin zone in all other layers is gas-saturated, S_w = 3%.

Figure 4.13 shows the actual radial invasion profile throughout the sequence, reconstructed multi-detector decays, simulated neutron/density porosity logs in a sandstone matrix, and borehole- and diffusion-corrected multi-detector Sigma logs. The overall match between synthetic and reconstructed time decays is satisfactory. Notice that the match in the SSn time decay is not as good (the left-most decays of track (b)); however, this does not necessarily mean that the estimation of virgin Sigma and radial length of invasion is not correct. Since there exist three detector decays and the purpose is to estimate only two unknown parameters, the algorithm is able to closely estimate the right configuration, especially at intermediate radial lengths of invasion and high Sigma contrast, which is the case in the section of the mismatch in SSn time decays.

Figure 4.13 also displays the incorrect separation in borehole- and diffusion-corrected Sigma logs at the top uninvaded formation on track (d), which results from the error associated with deriving an environmentally corrected intrinsic formation Sigma from

apparent Sigma from time decay curves. Any algorithm that were to estimate invasion from only the separation of borehole- and diffusion-corrected Sigma logs in the top layer, as proposed by other available multi-detector Sigma interpretation methods, would incorrectly estimate some amount of invasion, when there is not actual invasion and the three Sigma logs display different values only as a consequence of the diffusion correction, which is not perfect. I will show how the inversion algorithm can avoid relying on these environmental corrections and accurately identify the lack of invasion in the top layer.

Figure 4.14 shows estimated and actual virgin Sigma and reconstructed apparent Sigma logs for the SSn, LSn, and Near detectors, (a), (b), and (c), respectively. Borehole- and diffusion-corrected Sigma logs are shown on track (d). The figure also shows estimated and actual radial length of investigation (e), a sketch of the borehole, invasion profile and formation (f), and estimated water saturation derived from Sigma not corrected and corrected (through the 1D radial inversion) for invasion effects (g).

Figure 4.14 reveals two important aspects of the inversion: first, the impact of the mismatch on the reconstructed time-decays, which is reflected in a mismatch in apparent Sigma logs in track (a) and (b) at some depths, affects mostly the estimated radial length of invasion in track (e) and not the estimated virgin Sigma shown in tracks (a), (b) and (c). Observe that the match of the decays is excellent in the Near detector, good in the LSn detector, and it is only off in the SSn detector mostly at intermediate radial lengths of invasion. Nonetheless, the inversion always allows to assess whether there is invasion or not, and always gives a sense of the radial extension of the invasion front that allows to

better understand other shallow-sensing nuclear logs. For instance, I observe that the estimated invasion profile enables understanding the loss of neutron-density crossover in a gas-bearing formation with minimum irreducible water saturation in panel (c) in **Figure 4.13**.

The second important aspect in **Figure 4.14** is that the algorithm is accurate in estimating actual formation virgin Sigma in the presence of shallow invasion and this corrected Sigma significantly improves the estimation of Sigma-derived water saturation shown in track (g). Notice on panel (g) in **Figure 4.14** how using the short-spaced gamma-ray detector (SSn) Sigma alone to calculate water saturation leads to water saturation values notably different from the actual ones. Water saturation calculated from Sigma corrected for invasion effects using the inversion algorithm follows closely the actual water saturation of the model. The multi-detector time-decay inversion can correctly converge to the true formation Sigma for most radial lengths of invasion in the sequence, even up to 25 cm deep. However, as expected, at radial lengths of invasion larger than 25 cm the three detectors are less sensitive to the virgin zone, and virgin Sigma and water saturation begin to deviate from the actual model properties.

I indicate the uncertainty of the inversion using both covariance-based error bars and color flags derived from the Confidence Index shown in equation 4.28. Color flags reflect the increase in possible instability of the inversion as radial length of invasion increases, regardless of the size of the error bars. Error bars reflect both the presence of noise in the measured decays, the goodness of the time-decay reconstruction, and the

sensitivity of the multi-detector inversion at the estimated parameter solution. The error bars are small in this example because the contrast between invasion- and virgin-zone Sigma is large, which enhances the uniqueness of the problem at each radial length of invasion, and because the algorithm fits the multi-detector decays fairly well except for the SSn decays in some cases. The error bars are somewhat larger in the mid sections where the SSn time-decay reconstruction was poor.

4.5.2 Synthetic Case II

Synthetic Case II aims to test the ability of the inversion scheme to handle cases such as resistive and conductive invasion profiles, and low virgin- and invasion-zone Sigma contrasts to estimate radial length of invasion, virgin formation Sigma, and ultimately, water saturation throughout a sequence. **Figure 4.15** shows the invasion profile, synthetic decays with noise corresponding to logging at 0.25 cm/s (30 fph), simulated LWD neutron and density porosity logs in a sandstone matrix with neutron/density crossover affected by invasion and matrix effects, borehole- and diffusion-corrected Sigma logs, and volumetric mineral and fluid composition of the rocks in the sequence. The sequence represents a typical in-situ fluid distribution with gas, oil, and capillary-bound water. This sequence bears gas at the top and oil at middle depths. Water saturation shows a capillary transition toward the water leg at the bottom. Notice the presence of a gas porosity crossover at the top masked by the presence of deep invasion and clay content at the second and third top layers. **Table 4.3** describes the properties assumed for the layered formations, which were generated using SNUPAR.

Figure 4.16 shows actual and estimated virgin-zone Sigma with error bars and reconstructed apparent Sigma logs for the SSn, LSn, and Near detectors, labeled (a), (b), and (c), respectively. Borehole- and diffusion-corrected Sigma logs are shown on track (d), and actual and estimated radial length of invasion with error bars are shown on track (e). The figure additionally shows a sketch of borehole, invasion, and formation (f), and the true water saturation compared to the saturation derived from the SSn Sigma log and from the 1D radial inversion (g) for Synthetic Case II. Tracks (a) through (c) describe the excellent match between actual and reconstructed time decays, which translates into excellent match in apparent Sigma for the three detectors and accurate estimations of virgin Sigma even in deeply invaded layers and in sections with low Sigma contrast. Observe in track (d) that Near Sigma is higher than SSn Sigma, which is higher than LSn Sigma at the top of the sequence, indicating shallow invasion of high-Sigma (66.7 c.u., 123 NaCl kppm) WBM into low-Sigma gas-bearing rocks. However, the order of the Sigma logs is interchanged at the bottom of the sequence, reflecting the invasion of the 123-kppm [NaCl] WBM into the higher salinity water leg (97 c.u., 195 kppm). Even though WBM has a considerable amount of salt which would ideally generate a significant Sigma contrast in the oil-bearing zone, the presence of salty connate water increases the average virgin Sigma value in oil-bearing zones, such that the virgin- and invasion-zone Sigma contrast in the middle section is poor.

The distance between the dashed black and blue solid lines in **Figure 4.16** on tracks (a) through (c) indicate Sigma contrast throughout the sequence. Observe that Sigma

contrast is especially low at the top of the water leg (track (e) at 30 m), so that the estimation of radial length of invasion is poor only in this section. The size of the error bars and *CI* color flags warn the user about the high uncertainty of inversion results in these low Sigma contrast zones. Notice also the agreement between error bar size and *CI*; the deeper the invasion front, the lesser the sensitivity of the detectors to the virgin zone. This behavior results in larger error bars and low *CI* as radial length of invasion increases.

Virgin Sigma corrected for invasion effects leads to more accurate calculations of water saturation. Note on panel (g) in **Figure 4.16** that the correction is especially important in the conductive-invasion zones at the top gas section, and in the resistive-invasion zones at the bottom brine leg because in these zones there is a significant contrast between the absorption properties of in-situ and invasion fluids. At the middle section, the correction does not have an important effect because the average Sigma of the oil section is close to Sigma of the invasion zone. Calculating water saturation using the conventional one gamma-ray detector approach (SSn), leads to overestimation of water saturation in the gas zone (as much as 33%), and underestimation of water saturation below the free water level (as much as 27%).

4.6 FIELD RESULTS

The field case applies the 1D radial inversion to assess the presence of shallow invasion in a high-porosity, gas-bearing formation drilled with synthetic-based mud (SBM), and to correct the measurement for possible shallow-invasion effects. SBM salinity is 77 kppm [NaCl equivalents] in the borehole and filtrate salinity is 136 [NaCl equivalents]

kppm as reported from mud filtration tests. The density-derived borehole size log indicates that the borehole is smooth and there are no significant tool standoffs. Therefore, any major difference in the Sigma detectors' response might be an indication of shallow invasion; LSn and Near decays indicate the presence of statistical noise; SSn decays are smooth due to their higher count rate.

Figure 4.17 shows reconstructed multi-detector decays in a 10-ft gas section; the time decay fit is satisfactory and the algorithm properly accounts for the presence of statistical noise. **Figure 4.18** shows inversion results obtained for the 10-ft gas section: borehole- and diffusion-corrected Sigma logs and reference invasion-zone Sigma (a), estimated virgin-zone Sigma with error bars and *CI* (b), estimated radial length of invasion with error bars and *CI* (c), sketch of borehole, invasion profile and formation (d), neutron-porosity, gamma-gamma density-porosity and neutron-gamma density-porosity logs (e), phase resistivity logs (f), and SSn-Sigma derived, resistivity-derived, and 1D radial inversion derived water saturation (g). To estimate water saturation, I calculated connate water salinity equal to 140 kppm [NaCl] by matching the SSn Sigma and high-frequency shallow phase resistivity logs (P16H) in a clean sandstone section.

The estimation of radial length of invasion allows to better understand the behavior of other shallow-sensing nuclear measurements such as neutron and density logs. Notice how the largest separation between neutron and density porosity logs in (e) coincides with the uninvaded zone at the center of the formation in (d) and how neutron and density logs become closer when water saturation or radial length of invasion increase. Sigma-derived

water saturation shows more deflections than resistivity-derived water saturation because of the smaller volume of investigation of Sigma compared to resistivity measurements. Shoulder-bed effects are not regarded as significant because the thickness of the gas formation is larger than the spacing between the pulsed-neutron source and the long-spaced detector. Nonetheless, the model presented in this chapter does not consider the geometrical effects on measured decays due to the relative angle between well and the formations.

4.7 DISCUSSION

Interpretation of Sigma logs is important in formation evaluation because they can be used to calculate water saturation in environments where resistivity log interpretation is challenging. The accuracy in bulk calculated Sigma is important, especially in low-porosity, low-connate water salinity environments. But bulk formation Sigma can be highly affected by the presence of mud filtrate in the near-wellbore zone. Despite the common belief that invasion does not take place prior to the acquisition of LWD measurements, it has been shown that invasion can take place between inches and up to even several feet into the formation. Nuclear time-decay measurements are shallow-sensing and are therefore highly affected by shallow invasion that typically occurs in LWD conditions. Whenever invasion occurs between 0 and approximately 20 cm, the measurement can be corrected by using three nuclear decay measurements, each affected to a different degree by invasion, to estimate the actual virgin formation bulk Sigma. The correction of formation Sigma for shallow invasion leads to a more accurate calculation of water

saturation. Recent studies attempted such correction using borehole- and diffusion-corrected Sigma logs. However, the correction affects the separation of the curves and might, therefore, lead to inaccurate interpretations. Presence of shoulder-bed effects on the measurement can generate inaccurate results in those methods as well as in the method proposed in this chapter. The coupled effect of invasion and shoulder beds will be discussed in the following chapter.

4.8 CONCLUSIONS

I developed a nonlinear gradient-based algorithm to invert multi-detector LWD thermal-neutron and gamma-ray time decays in mud-filtrate invaded hydrocarbon-bearing formations. The algorithm enables the estimation of formation Sigma, free of invasion effects, as well as radial length of invasion. I tested the method to ascertain its reliability in a set of multiple realizations with random noise at different radial lengths of invasion and virgin- and invasion-zone Sigma contrasts. The distribution of the estimations from a multiple realization study was used to calculate a Confidence Index (*CI*) that was used together with covariance-based error bars to estimate the uncertainty of model estimations.

Results indicate that the method is especially useful to assess radial length of invasion, correct formation Sigma for invasion effects, and accurately calculate resistivity-independent water saturation from LWD Sigma logs in shallow-invaded formations. If there is only a small difference between the salinity of drilling mud and formation fluid, and/or if the rock has low porosity, the contrast in Sigma between virgin and invasion zones is not sufficient to assess invasion. Fortunately, in these cases the inversion to correct for

invasion is not necessary. Additionally, the method is to be used to isolate invasion effects in thick formations, because this 1D implementation of the inversion cannot simultaneously account for combined invasion and shoulder-bed effects. The multi-detector Sigma inversion method is ideally suited to improve the petrophysical evaluation of high-porosity, hydrocarbon-bearing formations invaded by salty mud filtrate.

Inversion of multi-detector decays provides additional information to the one derived from interpretation of other borehole measurements. Results in a synthetic example indicate that calculating water saturation using the conventional approach with a single gamma-ray detector (SSn) leads to overestimation of water saturation in a gas zone (as much as 33%), and underestimation of water saturation in a water level (as much as 27%) if the Sigma is not corrected for shallow-invasion effects. Interpretation of a field example demonstrated how quantification of shallow-invasion effects allows better understanding of the behavior of neutron-density log crossover in hydrocarbon-bearing formations invaded by mud filtrate. The field example also demonstrated how the improved vertical resolution of the Sigma log compared to resistivity enables to identify local variations in water saturation which are averaged by resistivity measurements. Next chapters will include the correction for shoulder-bed and well-deviation effects, as well as the combination of the inversion outputs with other LWD measurements for comprehensive petrophysical assessment.

Table 4.1: Summary of petrophysical properties assumed for the virgin and invasion zone materials corresponding to synthetic decays used for inversion in **Figure 4.13**. Filtrate salinity is 200 [NaCl] kppm and filtrate Sigma is 98 c.u.

Lithology	**In-situ fluid**	**Porosity (p.u.)**	**Migration length (cm)**		**Intrinsic Sigma (c.u.)**		
			Virgin L_{m_v}	**Invaded** L_{m_i}	**In-situ fluid** Σ_f	**Virgin** Σ_v	**Invaded** Σ_i
Sandstone	Oil	34	15.17	14.38	21.6	10.4	36.2

Table 4.2: Summary of petrophysical properties assumed for the virgin- and invasion-zone materials corresponding to synthetic decays used for Synthetic Case I. Filtrate salinity is 200 [NaCl] kppm and filtrate Sigma is 98 c.u.

Lithology	**In-situ fluid**	**Porosity (p.u.)**	**Migration length, (cm)**		**Intrinsic Sigma, (c.u.)**			**Water Saturation** S_w
			Virgin L_{m_v}	**Invaded** L_{m_i}	**In-situ fluid** Σ_f	**Virgin** Σ_v	**Invaded** Σ_i	
Sandstone	Gas	30	26.8	15.3	7.0*	5.3	30.1	0.03

*Gas Sigma calculated at 24131.65 kPa (3500 psia) and 150 ^{o}F.

Table 4.3: Summary of petrophysical properties assumed for the virgin- and invasion-zone materials corresponding to layered formations in Synthetic Case II. Gas Sigma and density are 5.7 c.u. and 0.14 g/cm^3, respectively, at 150 ^{o}F and 24131.65 kPa (3500 psia). Oil (87% Carbon, 13% Hydrogen) Sigma and density are 21.26 c.u. and 0.82 g/cm^3, respectively. Drilling fluid is 123-kppm [NaCl] WBM, and filtrate Sigma, $\Sigma_{mf,}$ is 66.7 c.u.

Layer	**Thickness (cm)**	**Porosity (p.u.)**	**Mineral volumetric fractions, (v/v)**			**In-situ fluid saturations, (v/v)**			**Intrinsic Sigmas, (c.u.)**			**Radial length of invasion (cm)** r_i
			quartz	**calcite**	**clay**	**oil** S_o	**gas** S_g	**water** S_w	**virgin** Σ_v	**invaded** Σ_i	**matrix** Σ_m	
1	243.8	21	0.68	0.1	0.01	0	0.95	0.05	6.2	18.1	5.2	10.2
2	243.8	30	0.04	0.44	0.22	0	0.92	0.08	13.9	30.1	12.7	15.2
3	243.8	28	0.16	0.3	0.26	0	0.9	0.1	15.0	29.5	13.7	20.3
4	243.8	30	0.56	0.07	0.07	0	0.88	0.12	10.2	25.2	6.5	10.2
5	243.8	28	0.6	0	0.12	0	0.88	0.12	11.0	25.1	8.1	15.2
6	243.8	26	0.29	0	0.45	0	0.86	0.14	19.9	32.5	19.1	7.6
7	243.8	21	0.36	0.43	0	0	0.85	0.15	8.7	18.7	5.9	12.7
8	243.8	27	0.62	0.09	0.02	0	0.82	0.18	10.0	22.1	5.1	17.8
9	243.8	29	0	0.13	0.58	0.8	0	0.2	29.3	38.1	23.7	5.1
10	243.8	25	0.59	0.16	0	0.76	0	0.24	13.6	20.5	4.8	10.2

Table 4.3 (continued):

11	243.8	27	0	0.2	0.53	0.71	0	0.29	29.3	35.7	22.4	5.1
12	243.8	27	0.59	0.05	0.09	0.67	0	0.33	18.3	23.8	7.3	10.2
13	243.8	29	0.55	0.01	0.15	0.65	0	0.35	21.0	26.5	9.0	12.7
14	243.8	25	0.45	0.23	0.07	0.61	0	0.39	18.5	22.5	7.3	7.6
15	243.8	27	0.32	0.1	0.31	0.56	0	0.44	26.4	29.7	14.8	12.7
16	243.8	24	0.69	0.01	0.06	0.4	0	0.6	21.0	21.0	6.3	15.2
17	243.8	21	0.14	0.19	0.46	0.2	0	0.8	33.3	30.1	20.4	17.8
18	243.8	24	0.07	0.38	0.31	0	0	1	35.8	28.5	15.8	7.6
19	243.8	22	0.07	0.28	0.43	0	0	1	36.8	30.2	19.6	5.1
20	243.8	22	0.05	0.28	0.45	0	0	1	37.3	30.7	20.3	10.2
21	243.8	30	0.68	0.01	0.01	0	0	1	32.5	23.5	4.4	15.2
22	243.8	25	0.17	0.48	0.1	0	0	1	31.5	23.9	9.1	20.3
23	243.8	28	0.68	0.03	0.01	0	0	1	30.7	22.3	4.5	15.2
24	243.8	29	0.52	0.18	0.01	0	0	1	32.0	23.3	5.0	7.6

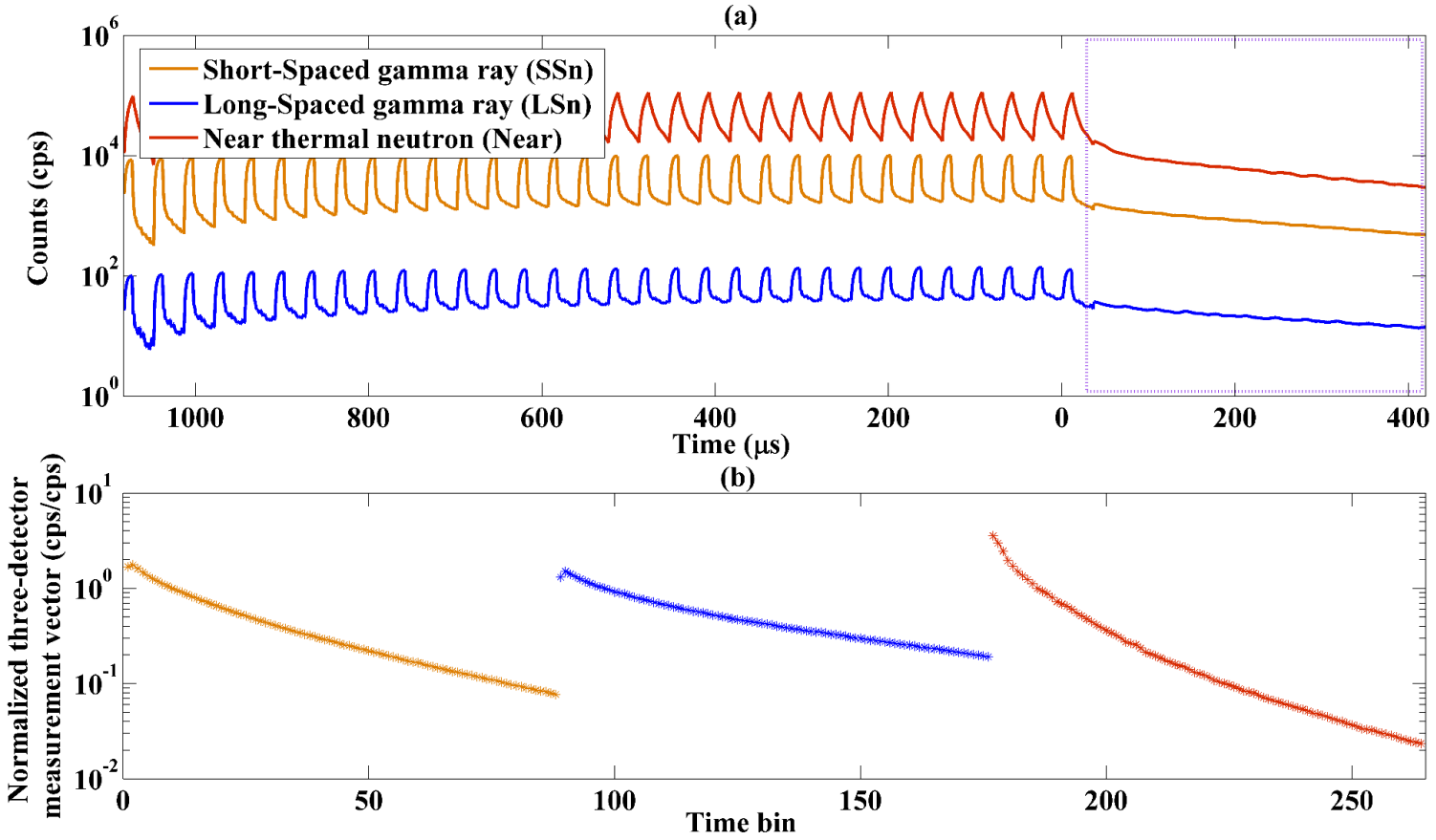

Figure 4.1: (a) Synthetic decays for the 32 pulses of the pulsed-source LWD tool under study for the case of 34-p.u. fresh-water bearing sandstone invaded 12.7-cm (5-in) deep by 200-kppm [NaCl] WBM, and (b) portion of the actual time decays used for Sigma calculation and defined as the measurement vector, **d,** in this dissertation (corresponds to the portion of the signal inside the dashed square at the top).

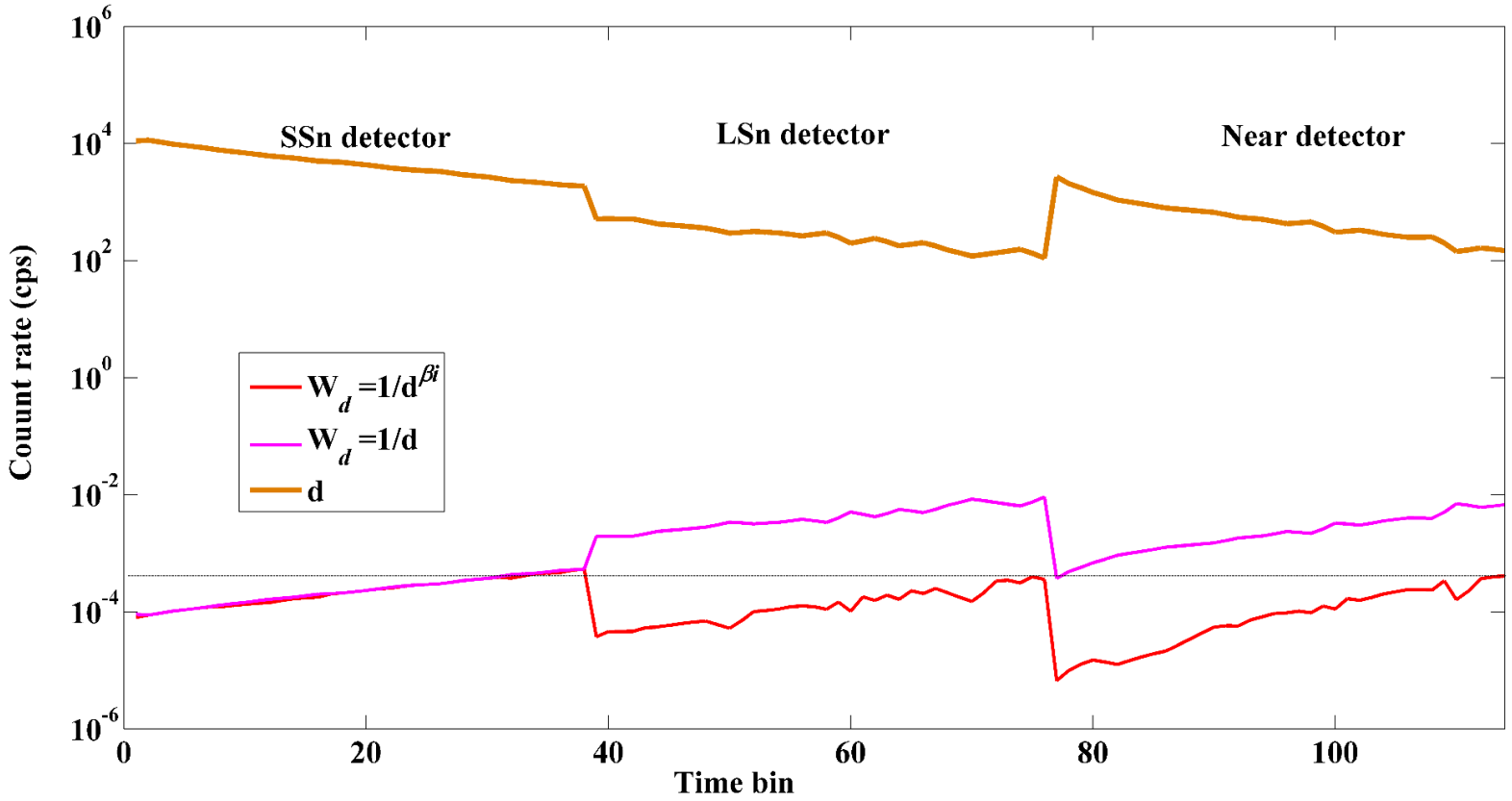

Figure 4.2: Data vector, **d**, for one measurement of the multi-detector LWD Sigma tool (burnt-orange solid line) and corresponding relative (magenta solid line) and modified (red solid line) diagonals of the data weight matrix, $\mathbf{W}_d$. The dashed horizontal black line indicates the similar importance assigned to the late-time components of the three signals.

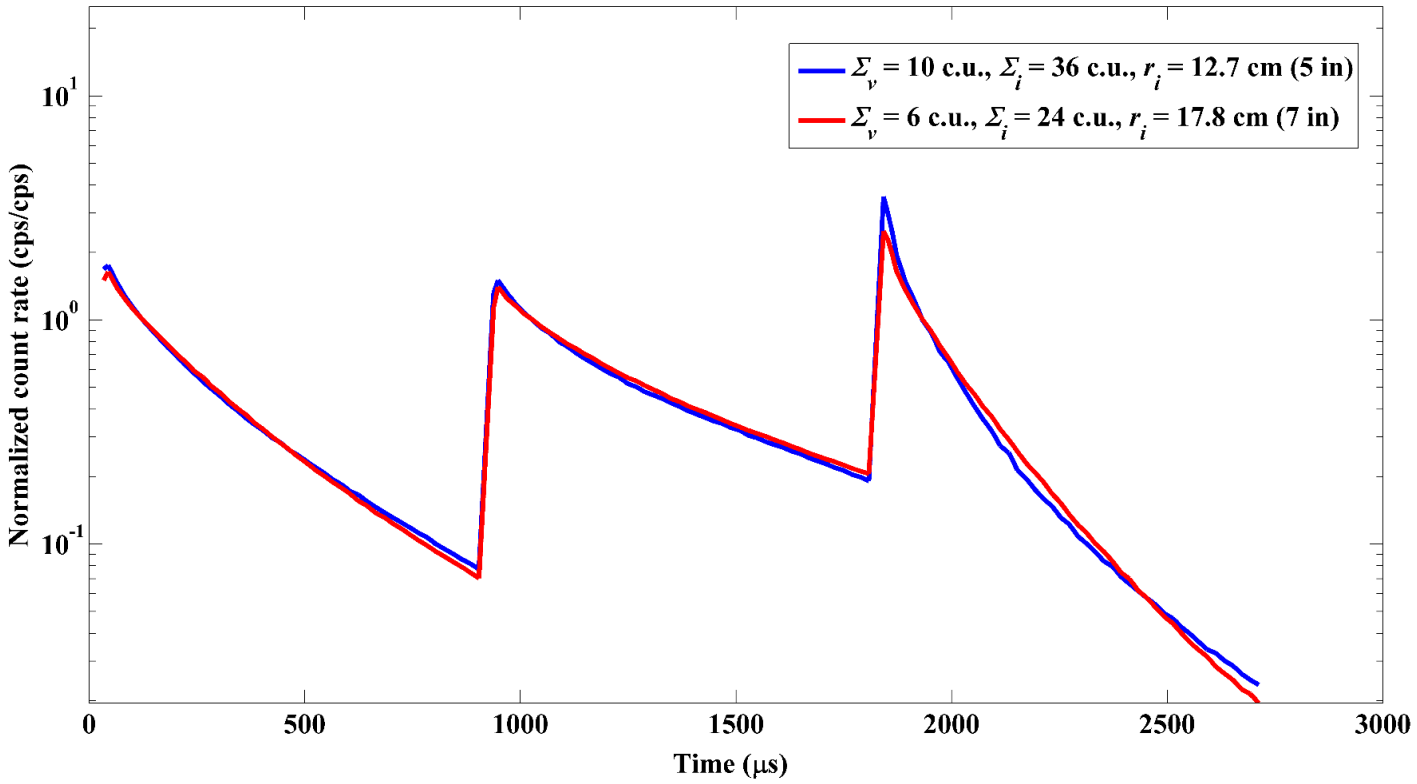

Figure 4.3: Simulated multi-detector signals for two different virgin rocks (Σ_v), invaded by fluids with different salinity (Σ_i) at two different radial lengths of invasion (r_i). This figure illustrates the possible non-uniqueness of the multi-detector decay measurements and the importance of using a reference value for invasion-zone Sigma (Σ_i) to limit the region of solution space.

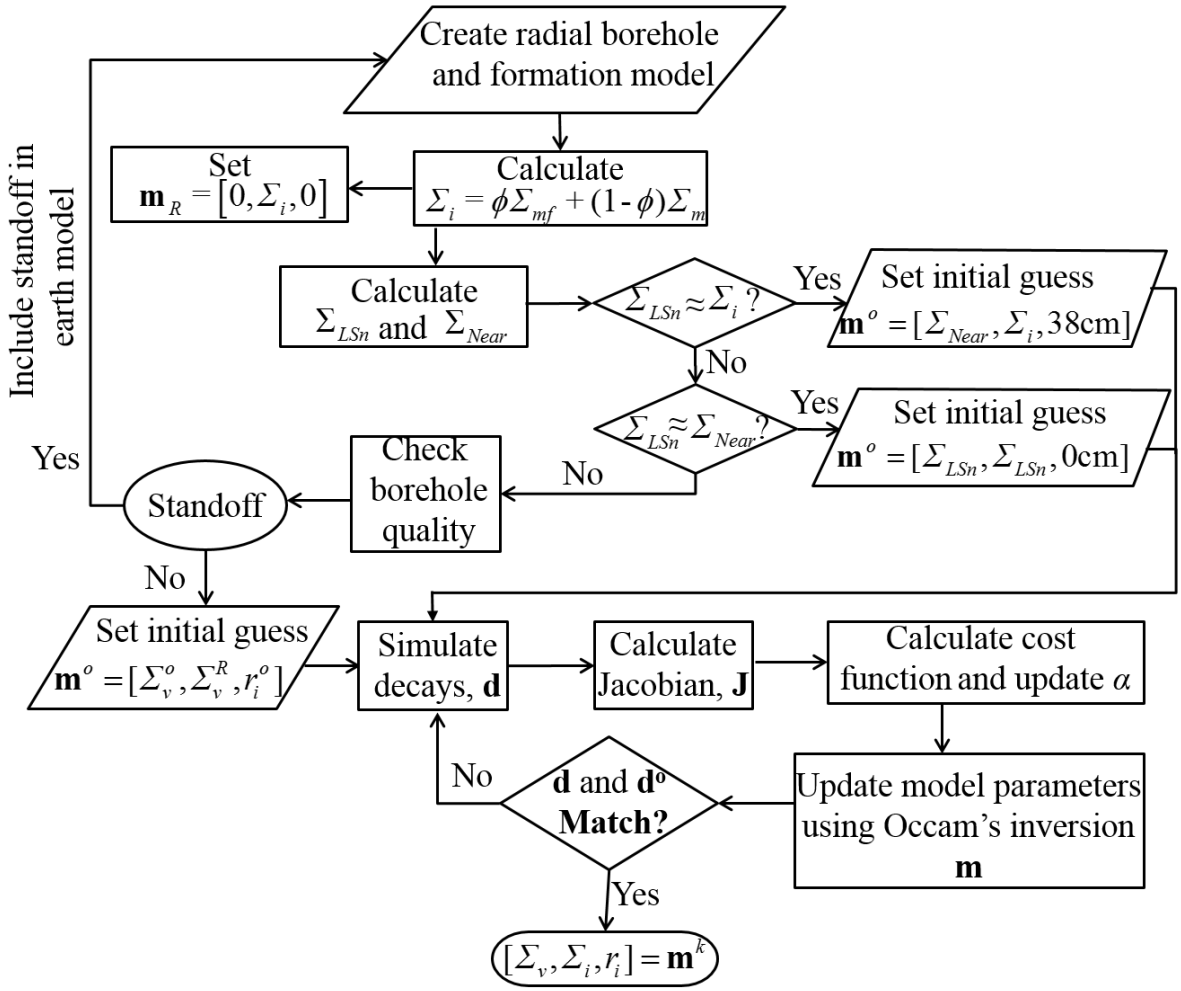

Figure 4.4: One-dimensional radial inversion flowchart for multi-detector thermal-neutron and gamma-ray decays. Σ_i is calculated invasion-zone Sigma, Σ_{LSn} and Σ_{Near} are borehole- and diffusion-corrected LSn and Near detector Sigmas, respectively. $\mathbf{m}_R$ is model properties reference vector, $\mathbf{m}^o$ is an initial smart guess for the model properties, **d** is the numerically simulated set of multi-detector decays, $\mathbf{d}^o$ is the measured multi-detector set of decays, $\mathbf{m}^k$ is the set of model properties at iteration *k*.

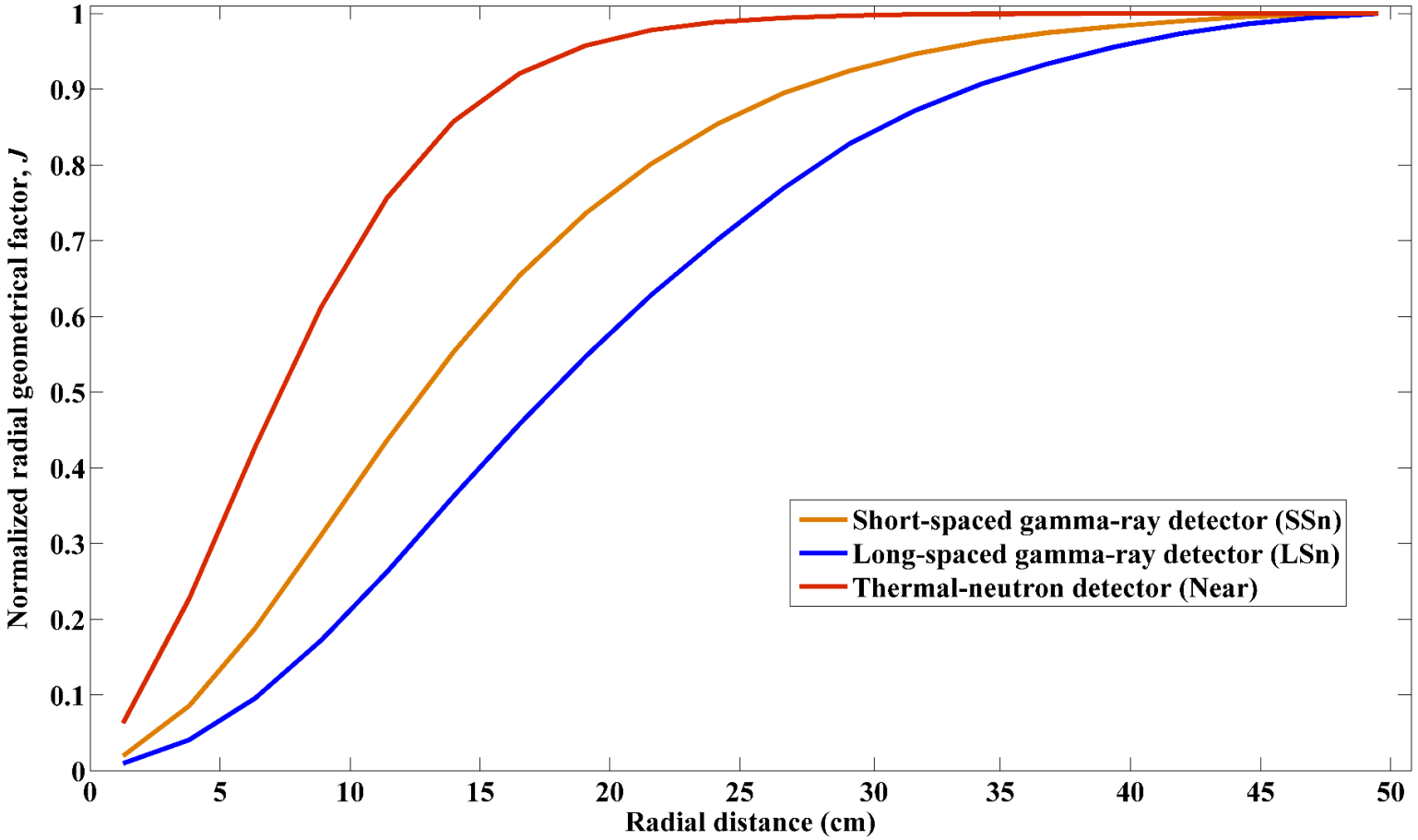

Figure 4.5: Radial geometrical factors for the SSn (yellow solid line), LSn (blue solid line), and Near (red solid line) detectors, respectively, of the LWD tool under study in a 34-pu. Fresh water saturated sandstone formation calculated using the Monte Carlo N-Particle (MCNP, X-5 Monte Carlo Team, 2003) code.

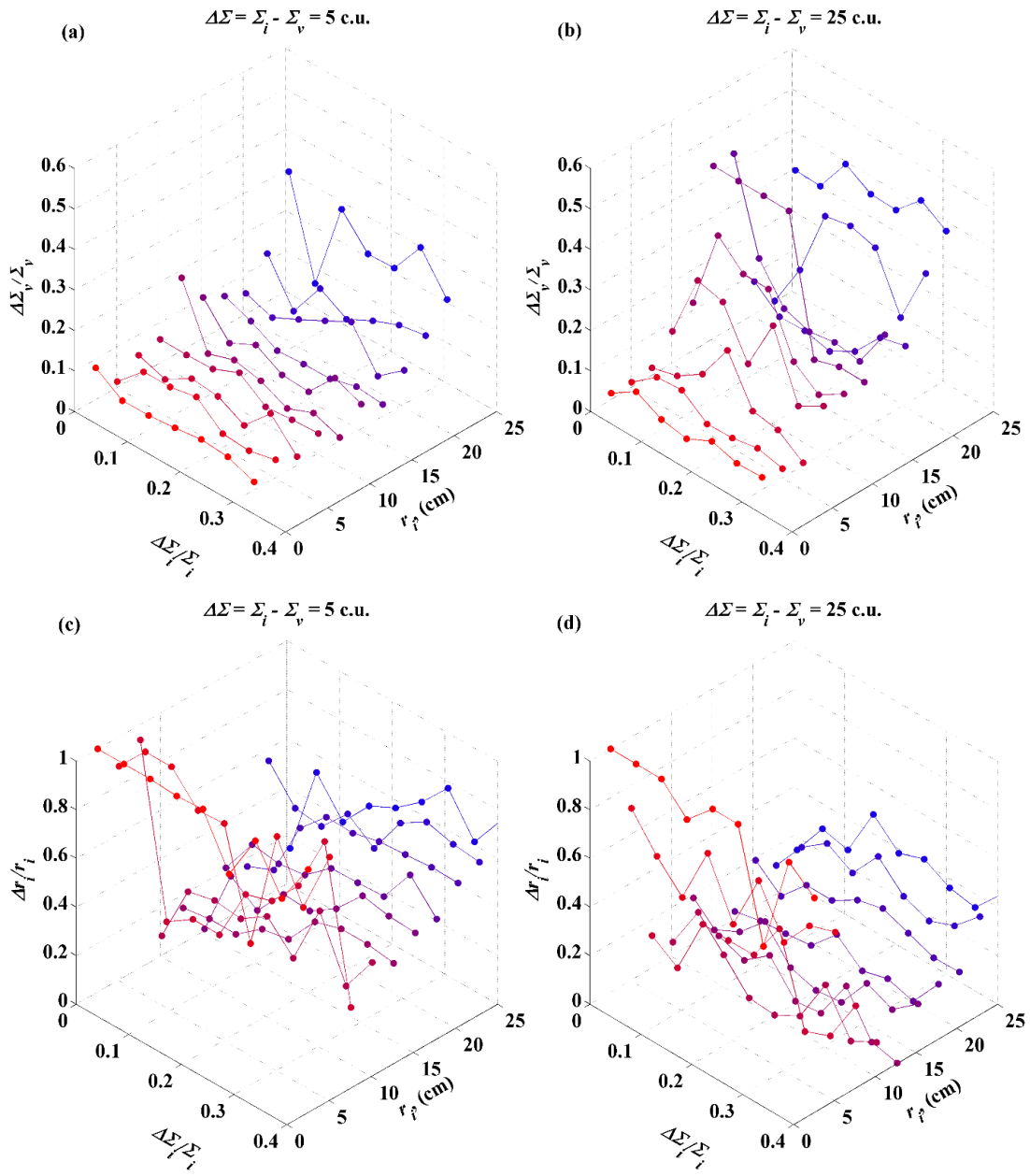

Figure 4.6: Relative error on estimated virgin Sigma as a function of relative error on guessed invasion-zone Sigma, ($\Delta\Sigma_i / \Sigma_i$), and radial length of invasion for invasion- and virgin-zone Sigma contrast of 5 c.u. (a) and 25 c.u. (b), and relative error on radial length of invasion as a function of relative error on guessed invasion-zone Sigma, ($\Delta\Sigma_i / \Sigma_i$), and radial length of invasion for invasion- and virgin-zone Sigma contrast of 5 c.u. (c) and 25 c.u. (d). Colors indicate different radial lengths of invasion.

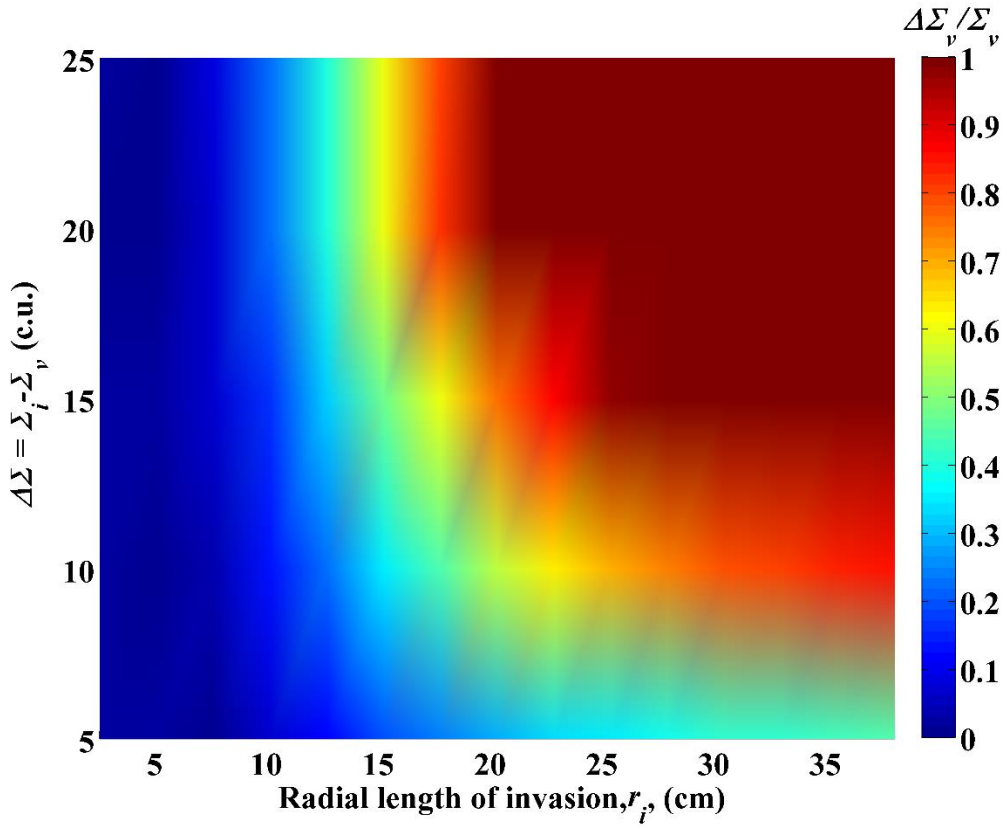

Figure 4.7: Relative error on virgin Sigma not corrected for invasion effects induced by piston-like invasion of salty filtrate as a function of radial length of invasion and invasion-virgin zone Sigma contrast.

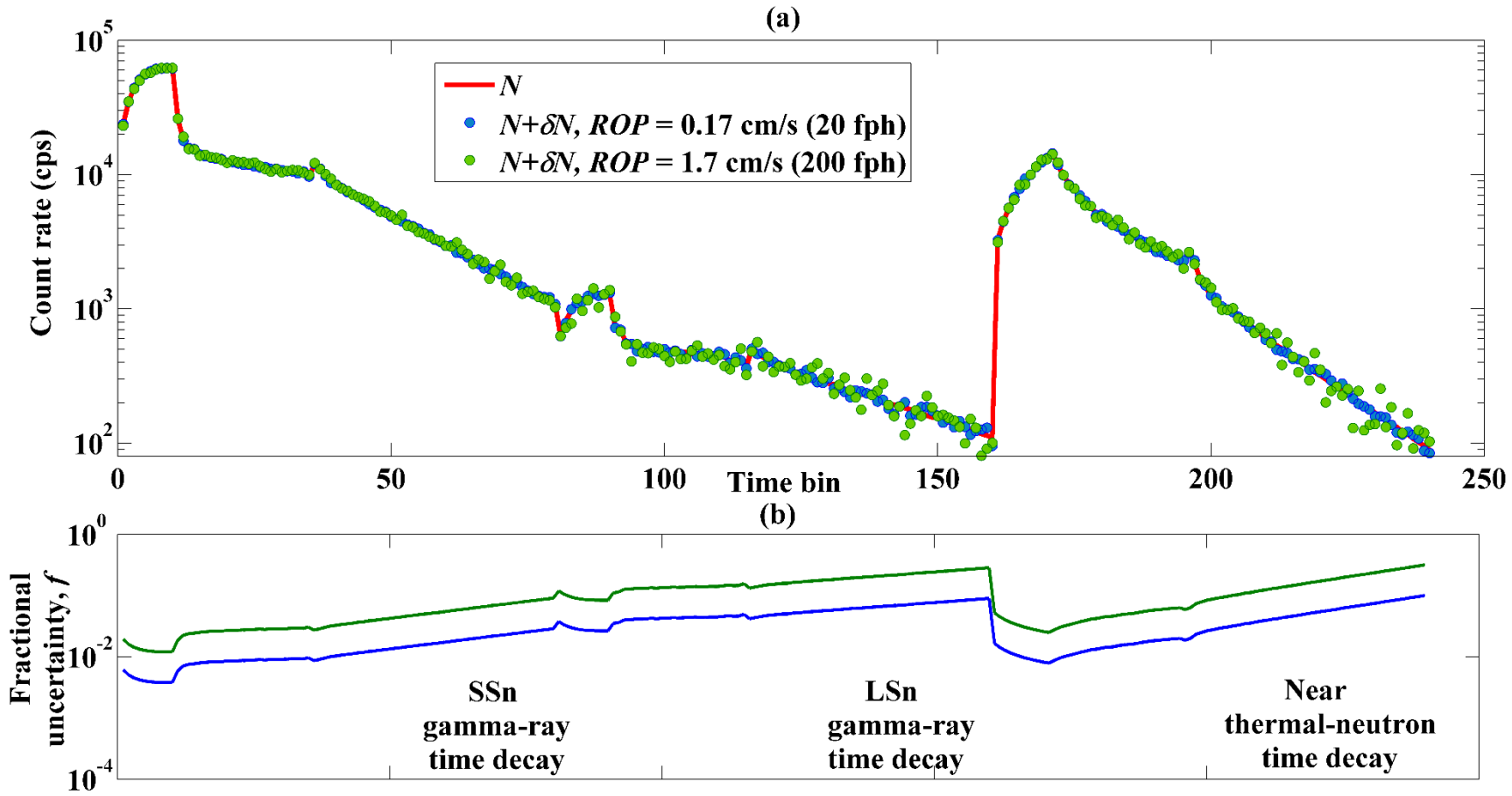

Figure 4.8: (a) Multi-detector synthetic signal without noise (red solid line) and simulated noisy signal in a 10-c.u. material while drilling at *ROP* equal to 0.17 cm/s (blue markers) and 1.7 cm/s (green markers), and (b) fractional uncertainty $\mathbf{f} = \sqrt{N}/N$ for both penetration rates described in the top panel.

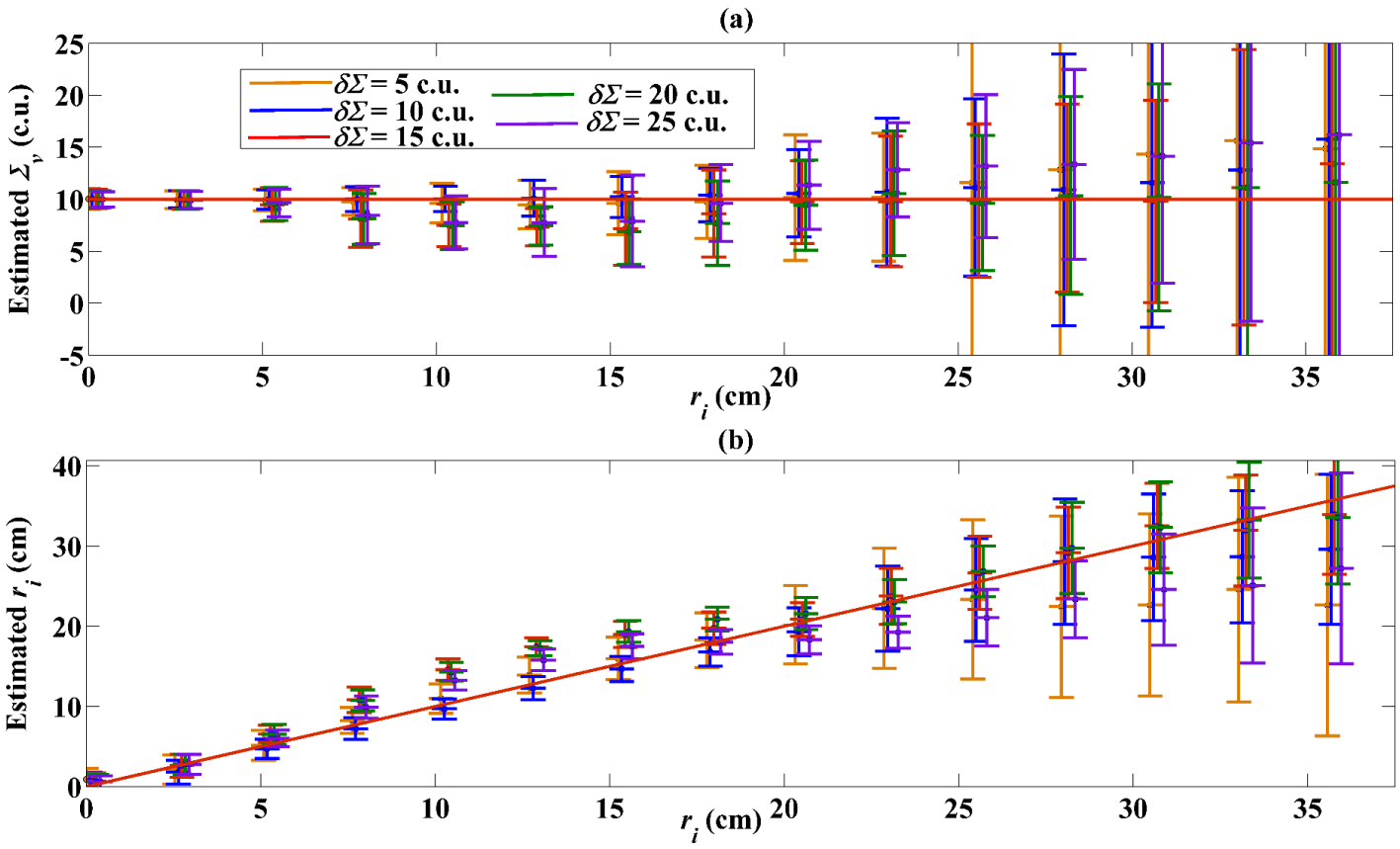

Figure 4.9: (a) Estimated Virgin Sigma and (b) radial length of invasion as a function of actual radial length of invasion and flushed/virgin Sigma contrast for the cases of brines of different salinities that are piston-like invading a 34-p.u. freshwater-bearing sandstone formation. The colors represent Sigma contrast between virgin and invasion zones. The vertical bars represent the standard deviation of the distribution of estimated properties after a multiple realization study on synthetic decays with noise corresponding to drilling at 0.255 cm/s (30 fph). The bar midpoints represent the mean of the properties' distribution.

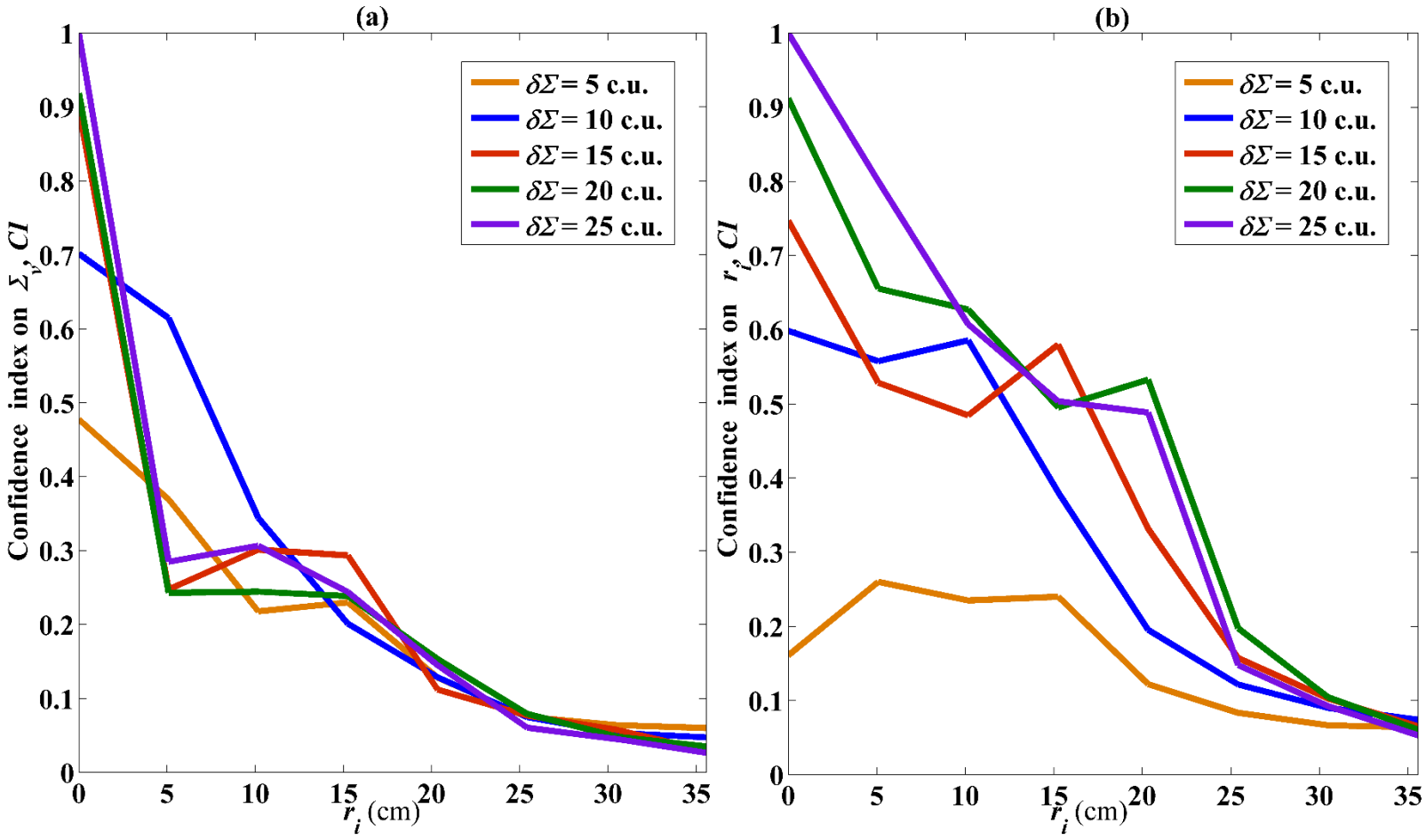

Figure 4.10: (a) Virgin Sigma Confidence Index (*CI*) as a function of radial length of invasion and Sigma contrast, and (b) radial length of invasion Confidence Index (*CI*) as a function of radial length of invasion and Sigma contrast. The colors represent contrast between virgin- and invasion-zone Sigmas for brines of different salinities piston-like invading a 34-p.u. freshwater-bearing sandstone formation.

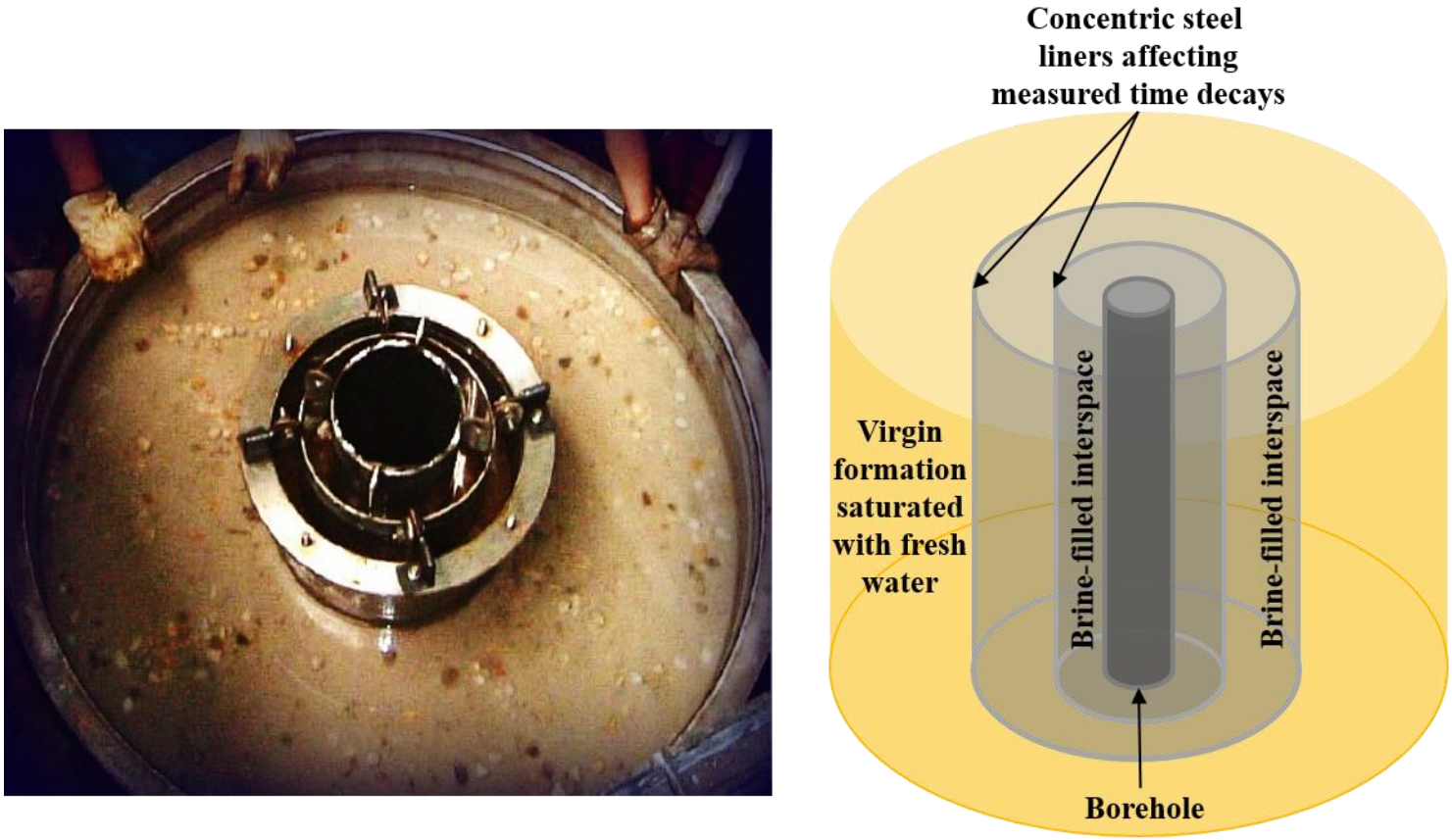

Figure 4.11: Laboratory formation used to simulate invasion of 200-kppm [NaCl] brine into a fresh water saturated 34-p.u. sandstone. The metallic cylinders in the center of the sandstone block are 1-mm thick steel liners used to physically separate virgin and invasion zones. These liners affect measured multi-detector time decays.

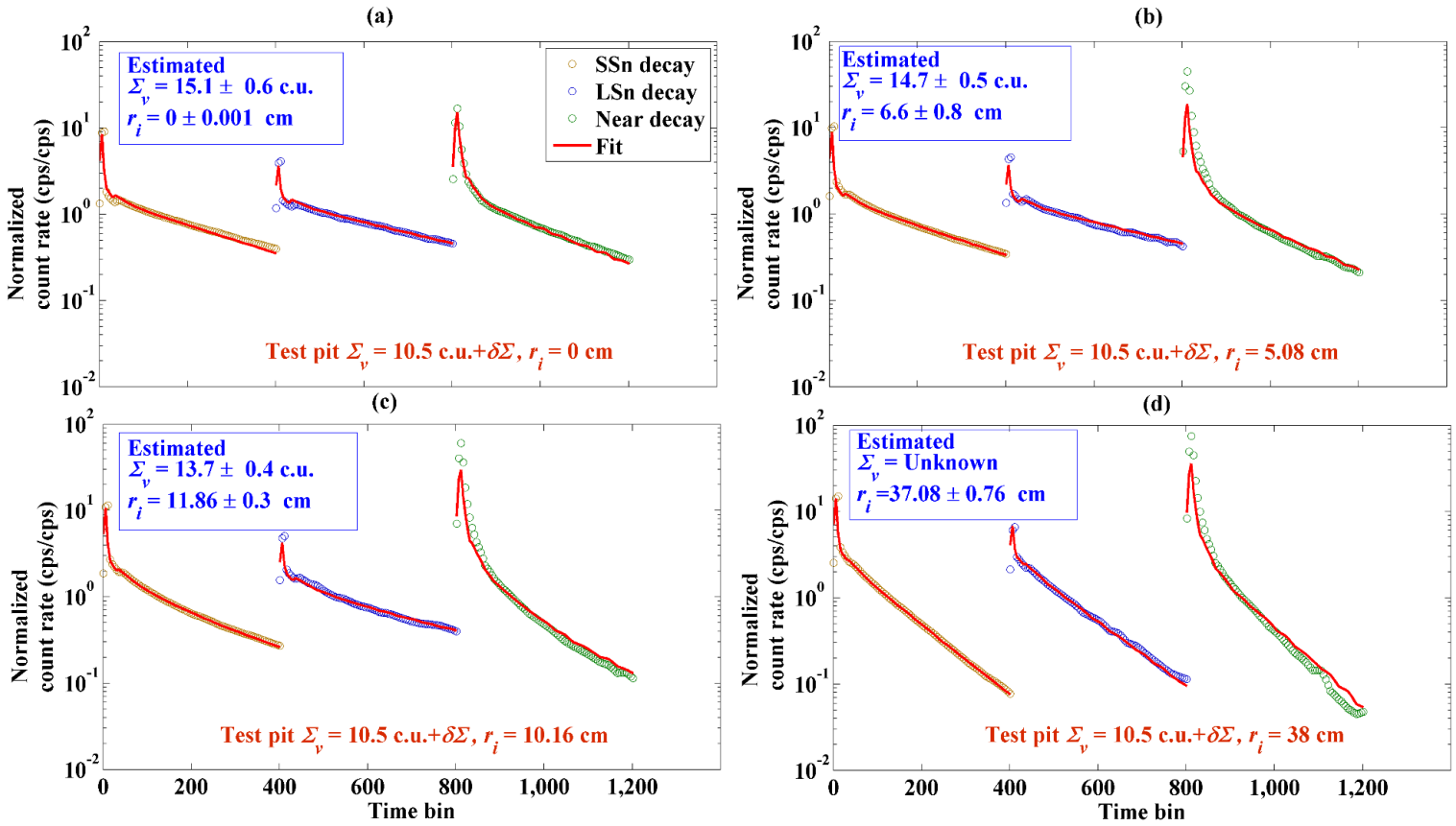

Figure 4.12: Reconstruction (red solid lines) of test-pit experimental measurements (colored markers). Insets at the top left of each diagram show the estimated virgin Sigma and radial length of invasion with standard deviations. Insets at the bottom right of each diagram describe the actual model properties at radial lengths of invasion corresponding to 0 cm (a), 5.08 cm (b), 10.16 cm (c), and full invasion (d) of 200-kppm [NaCl] brine into a 34-p.u. fresh-water saturated sandstone. Note: misfit between actual and inverted Sigma values are due to the presence of steel liners separating invaded and uninvaded zones in the experimental setup, which are not included in the inversion model.

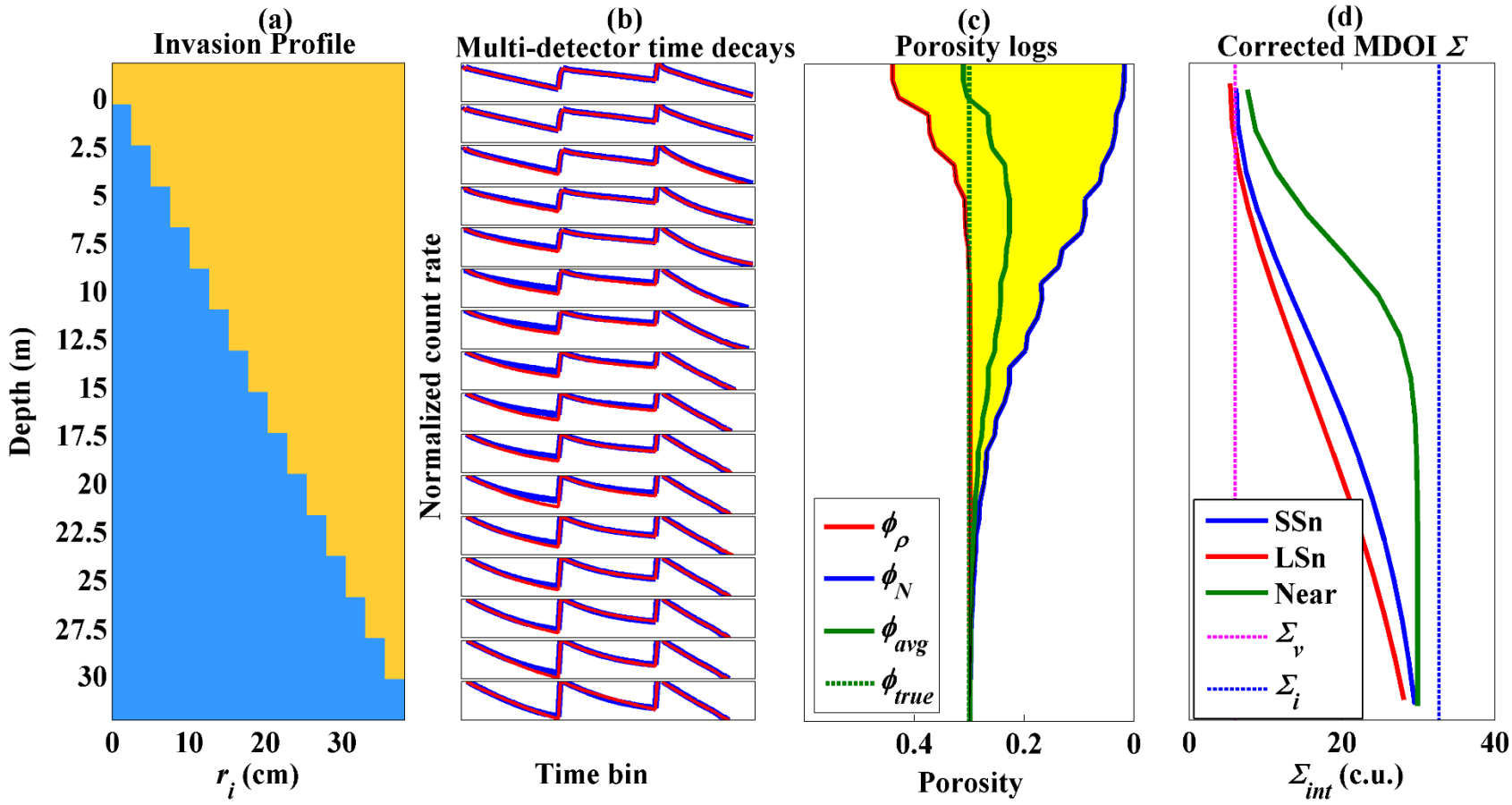

Figure 4.13: (a) Diagram of layers and radial invasion, (b) measured and fitted multi-detector decays, (c) simulated porosity logs in sandstone units, and (d) borehole and diffusion corrected multi-detector Sigma logs for Synthetic Case I. Layer thickness is 2.43 m (8 ft). Each set of decays is simulated at the bed center to avoid shoulder-bed effects.

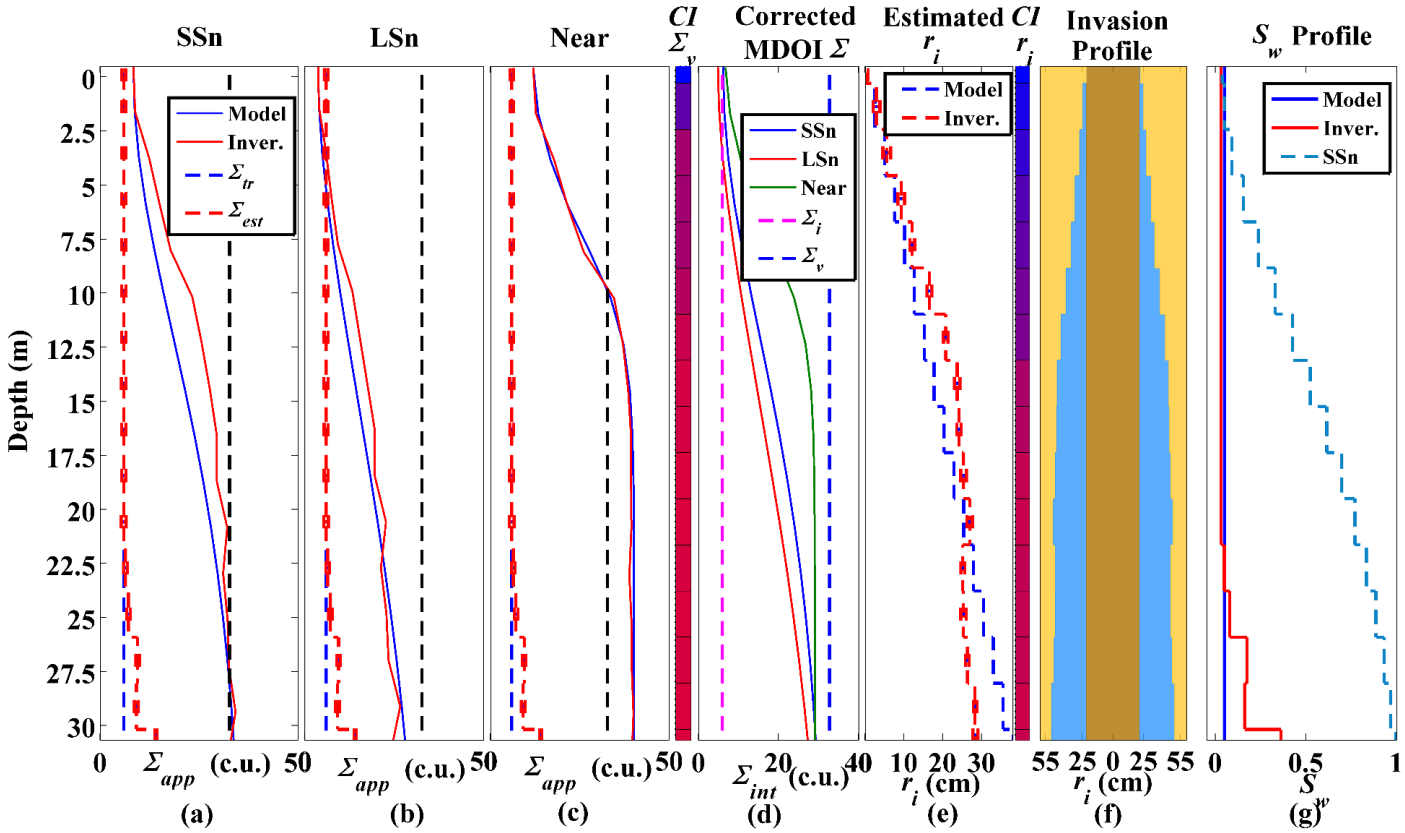

Figure 4.14: Inversion results for Synthetic Case I. (a), (b), and (c) synthetic (blue solid line) and fitted (red solid line) apparent Sigma for the SSn, LSn, and Near detectors, respectively, and true model (blue dashed line) and estimated (red dashed line) virgin formation Sigma with error bars, and reference invasion-zone Sigma (black dashed line), (d) Multi-detector diffusion- and borehole-corrected Sigma logs, and model virgin-zone (magenta dashed line) and invasion-zone (blue dashed line) Sigma, (e) Actual (blue dashed line) and estimated (red dashed line) radial length of invasion with error bars, (f) Diagram of borehole, invasion, and formation, (g) Actual (blue solid line), estimated (red solid line), and SSn-calculated (blue dashed line) water saturation. SSn-calculated water saturation represents the estimated water saturation calculated directly from the borehole- and diffusion-corrected SSn Sigma log without correction for invasion effects.

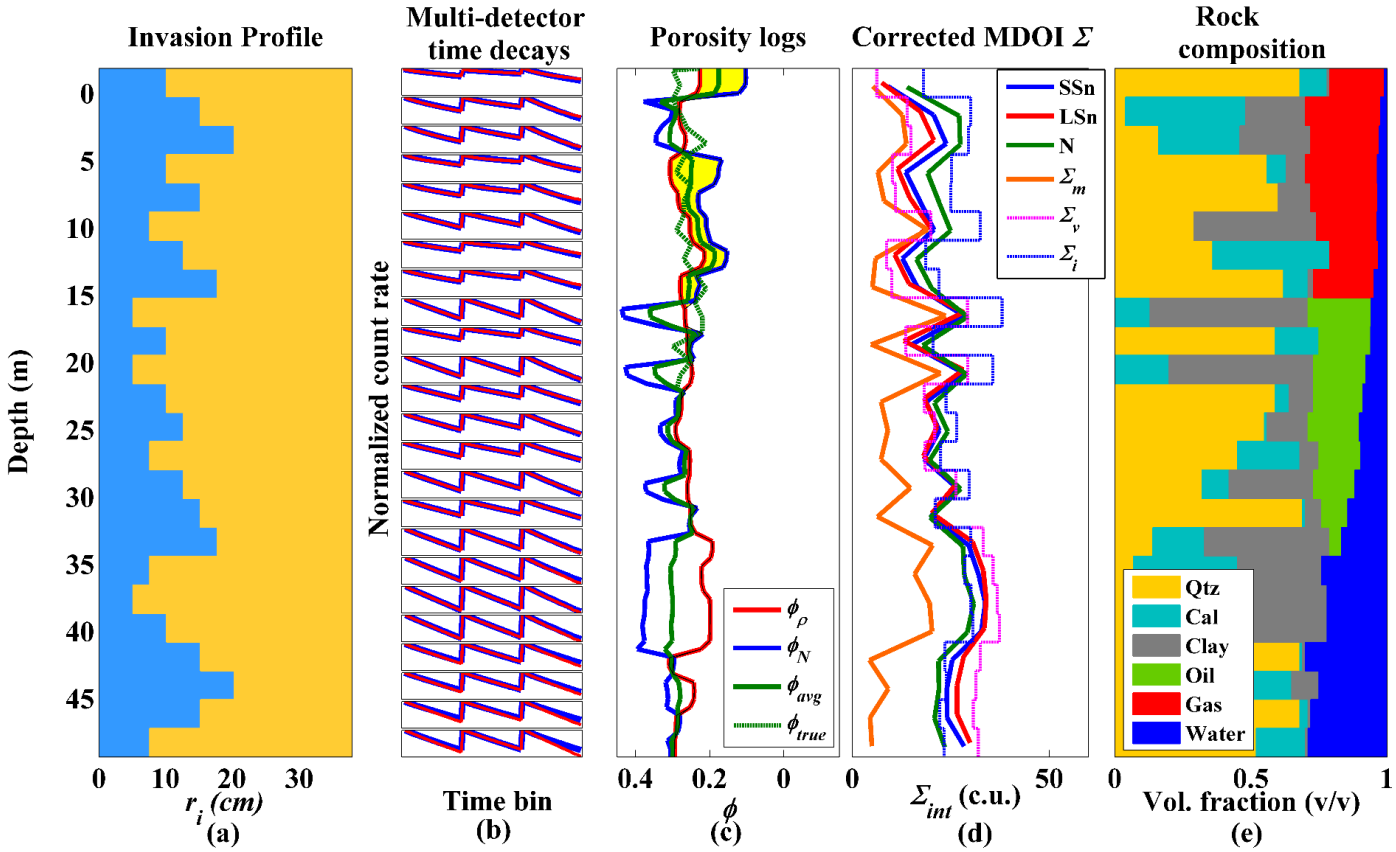

Figure 4.15: (a) Diagram of layers and radial invasion, (b) synthetic (blue solid lines) and fitted (red solid lines) multi-detector decays, (c) simulated LWD density (red solid line), neutron (blue solid line), squared averaged (green solid line), and actual porosity (green dashed line) logs in limestone units, (d) borehole- and diffusion-corrected multi-detector (SSn, LSn, and N) Sigma logs , calculated matrix Sigma log (orange solid line), and actual virgin- and invasion-zone Sigmas per layer (magenta and blue dashed lines, respectively), and (e) rock volumetric mineral and fluid compositions for Synthetic Case II.

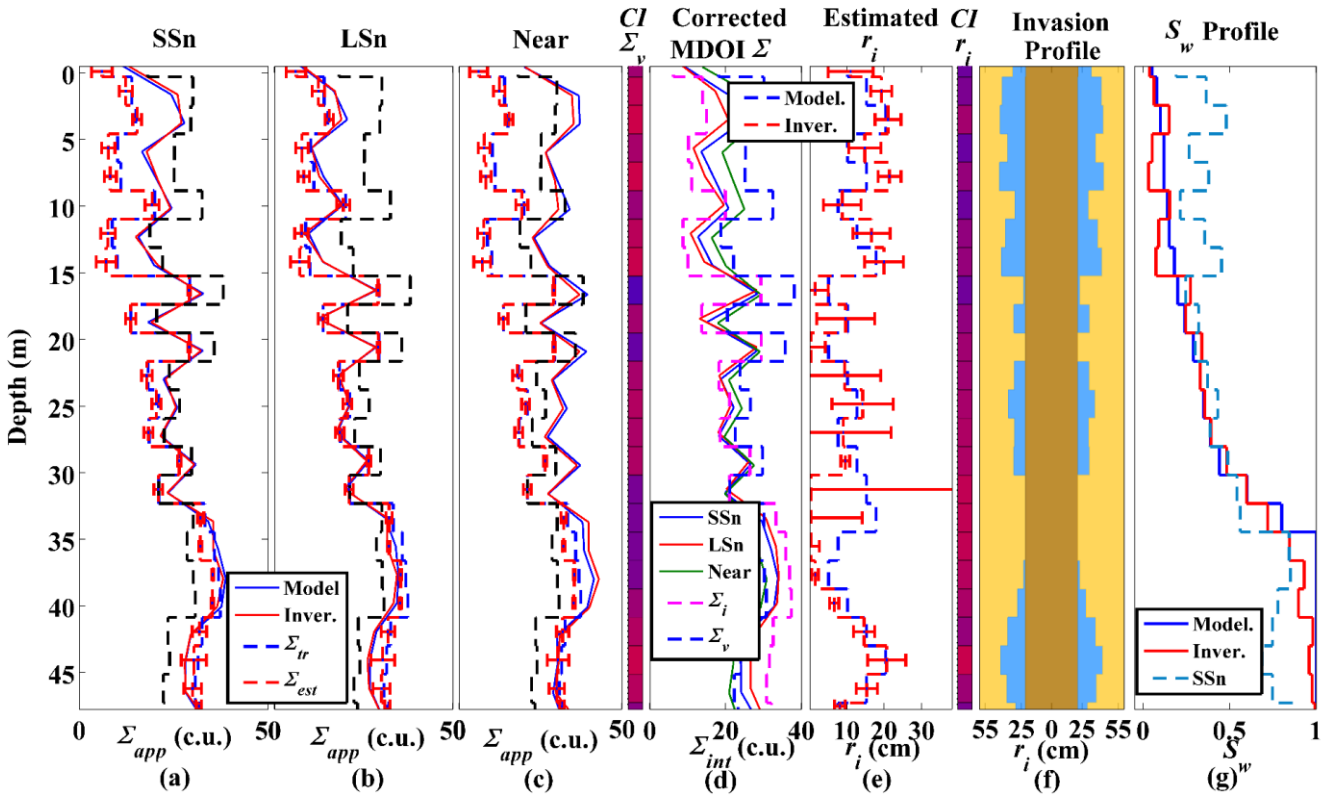

Figure 4.16: Inversion results for Synthetic Case II. (a), (b), and (c) synthetic (blue solid line) and fitted (red solid line) apparent Sigma for the SSn, LSn, and Near detectors, respectively, and true model (blue dashed line) and estimated (red dashed line) virgin formation Sigma with error bars, and reference invasion-zone Sigma (black dashed line), (d) Multi-detector diffusion- and borehole-corrected Sigma logs, and model virgin-zone (magenta dashed line) and invasion-zone (blue dashed line) Sigma, (e) True (blue dashed line) and estimated (red dashed line) radial length of invasion with error bars, (f) Diagram of borehole, invasion, and formation, (g) True (blue solid line), estimated (red solid line), and SSn-calculated (blue dashed line) water saturation. The SSn-calculated water saturation represents the estimated water saturation calculated directly from the borehole- and diffusion-corrected SSn Sigma log without correction for invasion effects.

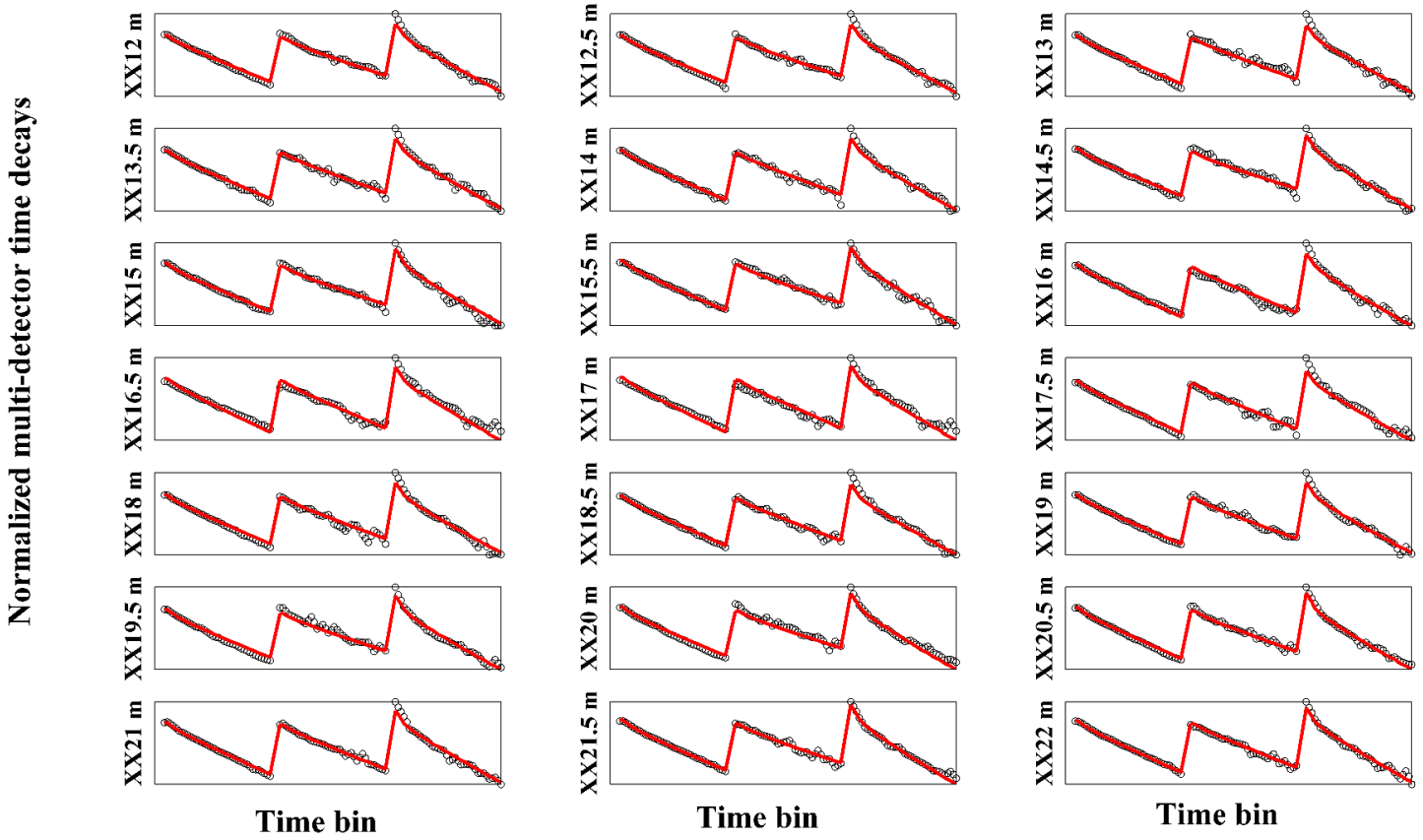

Figure 4.17: Field case multi-detector fitted (red solid line) and measured (black markers) time decays in the 3.048-m (10-ft) section corresponding to the gas-bearing formation penetrated by a 40^{o} deviated well.

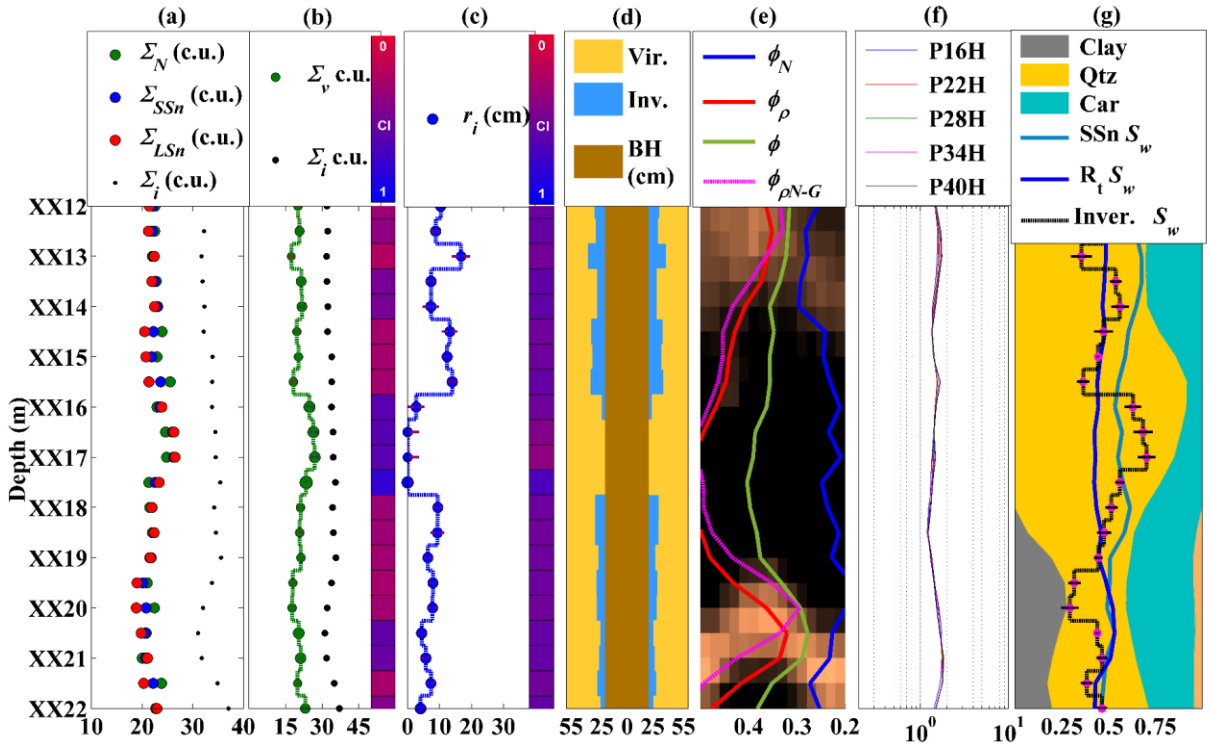

Figure 4.18: One-dimensional inversion-based interpretation of multi-detector decay curves in a 10-ft gas-bearing formation. SBM filtrate salinity is 137 kppm [NaCl equivalent] and filtrate Sigma is 72.3 c.u. Gas Sigma calculated at reservoir and temperature pressure equals 2 c.u. (a) Borehole and diffusion corrected multi-detector Sigma logs (N, SSn, and LSn) and assumed invasion-zone Sigma, (b) estimated virgin Sigma (green squared log) with error bars, assumed invasion Sigma (black markers), and confidence index (*CI*), (c) estimated radial length of invasion with confidence index and error bars, (d) diagram of estimated radial length of invasion, borehole, and formation, (e) neutron (blue solid line), gamma-gamma density (red solid line), averaged squared (solid green line), and neutron-gamma density (magenta solid line) porosity logs in limestone units, (f) high-frequency phase resistivity logs, and (g) mineral composition from spectroscopy and calculated water saturation from SSn Sigma (light-blue solid line), resistivity (dark-blue solid line), and estimated after correcting formation Sigma for invasion effects with the 1D radial inversion (black dashed line).

Chapter 5: Two-Dimensional Inversion-Based Interpretation of Logging-While-Drilling Sigma Measurements

Identification and petrophysical evaluation of thinly bedded formations using resistivity measurements can be problematic due the large measurement volume of investigation and nonlinear changes in tool response generated when shale laminae, which create least-resistance paths. Logging-While-Drilling (LWD) Sigma logs can overcome these problems because Sigma measurements have a smaller volume of investigation. LWD Sigma logs are additionally useful to detect invasion in the shallow near-wellbore zone. In the case of thick formations, separation of multi-detector Sigma logs may indicate the presence of invasion. However, measurements acquired in thinly bedded formations drilled at overbalance pressures are affected not only by invasion, but also by shoulder-bed effects and the separation of the logs does not necessarily confirm the presence of invasion. The purpose of this chapter is to develop a method to perform inversion-based interpretation of LWD Sigma measurements to reveal actual formation properties devoid of invasion and shoulder-bed effects and, consequentially, to improve the estimation of water saturation from Sigma logs. In this chapter I develop a 2D inversion method that enables the estimation of virgin-zone Sigma and radial length of invasion in formations with thicknesses smaller than the vertical resolution of the detectors while accounting for well-deviation effects. The method is tested with two synthetic and two field cases. Results indicate that the 2D inversion-based interpretation method improves the calculation of

water saturation from Sigma logs affected by environmental and geometrical effects. Conventional interpretation of Sigma logs can lead to the overestimation of water saturation by as much as 50% resulting from shoulder-bed effects in univaded formations, and as much as 100% in zones simultaneously affected by invasion, shoulder-bed and well-deviation effects.

5.1 INTRODUCTION

LWD Sigma logs are useful to complement the interpretation of LWD resistivity measurements or to perform resistivity-independent quantitative analysis, such as calculations of water saturation. Connate water salinity, porosity, and water saturation are proportional to formation conductivity and Sigma. The correlation between both measurements makes Sigma additionally useful for qualitative analyses, such as geosteering. Both LWD Sigma and propagation resistivity measurements have similar vertical resolution of approximately 30.48 cm. However, resistivity measurements have a larger volume of investigation because their depth of investigation is approximately 68 cm shallow/96 cm deep, compared to 15 cm shallow/30 cm deep for Sigma measurements (Griffiths, 2010). Accordingly, resistivity logs are more affected than Sigma logs by geometrical and shoulder-bed effects in deviated wells; Sigma logs are thus better suited to detect and evaluate thinly bedded formations in deviated wells. Simpson et al. (2010) described how Sigma logs facilitated the identification of hydrocarbon-bearing low-contrast, low-resistivity (LCLR) pays otherwise bypassed by standalone use of resistivity logs.

Despite all the advantages, interpretation of multi-detector Sigma logs can be complicated. Thermal-neutron and gamma-ray decays in layers roughly thinner than 90 cm (3 ft) are affected by adjacent formations. Interpretation of thermal-neutron and gamma-ray time decays in thinly bedded formations is challenging because each detector senses different portions of the layers. Depending on the petrophysical properties of the layers and rate of penetration, *ROP*, each detector measurement is affected by filtrate invasion at a different extent. Additionally, time decays of nuclear particles are affected by borehole and diffusion effects, as well as statistical noise as a function of source-detector spacing and the type of particles measured, i.e. gamma rays or thermal neutrons.

The effect of adjacent beds on borehole measurements, referred to as shoulder-bed effect, was early documented in the interpretation of resistivity logs (Suau et al, 1973). Sensing multiple thin layers within the volume of investigation of the logging tool results in averaged log values that do not represent actual properties of any of the layers. Experimental measurements and analytical models (Chemali et al., 1983; Frenkel et al. 1997) were used to develop corrections to estimate formation resistivity. Similar methods using three-layer effective models led to the correction of LWD propagation measurements (Yang et al., 2005). Shoulder-bed effects produce false separation of array measurements in uninvaded formations for their hydrocarbon potential (Xiao et al., 2003). The effect is also accentuated in the case of deviated wells penetrating thinly bedded formations (Hardman et al., 1987). Low-resistivity adjacent formations can lead to overlooking of hydrocarbon-bearing thinly bedded formations (Warrillow et al., 1995). The best manner

to reduce shoulder-bed and deviation effects from resistivity measurements is through inversion using a 3D model that represents the physics of the measurement (Rasmus et al., 2009).

Shoulder-bed and well-deviation effects are not exclusive to resistivity measurements. Nuclear logs, such as neutron, density, spectroscopy, and Sigma, are also highly affected by these effects despite their smaller volume of investigation compared to resistivity logs. Mendoza et al. (2010a) corrected nuclear porosity measurements for shoulder-bed and geometrical effects in deviated wells using a 3D fast-forward algorithm and linear inversion to estimate layer-by-layer porosities. Similarly, Ijasan et al. (2013b) developed a fast inversion algorithm for nuclear porosity and LWD propagation measurements that allowed the simultaneous isolation of environmental and geometrical effects from both measurements, which led to improved estimations of hydrocarbon pore volume.

Shoulder-bed and invasion effects on Sigma logs have been studied separately; there exists no study published on the correction of these combined effects because of the complexity of the problem. Haley (1995) developed a log response equation to interpret Sigma logs in sand-shale laminated systems. Mimoun et al. (2010) developed a rapid simulation method for cased-hole pulsed-neutron measurements and a 1D inversion scheme to estimate layer-by-layer formation Sigma. Both methods are based on thermal-neutron diffusion transport corrections and disregard the effect of mud-filtrate invasion. The effect of invasion was studied by Allen et al. (1965) using multi-group neutron

diffusion theory; their study recognizes the significant impact of shallow invasion on Sigma logs, and reports the variable depth of investigation of the detector response as a function of radial length of invasion. A rapid-simulation algorithm to reproduce multi-detector time decays was presented in Chapter 3 and was embedded within a 1D radial inversion algorithm in Chapter 4. The algorithms proved to be effective to reduce invasion effects on LWD Sigma logs while taking into consideration detector-specific borehole and diffusion effects. However, the 1D radial inversion method is not sufficient to reduce shoulder-bed effects on Sigma logs acquired in thinly bedded formations. Such correction requires a 2D algorithm that accounts for the relative variations in detector response due to the absorption properties of several virgin sublayers and their respective invasion zones.

The main objective of this chapter is to develop a 2D inversion algorithm to estimate layer-by-layer virgin-zone Sigma and radial length of invasion in thinly bedded formations penerated by high-angle/horizontal (HAHZ) wells. Previous studies addressed only the inversion of layer-by-layer univaded formation Sigma in thin layers. I increased the level of complexity by addressing a realistic logging environment and by utilizing a 3D forward simulation method that accounts for the different vertical, azimuthal, and radial resolutions of each of the detectors of a commercial LWD Sigma tool. Furthermore, raw multi-detector decay measurements, only corrected for background gamma radiation and dead time (Ortega et al., 2013), are used to output actual formation properties by simultaneously reducing borehole and diffusion effects. This chapter is organized as follows: First, I present the formulation of the 2D inversion method. Next I describe a

method to rapidly calculate the Jacobian sensitivity matrix necessary to perform the nonlinear inversion of multi-detector decays, and a method to assess uncertainty of the estimations. Finally, I document synthetic and field examples that benchmark the performance of the multi-detector thermal-neutron and gamma-ray decay inversion method to estimate water saturation compared to using uncorrected Sigma and resistivity logs.

5.2. TWO-DIMENSIONAL INVERSION OF MULTI-DETECTOR TIME DECAYS

5.2.1 Formulation

Measurements of thermal-neutron and gamma-ray decays acquired in formations with thicknesses smaller than the vertical resolution of the LWD Sigma tool are challenging not only to simulate, but also to invert due to the nonlinear nature of detector responses with respect to changes in the nuclear properties of the materials in the formation. **Figure 5.1a** displays a formation configuration in which the three detectors of the LWD Sigma tool sense different portions of a layered stratigraphic sequence. Colored areas represent vertical sensitivity functions for each detector. The figure shows that the Near detector is only sensing layers 6, 7, and 8, the SSn detector senses layers 4, 5, 6, 7 and 8, while the LSn detector senses layers 1 through 8. Ultimately, the output of the multi-detector measurement is a function of the properties of the top eight layers. Changes in the properties of the formations generate nonlinear changes on measured time decays. The problem can be summarized as

$$G(\mathbf{m}) = G\begin{bmatrix} \Sigma_1 \\ \Sigma_2 \\ \Sigma_3 \\ \vdots \\ \vdots \\ \Sigma_8 \end{bmatrix} = \begin{bmatrix} \mathbf{n}_1(t) \\ \mathbf{n}_2(t) \\ \mathbf{n}_3(t) \end{bmatrix}, \tag{5.1}$$

where G is a numerical method to simulate $\mathbf{n}_1(t)$, $\mathbf{n}_2(t)$, and $\mathbf{n}_3(t)$ as a function of formation properties, $\mathbf{m}$, and t is time. In this case, $\mathbf{m}$ is a vector that contains virgin formation Sigma of each of the layers involved in the analysis. $\mathbf{n}_1(t)$ and $\mathbf{n}_2(t)$ are the gamma-ray decay curves and $\mathbf{n}_3(t)$ is the thermal-neutron decay curve for the SSn, LSn, and Near detectors of the LWD tool, respectively. In Chapter 2, $\mathbf{n}(t)$ was defined as a detector-specific time decay for the irregular time bins of the pulsed-neutron commercial tool under study from 0 μs to 415 μs, where time 0 μs is the time at which the last pulse is generated.

The inverse problem of estimating intrinsic Sigma of each layer requires measurements at different depth locations so that the number of available measurement points is larger than the number of formation properties to be estimated (overdetermined inverse problem). If *n* measurements are performed along the well axis, the fast-forward simulation numerical method for the case of *m* layered formations can be written as

$$G\begin{bmatrix}\Sigma_1\\ \Sigma_2\\ \Sigma_3\\ \vdots\\ \vdots\\ \Sigma_m\end{bmatrix}=\begin{bmatrix}\begin{pmatrix}\mathbf{n}_1(t)\\ \mathbf{n}_2(t)\\ \mathbf{n}_3(t)\end{pmatrix}_{j=1}\\ \begin{pmatrix}\mathbf{n}_1(t)\\ \mathbf{n}_2(t)\\ \mathbf{n}_3(t)\end{pmatrix}_{j=2}\\ \vdots\\ \vdots\\ \begin{pmatrix}\mathbf{n}_1(t)\\ \mathbf{n}_2(t)\\ \mathbf{n}_3(t)\end{pmatrix}_{j=n}\end{bmatrix}. \tag{5.2}$$

Actual measurements acquired in sequences of thinly bedded formations are, in reality, also affected by shallow-invasion effects. Since the Pulsed Neutron Generator is not located immediately adjacent to the drill bit, invasion arises because of the exposure of the rock to drilling fluid at overbalance pressure from the time the drill bit penetrates the formation until the measurement is acquired. **Figure 5.1b** shows a typical configuration for multi-detector decay measurements in thinly bedded, invaded formations. Notice that measurements at each depth location are simultaneously affected by several virgin formations and their respective invasion zones. Additionally, each detector senses a different portion of the layered sequence. The multi-detector decay forward modeling problem in the case of m thinly bedded and invaded layers, i.e., i=1:m, and n logging depth locations, i.e., j=1:n, can be written as

$$G\begin{bmatrix}\begin{pmatrix}\Sigma_v\\ \Sigma_i\\ r_i\end{pmatrix}_{i=1}\\ \begin{pmatrix}\Sigma_v\\ \Sigma_i\\ r_i\end{pmatrix}_{i=2}\\ \vdots\\ \vdots\\ \begin{pmatrix}\Sigma_v\\ \Sigma_i\\ r_i\end{pmatrix}_{i=m}\end{bmatrix}=\begin{bmatrix}\begin{pmatrix}\mathbf{n}_1(t)\\ \mathbf{n}_2(t)\\ \mathbf{n}_3(t)\end{pmatrix}_{j=1}\\ \begin{pmatrix}\mathbf{n}_1(t)\\ \mathbf{n}_2(t)\\ \mathbf{n}_3(t)\end{pmatrix}_{j=2}\\ \vdots\\ \vdots\\ \begin{pmatrix}\mathbf{n}_1(t)\\ \mathbf{n}_2(t)\\ \mathbf{n}_3(t)\end{pmatrix}_{j=n}\end{bmatrix}, \tag{5.3}$$

Where Σ_v, Σ_i, and r_i are the intrinsic virgin-zone Sigma, invasion-zone Sigma, and radial length of invasion for the i-th layer, i=1:m, and $\begin{pmatrix}\mathbf{n}_1(t)\\ \mathbf{n}_2(t)\\ \mathbf{n}_3(t)\end{pmatrix}_j$ are the measured decays at the j-th depth location, j=1:n, and

$$\mathbf{m}=\begin{bmatrix}\begin{pmatrix}\Sigma_v\\ \Sigma_i\\ r_i\end{pmatrix}_{i=1}\\ \vdots\\ \begin{pmatrix}\Sigma_v\\ \Sigma_i\\ r_i\end{pmatrix}_{i=m}\end{bmatrix}.$$

I invoke an inversion scheme similar to that one implemented in Chapter 4 on 1D multi-detector decay inversion and extend it to two dimensions to simultaneously account for invasion and shoulder-bed effects on particle time decays. The modified version of

Occam's inversion algorithm introduced in Chapter 4, a gradient-based nonlinear inversion method, is used to iteratively estimate virgin-zone Sigmas, invasion-zone Sigmas, and radial lengths of invasion in each layer that reproduce the raw decay measurements at several depth locations. Occam's 2D inversion scheme, including modified data-weighting and reference matrices, introduced in Chapter 4 is

$$\left[\left(\mathbf{W}_d \cdot \mathbf{J}(\mathbf{m}^k)\right)^T \cdot \left(\mathbf{W}_d \cdot \mathbf{J}(\mathbf{m}^k)\right) + \alpha^2 \mathbf{I}\right]\mathbf{m}^{k+1} = \mathbf{J}(\mathbf{m}^k)^T \left[\left(\mathbf{W}_d{}^T \cdot \mathbf{W}_d\right) \cdot \left(\mathbf{d} - G(\mathbf{m}^k) + \mathbf{J}(\mathbf{m}^k)\mathbf{m}^k\right)\right] + \alpha^2 \mathbf{m}_R^T \quad , \tag{5.4}$$

where $\mathbf{m}^k$ is the vector containing virgin- and invasion-zone Sigmas and radial lengths of invasion of the the sublayers in the model at iteration *k*, $\mathbf{m}^{k+1}$ is the updated model at iteration *k+1*, $\mathbf{J}(\mathbf{m}^k)$ is the Jacobian sensitivity matrix containing the derivatives of the multi-detector decays at all measurement points with respect to the three model properties of all the sublayers in the layered sequence, $G(\mathbf{m}^k)$ is the output of the fast-forward model of multi-detector decays at iteration *k*, α is the updated regularization parameter which is adjusted as a function of the updated cost function, and $\mathbf{d}$ is the measurement vector that consists of *n* multi-detector time decays to be replicated. The main difference with respect to the 1D multi-detector inversion developed in Chapter 4 relies on the content of the measurement vector, $\mathbf{d}$, the number of formation properties to be estimated, $\mathbf{m}$, and, most importantly, on the entries of the Jacobian sensitivity matrix, $\mathbf{J}$. A modified data-weighting matrix $\mathbf{W}_d$ is used and has the same structure of the data-weighting matrix defined by

equation 4.6. The reference vector, $\mathbf{m}_R$, is used to mititgate the non-uniqueness of the inverse problem by providing a reference value for invaded-zone Sigma, Σ_i, and is calculated as defined by equation 4.9.

5.2.2 Jacobian Calculation

The Jacobian sensitivity matrix is a crucial and difficult-to-calculate component of the 2D inversion algorithm. This matrix must account for the relative change in detector response as a function of the petrophysical properties of all the layers in the system, as well as the variable radial extent of mud-filtrate invasion into each of these layers in the 3D volume of sensitivity specific for each detector. The Jacobian matrix for the 2D inversion of thinly bedded and invaded formations can be written as

$$\mathbf{J} = \left\{ \begin{matrix} \text{Measurement points} \\ j = 1 \rightarrow j = n \end{matrix} \right. \overset{\text{Model sublayers}}{\overbrace{\begin{matrix} i = 1 \rightarrow i = m \end{matrix}}} \left\{ \begin{matrix} \left[\begin{matrix} \frac{\partial \mathbf{n}_1(t)}{\partial \Sigma_v} & \frac{\partial \mathbf{n}_1(t)}{\partial \Sigma_i} & \frac{\partial \mathbf{n}_1(t)}{\partial r_i} \\ \frac{\partial \mathbf{n}_2(t)}{\partial \Sigma_v} & \frac{\partial \mathbf{n}_2(t)}{\partial \Sigma_i} & \frac{\partial \mathbf{n}_2(t)}{\partial r_i} \\ \frac{\partial \mathbf{n}_3(t)}{\partial \Sigma_v} & \frac{\partial \mathbf{n}_3(t)}{\partial \Sigma_i} & \frac{\partial \mathbf{n}_3(t)}{\partial r_i} \end{matrix} \right]_1^1 & \cdots & \left[\begin{matrix} \frac{\partial \mathbf{n}_1(t)}{\partial \Sigma_v} & \frac{\partial \mathbf{n}_1(t)}{\partial \Sigma_i} & \frac{\partial \mathbf{n}_1(t)}{\partial r_i} \\ \frac{\partial \mathbf{n}_2(t)}{\partial \Sigma_v} & \frac{\partial \mathbf{n}_2(t)}{\partial \Sigma_i} & \frac{\partial \mathbf{n}_2(t)}{\partial r_i} \\ \frac{\partial \mathbf{n}_3(t)}{\partial \Sigma_v} & \frac{\partial \mathbf{n}_3(t)}{\partial \Sigma_i} & \frac{\partial \mathbf{n}_3(t)}{\partial r_i} \end{matrix} \right]_m^1 \\ \vdots & \ddots & \vdots \\ \left[\begin{matrix} \frac{\partial \mathbf{n}_1(t)}{\partial \Sigma_v} & \frac{\partial \mathbf{n}_1(t)}{\partial \Sigma_i} & \frac{\partial \mathbf{n}_1(t)}{\partial r_i} \\ \frac{\partial \mathbf{n}_2(t)}{\partial \Sigma_v} & \frac{\partial \mathbf{n}_2(t)}{\partial \Sigma_i} & \frac{\partial \mathbf{n}_2(t)}{\partial r_i} \\ \frac{\partial \mathbf{n}_3(t)}{\partial \Sigma_v} & \frac{\partial \mathbf{n}_3(t)}{\partial \Sigma_i} & \frac{\partial \mathbf{n}_3(t)}{\partial r_i} \end{matrix} \right]_1^n & \cdots & \left[\begin{matrix} \frac{\partial \mathbf{n}_1(t)}{\partial \Sigma_v} & \frac{\partial \mathbf{n}_1(t)}{\partial \Sigma_i} & \frac{\partial \mathbf{n}_1(t)}{\partial r_i} \\ \frac{\partial \mathbf{n}_2(t)}{\partial \Sigma_v} & \frac{\partial \mathbf{n}_2(t)}{\partial \Sigma_i} & \frac{\partial \mathbf{n}_2(t)}{\partial r_i} \\ \frac{\partial \mathbf{n}_3(t)}{\partial \Sigma_v} & \frac{\partial \mathbf{n}_3(t)}{\partial \Sigma_i} & \frac{\partial \mathbf{n}_3(t)}{\partial r_i} \end{matrix} \right]_m^n \end{matrix} \right\}_{3 \cdot tb \cdot n \;\; x \;\; 3 \cdot m}$$

where each row (from top to bottom, superscripts $j = 1$ to n) contains the derivatives of each three-detector time decay measurement with respect to virgin-zone Sigma, invasion-zone Sigma, and radial length of invasion for all the sublayers in the model (from left to right, subscripts $i = 1$ to m). The size of the Jacobian sensitivity matrix is $3 \cdot tb \cdot n$ rows, which correspond to three time decays with *tb* number of time bins each, measured at *n* depth locations, and $3 \cdot m$ columns, which correspond to three formation properties for *m* number of model sublayers.

The efficiency of the inversion algorithm relies mostly on the calculation of the Jacobian matrix. It can be calculated numerically, but it is not practical for petrophysical applications where large volumes of data need to be processed. Instead, I make use of a-priori knowledge of the sensitivity functions of the detectors and the fast-forward model to analytically calculate the derivatives. . Extending the work on 1D radial inversion of multi-detector time decays introduced in Chapter 4, the analytical expression for the fast-forward multi-detector decay model at measurement point *j* can be expressed as

$$\mathbf{n}\left(\mathbf{r}_R, t, j\right) = \sum_{i=1}^{m} \gamma^i \cdot \left\{ \left[\int_0^{r_i(i)} \mathrm{FSF}\left(\mathbf{r}_R, \mathbf{r}_i, \Sigma_{a_B}\right) d\mathbf{r} \right] \mathbf{n}_i\left(\mathbf{r}_R, t, i\right) + \left[\int_{r_i(i)}^{\infty} \mathrm{FSF}\left(\mathbf{r}_R, \mathbf{r}_i, \Sigma_{a_B}\right) d\mathbf{r} \right] \mathbf{n}_v\left(\mathbf{r}_R, t, i\right) \right\} \tag{5.5}$$

where γ^i is the total sensitivity of detector $\mathbf{r}_R$ to sublayer *i* (calculated from the 3D earth model and FSFs used by the inversion algorithm), $\mathbf{n}\left(\mathbf{r}_R, t, j\right)$ is the bulk detector-dependent time decay for depth location sub-*j*, *m* is the number of model sublayers, $\mathrm{FSF}\left(\mathbf{r}_R, \mathbf{r}_i, \Sigma_{a_B}\right)$ is the portion of an average FSF for all the materials within the volume of investigation (at average background Sigma, Σ_{a_B}) of detector $\mathbf{r}_R$ located at sublayer *i*, $\mathbf{n}_i\left(\mathbf{r}_R, t, i\right)$ is the time- and detector-dependent decay at invasion zone in sublayer *i*, $\mathbf{n}_v\left(\mathbf{r}_R, t, i\right)$ is the time- and detector-dependent decay at virgin zone in sublayer *i*, $r_i(i)$ is radial length of invasion at sublayer *i*, and $\mathbf{r}_i$ is the position vector of sublayer *i*. Because the integral of the FSF in the radial direction is defined as the radial geometrical factor, *J*, I express

$$J(\mathbf{r}_R, r_i(i), \Sigma_{a_B}) = \int_0^{r_i(i)} \mathrm{FSF}\left(\mathbf{r}_R, \mathbf{r}_i, \Sigma_{a_B}\right) d\mathbf{r}\,. \tag{5.6}$$

Equation 5.5 can then be rewritten as

$$\mathbf{n}\left(\mathbf{r}_R, t, j\right) = \sum_{i=1}^{m} \gamma^i \cdot \left\{ J(\mathbf{r}_R, r_i(i), \Sigma_{a_B}) \cdot \mathbf{n}_i\left(\mathbf{r}_R, t, i\right) + \left[1 - J(\mathbf{r}_R, r_i(i), \Sigma_{a_B})\right] \cdot \mathbf{n}_v\left(\mathbf{r}_R, t, i\right) \right\}, \tag{5.7}$$

To account for the sensitivity of the detector response to radial length of invasion, analogously to the approach introduced in Chapter 4, the radial geometrical factor is expressed in terms of a fitted third-degree polynomial specific to each detector, which is a function of radial length of invasion, i.e.

$$J(\mathbf{r}_R, r_i(i), \Sigma_{a_B}) = \left[a(\mathbf{r}_R) r_i(i)^3 + b(\mathbf{r}_R) r_i(i)^2 + c(\mathbf{r}_R) r_i(i) + d(\mathbf{r}_R) \right], \tag{5.8}$$

where $a(\mathbf{r}_R)$, $b(\mathbf{r}_R)$, $c(\mathbf{r}_R)$, and $d(\mathbf{r}_R)$ are detector-specific constants fitted to $J(\mathbf{r}_R, r_i(i), \Sigma_{a_B})$ for an average background FSF. The constants are calculated separately for each detector, and each depth location. Additionally, these constants are updated at each iteration due to the dependency of the sensitivity factor on Sigma of the logging environment. In the case of thinly bedded formations, I select an average background FSF corresponding to an average background Sigma Σ_{a_B}, which is defined as follows

$$\Sigma_{a_B} = \int d\mathbf{r} \mathrm{FSF}\left(\mathbf{r}_R, \mathbf{r}_i, \Sigma_{a_{ref}}\right) \Sigma_a(\mathbf{r})\,. \tag{5.9}$$

Σ_{a_B} is an FSF-weighted average of all the Sigmas within the volume of sensitivity of each detector.

Initially, I select a detector-specific FSFs for a 10-c.u. material (selected by default) to weight the Sigmas of the model, i.e, $\Sigma_{a_{ref}}$ = 10 c.u. This weighted Sigma, Σ_{a_B}, is then used to select detector-specific FSFs that are used to weight model Sigmas in space. FSFs are selected from the FSF library used by the fast-forward model introduced in Chapter 3.

The multi-detector forward simulation model at measurement point *j* for sublayers *i*=1:*m* is then written as

$$\mathbf{n}(\mathbf{r}_R, t, j) = \sum_{i=1}^{m} \gamma^i \cdot \left\{ \begin{array}{l} \left[a(\mathbf{r}_R) r_i(i)^3 + b(\mathbf{r}_R) r_i(i)^2 + c(\mathbf{r}_R) r_i(i) + d(\mathbf{r}_R) \right] \cdot \mathbf{n}_i(\mathbf{r}_R, t, i) + \\ \left[1 - a(\mathbf{r}_R) r_i(i)^3 - b(\mathbf{r}_R) r_i(i)^2 - c(\mathbf{r}_R) r_i(i) - d(\mathbf{r}_R) \right] \cdot \mathbf{n}_v(\mathbf{r}_R, t, i) \end{array} \right\}. \quad (5.10)$$

The derivatives in the Jacobian matrix required to perform the 2D inversion can be rapidly calculated for sublayer *i* and measurement point *j* using the following analytical expressions

$$\left. \frac{\partial \mathbf{n}(\mathbf{r}_R, t, j)}{\partial \Sigma_v} \right|_i^j = \sum_{i=1}^{m} \gamma^i \left[\left(1 - a(\mathbf{r}_R) r_i(i)^3 - b(\mathbf{r}_R) r_i(i)^2 - c(\mathbf{r}_R) r_i(i) - d(\mathbf{r}_R) \right) \cdot \frac{\partial \mathbf{n}(\mathbf{r}_R, t, i)}{\partial \Sigma_v} \right], \quad (5.11)$$

$$\left. \frac{\partial \mathbf{n}(\mathbf{r}_R, t, j)}{\partial \Sigma_i} \right|_i^j = \sum_{i=1}^{m} \gamma^i \left[\left(a(\mathbf{r}_R) r_i(i)^3 + b(\mathbf{r}_R) r_i(i)^2 + c(\mathbf{r}_R) r_i(i) + d(\mathbf{r}_R) \right) \cdot \frac{\partial \mathbf{n}(\mathbf{r}_R, t, i)}{\partial \Sigma_i} \right], \quad (5.12)$$

and

$$\left. \frac{\partial \mathbf{n}(\mathbf{r}_R, t, j)}{\partial r_i} \right|_i^j = \sum_{i=1}^{m} \gamma^i \left[\left(3a(\mathbf{r}_R) r_i(i)^2 + 2b(\mathbf{r}_R) r_i(i) + c(\mathbf{r}_R) \right) \cdot \left(\mathbf{n}_i(\mathbf{r}_R, t, i) - \mathbf{n}_v(\mathbf{r}_R, t, i) \right) \right]. \quad (5.13)$$

5.2.3 Assessment of Uncertainty

Inversion of virgin-zone Sigma and radial length of invasion in acquisition conditions where the detectors are simultaneously sensing several formations can be highly non-unique. The uncertainty in the estimation increases as formation thickness decreases and virgin- and invasion-zone Sigma contrast decreases. Additionally, the 2D inversion algorithm might occasionally converge more rapidly in logging environments where time decays are smooth due to the lack of strong absorbers, which is the case in hydrocarbon-bearing formations. In shales, time decays are typically affected by statistical noise because shales contain strong absorbers that generate lower count rates.

The uncertainty of the estimations presented in this chapter is assessed using the modified covariance-matrix method introduced in Chapter 4. In addition, estimations of virgin formation Sigma and radial length of invasion are presented with the Confidence Index (*CI*) described in Chapter 4, section 4.3.3. *CI* is presented in the form of color tracks; one is presented next to the estimations of virgin-zone Sigma, and one is presented next to the estimations of radial length of invasion. Error bars are useful to diagnose cases in which the algorithm does not converge and cannot reconstruct the set of measured decays. Appropriate assessment of uncertainty requires inspecting error bars and *CI* concurrently.

5.3 SYNTHETIC RESULTS

The 2D inversion method was tested with two synthetic and two field cases. Synthetic cases include shallow-invaded and thinly bedded formations in a vertical well and a highly deviated well. In these examples, multi-detector time decays are affected by

geometrical and environmental effects at a degree that conventional interpretation of the measurements leads to biased petrophysical interpretations. Field cases illustrate the potential of the inversion to detect shallow invasion in measurements simultaneously affected by shoulder beds and geometrical effects due to well deviation. All cases indicate that it is possible to accurately estimate water saturation in realistic logging environments using Sigma logs if the inversion algorithm is used to reduce invasion and shoulder-bed effects. I show how implementation of the method, despite requiring more effort than conventional interpretation, leads to more robust petrophysical assessments that enable the understanding of other borehole measurements, such as neutron and density logs.

5.3.1 Synthetic Case I

Synthetic Case I comprises a sequence of 0.2286-m (0.75-ft) siliciclastic layered formations in which 200-kppm [NaCl] mud filtrate has been assumed to invade permeable gas-bearing sandstone formations at different radial lengths of invasion, as shown in **Figure 5.2**. High mud-filtrate salinity, even though unusual in common logging situations, was assumed in order to generate significant invasion effects on Sigma logs. Connate water salinity is 80 kppm [NaCl]. Formations are assumed to be penetrated by a vertical well in which multi-detector LWD decays are simulated every 0.1524 m for the commercial multi-function tool under study. Filtrate invasion is in the range of 5.08 cm to 20.32 cm in the sandstone layers. **Table 5.1** displays the assumed petrophysical properties of the formations in the configuration calculated using Schlumberger Nuclear Parameter calculation program, SNUPAR (McKeon et al., 1989).

Figure 5.3 shows Sigma logs derived from synthetic and reconstructed time decays (solid blue and red lines), as well as actual and estimated layer-by-layer virgin-zone Sigmas (dashed blue and red lines) with error bars for the SSn, LSn, and Near detectors, respectively, (a), (b), and (c), along with reference invasion-zone Sigma (black dashed line). Borehole- and diffusion-corrected Sigma logs (solid lines) and actual virgin- and invasion-zone layer-by-layer Sigmas (dashed lines) are shown on track (d), along with the actual and estimated invasion profile with confidence index, *CI*, on track (e). Track (f) shows a sketch of the borehole, invasion profile and formation, and track (g) shows estimated water saturation derived from uncorrected Sigma (one-detector SSn) and corrected Sigma for shoulder-bed and invasion effects (through the 2D inversion) compared to actual layer-by-layer formation water saturation.

The combined effect of shoulder beds and shallow invasion on LWD Sigma measurements is evidenced on track (d) in **Figure 5.3**: In the case of invaded layers, the three logs display Sigma values that are inconsistent with the virgin-zone Sigma value and read higher values due to the salinity of mud filtrate. The effect is accentuated in the third permeable layer (at 1 m) because of deeper radial length of invasion (20.32 cm). Observe that the permeable layers at the top (0.13 m) and at the bottom (2 m) have invasion fronts of similar radial extension, but the separation between the curves is larger at the top permeable layer because of the additional shoulder-bed effects caused by adjacent shale formations. Additionally, observe that the three Sigma logs do not overlap across the shale formations, even though these formations are not invaded. This behavior takes place

because the formations are 0.2286-m thick, which is below the vertical resolution of the Near detector (approximately 0.3048 m), and all measurements are considerable affected by shoulder-bed effects.

Virgin-zone Sigmas estimated from the 2D inversion agree notably well with actual formation Sigmas (a), (b), and (c), which translates to accurate estimations of water saturation, (g). I estimate water saturation using a volumetric mixing formula and by assuming the matrix composition is known, from which matrix Sigma is calculated and reported in **Table 5.1**. Gas Sigma equals 7 c.u. is calculated using SNUPAR at assumed conditions of 24132.65 kPa (3500 psia) and 150^{o}F. Not correcting for invasion effects results in virgin-zone Sigma values much higher than actual values, leading to overestimated water saturation, which can be appreciated by comparing the dashed and solid blue lines on track (g). The effectiveness of the correction is a function of radial length of invasion because detectors lose sensitivity to the virgin zone as radial length of invasion increases. This behavior is reflected in the poor estimation of water saturation in the permeable layer at 1 m where invasion is (20.32 cm). Moreover, shale shoulder beds, which are strong absorbers, can increase water saturation further and result in water saturation values above 1, as depicted by the dashed line on track (g).

The 2D inversion algorithm also provides additional information about radial length of invasion in the sequence of layers. Radial length of invasion within this shallow near-wellbore zone would be very difficult to estimate using other measurements, such as array resistivity (Ortega et al., 2013). The distinct difference in depth of investigation of

the three detectors in the shallow near-wellbore zone permits one to recognize the impact of invasion on other nuclear measurements that are also shallow-sensing, such as neutron and density.

Figure 5.3 shows the simultaneous use of covariance-derived error bars and color flags given by the confidence index (*CI*) as a function of radial length of invasion and Sigma contrast. The confidence index permits to see the increase in uncertainty in virgin-zone Sigma as radial length of invasion increases. It also allows to see increased uncertainty in radial length of invasion as invasion is deeper. Error bars and *CI* display the high uncertainty in the estimation of radial length of invasion in shale layers as a consequence of the small contrast between actual shale Sigma and Sigma if the shale were invaded.

5.3.2 Synthetic Case II

This synthetic example shows the full potential of the 2D algorithm in isolating simultaneous shoulder-bed, shallow invasion, and the added complexity of high-angle well-deviation effects. I generate three detector thermal-neutron and gamma-ray decays in a sequence that comprises three 15.24 cm (0.5 ft) oil-bearing sandstone formations inter-bedded within impermeable shale layers that are penetrated by the high-angle well (85^{o}), as sketched in **Figure 5.4**. The oil-bearing layers are invaded at different radial lengths by 200-kppm [NaCl] mud filtrate. Connate water salinity is 80 kppm [NaCl]. **Table 5.2** shows assumed petrophysical properties of the layers in the sequence calculated using SNUPAR. It should be noted that the relative angle between the layers and the well is not to scale. Notice in

Figure 5.4 shows that due to the high angle between well and formation bedding plane, the detectors sense significantly different portions of the configuration at different azimuthal sectors. This configuration is difficult to interpret using conventional methods due to the simultaneous contribution to detector responses from several portions of the formations toward each measurement point. Although larger relative angle between formations and well axis represents increased measured thickness (compared to stratigraphic thickness), in the case of thinly bedded formations, high-angled measurements accentuate the effect of shoulder beds due to the presence of several formations within the volume of investigation of the detectors.

I explain the complexity of the measurement by first looking at multi-detector Sigma logs derived from forward-simulated decays with and without invasion effects. Simulations without invasion enable to observe the pronounced effect of well deviation and shoulder beds on detector response, and simulations with invasion allow to observe the full complexity of having all the described environmental and geometrical effects convoluted into the detector's response. **Figure 5.5** illustrates forward-simulated azimuthally averaged logs with and without invasion (a), forward-simulated multi-sector Sigma measurements without considering invasion (b) and when considering invasion (c). Observe in **Figure 5.5a** that the good vertical resolution of the thermal neutron Near detector permits the detection of 15.24-cm layers, while the gamma-ray detectors average the properties of the sand and shale layers into a single bulk response.

LWD Sigma images in **Figure 5.5b** and **Figure 5.5c** reflect how the focused azimuthal sensitivity of the thermal-neutron Near detector enables the recognition of the relative angle between well and formations similarly to density images. The LSn detector shows only one bulk formation with averaged properties. **Figure 5.5c** sums the effect of shallow invasion on the Sigma images. The Near detector, being shallow sensing, shows that the effect of shallow invasion completely masks the response of the bottom sandstone formation. The main challenge of combined shoulder-bed and invasion effects is that the LSn detector is largely affected by shoulder-bed effects and the Near detector is largely affected by shallow invasion; the effect is intermediate in the SSn detector.

I display 2D inversion results in **Figure 5.6**. The figure shows Sigma logs derived from synthetic and reconstructed time decays (solid blue and red lines) and actual and estimated layer-by-layer virgin-zone Sigmas (dashed blue and red lines) with error bars for the SSn, LSn, and Near detectors, (a), (b), and (c), respectively, along with reference invasion-zone Sigma (black dashed line) and confidence index *CI*. Borehole- and diffusion-corrected Sigma logs (solid lines) and actual virgin- and invasion-zone layer-by-layer Sigmas (dashed lines) are shown on track (d), and actual and estimated invasion profile with confidence index *CI* is shown on track (e). A sketch of the borehole, invasion profile and formation is also included (f), and track (g) shows estimated water saturation derived from uncorrected Sigma (one-detector SSn) and corrected for shoulder-bed and invasion effects using the 2D inversion compared to actual layer-by-layer formation water saturation.

The good match between Sigma logs derived from synthetic and reconstructed decays in **Figure 5.6** leads to an excellent match in virgin-zone Sigma, even in the middle and bottom sand formations where *CI* is low due to deeper invasion. The 2D inversion was also able to accurately estimate radial length of invasion in all the layers. The correction is reflected in a reliable prediction of water saturation on track (g). In this case, conventional interpretation leads to values of water saturation below 0 and above 1. As previously mentioned, this is one of the most complex situations that might be encountered in real Sigma logging. Results reflect the potential of the method to aid in the isolation of environmentally and geometrically affected thermal-neutron and gamma-ray time decays (Sigma logs) that can be used to accurately estimate water saturation in situations where resistivity logs lack of quality or where interpretation is difficult, e.g. carbonates or low-contrast low-resistivity laminated formations.

5.4 FIELD RESULTS

5.4.1 Field Case I

Field Case I consists of LWD measurements acquired with the commercial LWD tool under study in a sequence of thinly bedded siliciclastic formations in an offshore deviated well drilled with 136-kppm [NaCl] synthetic-based mud (SBM). Calcite is present throughout the sequence as revealed by gamma-ray spectroscopy logs, most likely in the form of cement. Connate water salinity is approximately 130 kppm [NaCl] based on analysis of water samples in nearby wells. **Figure 5.7** shows a sketch of the well trajectory

along with the SSn Sigma log. The section of interest is the gas-bearing section, as indicated in the figure, where well deviation is approximately 45^{o}. I assess the presence of gas from neutron and density log analysis. This section is of particular importance because Sigma of gas and Sigma of high-salinity filtrate generate large Sigma contrast between virgin and invasion zones, which is ideal to evaluate filtrate invasion using the multi-detector Sigma measurement. Shallow invasion is suspected due to approximately 1 hour of exposure to drilling fluids before the LWD measurements were acquired, known from penetration rate (*ROP*) logs. Additionally, the measurements are affected by shoulder bed effects due to the presence of formations with thicknesses below 0.3 m, and by well-deviation effects caused by the large relative angle between well axis and formation dip plane.

Figure 5.8 shows LWD nuclear (gamma-ray, neutron, density, Sigma logs and decay curves, and spectroscopy) and resistivity logs (high-frequency phase resistivity) acquired in the gas-bearing laminated section. The purpose of this figure is to display the most important nuclear measurements acquired by the multi-function LWD tool and the three-detector time decays required to perform the inversion. The three sets of decays shown on tracks (f), (g), and (h) are the data vectors to be reconstructed using the 2D inversion algorithm. Notice the smoothness of the SSn time decays and the increase of statistical noise in the late-time windows of the LSn and Near detector time decays. Track (i) displays multi-detector Sigma logs derived from the three sets of decays, as delivered by the service company after applying borehole and diffusion corrections.

Intuition suggests that the separation of the multi-depth-of-investigation (MDOI) Sigma logs should be used analogously to resistivity measurements to identify the presence of invasion. However, the problem at hand is not that simple. In the case of thick formations, separation of the curves is affected not only by the presence of invasion, but also by detector-dependent borehole/diffusion corrections. In this situation the three-detector decays are additionally affected at a different level by shoulder-bed effects. This is why the separation of the curves does not seem to follow any pattern, and appears to be random. Analysis of the separation of multi-detector Sigma logs in the two synthetic examples shown before suggests that it is not possible to qualitatively interpret the separation of the logs, since they integrate several environmental and geometrical effects. The best way to approach the interpretation of multi-detector decay curves, then, is to simultaneously decouple shoulder-bed and shallow invasion effects while reproducing the measured decay curves by applying the 2D inversion with pre-defined bed-boundary locations.

Figure 5.9 presents inversion results for Field Case I. Track (a) shows borehole- and diffusion-corrected multi-detector Sigma logs derived from re-constructed time decays along with the invasion-zone reference log. Estimated virgin-zone Sigma with error bars and *CI* (b), and estimated radial length of invasion with error bars and *CI* (c), are also shown. A sketch of borehole, formation and invasion profile is included in track (d). I also show a compensated density image, neutron and density porosity logs, squared averaged porosity logs, along with assumed bed boundaries (e), and high-frequency phase resistivity

logs (f). Spectroscopy logs are shown along with results of estimated water saturation from one-detector uncorrected SSn Sigma log, resistivity log, and 2D inversion corrected Sigma log (g). Additionally, a comparison of the vertical resolution of the shallowest resistivity measurement (P16H) to SSn Sigma logs is displayed on track (h). Bed boundary locations were calculated using the sinusoidal sharp boundaries observed in the compensated density image.

Deflections in the SSn Sigma log on track (h) better agree than resistivity logs with deflections observed in the compensated density image, and neutron and density logs because all nuclear measurements have similar volumes of investigation, typically smaller than the volume of investigation of propagation measurements. The shallow resistivity log, having a larger volume of investigation than all nuclear measurements, appears flatter because each measurement point is averaging the properties of several thin layers. Moreover, the inversion of multi-detector decays helps to understand the behavior of neutron and porosity crossovers. Notice how deep invasion causes a suppression of the neutron and density gas crossover at X29.5 and X34.5 m. Nonetheless, there are sections were the crossover is suppressed even though there is no invasion. This is because these layers exhibit significantly high water saturations, as calculated from 2D-inversion corrected virgin-zone Sigma.

Water saturation from the 2D inversion is compared to water saturation from the shallow resistivity measurement and to uncorrected one-detector SSn Sigma on track (g). As indicated above, the improved vertical resolution of the Sigma inversion results in larger

deflections in water saturation throughout the thinly bedded sequence. The inversion identifies hydrocarbon-bearing zones where water saturation is as much as 100% less than predicated by the uncorrected SSn-Sigma derived water saturation, e.g., formations at X26.5, and X34.5 m. These estimations, however can be, affected by deep invasion. The resistivity log seems undisturbed by the presence of shallow invasion, which agrees with the observations of Ortega et al. (2013) in simulations of Sigma and PH resistivity logs in shallow invaded formations, and the radial geometrical factors shown in Chapter 1. The study describes how the resistivity log is minimally affected by the presence of invasion within the shallow near-wellbore section in thick layers. Considering the sequence under study includes averaged measurements of several thin layers, some with shallow invasion and some uninvaded, the expected effect of invasion on the resistivity measurement is even smaller than reported in their study.

An important feature displayed in **Figure 5.9** is that formations with deeper invasion show smaller *CI* in virgin-zone Sigma, which is reflected in larger error bars in water saturation. This is resultant of the loss of sensitivity to the virgin zone when the radial length of invasion is deep. Results of the 2D inversion should be carefully analyzed and estimations of water saturation are to be trusted only when invasion remains shallow (within 20 cm approximately) and when there exists enough Sigma contrasts between virgin- and invasion-zone Sigmas.

5.4.2 Field Case II

Field Case II is oriented to exhibit the potential of the 2D inversion algorithm to simultaneously isolate shoulder-bed and well-deviation effects (rather than invasion effects) from LWD Sigma logs acquired in a laminated sequence in the North Sea. These field decays are highly affected by geometrical effects, as the well penetrates a sequence of thinly bedded formations at an angle of approximately 70^{o} in the section of interest. **Figure 5.10** illustrates the well trajectory along with the SSn Sigma log and indicates the location of the laminated section of interest. The assessment of invasion in this case is challenging because mud filtrate salinity is 46 [NaCl] kppm and porosity is not significantly high (~15%); therefore, invaded- and virgin–zone Sigma contrast is low, resulting in high uncertainty in estimated radial length of invasion. Connate water salinity is approximately 35 kppm [NaCl] (Hansen, 2009). This case is interesting for the application of Sigma logs because it is a showcase of LWD propagation resistivity log displaying horn effects due to relative changes in well deviation and possible resistivity anisotropy. Sigma measurements are better suited than resistivity to estimate water saturation in this sequence because of the greater vertical resolution of Sigma logs compared to resistivity logs, and also because it is easier to decouple shoulder-bed effects from Sigma than from resistivity measurements, given the differences in effective volume of investigation.

Figure 5.11 shows inversion results for Field Case II. Borehole- and diffusion-corrected multi-detector Sigma logs derived from re-constructed time decays along with

invasion-zone Sigma reference log are shown on track (a). I also show estimated virgin-zone Sigma with error bars and *CI* (b), and estimated radial length of invasion with error bars and *CI* (c). A sketch of borehole, formation and invasion profile is included on track (d). A compensated density image, neutron and density porosity logs, squared averaged porosity logs, assumed bed boundaries (e), and high-frequency phase resistivity logs (f) are also shown. Spectroscopy logs are presented with results of water saturation from one-detector uncorrected SSn Sigma log, P16H resistivity log, and 2D inversion corrected Sigma log (g). In addition, a comparison of the shallowest propagation resistivity measurement (P16H) to SSn Sigma log is displayed on track (h). Bed boundary locations were calculated using the compensated density image.

Results from 2D inversion suggest that either invasion is minimal throughout the sequence or, because of the low invasion-virgin zone Sigma contrast, the impact of shallow invasion on virgin-zone Sigma is minimal, as discussed in Chapter 4. This is why water saturation calculated using the uncorrected SSn log and the 2D corrected Sigmas in track (g) are fairly similar along the thickest formations. The most significant differences between both curves are observed across thin layers at XX76 m, XX84 m, and XX86 m, where the 2D inversion improves the vertical resolution of the Sigma log and therefore enables to identify larger hydrocarbon saturations than would be estimated if shoulder-bed and well-orientation effects were not properly isolated. The advantage of the inversion to decouple these effects is especially evident in the section between XX84 m and XX89 m where the inversion allows to detect formations with low water saturation interbedded

between shale formations. Interpretation of the resistivity log alone, which averages all the thin layer properties, would lead to the overlooking of hydrocarbon-bearing formations. I find in this section that using the uncorrected SSn-derived water saturation would lead to overestimation of water saturation by as much as 50% in oil-bearing thin layers. This case is similar to the low-resistivity low-contrast case reported by Simpson et al. (2010) in Louisiana sands, where Sigma logs were crucial to identify and evaluate the thinly bedded hydrocarbon bearing formations.

Lastly, I discuss the differences between water saturation calculated from 2D inversion corrected Sigma and from PH resistivity logs related to different measurement volumes of investigation. Track (h) in **Figure 5.11** displays stretched versions of the shallowest PH resistivity log and SSn Sigma log, both displayed over the compensated density image. Observe that the resistivity log appears flat throughout the thin layers and is affected by horn effects. Also observe that the SSn Sigma log displays deflections that better agree with the density image and neutron and density logs, and that the SSn Sigma log is less affected by shoulder-bed effects than the resistivity log. Even the uncorrected SSn Sigma log displays much better vertical resolution than the resistivity log. The flatness in the resistivity log results in estimated water saturation that appears constant, which is due to the averaging of thin layers that stems from the large volume of sensitivity of the resistivity measurement. Horns in resistivity also generate anomalous values of water saturation at XX82 m. In addition, even though the contrast in invaded- and virgin-zone

Sigma in this field case is not significant, the estimated invasion profile agrees well with the behavior of the neutron-density gas crossover.

5.5 DISCUSSION

In this chapter I reduced invasion, shoulder-bed, and well-deviation effects on Sigma logs. Nonetheless, gamma-ray spectroscopy, density porosity, and neutron porosity logs can also be highly affected by shoulder-bed and well-deviation effects. The calculation of water saturation from the results obtained with the 2D inversion algorithm can be further improved if shoulder-bed and well-deviation effects are mitigated from spectroscopy and porosity logs because the estimation of water saturation from Sigma logs requires knowledge of matrix Sigma, which is derived from the volumetric mineral concentrations estimated from the spectroscopy log, together with knowledge of total porosity derived from neutron and density logs.

5.6. CONCLUSIONS

LWD Sigma measurements may sometimes be better suited for petrophysical evaluation of thinly bedded formations than resistivity measurements because of their smaller volume of investigation. This situation is especially true in the case of deviated wells penetrating thinly bedded formations, where resistivity logs average the properties of various layered formations and can display “horns” and anisotropy effects. I developed a 2D inversion algorithm that makes use of a rapid 3D multi-detector decay simulation method and enables simultaneously reducing shoulder-bed, shallow invasion, well-

deviation, borehole, and diffusion effects to estimate actual virgin-zone Sigma and radial length of invasion. The inversion algorithm makes the environmentally affected Sigma logs suitable for use in quantitative analysis of water saturation. I used error bars and a confidence index to diagnose when deep invasion generates high uncertainty in virgin-zone Sigma, and consequentially, in Sigma-derived water saturation.

Invasion effects should be eliminated as much as possible from LWD Sigma logs, especially when drilling with high-salinity mud. Invasion of salty mud filtrate results in overestimated water saturation in hydrocarbon-bearing formations. The overestimation is greater if there are shoulder high-Sigma layers, such as shales, affecting the measurement in hydrocarbon zones. This behavior can lead to overlooking thin hydrocarbon-bearing formations. Application of the 2D inversion in field cases allowed to quantify lower water saturation in hydrocarbon-bearing formations interspaced between shales than suggested by one-detector, uncorrected Sigma or resistivity log analyses. Water saturation was as much as 50% lower in the case of oil-bearing formations affected mostly by shoulder-bed and well-deviation effects, and as much as 100% lower in the case of gas-bearing thinly bedded formations additionally affected by high-salinity filtrate invasion. Furthermore, the estimation of radial length of invasion improved the diagnosis of neutron-density crossovers.

All the benefits of the 2D inversion algorithm notwithstanding, the reduction of invasion effects on Sigma logs requires high contrast between virgin- and invasion-zone Sigmas. Likewise, calculation of water saturation from Sigma is only accurate in logging

environments with salty connate water, where there exists sufficient contrast between water and hydrocarbon Sigma to enable quantitative differentiation. Furthermore, noise in multi-detector time decays and/or presence of standoff not accounted for in the 3D forward model can lead to inaccurate estimations of radial length of invasion that can impact water saturation calculated from estimated virgin-zone Sigma. Additionally, filters typically applied by services companies on nuclear measurements to improve statistical quality directly impact the vertical resolution of the measurements and limit the advantage of Sigma over resistivity logs to evaluate thinly bedded formations.

Based on observations of field measurements in deviated wells, I advise the use of Sigma logs to complement resistivity-based geosteering. Sigma logs correlate notably well with neutron, density and spectroscopy measurements because of their similar volumes of investigation, in contrast with propagation resistivity measurements. Differences in volume of investigation are especially important in the case of deviated wells; in such situation, nuclear measurements are better suited to identify and evaluate thinly bedded formations. Even though quantitative applications require good statistical quality of measured time decays, fast processing of the late-time components of the SSn detector signal has the potential to be used in real time to complement the use of deep resistivities, or even for standalone geosteering applications if the Sigma measurement devices were to be assembled closer to the drill bit. The second field case examined in this chapter indicated that standalone readings of the resistivity log would have been challenging to use for

geosteering purposes; Sigma logs allow to better observe when the well enters and exits low-Sigma, hydrocarbon-bearing formations and high-Sigma, shale layers.

Table 5.1: Summary of assumed lithology, thickness, porosity, water saturation (S_w), gas saturation (S_g), virgin-zone Sigma (Σ_v), invaded-zone Sigma (Σ_i), and matrix Sigma (Σ_m), and radial length of invasion (r_i) for the formations corresponding to Synthetic Case I. Filtrate salinity is 200 kppm [NaCl], Σ_{mf} = 96.6 c.u., connate water salinity is 80 kppm [NaCl], and Σ_w = 50.3 c.u.

Layer	**Lithology**	**Thickness (m)**	**Porosity (p.u.)**	S_w	S_g	Σ_v (c.u.)	Σ_i (c.u.)	Σ_m (c.u.)	r_i (cm)
1	Shale	0.2286	20	1	0	30.06	30.06	25	0
2	Sand	0.2286	25	0.1	0.9	6.21	27.53	4.5	5.08
3	Shale	0.2286	20	1	0	30.06	30.06	25	0
4	Sand	0.2286	30	0.15	0.85	7.20	32.13	4.5	10.16
5	Shale	0.2286	20	1	0	30.06	30.06	25	0
6	Sand	0.2286	28	0.2	0.8	7.62	30.29	4.5	20.32
7	Shale	0.2286	20	1	0	30.06	30.06	25	0
8	Sand	0.2286	22	0.3	0.7	7.91	24.76	4.5	15.24
9	Shale	0.2286	20	1	0	30.06	30.06	25	0
10	Sand	0.2286	32	0.4	0.6	10.84	33.97	4.5	5.08

Table 5.2: Summary of assumed lithology, thickness, porosity, water saturation (S_w), gas saturation (S_g), virgin-zone Sigma (Σ_v), invaded-zone Sigma (Σ_i), and matrix Sigma (Σ_m), and radial length of invasion (r_i) for the formations corresponding to Synthetic Case II. Filtrate salinity is 200 kppm [NaCl], Σ_{mf} = 96.6 c.u., connate water salinity is 80 kppm [NaCl], and Σ_w = 50.3 c.u.

Layer	**Lithology**	**Thickness (m)**	**Porosity (p.u.)**	S_w	S_g	Σ_v (c.u.)	Σ_i (c.u.)	Σ_m (c.u.)	r_i (cm)
1	Shale	0.1524	20	1	0	30.06	30.06	25	0
2	Sand	0.1524	25	0.1	0.9	9.13	27.53	4.5	5.08
3	Shale	0.1524	20	1	0	30.06	30.06	25	0
4	Sand	0.1524	30	0.15	0.85	10.51	32.13	4.5	10.16
5	Shale	0.1524	20	1	0	30.06	30.06	25	0
6	Sand	0.1524	28	0.2	0.8	10.54	30.29	4.5	20.32
7	Shale	0.1524	20	1	0	30.06	30.06	25	0

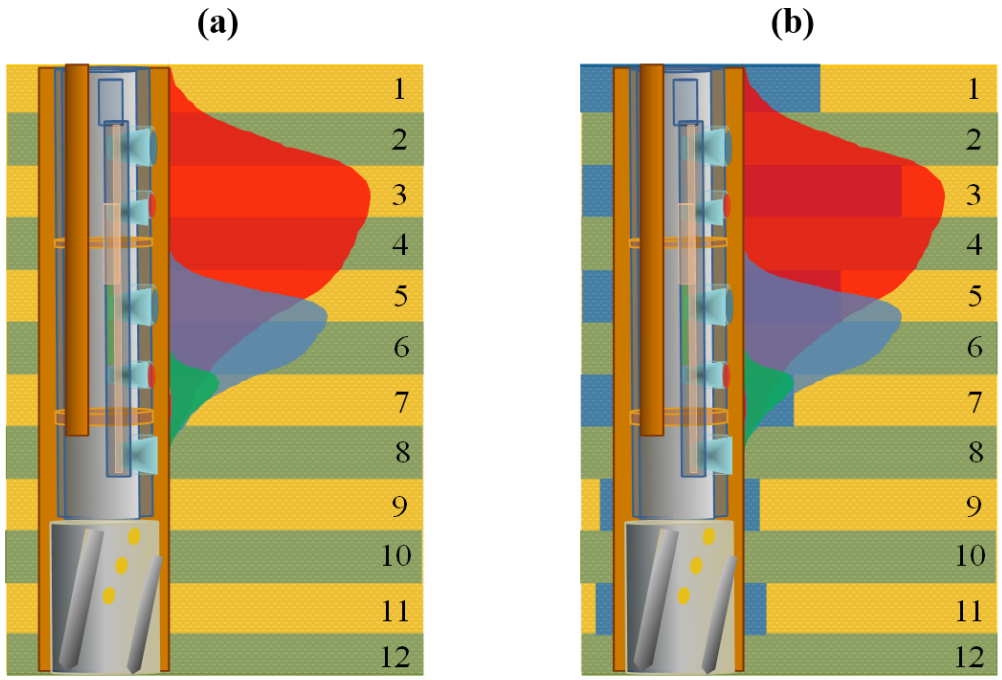

Figure 5.1: Sketch of Near (green), SSn (blue), and LSn (red) detector spatial sensitivity projected on thinly bedded formations without invasion (a), and with shallow invasion in permeable layers (b). The figure illustrates the complexity of estimating layer-by-layer properties under an acquisition condition where actual formation properties are simultaneously masked by shoulder-bed and shallow-invasion effects.

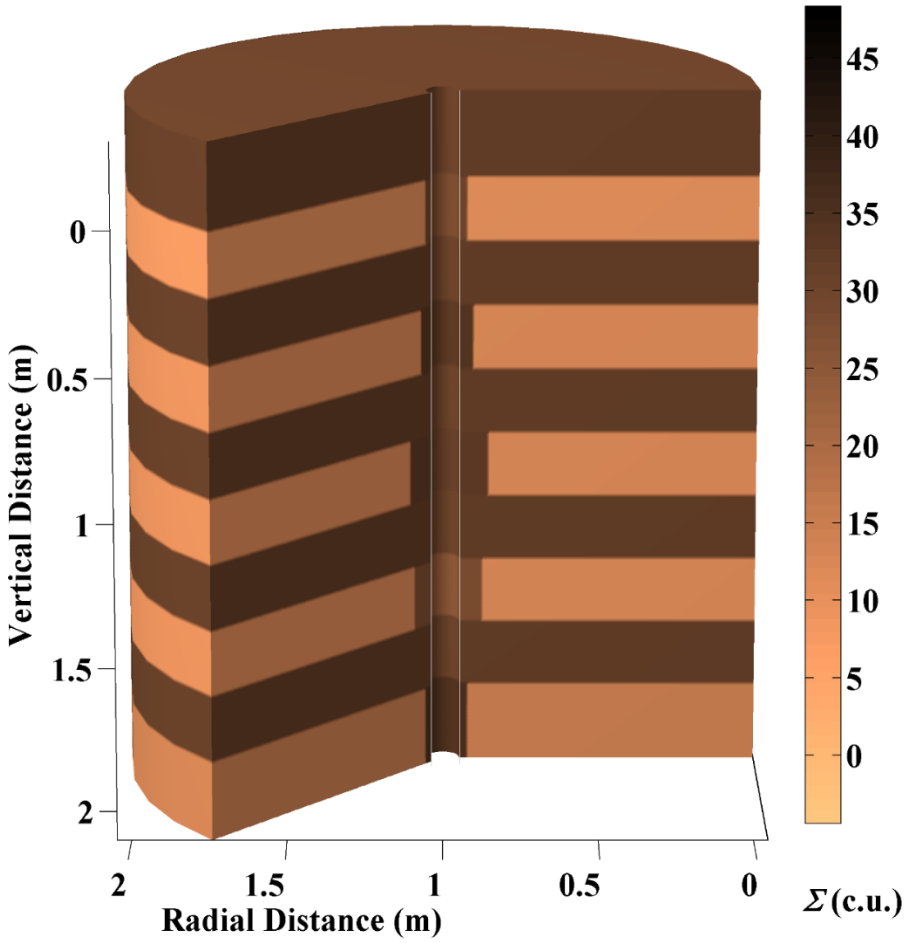

Figure 5.2: Representation of intrinsic Sigmas of the assumed siliciclastic sequence of 0.1524-m (0.5 ft) thick formations with shallow invasion in the permeable layers for Synthetic Case I. Water-based mud filtrate of 150 kppm [NaCl] invades gas-bearing formations of different connate water saturation. High-Sigma (dark) uninvaded formations represent shales.

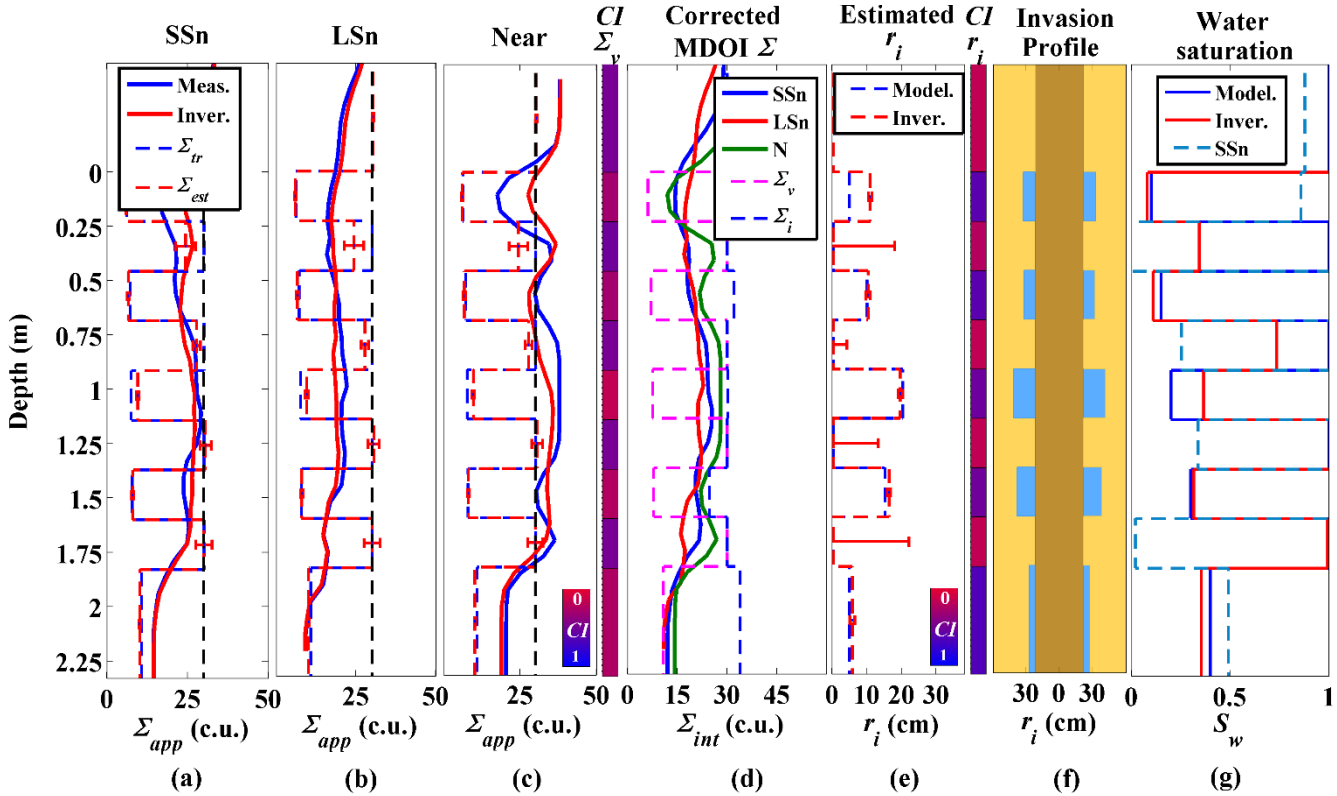

Figure 5.3: Inversion results for Synthetic Case I. (a), (b), and (c) Measured (blue solid line) and fitted (red solid line) apparent Sigma for the SSn, LSn, and Near detectors, respectively, and true model (blue dashed line) and estimated (red dashed line) virgin formation Sigma with error bars, and reference invasion-zone Sigma (black dashed line). (d) Multi-detector diffusion- and borehole-corrected Sigma logs, model virgin-zone (magenta dashed line) and invasion-zone (blue dashed line) Sigma, (e) actual (blue dashed line) and estimated (red dashed line) radial length of invasion with error bars, (f) diagram of borehole (brown), invasion (blue), and formation (yellow), and (g) actual (blue solid line), estimated (red solid line), and SSn-calculated (blue dashed line) water saturation. SSn-calculated water saturation represents the estimated water saturation calculated directly from the borehole- and diffusion-corrected SSn Sigma log at bed centers, without correcting for coupled shallow invasion and shoulder-bed effects.

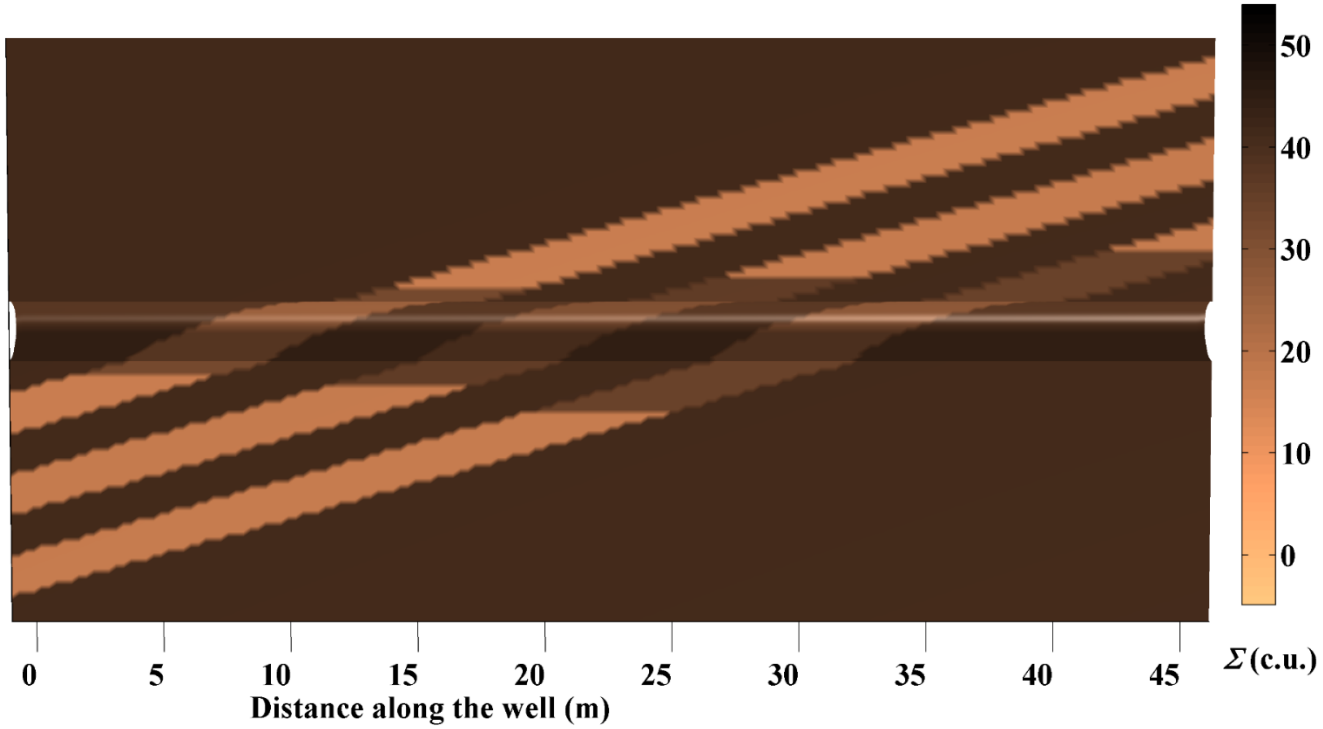

Figure 5.4: Representation of intrinsic Sigmas of assumed 0.1524-m (0.5 ft) thick oil-bearing sandstone formations embedded within shale formations and penetrated by an 85° deviated well for Synthetic Case II. Water-based mud of 200 kppm [NaCl] invades oil-bearing formations of different connate water saturation. The radial profile of invasion is assumed azimuthaly uniform in the three permeable layers.

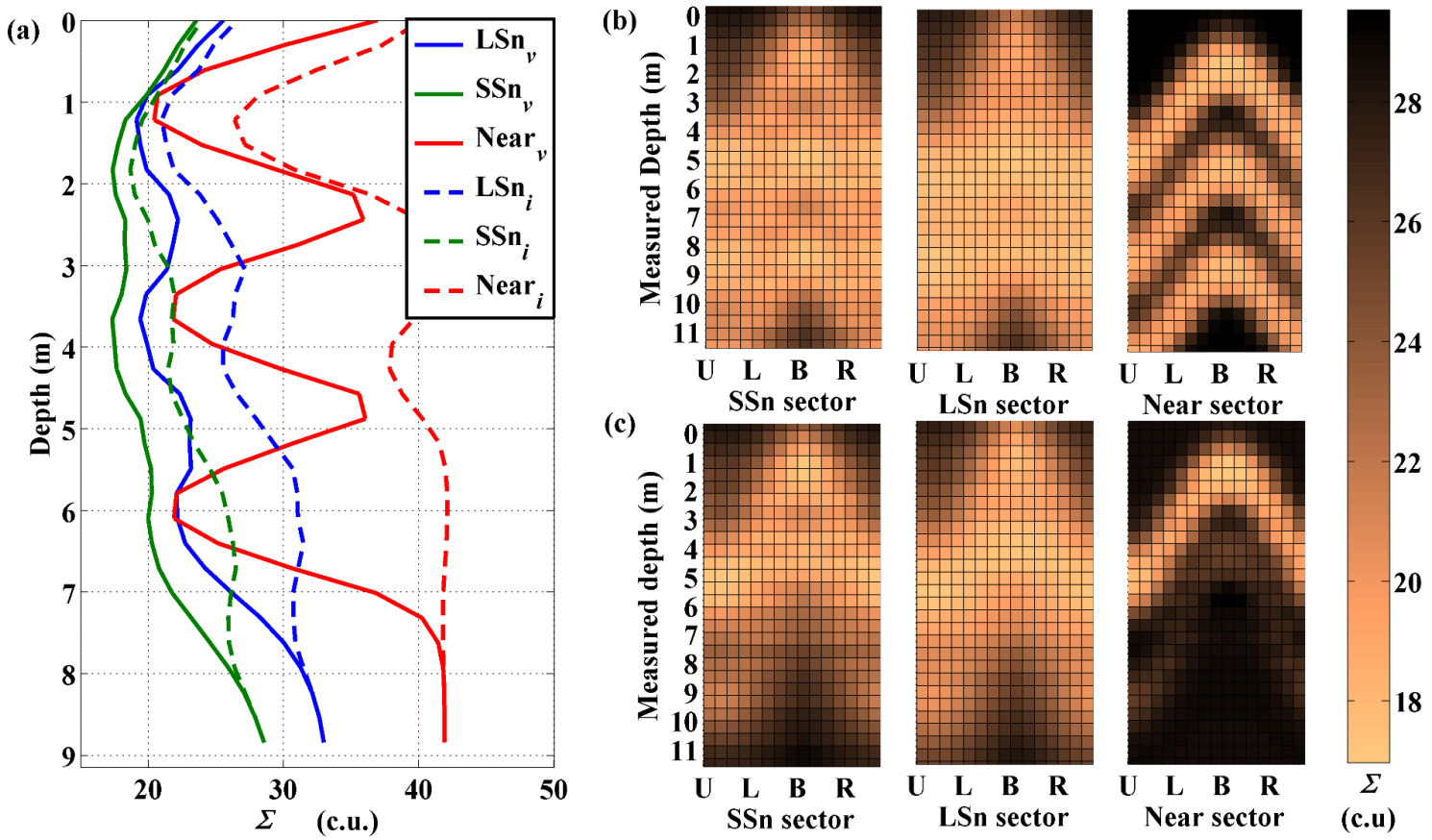

Figure 5.5: (a) Upper sector apparent multi-detector LWD Sigma logs for univaded (solid lines) and invaded (dashed lines) oil-bearing sandstone formations in Synthetic Case II. (b) Multi-detector LWD Sigma images in virgin formations, and (c) Multi-detector LWD Sigma images assuming invasion of 5.08 cm, 10.16 cm, and 20.32 cm in the three oil-bearing sandstone formations.

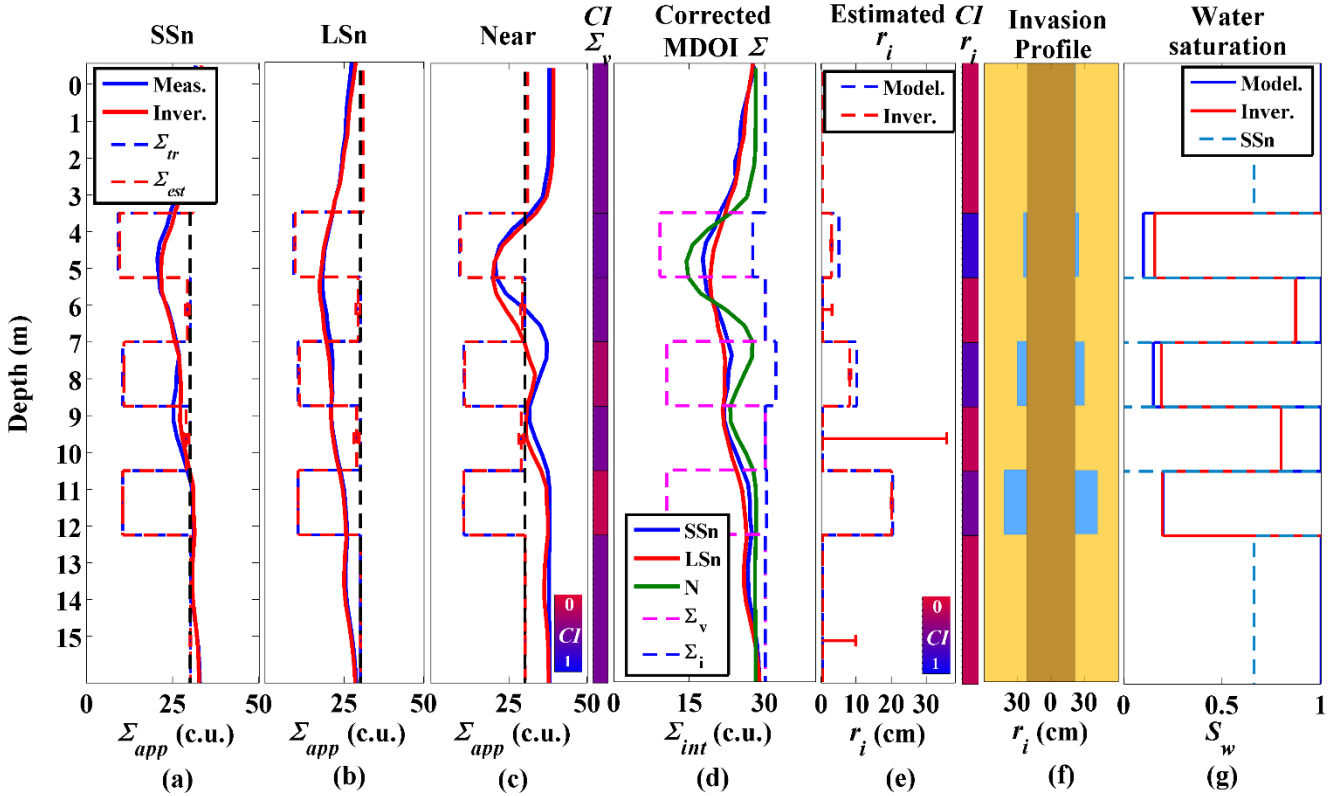

Figure 5.6: Inversion results for Synthetic Case II. (a), (b), and (c) Measured (blue solid line) and fitted (red solid line) apparent Sigma for the SSn, LSn, and Near detectors, respectively, and true model (blue dashed line) and estimated (red dashed line) virgin formation Sigma with error bars, and reference invasion-zone Sigma (black dashed line). (d) Multi-detector diffusion- and borehole-corrected Sigma logs, model virgin-zone (magenta dashed line) and invasion-zone (blue dashed line) Sigma, (e) actual (blue dashed line) and estimated (red dashed line) radial length of invasion with error bars, (f) diagram of borehole (brown), invasion (blue), and formation (yellow), and (g) actual (blue solid line), estimated (red solid line), and SSn-calculated (blue dashed line) water saturation. SSn-calculated water saturation represents the estimated water saturation calculated directly from the borehole- and diffusion-corrected SSn Sigma log at bed centers, without correcting for coupled shallow invasion and shoulder-bed effects.

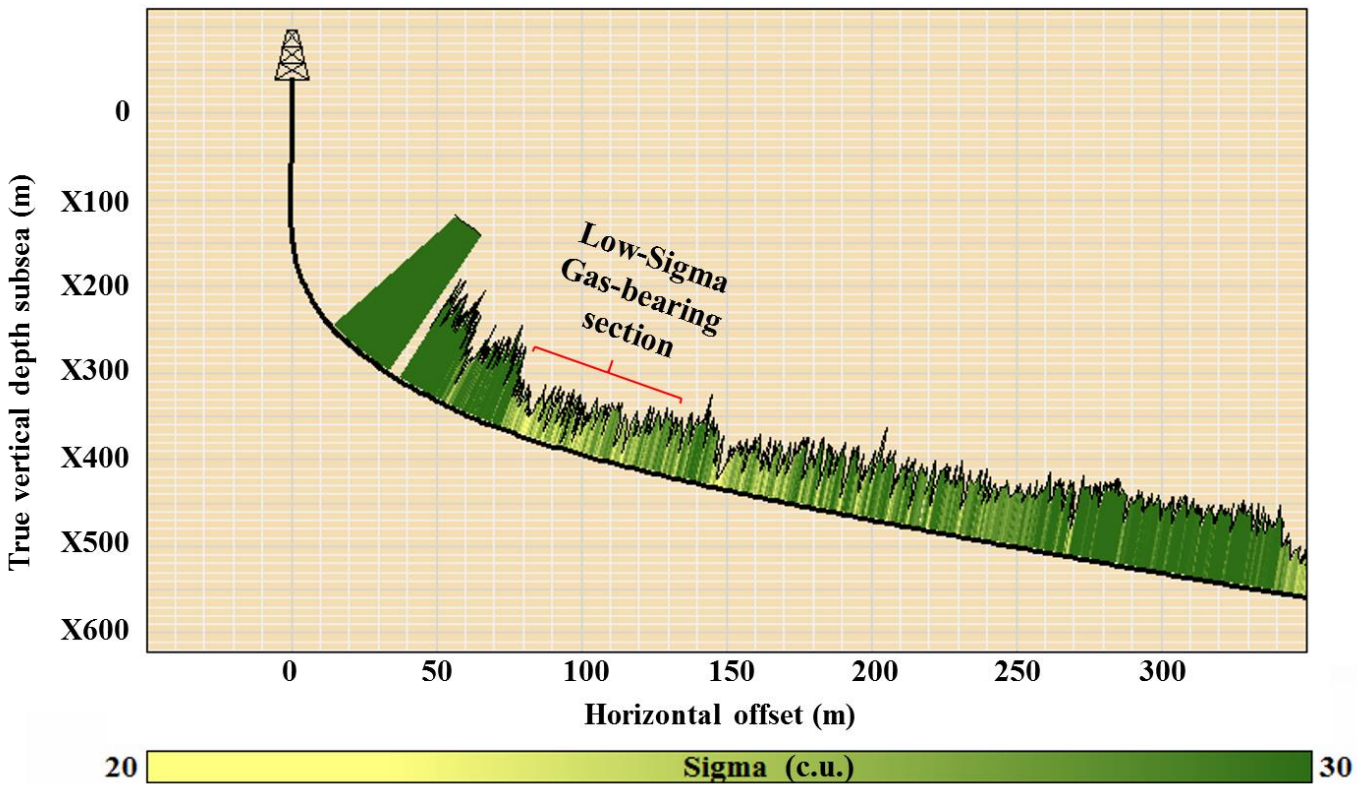

Figure 5.7: Well trajectory and borehole- and diffusion-corrected SSn Sigma log for Field Case I. The section of interest corresponds to the low-Sigma gas-bearing thinly bedded section penetrated at an angle of approximately 45°. Multi-detector Sigma measurements are mostly affected by shoulder-bed and shallow-invasion effects, and to some extent also by well-deviation effects.

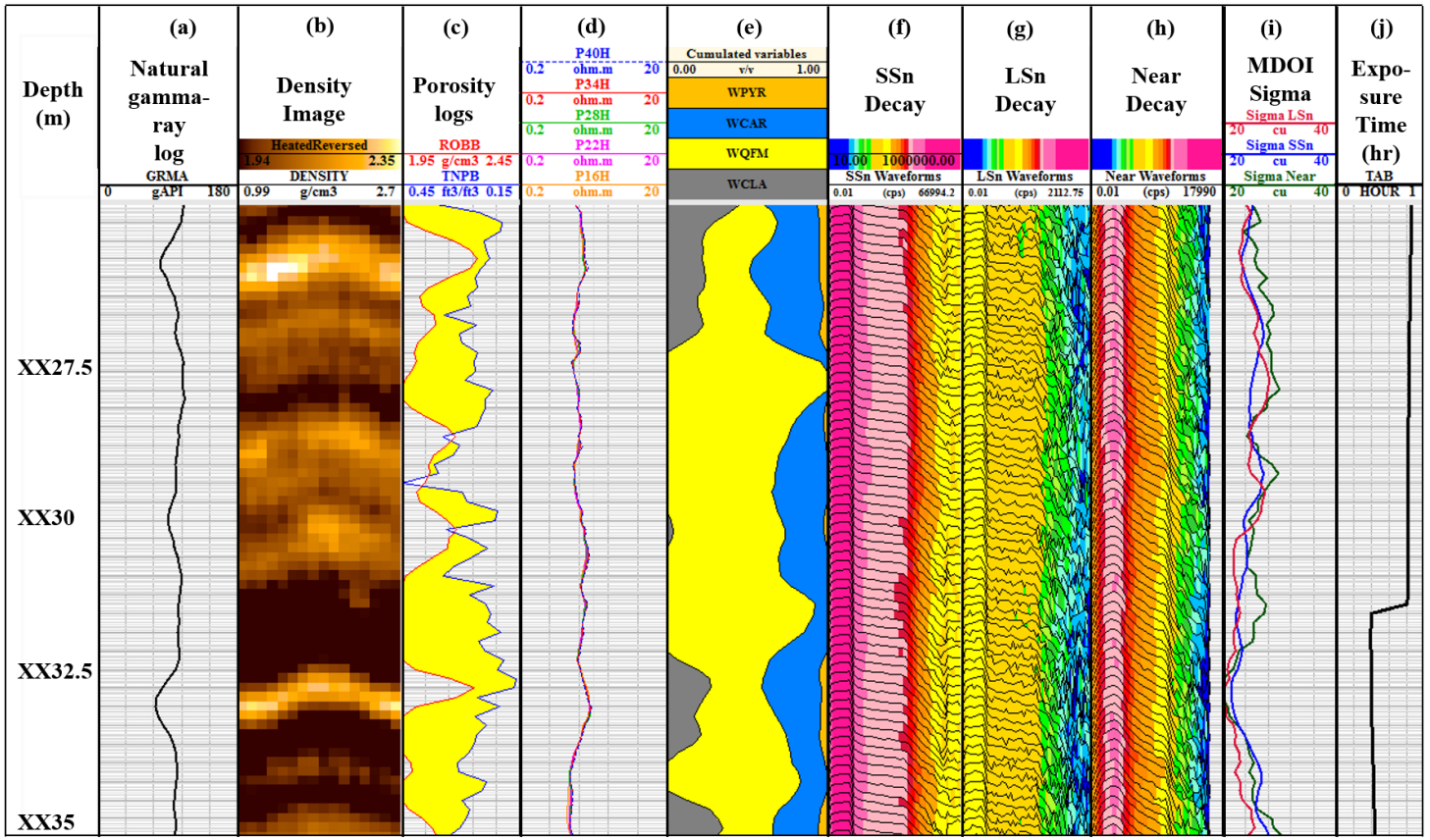

Figure 5.8: Set of LWD measurements corresponding to Field Case I. (a) Natural gamma-ray log, (b) compensated density image, (c) neutron and density porosity logs in limestone p.u., (d) high-frequency phase (PH) resistivity logs, (e) spectroscopy log, (f),(g), and (h) background-corrected field time-decays for the SSn, LSn, and Near detectors, respectively, (i) borehole- and diffusion-corrected multi-depth-of-investigation, MDOI, Sigma logs, and (j) time of exposure to mud filtrate before the acquisition of LWD measurements.

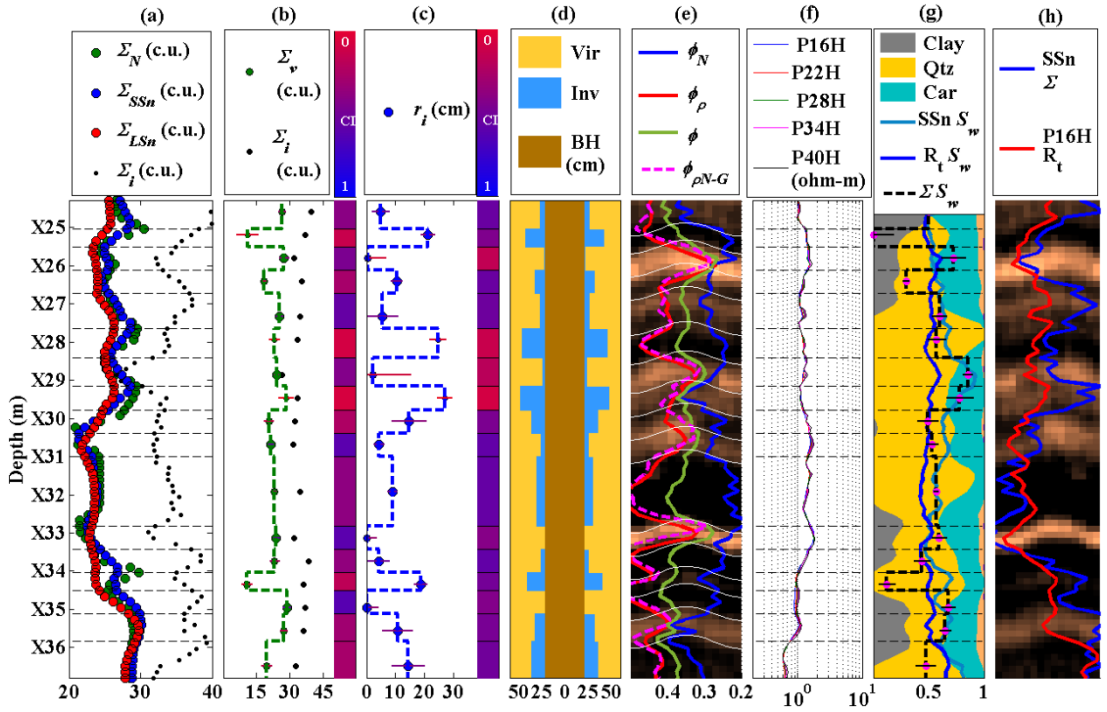

Figure 5.9: 2D inversion-based interpretation of multi-detector decay curves for Field Case I. SBM filtrate salinity is 137 kppm [NaCl equivalent] and filtrate Sigma is 72.3 c.u. Gas Sigma calculated at reservoir and temperature pressure equals 2 c.u. (a) Borehole and diffusion corrected multi-detector Sigma logs (Near, SSn, and LSn) and assumed invasion-zone Sigma, (b) estimated virgin-zone Sigma (green squared log) with error bars, assumed invasion-zone Sigma (black markers), and confidence index (*CI*), (c) estimated radial length of invasion with confidence index and error bars, (d) diagram of borehole (brown), invasion (blue), and formation (yellow), (e) neutron (blue solid line), gamma-gamma density (red solid line), averaged squared (solid green line), and neutron-gamma density (magenta solid line) porosity logs in limestone units, (f) high-frequency phase resistivity logs, (g) mineral composition from spectroscopy and calculated water saturation from SSn Sigma (light-blue solid line), resistivity (dark-blue solid line), and estimated after correcting formation Sigma for shallow-invasion, shoulder-bed, and well-deviation effects using the 2D inversion (black dashed line), and (h) comparison of the shallowest sensing phase resistivity log (P16H) and SSn Sigma log.

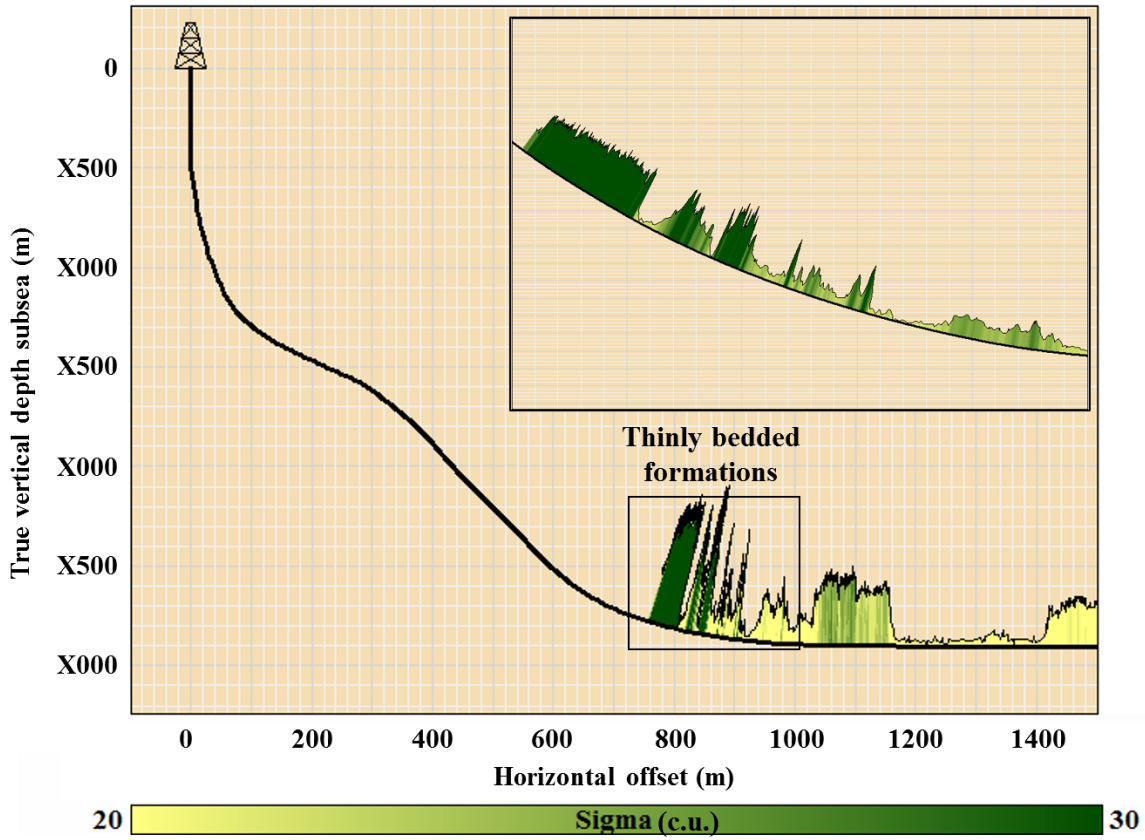

Figure 5.10: Well trajectory and borehole- and diffusion-corrected SSn Sigma log for Field Case II. The section of interest corresponds to the low-Sigma oil-bearing thinly bedded section penetrated at an angle of approximately 70º. Multi-detector Sigma measurements are mostly affected by shoulder-bed and well-deviation effects. The effect of filtrate invasion is not strong in this field example due to the similar absorption cross section of low-salinity mud filtrate and oil-bearing formations with partial water saturations.

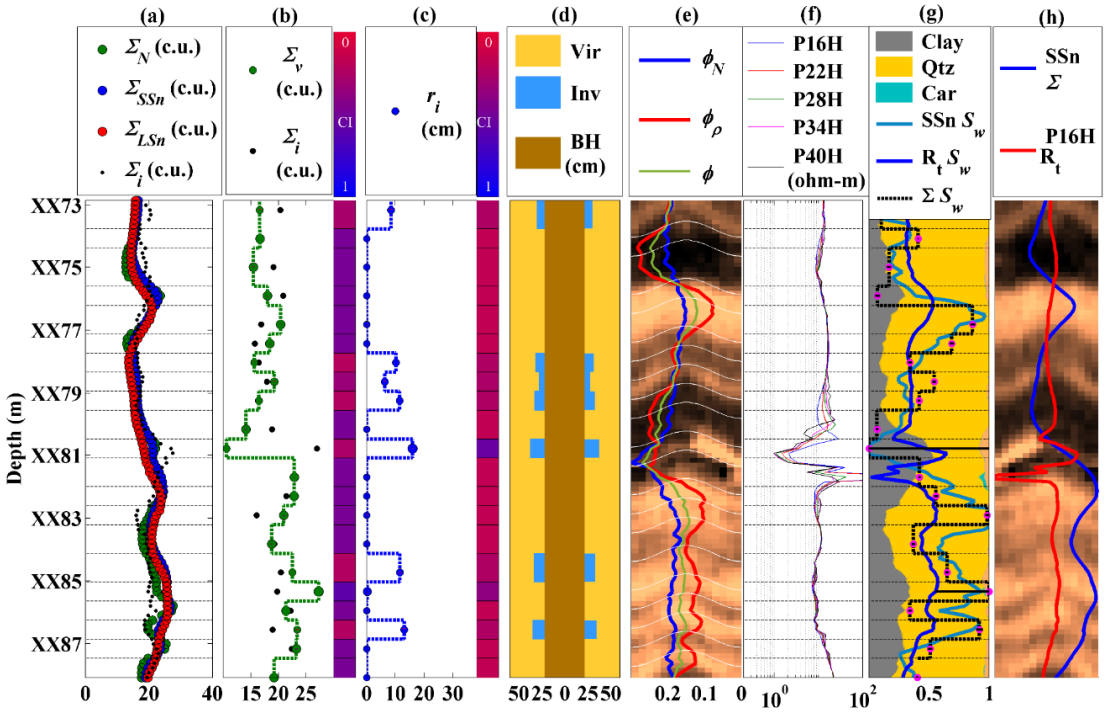

Figure 5.11: 2D inversion-based interpretation of multi-detector decay curves for Field Case II. SBM filtrate salinity is 46 kppm [NaCl equivalent] and filtrate Sigma is 38 c.u. (a) Borehole and diffusion corrected multi-detector Sigma logs (Near, SSn, and LSn) and assumed invasion-zone Sigma, (b) estimated virgin-zone Sigma (green squared log) with error bars, assumed invasion-zone Sigma (black markers), and confidence index (*CI*), (c) estimated radial length of invasion with confidence index and error bars, (d) diagram of borehole (brown), invasion (blue), and formation (yellow), (e) neutron (blue solid line), gamma-gamma density (red solid line), averaged squared (solid green line), and neutron-gamma density (magenta solid line) porosity logs in limestone units, (f) high-frequency phase resistivity logs, (g) mineral composition from spectroscopy and calculated water saturation from SSn Sigma (light-blue solid line), resistivity (dark-blue solid line), and estimated after correcting formation Sigma for shallow-invasion, shoulder-bed, and well-deviation effects using the 2D inversion (black dashed line), and (h) comparison of the shallowest sensing high-frequency, phase resistivity log (P16H) and SSn Sigma log.

Chapter 6: New Analytical Method to Calculate Matrix- and Fluid-Corrected Total Porosity

Accurate petrophysical interpretation based solely on nuclear measurements is largely dependent on good estimations of total porosity. The performance of the inversion algorithms presented in previous chapters is a function of a good estimation of invasion-zone Sigma, which is a function of total porosity, to reduce non-uniqueness. Additionally, calculation of water saturation using the linear mixing law for Sigma requires an accurate estimation of total porosity. Nonetheless, estimation of total porosity from neutron and density porosity logs poses a challenge because these logs are substantially affected by fluid and matrix-composition effects. Conventional interpretation of neutron and density porosity logs often includes corrections for shale concentration in which the main objective is to improve the calculation of non-shale porosity in hydrocarbon-bearing zones. Neutron and density porosity readings across shale zones are typically averaged using the root-mean-square (RMS) method.

In this chapter, I introduce a new and simple analytical expression for total porosity that effectively separates both matrix and fluid effects on neutron and density porosity logs. The expression stems from a new nonlinear mixing law for neutron migration length that is coupled with the linear density mixing law to calculate total porosity and fluid density. The method is applied in two sequential steps: first, separate corrections for only matrix effects are implemented to enhance the neutron-density crossover for qualitative interpretation of fluid type. Next, the coupled equation is used to estimate fluid density and

actual porosity devoid of matrix and fluid effects. Calculated porosity and fluid density can be further used to calculate water saturation from density logs. One notable feature of this method is the ease with which it can be applied to obtain accurate and reliable results. Application of the method only requires knowledge of single-component nuclear properties and mineral volumetric concentrations. Nuclear properties can be obtained from a set of charts for multiple fluid types and minerals provided in this chapter, while mineral concentrations can be calculated based on available triple combo logs or gamma-ray spectroscopy logs.

Two synthetic and four field examples (two conventional and two shale-gas reservoirs) are used to test the method. Firstly, I describe an application in a conventional siliciclastic sedimentary sequence where only shale concentration calculated from gamma-ray logs is required to improve the estimation of porosity in shaly sections. Second, I document several applications in which gamma-ray spectroscopy logs are used together with a reliable hypothesis for clay type to define mineral properties. Results compare well to NMR and core measurements, and the new method outperforms the conventional RMS procedure, especially in the cases of gas-bearing, low-porosity organic shale. The new analytical method can be readily implemented on an Excel spreadsheet and requires minimal adjustments for its implementation.

6.1 INTRODUCTION

Estimation of total porosity using borehole nuclear tools is a crucial task in formation evaluation because porosity determines the storage capacity of rocks, important

reservoir performance predictions stem from it. Total porosity is calculated –not measured- from nuclear borehole measurements that rely on variations in nuclear properties of materials that control neutron and gamma-ray transport, such as bulk density and migration length. Migration length defines the average distance that fast neutrons travel until they are thermalized and absorbed by formation nuclei. Typically, total gamma-ray or neutron count rates are indicative of nuclear properties of rocks that are related to porosity, e.g., bulk density, hydrogen index, and migration length. The transformation from count rates to nuclear properties, however, is not straightforward and is subject to several assumptions related to matrix and fluid composition. These assumptions have a great impact in the case of shale-gas reservoirs because the properties of gas and shale matrix deviate significantly from the conventional assumptions of a hydrogen-free matrix and full water saturation.

Neutron porosity measurements include a fast-neutron source and one or two detectors that count total high-energy neutrons (epithermal measurement) or low-energy neutrons (thermal measurement) per unit time. Compensated neutron tools use the ratio of detector count rates to minimize environmental effects (Alger et al., 1972). Count rates or count-rate ratios are correlated to laboratory measurements performed on homogeneous, water-saturated blocks (usually limestone solid composition) with different porosities. Thus, a correlation is derived between total count rate or ratio and water-filled porosity. Field logs of neutron count rates are then converted to equivalent limestone porosity units using the calibration obtained in the laboratory. Total neutron count rates vary with porosity because water contains hydrogen, the chemical element closest in mass to

neutrons; elastic collisions with hydrogen nuclei generate significant energy losses that decrease detector count rates. Physically, thermal neutron count rates are a function of slowing-down length (L_s), which defines the average distance that a fast neutron travels until it reaches thermal energies, and diffusion length (L_d), which describes the average distance that a thermal-neutron diffuses into the medium before absorption takes place. Both parameters are combined into one parameter referred to as migration length (L_m) that quantifies the neutron absorption capacity of rocks.

Thermal-neutron measurements were designed to discriminate between fluid (with significant hydrogen concentration) and matrix (with negligible hydrogen concentration) components of the rock. Deviations from this assumption cause abnormal neutron porosity responses. In the case of shale, which contains hydroxyls that slow down neutrons, conversion of detector count rates to limestone porosity units results in overestimated porosity. In the case of gas-bearing formations, conversion of detector count rates to porosity gives rise to underestimated neutron porosity because of the large migration length of gas compared to water. Nonetheless, this tool response is not totally disadvantageous. Low readings of neutron porosity compared to density porosity are used to qualitatively identify rock formations bearing gas or light oil (Alger et al., 1972). In the case of hydrocarbon-rich shaly formations, the effect of gas and shale is opposite and results in neutron porosity measurements that are often difficult to interpret.

Density porosity measurements are based on detection of gamma rays emitted by an intermediate-energy, gamma-ray source that collide with formation electrons and are

scattered at reduced energy due to Compton scattering. The total reduction in gamma-ray flux due to Compton scattering is a function of electron density, which is correlated to formation bulk density for most common materials in the subsurface. Typical logging tools include two detectors to compensate for borehole and mudcake effects (Wahl et al., 1964). Calculation of porosity from density measurements involves a volumetric mixing law together with explicit assumptions about matrix and fluid density. Knowledge about matrix composition from basic well-log analysis or from advanced spectroscopy logs is sufficient to estimate matrix-corrected porosity. This is possible because bulk density follows a linear mixing law. Conversely, the mixing law for neutron migration length is nonlinear and there are no analytical relationships published so far to estimate matrix-corrected neutron porosity in an analogous way to density porosity.

Early studies on thermal-neutron logs reported the effect of hydrated minerals and hydrocarbons on neutron porosity. Minerals such as anhydrite and gypsum have measurable effects on thermal-neutron logs due to presence of chemically attached water molecules which also lead to overestimation of neutron porosity (Savre, 1963). Assuming water saturation in the calculation of porosity from neutron and density measurements can lead to errors of approximately 10% in the case of oil-bearing, and as high as 40% in the case of gas-bearing rocks (Alger et al., 1963). An important breakthrough concerning the correction of neutron porosity logs for presence of hydrocarbon in a clean matrix was proposed by Gaymard and Poupon (1968). The correction invoked density and hydrogen index (HI) of hydrocarbons into the mixing laws for bulk density and bulk HI. However,

Gaymard and Poupon's method assumes that thermal-neutron response can be quantified solely as a function of HI. In reality, there are other elements such as oxygen and carbon that account for non-negligible neutron energy losses and, therefore, have a significant impact on neutron measurements (Ellis et al., 1987). Gaymard and Poupon also proposed the so-called root-mean-square method (RMS) to average neutron and density porosities to approximate total rock porosity, namely,

$$\phi_{RMS} \approx \sqrt{\frac{\phi_\rho^2 + \phi_N^2}{2}}$$

where ϕ_N and ϕ_ρ are neutron and density porosity, respectively, and ϕ_{RMS} is the root-mean-square approximation for total porosity.

Recent interest in the exploration and development of hydrocarbon-bearing shales has brought the attention into the reliability of neutron logs to evaluate total porosity. Gas shale environments deviate largely from shale-free, water-saturated formations assumed in the conversion of neutron count rates to porosity. Gas-bearing shales represent a reversed situation in the neutron measurement where neutrons are mostly slowed down and absorbed by the matrix portion rather than by gas-filled pores in the rock.

Evaluation of conventional reservoirs disregards the effect of hydroxyls and gas on source rocks. Several authors advanced corrections to neutron and density porosity logs in shaly hydrocarbon-bearing sandstone formations. Corrections for shale effects had been widely performed using neutron and density crossplots, selecting wet-clay properties based on a pre-defined procedure that does not take into account actual clay type, and using linear

approximations for neutron porosity (Wu et al., 1978). La Vigne et al. (1994) specialized such method as a function of clay type; they also acknowledged errors introduced in the corrections stemming from linear approximations of neutron porosity, especially in the case of gas-bearing rocks. Additionally, Bardsley and Algermissen (1963) reported a correlation between neutron porosity and kerogen content in organic-rich shale formations. Recent advances in shale gas formation evaluation have been focused toward laboratory measurements of porosity rather than nuclear logs given the complexity of interpreting neutron logs in organic shale.

This chapter introduces a correction to neutron porosity logs based on a new mixing law for migration length that remains accurate when neutrons logs are simultaneously affected by presence of gas and shale. I show that the method works better in low-porosity rocks, where the matrix controls both neutron and density detector responses. The method corrects neutron-density porosity crossovers by reducing matrix effects, and most importantly, estimates total porosity devoid of fluid effects which compares well to NMR and core measurements.

The outline of the chapter is as follows: First, I introduce a new mixing law for migration length. Next, I combine the migration-length mixing law with the linear density mixing law to calculate total porosity, and compare it to the traditional RMS average method in two synthetic examples. The method is tested on four field examples that include interpretations using basic triple-combo logs acquired in a siliciclastic sedimentary

sequence as well as interpretations that rely on spectroscopy logs. All cases include comparisons to core data and some of them include comparisons to NMR porosity logs.

6.2. METHOD

6.2.1 Matrix-Corrected Neutron Porosity

The formation property that best quantifies thermal-neutron porosity measurements is migration length because it takes into account both slowing-down and diffusion phenomena that control low-energy neutron count rates (Allen et al., 1967). Rigorous calculation of migration length requires the use of libraries of interaction cross sections for multiple elements with neutrons at different energy levels from which weighted averages, based on the slowing-down and diffusion probability for each energy group, yield accurate estimations of migration length such as the one obtained by Schlumberger Nuclear Parameter calculation program SNUPAR (McKeon and Scott, 1989). Previous studies used SNUPAR to generate depth-by-depth migration lengths for various minerals in the rock matrix to produce a neutron porosity log that is consistent with the actual variable lithology encountered in realistic subsurface formations (Ijasan et al., 2013c).

To this date, there exists no publication examining the analytical relationship between migration length and total porosity in neutron measurements analogous to the linear mixing law for density logs. The reason for this is the difficulty in quantifying the nonlinear relationship between neutron count rates and volumetric concentrations of fluid and solid components present in a rock formation. I introduce an approximation for the

bulk inverse of migration length of a rock, referred to as $\xi = 1/L_m$ in this dissertation, in the form of a nonlinear volumetric combination of the rock's solid and fluid components, namely

$$\xi_{bulk} = \phi^{\eta}\xi_f + (1-\phi)^{\eta}\xi_m, \tag{6.1}$$

where ϕ is total porosity, ξ_f, ξ_m are fluid and matrix inverse of migration lengths, respectively, ξ_{bulk} is the rock's inverse of migration length, and η is an exponent introduced to account for nonlinear effects in bulk migration length. I use inverse of migration length (ξ) because detector count rates behave more linearly with respect to changes in ξ than with respect to changes in L_m (Mendoza et al., 2007). Measured bulk inverse of migration length ξ_{bulk} is calculated from as-delivered neutron porosity logs in limestone porosity units. **Figure 6.1** describes SNUPAR calculated correlations of inverse of migration length with neutron porosity in limestone porosity units for an AmBe and a 14-MeV neutron source. Notice in **Figure 6.1** that the parameter ξ varies quasi-linearly with porosity in a limestone rock, alike the exponential relationship between migration length and porosity. The following polynomial equations are used to convert neutron porosity logs in limestone porosity units to ξ as a function of type of source used (initial neutron energy):

$$\xi_{bulk} = -0.134\phi_N^4 + 0.354\phi_N^3 - 0.371\phi_N^2 + 0.191\phi_N + 0.0353, \tag{6.2}$$

for a 14-MeV neutron source, and

$$\xi_{bulk} = -0.124\phi_N^4 + 0.315\phi_N^3 - 0.325\phi_N^2 + 0.223\phi_N + 0.0365, \tag{6.3}$$

for an AmBe neutron source.

Figure 6.2 shows that if matrix and fluid ξ are known, in the case of a clean matrix, η = 0.5 allows to closely reproduce SNUPAR calculations of bulk inverse of migration length. Equation 6.1 can be rewritten for the case of shale-free rocks as

$$\xi_{bulk} = \sqrt{\phi}\xi_f + \sqrt{1-\phi}\xi_m . \tag{6.4}$$

Figure 6.2 describes the nonlinear variation of ξ as a function of porosity. The mixing law in equation 6.4 allows one to approximate closely SNUPAR calculated inverse of migration lengths for each case. The main idea behind equation 4 is that SNUPAR is not needed to obtain matrix-corrected neutron porosity because single-component inverse-of-migration-length values for fluid and matrix can be read from tables provided in this chapter and that the new mixing law can be used to obtain analytically values of neutron porosity in the actual matrix.

Figure 6.3 describes SNUPAR calculated values of ξ for mixtures of gas methane and decane ($C_{10}H_{22}$) as a function of pressure and temperature. Fluid density inputs for SNUPAR were calculated using a flash simulator available in UTAPWeLS which is based on Peng-Robinson's equation of state (Abdollahpour, 2011). **Figure 6.3** displays values of ξ_f in equation 6.4 for hydrocarbons over a wide range of gas molar fractions, χ_g, as a function of pressure and temperature. The gas molar fraction in the hydrocarbon fluid is defined as

$$\chi_g = \chi_{light} / \left(\chi_{light} + \chi_{heavy} \right), \tag{6.5}$$

where χ_{light} are the moles of a light hydrocarbon constituent assumed to be methane, and χ_{heavy} are the moles of a heavy hydrocarbon constituent assumed to be decane. χ_g = 1 represents dry gas and χ_g = 0 represents black oil. Intermediate fractions represent light oil and gas condensate.

Inverse of migration length, ξ, for oil varies slightly as a function of pressure and temperature because of the low compressibility of oil compared to gas. Significant changes in gas density as a function of pressure and temperature are responsible for the large variability of ξ of gas. The bubble pressure of the hydrocarbon determines at what pressure gas in solution is released from the hydrocarbon phase, which results in decreasing ξ as pressure decreases below bubble pressure and more gas comes out of solution. The release of gas is represented in **Figure 6.3** at the points in which ξ deviates from ξ for oil.

Figure 6.3 also shows ξ for water as a function of electrolyte concentration (NaCl kppm) at different pressures. The impact of pressure, temperature, and electrolyte concentration on ξ of water is negligible because of the low compressibility of water and the small effect of chlorine and sodium on neutron slowing-down and diffusion. Notice that ξ decreases as density decreases. Likewise, notice that water ξ is always larger than hydrocarbon ξ because the hydrogen index of water is larger. There is also a slight increase in ξ of water as electrolyte concentration increases due to the decrease of hydrogen index of water as electrolyte concentration increases.

Information in **Figure 6.3** is presented as reference in the case that forward calculations of neutron porosity log are desired, but it is not required in order to apply the matrix and fluid corrections developed in this chapter. **Table 6.1** summarizes information required to perform the corrections. This table provides values of ξ for various minerals common in subsurface formations and also for water at three values of electrolyte concentration. Notice that ξ depends on the initial neutron energy and therefore on the type of neutron source used. I describe ξ for an AmBe and a 14-MeV neutron source. The table is a reference to reproduce bulk migration length in the ideal case of a single-mineral matrix. Nonetheless, it is desirable to model neutron porosity logs in matrices that comprise multiple minerals. The matrix ξ can be assumed to closely follow a linear mixing law, namely

$$\xi_m = \sum_{i=1}^{n} \xi_{\min_i} V_i \,, \tag{6.6}$$

when gamma-ray spectroscopy logs are available. ξ_{min_i} is the inverse of migration length for mineral sub-*i*, n is the number of mineral components, V_i is the volumetric fraction of mineral sub-*i* in the matrix . Equation 6.6 assumes that only non-porous rock components are considered in the solid portion of the rock. In the case of shales, only the wet-clay mineral portion of the rock is entered in equation 6.6, which is given directly by gamma-ray spectroscopy logs. When only triple combo logs are available, the inverse of migration length of the solid components of the matrix can be expressed as:

$$\xi_m = \xi_{wc} \cdot V_{wc} + \xi_{ss} \cdot (1 - V_{wc}) \,, \tag{6.7}$$

where V_{wc} is the solid component of the shale portion of the rock, whether it is in the form of dispersed or laminated shale, which is given by $V_{wc} = C_{sh} \cdot (1 - \phi_{sh})$. C_{sh} is volumetric concentration of shale calculated from gamma-ray logs and ϕ_{sh} is shale porosity. ξ_{wc} is wet clay inverse of migration length, and ξ_{ss} is sand inverse of migration length. Wet-clay and sand mineral inverse of migration lengths can be read from **Table 6.1**. The method presented in this chapter assumes that if only triple combo logs are used in the matrix correction, the calculation of C_{sh} is performed using appropriate formulas for dispersed or laminated shale, depending on shale topology for the specific logging environment of application and that shale porosity is known. The approximation for inverse of migration length in shaly rocks that is introduced in this chapter works equally well in the instances of laminated and dispersed shale. Additionally, V_{wc} can be approximated as $V_{wc} = C_{sh}$ under the assumption of negligible shale porosity. I will show that in any case, the application of the matrix correction introduced in this chapter requires calibration of the properties of the shale rock portion until neutron and density porosity logs overlap in low-resistivity zones

I test whether the assumption of a linear volumetric mixing law for the minerals in the rock is accurate, especially for the case of shale in the matrix, in **Figure 6.4**. I compare the assumed linear mixing law for three minerals versus actual SNUPAR-calculated inverse of migration lengths for different volumetric concentrations of each material. Notice that in the case of calcite and quartz the linear mixing of minerals accurately

reproduces SNUPAR calculations because none of them is hydrated. However, in the case of wet clay in the matrix, the linear combination is not linear. Still, the deviation in inverse of migration length is not significant when a linear mixing law is used. For the sake of simplicity, I propose to use calculated C_{sh} from gamma-ray logs, in the case of siliciclastic sequences, or gamma-ray spectroscopy logs to approximate the term ξ_m following the linear mixing formula in equation 6.6 and using **Table 6.1**.

Thus far, it has been shown that the linear mixing law in equation 6.4 represents a close approximation to SNUPAR calculations for the case of non-shaly rocks; the equation is valid in both water and low-density gas bearing rocks. It was also shown that ξ of minerals can be assumed to mix linearly. Nonetheless, I seek to approximate the neutron porosity logs especially in the case of shaly matrices where hydroxyls in the matrix significantly impact bulk ξ. SNUPAR calculations suggested that the nonlinear behavior occurs mainly when there is large contrast in the migration length of materials in the matrix such as a clean matrix with water, or the opposite case of a shaly matrix with gas. In the case of water saturated shale, contributions to the slowing down of neutrons from both the matrix and the fluid are similar and therefore the linear mixing law becomes more linear. To account for these changes in the linearity of inverse of migration length due to presence of shale, I propose to define the coefficient η in equation 6.1 as

$$\eta = 0.5 \cdot (1 - C_{sh}) + 0.8 \cdot C_{sh}. \tag{6.8}$$

In the case of non-shaly formations $C_{sh} = 0$ and $\eta = 0.5$ as defined in equation 6.4, and in the case of shaly formations $C_{sh} = 1$ and $\eta = 0.8$, (which is closer to the linear mixing law where $\eta = 1$) to account for linearity in the mixing law given by the presence of hydrogen in the matrix. **Figure 6.5** compares approximations performed using equations 6.1 and 6.8 for rocks with matrices of different shale concentrations saturated with (a) water and (b) gas to SNUPAR calculations and linear approximations. The nonlinear approximation for ξ outperforms the linear mixing laws compared to SNUPAR and is satisfactory even in the presence of large concentrations of shale.

The matrix correction applied to the neutron log can be performed by estimating ξ_m using equation 6.6, assuming 100% water saturation, and solving equation 6.1 with η given by equation 6.8, namely

$$\xi_{bulk} = \phi_N^{\eta} \xi_w + (1-\phi)_N^{\eta} \xi_m , \tag{6.9}$$

where ξ_{bulk} is the neutron porosity log in limestone units converted to inverse of migration length using equations 6.2 or 6.3. The fluid term ξ_f is assumed to be ξ of water approximately equal to 0.078 cm^{-1} because at this point the purpose is only to correct for matrix effects to enable the qualitative assessment of hydrocarbon zones from corrected neutron-density crossovers. Total neutron porosity devoid of matrix effects, ϕ_N, can be calculated using a solver such as the ones available in Excel spreadsheets. The calculation of porosity that I introduce below does not assume water filled porous space.

6.2.2 Matrix-Corrected Density Porosity

The separation of matrix effects in calculated density porosity measurements is possible because bulk density follows a linear mixing law of the form

$$\phi_\rho = \frac{\rho_{bulk} - \rho_{\mathrm{m}}}{\rho_f - \rho_{\mathrm{m}}}, \tag{6.10}$$

where ρ_{bulk} is measured bulk density, ρ_m is matrix density, ρ_f is fluid density, and ϕ_ρ is density porosity corrected form matrix effects. In the case of correcting only for matrix effects, the fluid can be assumed to be water, ρ_w = 1 g/cm^3 for fresh water or can be interpolated from **Table 6.1** for brine given that the effect of electrolyte concentration on density is linear. Analogous to the matrix correction of neutron logs, matrix density can be calculated as

$$\rho_m = \sum_{i=1}^{n} \rho_{min_i} V_i, \tag{6.11}$$

when gamma-ray spectroscopy logs are available, or as

$$\rho_m = \rho_{sh} \cdot C_{sh} + \rho_{ss} \cdot (1 - C_{sh}), \tag{6.12}$$

when only triple combo logs are available; ρ_{sh} is the wet clay density, and ρ_{ss} is sand density.

6.2.3 Calculation of Total Porosity From Matrix- and Fluid-Corrected Nuclear Measurements

Calculation of neutron and density porosity in the actual matrix under the assumption of full water saturation has the advantage that hydrocarbon neutron-density crossovers masked by presence of wet clay can be corrected and logs can be used qualitatively to discriminate hydrocarbon zones from water-bearing zones. In this section, I couple the new mixing law for migration length with the linear mixing law for bulk density to obtain a new analytic expression to calculate actual total porosity without enforcing a specific matrix or fluid type. I do not seek to find a new way to average neutron and density measurements, but rather to establish physical relationships between both measurements that will enable the calculation of actual porosity solely based on bulk ρ and ξ.

The mixing law for inverse of migration length previously proposed is given by

$$\xi_{bulk} = \phi^{\eta}\xi_f + (1-\phi)^{\eta}\xi_m, \tag{6.13}$$

with $\eta = 0.5\cdot(1\text{-}C_{sh}) + 0.8\cdot C_{sh}$,

while the mixing law for bulk density is given by

$$\rho_{bulk} = \phi\rho_f + (1-\phi)\rho_m. \tag{6.14}$$

Up until now there exist two equations with three unknowns: ϕ, ξ_f, and ρ_f. The relationships between fluid nuclear properties ξ_f and ρ_f are now studied in order to decrease the number of unknowns in equations 6.13 and 6.14. I simulate inverse of

migration lengths using SNUPAR for fluids along a wide range of densities, from low-density methane at 6894.75 kPa (1000 psia) and 200 ^{o}F to fresh water. **Figure 6.6** describes results for density and inverse of migration length for various mixtures of hydrocarbon and water, which exhibit a linear relationship between the two nuclear properties. I modeled mixtures of dry gas, light hydrocarbon, and black oil with water. In the rest of this chapter I use the relationship in the middle of **Figure 6.6**, which corresponds to mixtures of hydrocarbon of intermediate lightness and water, because upper and lower solid lines correspond to extreme fluid compositions. Nonetheless, the user of the method can select the relationship that most appropriately describes the environment of application and follow the steps below. The relationship between fluid density and inverse of migration length can then be approximated as

$$\xi_f \approx 0.064\rho_f + 0.011, \tag{6.15}$$

where the constant 0.064 has units of cm^2/g and the constant 0.011 has units of cm^{-1}.

By substituting the relationship between fluid nuclear properties (equation 6.15) into the mixing law for inverse of migration length (equation 6.13) I obtain

$$\xi_{bulk} = \phi^{\eta}\left(0.064 * \rho_f + 0.011\right) + \left(1-\phi\right)^{\eta}\xi_m . \tag{6.16}$$

The expression for fluid density in equation 6.14 can be replaced into equation 6.16, leading to

$$\xi_{bulk} = \phi^{\eta}\left(0.064 * \left(\frac{\rho_{bulk} - \left(1-\phi\right)\rho_m}{\phi}\right) + 0.011\right) + \left(1-\phi\right)^{\eta}\xi_m . \tag{6.17}$$

By simplifying equation 6.17 I then obtain

$$0.064\left(\rho_{bulk}-\rho_m\right)\phi^{\eta-1}+(0.064\rho_m+0.011)\phi^{\eta}+\left(1-\phi\right)^{\eta}\xi_m-\xi_{bulk}=0\,. \tag{6.18}$$

Equation 6.18 can be re-written as

$$a\phi_T^{\eta-1}+b\phi_T^{\eta}+c\left(1-\phi_T\right)^{\eta}-d=0\,, \tag{6.19}$$

where:

$$a=0.064\left(\rho_{bulk}-\rho_m\right), \tag{6.20}$$

$$b=0.064\rho_m+0.011, \tag{6.21}$$

$$c=\xi_m\,, \tag{6.22}$$

and

$$d=\xi_{bulk}\,. \tag{6.23}$$

Equation 6.19 is used to calculate total porosity, ϕ_T, separating matrix and fluid effects from bulk density and neutron porosity measurements. This equation can be readily solved using any nonlinear solver such as the ones available in excel spreadsheets solely from the bulk density log, neutron porosity log converted to the inverse of migration length using equation 6.2 or 6.3, and calculated matrix density and inverse of migration length, ξ_m and ρ_m. I emphasize that ξ_m and ρ_m can be approximated assuming linear mixing laws for volumetric concentrations from spectroscopy measurements or calculations of shale volume when only triple combo logs are available. Additionally, fluid density can be calculated from the estimation of total porosity and actual matrix density log, as follows:

$$\rho_f = \frac{\rho_{bulk} - (1-\phi)\rho_m}{\phi}. \tag{6.24}$$

Water saturation can be calculated from the estimated value of fluid density and water density as

$$S_w = \frac{\rho_f - \rho_{hc}}{\rho_w - \rho_{hc}}, \tag{6.25}$$

which is convenient in the case of shale-gas reservoirs where ρ_{hc} can be estimated at reservoir pressure and temperature conditions, and is a large density contrast between gas and water.

In the following sections several synthetic and field examples are used to test the new method to calculate total porosity and correct neutron-density crossovers for matrix effects. First, I introduce a synthetic case in which porosities calculated using the new method and the RMS method are compared in cases of water-saturated sandstone, gas-saturated sandstone, water-saturated shaly sand, and gas-bearing shale for a wide range of porosities. Next, I describe a synthetic case in a sequence that includes low-porosity formations, various in-situ fluids, and large shale concentrations. Finally, I describe results obtained from four field cases: two cases correspond to conventional reservoirs, and two cases correspond to shale-gas reservoirs which confirm that correcting for matrix and fluid effects yields improved estimations of porosity, especially in the challenging case of shale-gas formations where the RMS method overestimates total porosity.

6.3 SYNTHETIC RESULTS

6.3.1 Synthetic Case I

The main objective of this synthetic example is to compare the RMS average porosity method and the new method to calculate total porosity on different ranges of porosity, and solid and fluid compositions. **Figure 6.7** compares calculated porosities from neutron and density porosity logs in limestone porosity units and averaged using the RMS method (left) versus corrected for matrix and fluid effects using the new method (right) for the case of water-bearing (a) and gas-bearing (b) sandstone. Blue markers identify neutron porosity while red markers identify density porosity. I inspect the relationship between neutron and density porosity separately to identify when they will display the characteristic hydrocarbon crossover and study the calculated value of total porosity (red solid line for the RMS method on the left, and green solid line for the new method on the right) compared to the unit-slope line.

The plots in **Figure 6.7a** show results for the case of water-bearing sandstone. On the top left, the effect of the matrix causes low neutron porosity values that generate an apparent gas crossover, while on the right it is observed that corrections for matrix effects using equations 6.9 and 6.10 lead to values of neutron and density porosity that almost overlay, thereby decreasing the false gas crossover. Comparison of the red and green solid lines leads to conclude that in this case the method improves the calculation of low porosities, while at larger porosities the new method exhibits slightly poorer performance. The slight deviation using the new method (green solid line on top right versus unit-slope

line) could be due to the imposed relationship between fluid density and inverse of migration length in equation 6.15.

Next, I examine combined non-shaly matrix and fluid effects in a gas-bearing sandstone formation in **Figure 6.7b**. On the bottom left, it is observed that neutron porosity is always lower than density porosity; the exaggerated crossover is due to the matrix effect and mostly the large gas effect, especially on neutron porosity, which leads to overestimated values of porosity, as indicated by the red solid line compared to the unit-slope line. On the bottom right, I observe that the matrix correction enhances the gas crossover that is a function of porosity and improves the accuracy of the method to calculate total porosity, as indicated by the green solid line when compared to the unit-slope line.

The most important test to the new method is to verify the calculation of porosity in cases where both matrix and fluid deviate largely from non-shaly matrix and water saturation when processing neutron count rates. **Figure 6.8** displays calculated porosity using both methods for the case of (a) water-bearing shaly sandstone, and (b) the extreme case of a 100% shale matrix saturated with gas. On the left panel in **Figure 6.8a**, the water-bearing shaly sand case, I observe that the effect of hydrogen on the matrix increases neutron porosity whereby neutron porosity becomes higher than density porosity. This behavior is widely known as the shale effect on neutron-density porosity logs, which was not considered important in the analysis of conventional reservoirs and needs to be taken into account in the evaluation of shale-gas reservoirs. The shale effect gives rise to

overestimated RMS porosity as indicated by the solid red line compared to the unit-slope line. On the right panel in **Figure 6.8a**, I observe that the new method correctly addresses the effect of shale on the matrix and makes both neutron and density porosities overlay in the water saturated shaly rock. This results in a better estimation of total porosity, as indicated by the green solid line, especially at low porosities, where matrix effects are dominant. Again, the deviation at higher porosities is caused by the imposed relationship between fluid density and inverse of migration length and it occurs at large porosities when fluid effects become dominant.

Finally, I inspect the performance of the correction on a gas-bearing 100% shale formation in **Figure 6.8b**. The left panel in **Figure 6.8b** shows how the effect of shale masks gas crossovers in the low-porosity range; neutron porosity is higher than density porosity in the 0 to 13 p.u. porosity range. At larger porosities, the hydrocarbon crossover is not masked, but large porosities are necessary to observe gas crossovers; such porosities are not common in shale-gas formations. I also observe that shale effects cause a significant overestimation of RMS porosity (as indicated by the red solid line) and the overestimation is especially large at low porosities, which are common in shale-gas formations. In **Figure 6.8b**, I observe that the correction for both shale and gas effects allows to accurately observe lower neutron than density porosity indicative of presence of gas even at porosities as low as 5% and that the correction results in an excellent match to actual model porosity (as indicated by the green solid line compared to the unit-slope line). Total porosity

calculated using the new method outperforms the RMS method significantly in the case of gas-bearing, low-porosity shale formations.

6.3.2 Synthetic Case II

This synthetic case compares porosities calculated from neutron and density logs using the RMS method and the new method in a challenging case that includes a low-porosity siliciclastic sequence with volumetric concentrations of shale between 40 and 80% and different saturating fluids. **Table 6.2** summarizes the properties assumed in the model; single-component nuclear properties were obtained from **Table 6.1**. **Figure 6.9** shows (a) volumetric mineral concentrations calculated from numerically simulated elemental yield logs, (b) simulated LWD neutron and density porosity logs in limestone porosity units (Ijasan et al., 2013b) with averaged RMS porosity, (c) matrix-corrected neutron and density porosity logs and calculated total porosity using the new method, (d) a comparison of RMS porosity and total porosity calculated using the new method to layer-by-layer model porosity, (e) and actual layer-by-layer mineral and fluid volumetric model.

Figure 6.9 suggests that the new method outperforms the RMS average method to calculate total porosity, especially in the case of low porosity rocks with large shale concentrations. Notice on track (b) that the neutron porosity log consistently reads higher than density porosity except for one zone (formation at 7 m). In fact, the crossover in this zone would also be masked if the logs were to be expressed in sandstone porosity units. The combined effect of shale and logs being expressed in limestone units generates this apparent hydrocarbon crossover that otherwise would be masked by the effect of shale on

the neutron log. Track (c) shows how the separation of matrix effects allows one to qualitatively discriminate fluid type in the formation. Presence of gas in the upper section of the column becomes evident and there is a slight crossover characteristic of heavier hydrocarbon in the oil leg. The crossover in neutron and density logs after applying the matrix correction is remarkable considering that porosity at the top gas section is in the range of 5 to 10%.

This synthetic example clearly shows the reliability of the method when calculating actual model porosity within a maximum error of 0.01 p.u. on track (d) in **Figure 6.9**. RMS porosity is highly overestimated all throughout the sequence except in layer 3. The reason for this behavior is that layer 3 has lower shale concentration and larger porosity than other gas-bearing layers, while the presence of gas cancels off the effect of hydroxyls in the shale portion of the rock, leading to a good estimation of porosity using RMS. Nonetheless, the effect is not canceled in gas-bearing layers 1, 2, 4, and 5 because porosity is low and shale concentration is high.

6.4 FIELD RESULTS

The objective of this section is to appraise the efficacy of the new method when calculating total porosity and correct neutron-density crossovers on several field datasets and to benchmark it against available core and/or NMR porosity. I consider two applications in conventional reservoirs that exemplify how to calculate matrix nuclear properties using only triple combo logs or gamma-ray spectroscopy logs. Then I consider

applications in two shale-gas examples where decreasing matrix and fluid effects is challenging and where the new method is superior to the RMS method.

The only adjustment to the method is related to establishing the properties for wet clay and siliceous minerals. Spectroscopy logs group multiple clay types, with different ρ and ξ, into one group called "clay". Similarly, some processing algorithms group quartz, feldspars, and micas into one group called "QFM", and these minerals might also display different nuclear properties. The best way to circumvent this limitation is to start the correction using nuclear properties from **Table 6.1** for the most dominant known clay types and quartz. If corrected neutron and porosity logs do not overlay across low-resistivity zones, i.e. water-bearing formations and non organic-rich shales, ρ and ξ are adjusted for the "clay" and "QFM' mineral groups until they match in those sections.

6.4.1 Field Case I

Field Case I considers a high-porosity turbidite sequence in the Gulf of Mexico where spectroscopy logs were not available and where I resort to triple combo logs to attempt the matrix correction. **Figure 6.10** shows (a) gamma-ray derived C_{sh} compared to core C_{sh}, (b) induction resistivity logs, (c) as-delivered neutron and density porosity logs in limestone p.u., (d) matrix-corrected neutron and density logs using the new method, RMS averaged, (e) matrix-and fluid-corrected porosities compared to NMR porosity and core porosity, and (f) calculated fluid density from the bulk density measurement and calculated total porosity. Spectral gamma-ray logs were not available to perform clay

typing. I find that ρ_{clay} = 2.8 g/cm^3, and ξ_{clay} = 0.067 cm^{-1} make neutron-density porosity logs overlay in the water-bearing sand at X700 m and in all the shale zones. . Shale porosity equal to 6 p.u. was estimated from NMR measurements in a shale formation Nuclear properties for the quartz portion of the matrix are read from **Table 6.1** for an AmBe neutron source.

Results in Figure **6.10** indicate on track (d) that the correction unmasks the crossover in the gas section at X627 m even though shale concentration is above 50%, which is confirmed by the lower density of the fluid calculated in track (f). The crossover is not evident in the clean hydrocarbon-bearing zones probably because they are saturated with dense oil, large water saturations or could be affected by mud-filtrate invasion. Notice the good agreement between calculated total porosity and core porosity in the clean sands on track (e). The RMS method also provides a good estimation of porosity in these sands because they exhibit large porosities while shale concentration is low, as discussed in Synthetic Case I. Nonetheless, the RMS method overestimates porosity in shaly sections because of the effect of hydroxyls in wet clay. I also observe on track (e) that total porosity calculated with the new method agrees well with NMR porosity and enables the calculation of low porosities in shaly sections. Estimations of permeability based on RMS averaged porosity would yield similar permeabilities throughout the sequence, but the new estimation of porosity would reflect the low-porosity, low-permeability nature of the shaly sections.

6.4.2 Field Case II

Field Case II is intended to verify the application of the method in a case where the RMS can provide a good estimation of porosity because the concentration of shale is small and porosity is high, but where the new method allows correcting the crossover between neutron and density measurements for qualitative assessments of hydrocarbon saturation. This field case is a North Sea siliciclastic sequence of highly laminated sand and shale alternations penetrated by a high-angle well. **Figure 6.11** shows (a) mineral compositions from gamma-ray spectroscopy measurements, (b) high-frequency phase resistivity logs, (c) LWD density and neutron porosity logs in limestone p.u., (d) neutron and density porosity corrected for matrix effects, (e) comparison of RMS porosity against matrix- and fluid-corrected porosity using the new method, and (f) calculated fluid density. Analogous to Field Case I, information is not available about clay type beyond the total amount of clay calculated from gamma-ray spectroscopy elemental yields. I find that ρ_{clay} = 2.86 g/cm^3, and ξ_{clay} = 0.06 cm^{-1} make neutron-density porosity logs overlay in the low-resistivity shaly zones. Nuclear properties for the quartz portion of the matrix are read from **Table 6.1** for the case of a 14-MeV neutron source.

Even though this section of the sequence involves fairly clean formations, the proposed correction allowed one to observe that the crossover in the clean sand sections is not a gas crossover but a typical crossover in an oil-bearing formation with significant porosity (about 20 p.u. in this case). This case is analogous to the synthetic case described in **Figure 6.8a** where using limestone porosity units results in an apparent gas crossover in

an oil- or water-bearing formation. Notice also that calculated fluid density using corrected porosity and calculated matrix density enables to see zones where the fluid is lighter; the zones are located in clean sections where corrected neutron and density logs display a crossover.

6.4.3 Field Case III

I now test the full potential of the new method in the evaluation of porosity, and fluid saturations in the case of a gas-bearing source rock and compare results to core measurements. This is an example of formation evaluation based solely on nuclear measurements (neutron, density, and spectroscopy). **Figure 6.12** displays (a) mineral compositions from wireline gamma-ray spectroscopy compared to X-ray Diffraction (XRD) mineral volume fractions, (b) resistivity logs, (c) neutron and density porosity logs in limestone p.u., (d) matrix-corrected neutron and density logs using the new method, (e) comparison of RMS porosity and matrix- and fluid-corrected total porosity using the new method to core measurements, (f) calculated fluid density, (g) calculated matrix density compared to core measurements, and (h) calculated water saturation assuming $\rho_w = 1$ g/cm^3 and gas density calculated at 32405.35 kPa (4700 psia) and 180 ^{o}F, $\rho_g = 0.16$ g/cm^3. The reservoir was assumed to be normally pressurized, where pressure was calculated equivalent to the hydrostatic pressure of the water column at the depth of interest.

The dominant clay types are chlorite, illite, and mixtures of illite/smectite as per XRD analysis. Density for these clay minerals spans the range from 2.52 to 2.76 g/cm^3, and ξ from **Table 6.1** spans the range from 0.0583 to 0.0953 cm^{-1} for an AmBe source.

The best way to select the values for wet clay ρ and ξ is to calculate matrix-corrected porosities so that both porosities overlay in a water section. In this case, I find that ρ_{clay} = 2.75 g/cm^3 and ξ_{clay} = 0.066 cm^{-1} make both neutron and density porosity overlay in zones that display the lowest values of resistivity. Additionally, to take into account that ξ for quartz and feldspars is approximately 0.027 cm^{-1}, but it is as high as 0.0655 cm^{-1} for micas such as muscovite, I also adjust the nuclear properties of the QFM group. I find that ξ = 0.04 cm^{-1} and ρ = 2.65 g/cm^3 work well for the QFM group to overlay neutron and density logs in clean zones with low resistivities. In this case, I neglect the effect of kerogen because available gamma-ray spectroscopy logs do not output kerogen volume fractions and because it is known from XRD data that kerogen concentration in these formations is between 1 to 5%. Therefore, it is not expected that kerogen has a large impact on the calculations.

There exist two important features to analyze in this example. First, I conclude that the formation contains gas in the section between X230 m and X290 m and the crossover was originally masked by the significant volume of hydrogen in the formation matrix. I conclude that this section contains gas because according to synthetic examples the only reason why a 10-p.u. crossover (approximately) is encountered in a rock whose porosity is smaller than 10% is that the saturating fluid is gas. Apparently there is also gas below X290 m but the crossover is small because porosity in this section is smaller than 5%. Second, it is observed that, analogous to observations in synthetic examples, the RMS average method overestimates total porosity when compared to core porosity in track (e). The new

method correctly subtracts the effect of hydrogen and yields a total porosity value that agrees well with core data. Additionally, I show in track (g) that the estimated matrix density agrees well with core measurements. The reason for this behavior is the good quality of the spectroscopy measurements, which is reflected in the comparison to XRD data in track (a).

Furthermore, I am able to estimate water saturation that compares well to core measurements on track (h). This is possible because of the correction in porosity and matrix density. The facts that I used gas density to calculate water saturation in (g) and that the match to core data is excellent further confirms that this is a low-porosity gas-bearing zone within the shaly source rock.

6.4.4 Field Case IV

This field case examines interpretation of wireline logs acquired in an East Texas field in the Haynesville shale formation. The formation is a gas source rock overlain by sandstone of the Cotton Valley group and underlain by a limestone of the Smackover formation; it is a laminated calcareous and siliceous mudstone known to store large volumes of gas. **Figure 6.13** shows (a) mineral volumetric fractions from gamma-ray spectroscopy logs compared to XRD mineralogy, (b) resistivity logs, (c) neutron and density logs in limestone p.u. compared to core total porosity, (d) matrix-corrected neutron and density logs using the new method compared to core total porosity, (e) RMS averaged, and matrix- and fluid-corrected total porosity using the new method compared to core and

NMR total porosity, (f) calculated fluid saturation, (g) estimated matrix density compared to core matrix density, and (h) calculated water saturation compared to core measurements.

Water saturation in this field example was calculated using corrected total porosity and matrix density log, and assuming gas density equal to 0.14 g/cm^3 at 32405.35 kPa (4700 psia) and 250 ^{o}F. Dominant clay types are chlorite and illite as per XRD analysis. In this case, I find that ρ_{clay} = 2.75 g/cm^3 and ξ_{clay} = 0.06 cm^{-1} make both curves overlap in zones that display the lowest values of resistivity. Analogous to the previous field case, I neglect the effect of kerogen because available gamma-ray spectroscopy logs do not output kerogen volume fractions and because it is known from XRD data that kerogen concentration is below 8%, whereby kerogen is not expected to have a large impact on the calculations.

The matrix and fluid correction on neutron and density logs allows one to observe a gas crossover otherwise masked by presence of shale, while the estimated total porosity is in good agreement with core measurements. Notice that gas crossovers at X050-X250 m and X375-X450 m were masked because of large neutron porosity values given by shale concentration of approximately 70% in these intervals. I also observe that the crossover becomes a function of total porosity, and that the RMS averaged porosity overestimates total porosity when compared to core and NMR data on track (e). Calculated water saturation agrees with the behavior of the resistivity log when comparing zones of similar porosity. Nonetheless, I observe that in these shaly formations resistivity logs reflect mostly changes in porosity rather than changes in water saturation. The reason for this

behavior is that because porosities are low, any change in water saturation has negligible effect in the bulk rock properties, and most importantly, that the large concentrations of shale generate least-resistance paths that control the resistivity log response in shaly formations.

6.5 DISCUSSION

One of the most important aspects of the matrix and fluid correction introduced in this chapter is the assumed nuclear properties, ξ and ρ, for minerals. I showed that assumed single-mineral nuclear properties can be read from **Table 6.1** and combined using the volumetric fractions from spectroscopy logs or calculated C_{sh} in the case of siliciclastic environments where only triple combo logs are available. Nevertheless, the selection of minerals which constitute the matrix can be difficult, especially because spectroscopy measurements group multiple clay minerals into one single clay group, and quartz, feldspars, and micas into another group called QFM. Constituents of such groups can display different values of ξ and ρ, but one average value has to be selected for the whole group. Therefore, clay typing becomes important to establish dominant properties for wet clay. I advise to begin the correction with nuclear properties for the most dominant clay type and quartz, verifying whether neutron and density logs overlay in low-resistivity zones. If this is not the case, then it is advisable to calibrate the properties for shale and sand components, especially ξ, until both porosities read the same value in a water zone or in a water saturated shale formation, i.e., low-resistivity formations.

6.6 CONCLUSIONS

I introduced a new mixing law of migration length, the nuclear property that governs thermal neutron porosity measurements. It is analogous to the linear mixing law for density but it takes into account nonlinear effects in the measurement due to presence of gas and shale. Neutron and density mixing laws were combined to obtain a new analytical expression for total porosity that is based solely on neutron and density porosity measurements and does not require assumptions regarding rock matrix or fluid composition. Matrix correction requires matrix density and inverse of migration length, ρ_m and ξ_m , which can be calculated using single-mineral values described in **Table 6.1** and gamma-ray spectroscopy logs, or calculated shale volumetric concentration in cases where only triple combo logs are available.

Matrix and fluid correction of neutron and density logs is applied in two sequential steps. First, separate matrix corrections assuming water saturation are applied to neutron and density porosity logs to unmask hydrocarbon crossovers affected by the presence of shale in the formation and enable the qualitative interpretation of fluid type. Synthetic and field results showed that shale effects can be isolated to unmask hydrocarbon crossovers that agree with core measurements and resistivity logs, even in organic-rich shale formations. Second, the new expression for total porosity can be used to calculate total porosity without averaging neutron and density or assuming a specific fluid saturation.

Field results indicate that the new calculation of total porosity compares well to core total porosity and NMR porosity and is more accurate than the traditional RMS

calculation, which overestimates porosity in shaly rocks. The improvement over the RMS method is especially noteworthy in the case of low-porosity, gas-bearing formations with large concentrations of shale such as in the case of shale-gas formations. Two field cases in shale-gas reservoirs showed that the new method can effectively estimate total porosity while the RMS average porosity method can lead to overestimated porosity up to 15 p.u. in formations with abundant shale concentration. Furthermore, field examples showed that the calculated matrix density can be used together with the new matrix- and fluid-corrected porosity to estimate water saturation in good agreement with core water saturation. Calculation of water saturation from density logs works better in gas-bearing environments where the contrast in nuclear properties between water and hydrocarbon is large, hence enabling their differentiation.

Table 6.1: Density, inverse of migration length for an AmBe and a 14-MeV neutron source, Sigma, and hydrogen index for various minerals and water of different salinities.

Name	ρ	ξ (cm^{-1})		Σ	**HI**
	g/cm^3	**AmBe**	**14 MeV**	**c.u.**	
Minerals					
Silicates					
Quartz	2.65	0.0284	0.0276	4.55	0
Zircon	4.5	0.0371	0.0363	5.27	0
Carbonates					
Calcite	2.71	0.0353	0.0341	7.08	0
Dolomite	2.85	0.0354	0.0343	6.86	0
Siderite	3.89	0.0585	0.0555	51.84	0
Oxidites					
Hematite	5.18	0.0580	0.0560	100.02	0
Magnetite	5.08	0.0552	0.0534	101.48	0
Hydroxy-apatite	3.17	0.0513	0.0487	11.40	0.057
Feldspars					
Orthoclase	2.52	0.0283	0.0275	15.51	0
Albite	2.59	0.0302	0.0293	7.59	0
Anorthite	2.74	0.0286	0.0279	7.33	0

Table 6.1 (continued)

Wet Clays					
Kaolinite	2.41	0.0868	0.0726	11.99	0.337
Muscovite	2.82	0.0655	0.0593	16.94	0.128
Glauconite	2.86	0.0401	0.0385	28.29	0.0415
Chlorite	2.76	0.0953	0.0801	11.16	0.359
Illite	2.52	0.0583	0.0529	11.57	0.12
Montmorillonite	2.12	0.0485	0.0441	9.14	0.113
Evaporites					
Halite	2.04	0.0224	0.0216	706.86	0
Anhydrite	2.98	0.0313	0.0304	12.53	0
Gypsum	2.35	0.1073	0.0835	18.73	0.493
Sylvite	1.86	0.0092	0.0090	528.82	0
Barite	4.09	0.0299	0.0295	18.16	0
Sulfides					
Pyrite	4.99	0.0235	0.0232	90.16	0
Coals					
Anthracite	1.47	0.0908	0.0681	9.76	0.372
Black coal	1.24	0.1112	0.0748	15.74	0.615
Lignite	1.19	0.1010	0.0688	14.01	0.553
Water (150^{o}F, 2500 psi)					
Fresh water	1	0.1264	0.0765	21.85	0.986
Brine (100 kppm NaCl)	1.05	0.1305	0.0780	57.71	0.952
Brine (250 kppm NaCl)	1.17	0.1289	0.0782	121.16	0.881

Table 6.2: Assumed properties for the formations in Synthetic Case II. Gas properties calculated at 10342.14 kPa (1500 psia) and 150ºF (0.07 g/cm^3). ξ_{sh} = 0.0801 cm^{-1} for wet chlorite and ξ_{ss} = 0.0276 cm^{-1} for quartz.

Layer	Thickness (m)	C_{sh} (v/v)	Porosity (p.u.)	Fluid
1	3.048	0.7	5	Gas
2	3.048	0.55	8	Gas
3	3.048	0.5	10	Gas
4	3.048	0.8	5	Gas
5	3.048	0.7	8	Gas
6	3.048	0.55	10	Oil
7	3.048	0.5	7	Oil
8	3.048	0.4	8	Oil
9	3.048	0.5	10	Fresh water
10	3.048	0.4	11	Fresh water

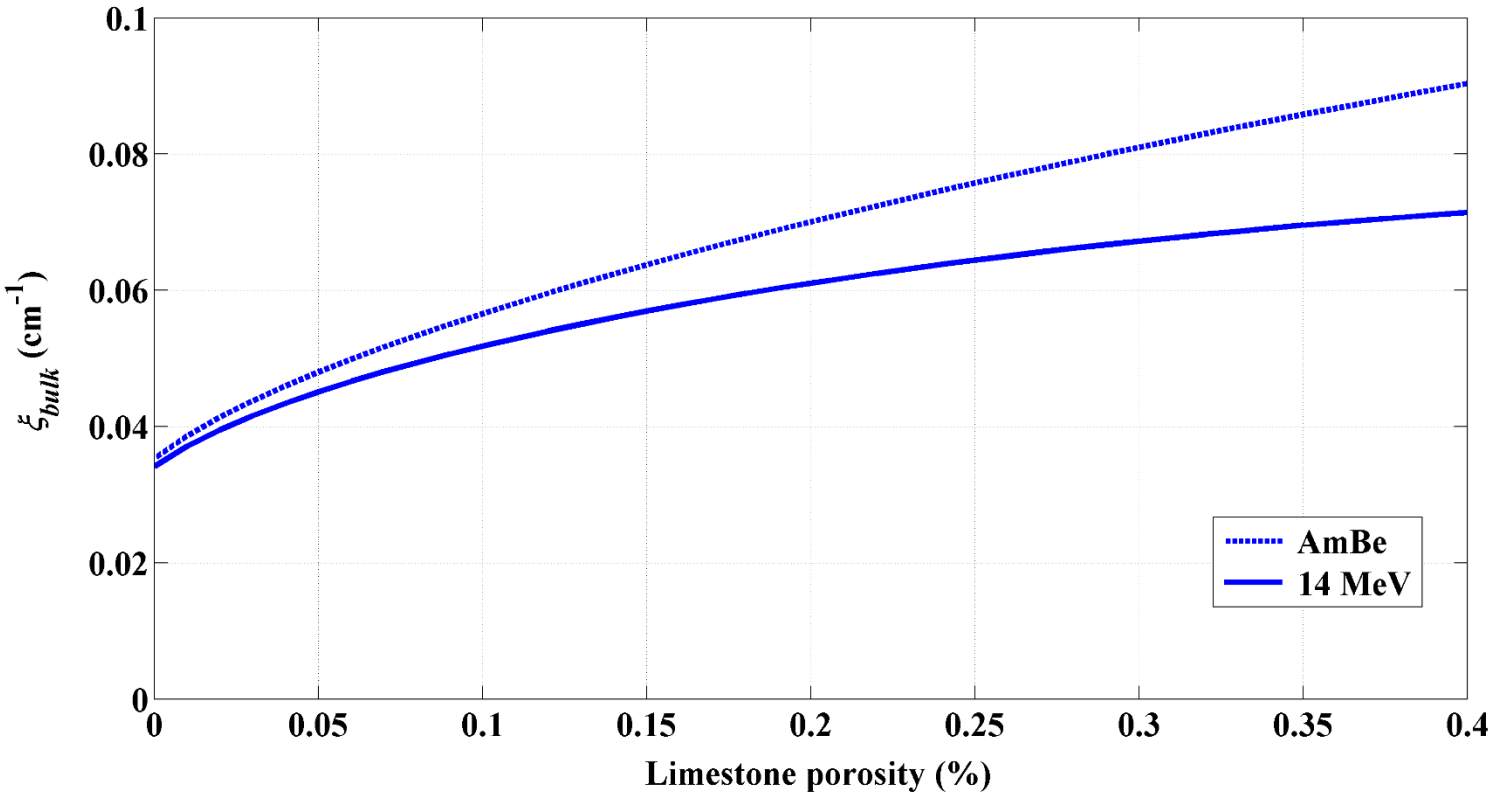

Figure 6.1: SNUPAR-derived bulk inverse of migration length (ξ_{bulk}) as a function of limestone water-filled porosity.

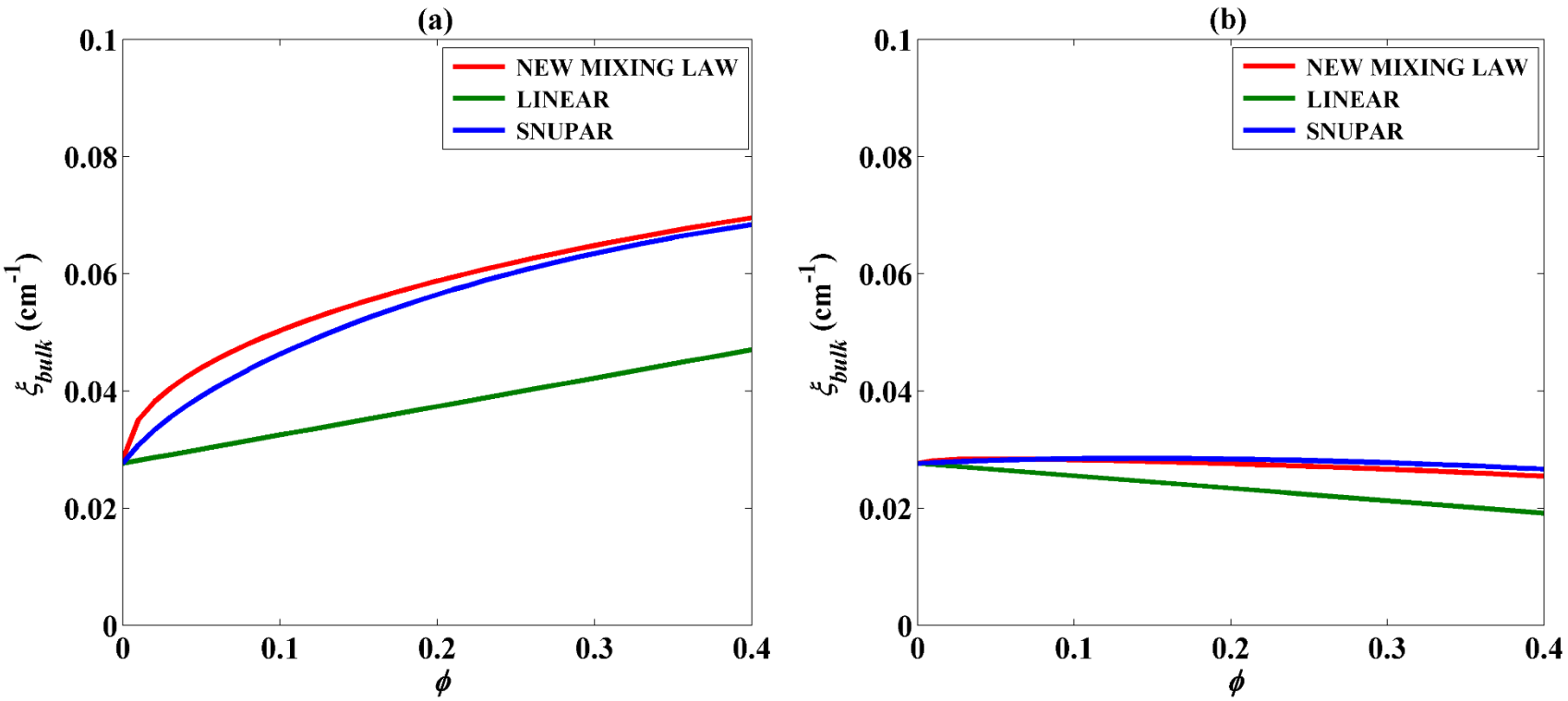

Figure 6.2: Comparison of ξ calculated using SNUPAR, a linear mixing law, and the new mixing law in equation 6.4 for the case of a sandstone matrix fully saturated with (a) fresh water and (b) gas at 150 ^{o}F and 6894.75 kPa (1000 psia) as a function of total porosity. Gas density is 0.04 g/cm^3 in (b).

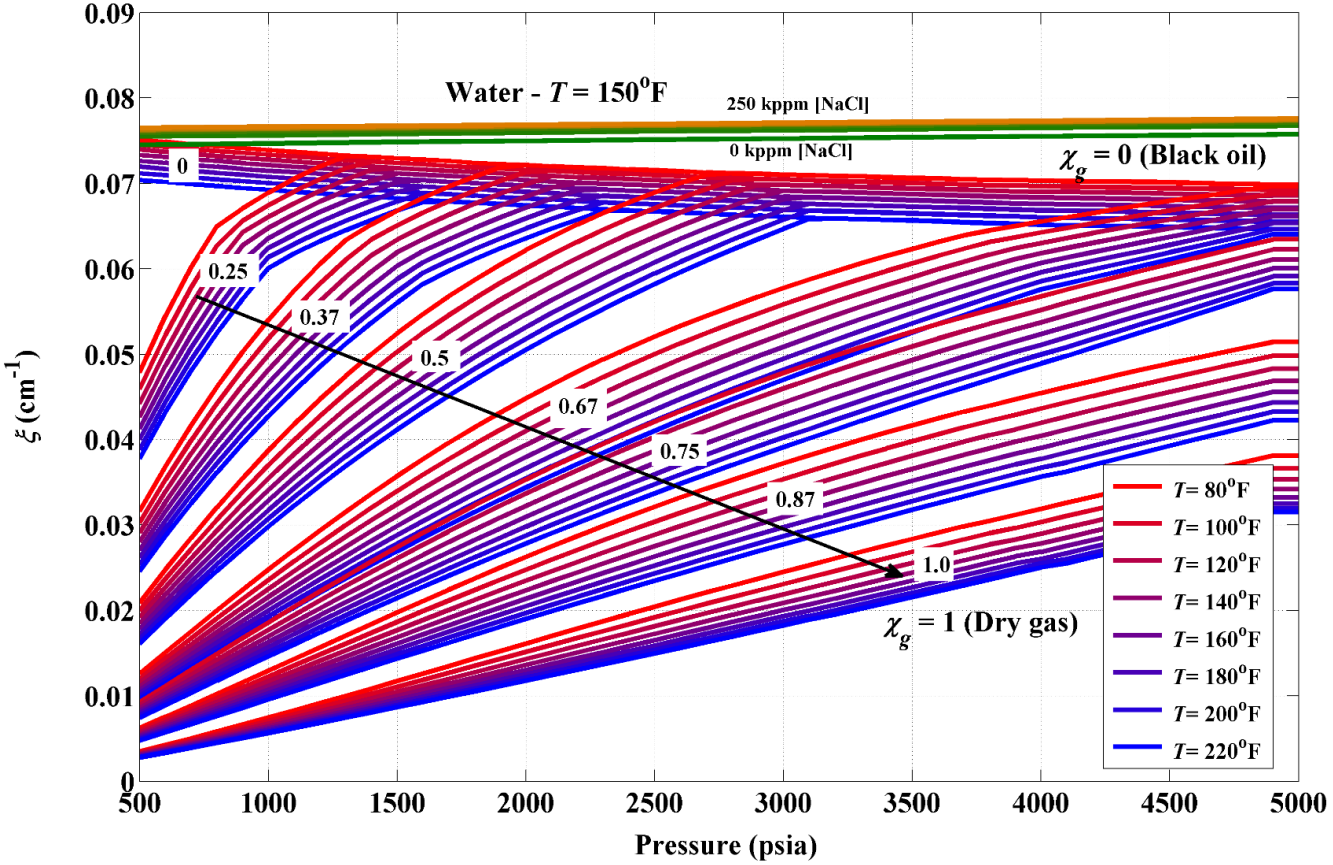

Figure 6.3: Inverse of migration length for hydrocarbons of different gas molar fractions, χ_g, (or lightness) in the range of dry gas to black oil and water of various electrolyte concentrations as a function of pressure and temperature.

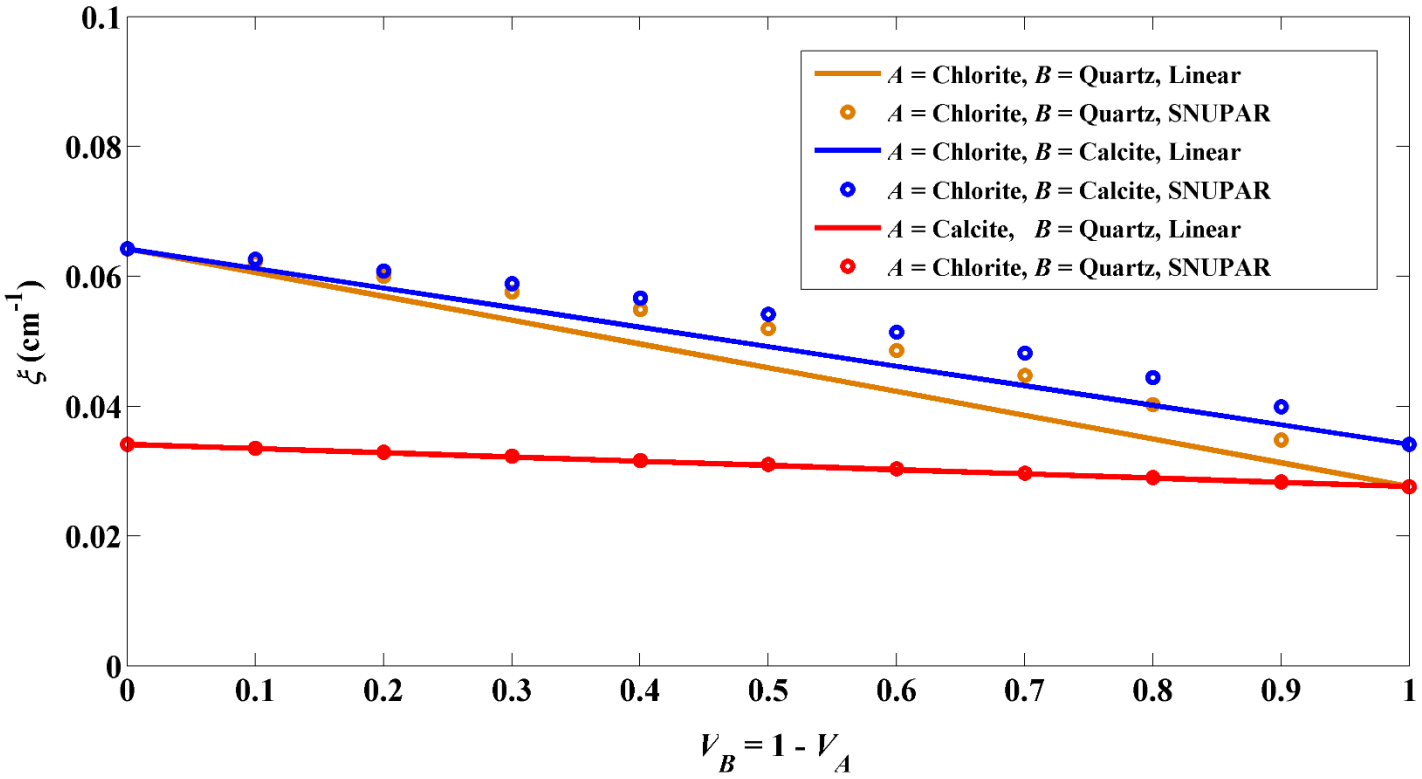

Figure 6.4: Comparison of linear mixing approximation for the inverse of migration length of mixtures of solid components *A* and *B* to SNUPAR calculations. The minerals considered for components *A* and *B* are quartz, calcite, and wet chlorite.

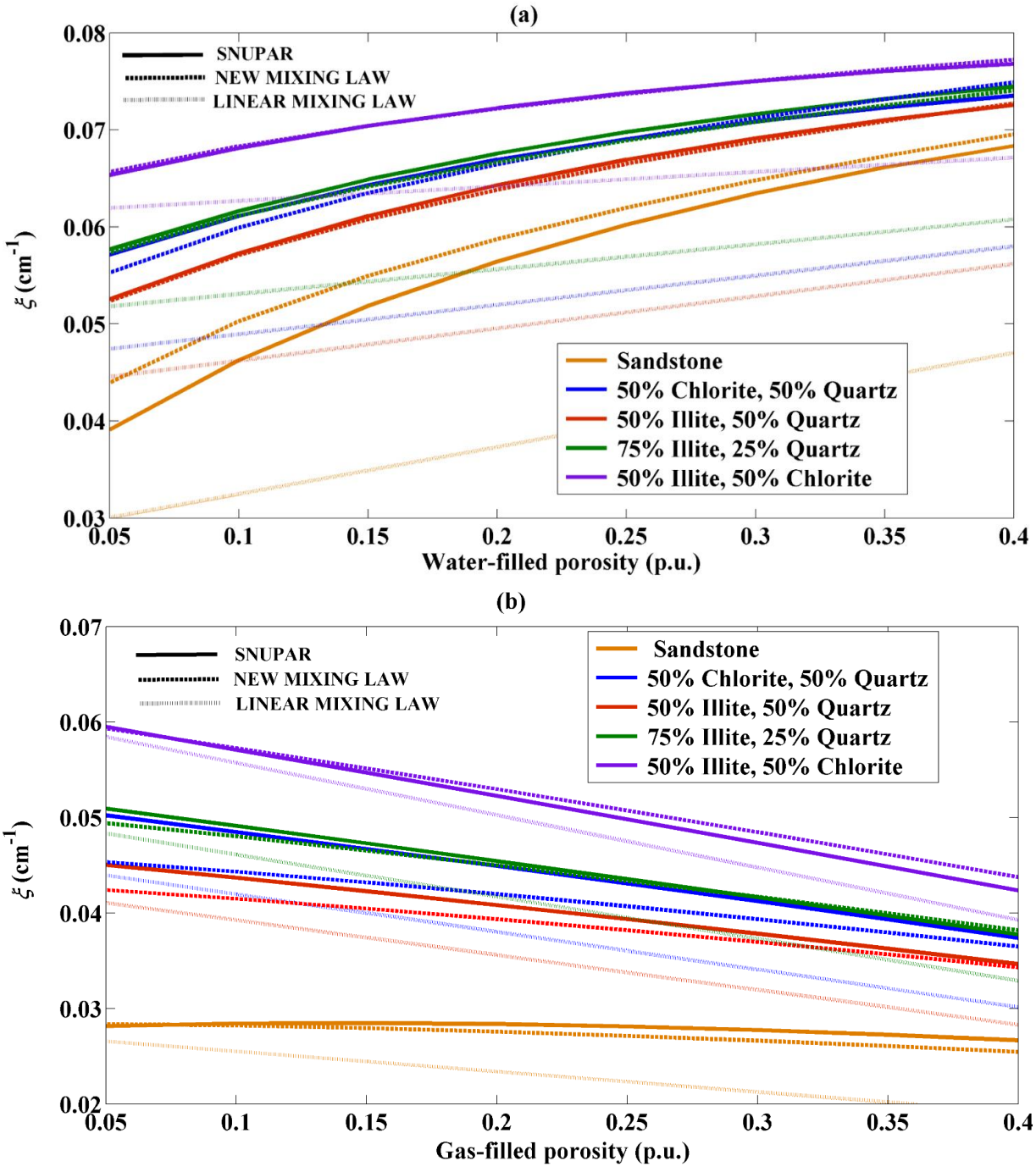

Figure 6.5: Comparison of calculated ξ using the new mixing law (dashed lines), SNUPAR (solid lines), and a linear-mixing law (dotted lines) for (a) water-filled and (b) gas-filled rocks with various matrix compositions; using η as a function of C_{sh} enables the accurate reproduction of SNUPAR results, which deviate significantly from a linear mixing law.

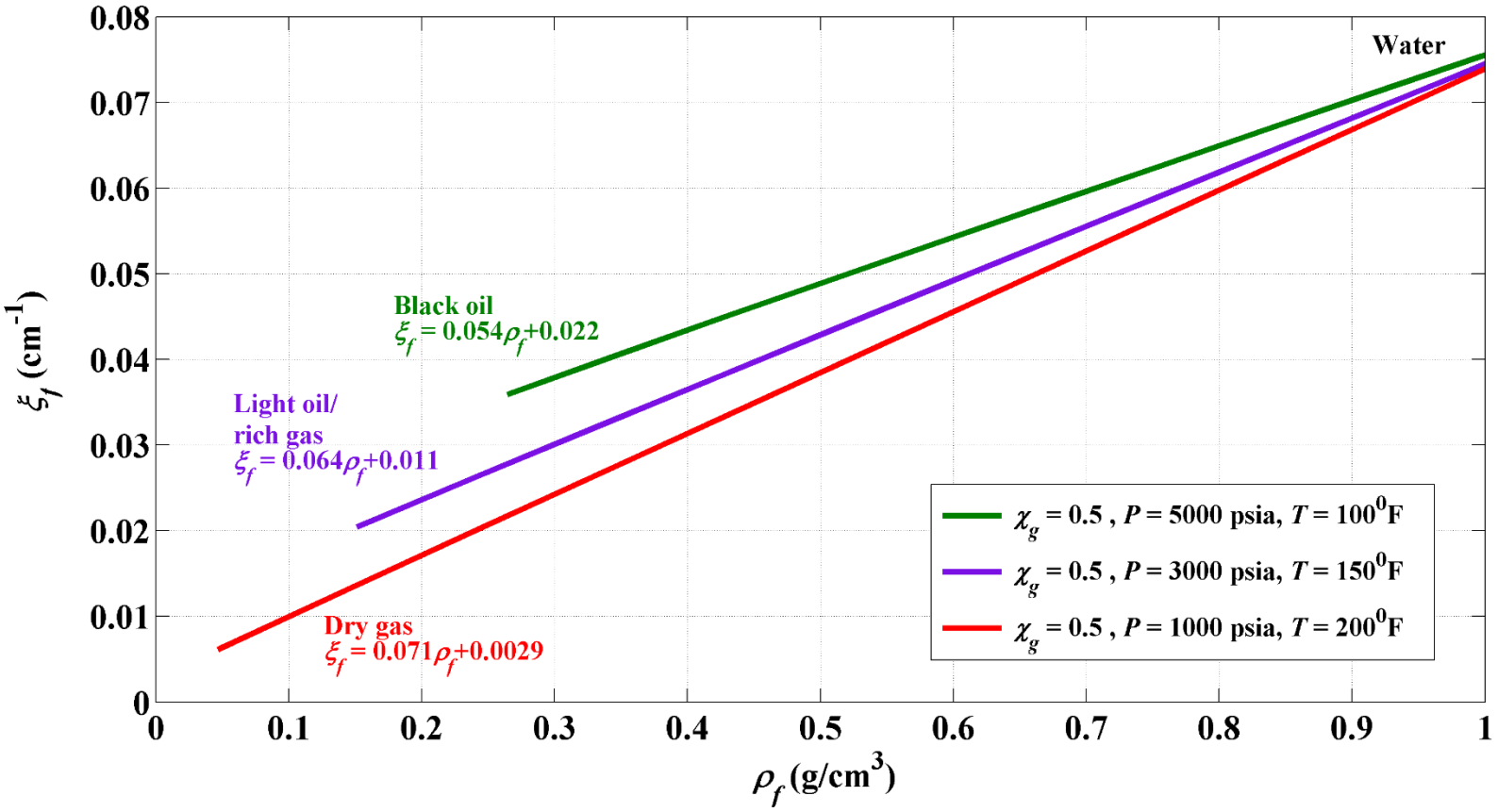

Figure 6.6: SNUPAR calculated relationship between ξ_f and ρ_f for various hydrocarbon and water mixtures displaying a linear relationship between both nuclear properties.

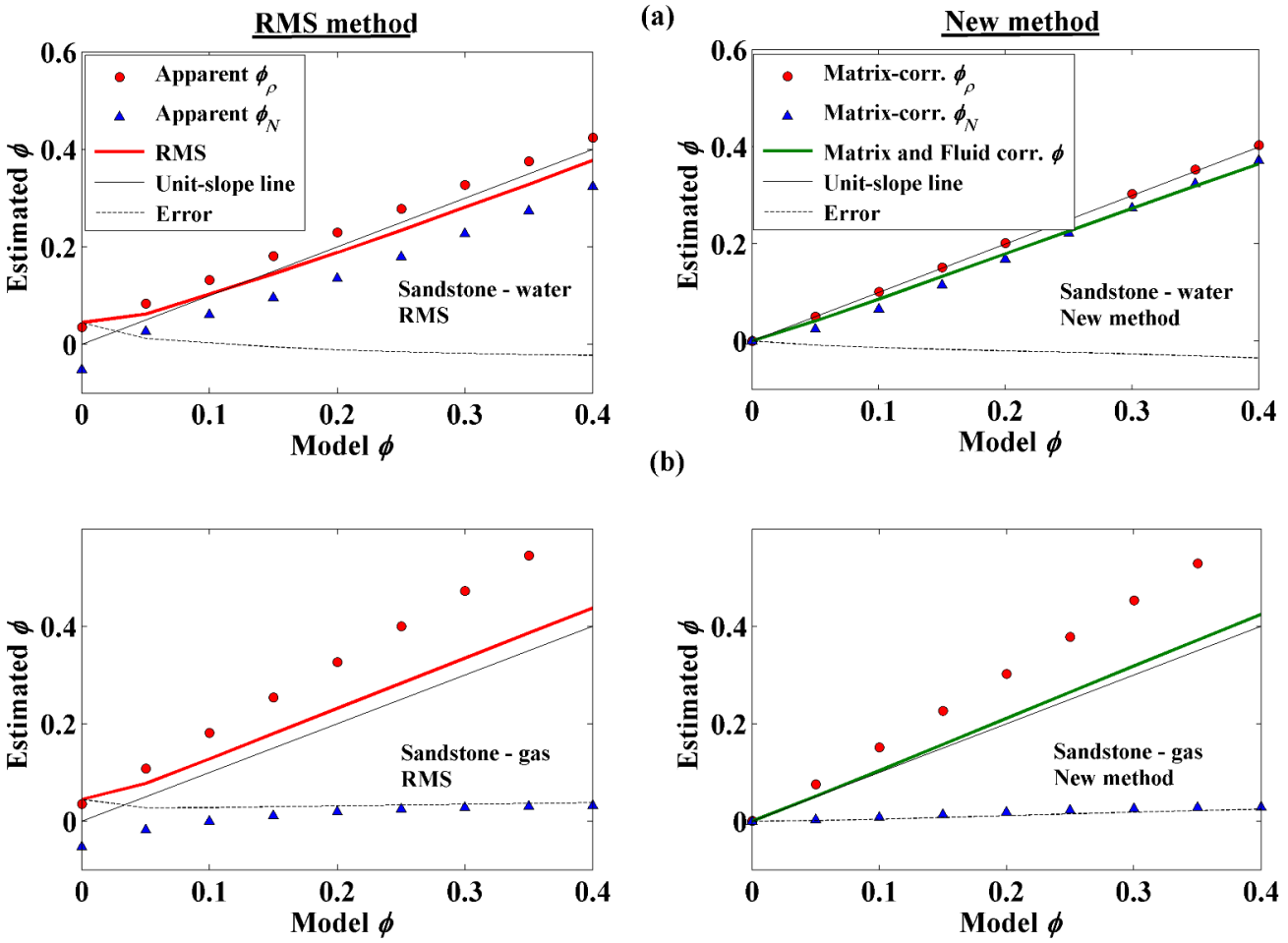

Figure 6.7: Results for Synthetic Case I. Calculated porosity using the RMS method (left) and the new method to approximate total porosity (right) in clean sandstone formations saturated with (a) water, and with (b) gas.

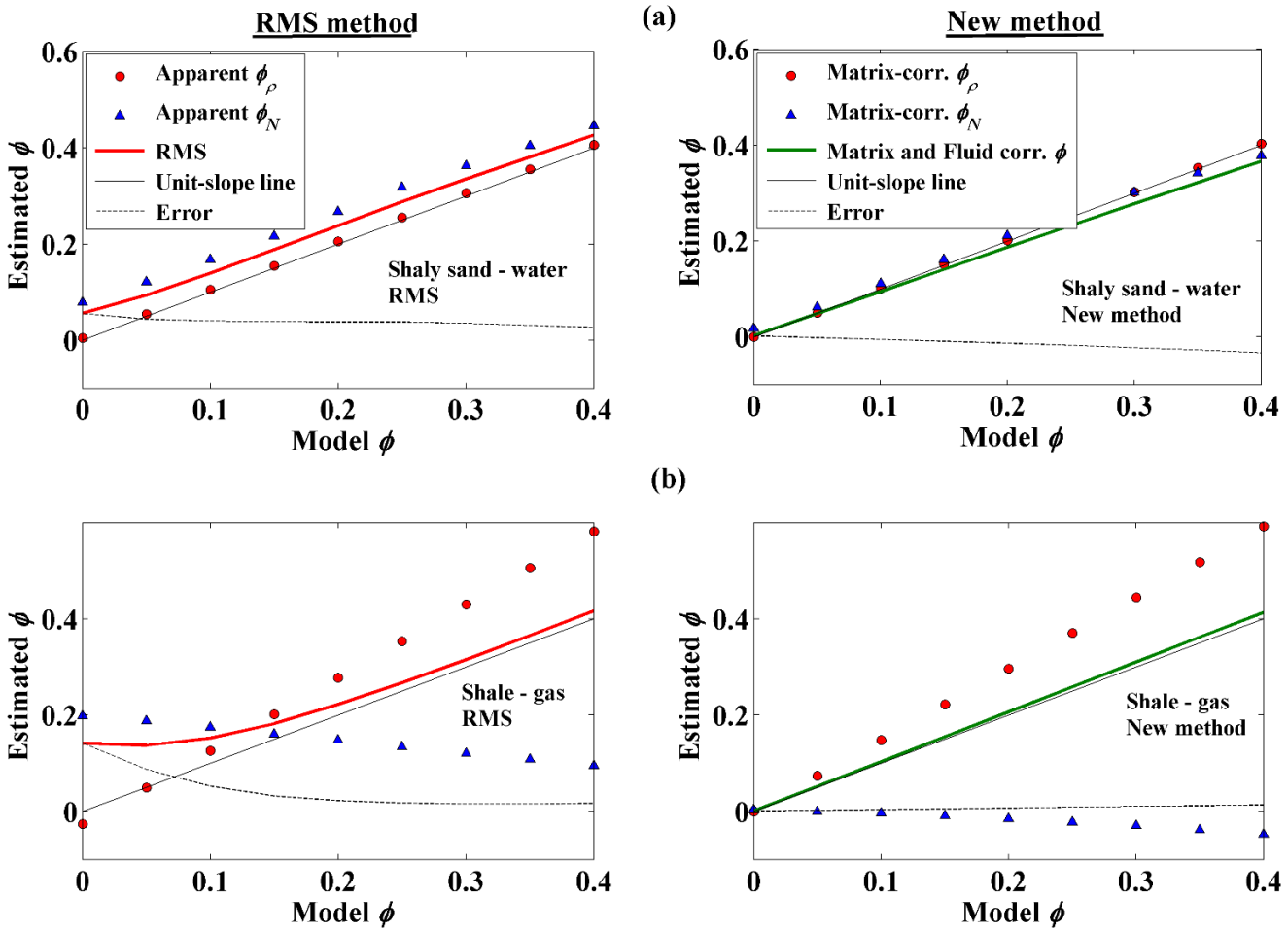

Figure 6.8: Results for Synthetic Case I. Calculated porosity using the RMS method (left) and the new equation for porosity (right) in (a) a 50% Chlorite-50% Quartz formation saturated with water, and in (b) a 100% wet Chlorite formation saturated with methane.

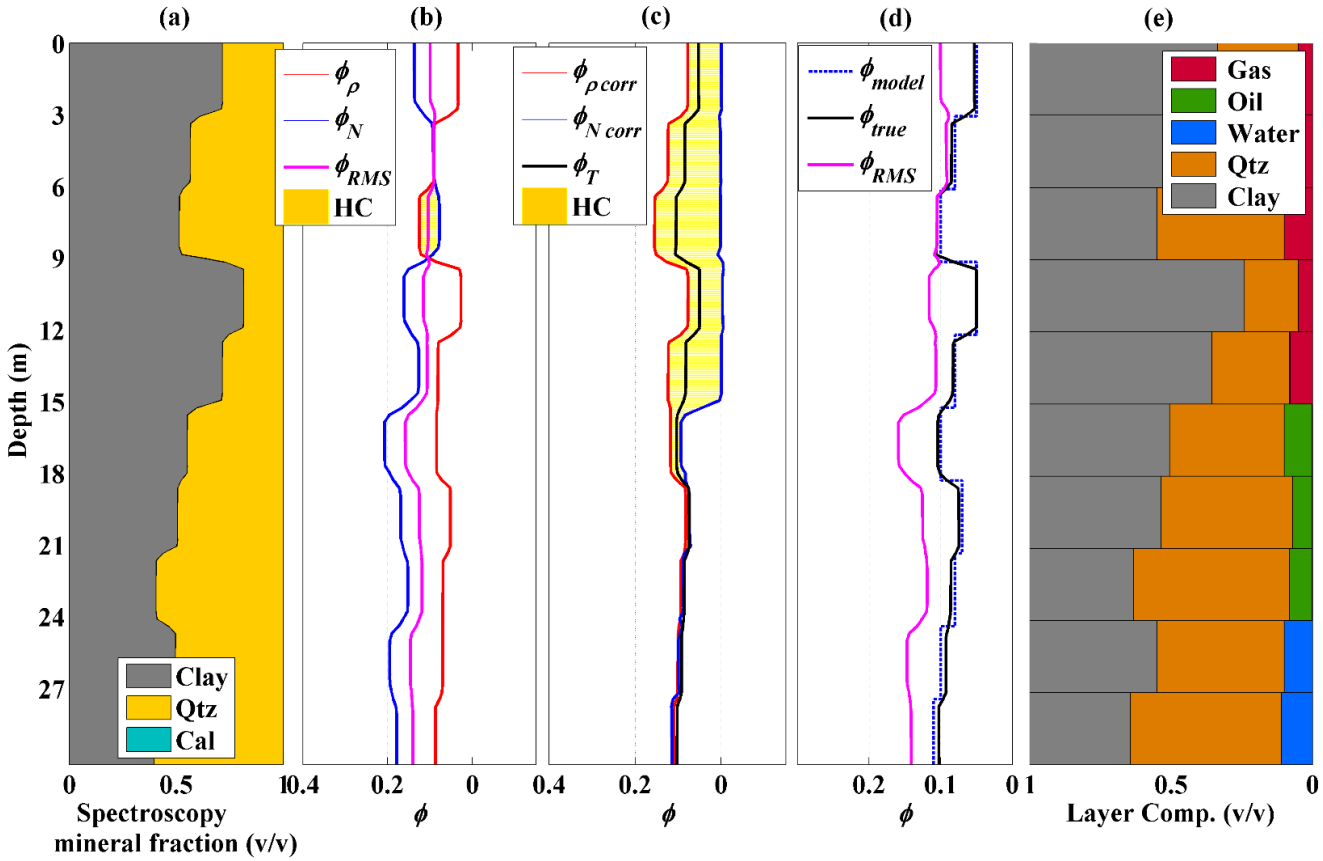

Figure 6.9: Results for Synthetic Case II. (a) Simulated gamma-ray spectroscopy log, (b) simulated thermal-neutron and density porosity logs in limestone p.u., and RMS averaged total porosity, (c) matrix-corrected neutron and density logs, and matrix- and fluid-corrected estimation of total porosity, (d) comparison of RMS averaged, matrix- and fluid-corrected, and actual model porosities, and (e) assumed mineral and fluid volumetric model.

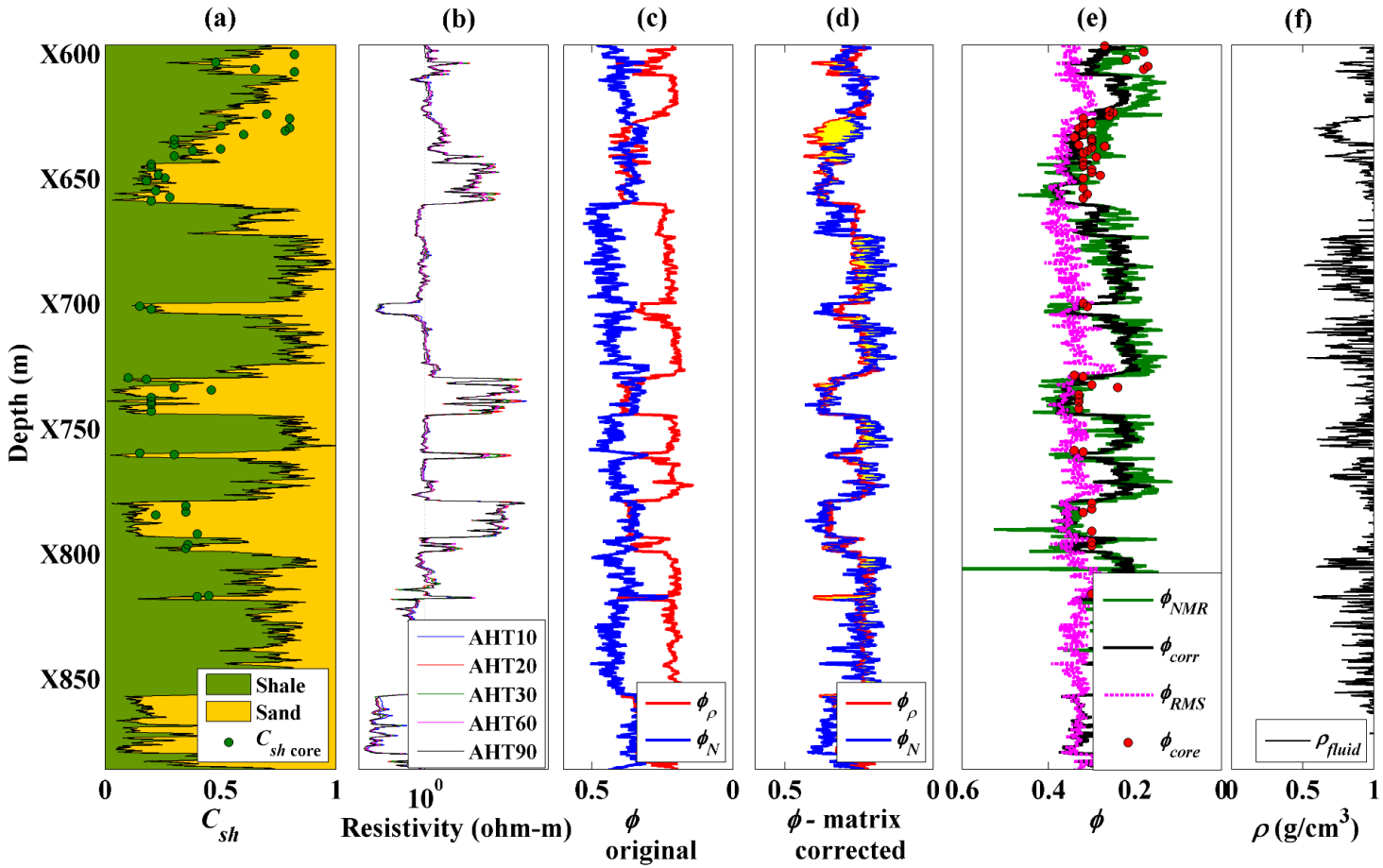

Figure 6.10: Field Case I. (a) Calculated C_{sh} from gamma-ray logs compared to core C_{sh}, (b) induction resistivity logs, (c) neutron and density porosity logs in limestone p.u., (d) matrix-corrected neutron and porosity logs using the new method, (e) comparison of RMS average porosity, matrix- and fluid-corrected porosity using the new method to NMR and core porosity, and (f) calculated fluid density.

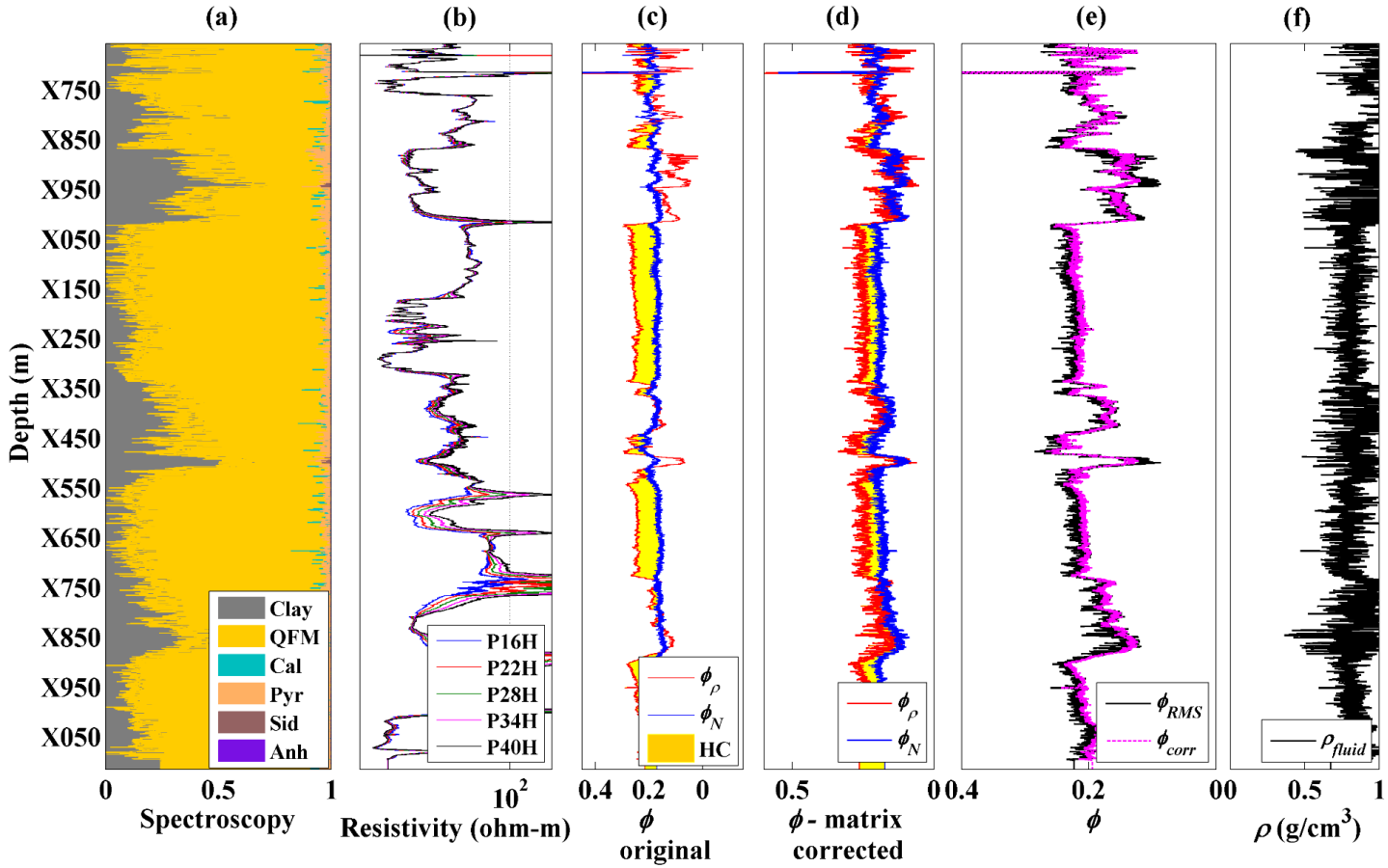

Figure 6.11: Field Case II. (a) Mineral composition from LWD gamma-ray spectroscopy measurements, (b) LWD high-frequency phase resistivity logs, (c) LWD neutron and density porosity logs in limestone p.u., (d) matrix-corrected neutron and porosity logs using the new method, (e) comparison of RMS average porosity, and matrix- and fluid-corrected porosity using the new method, and (f) calculated fluid density.

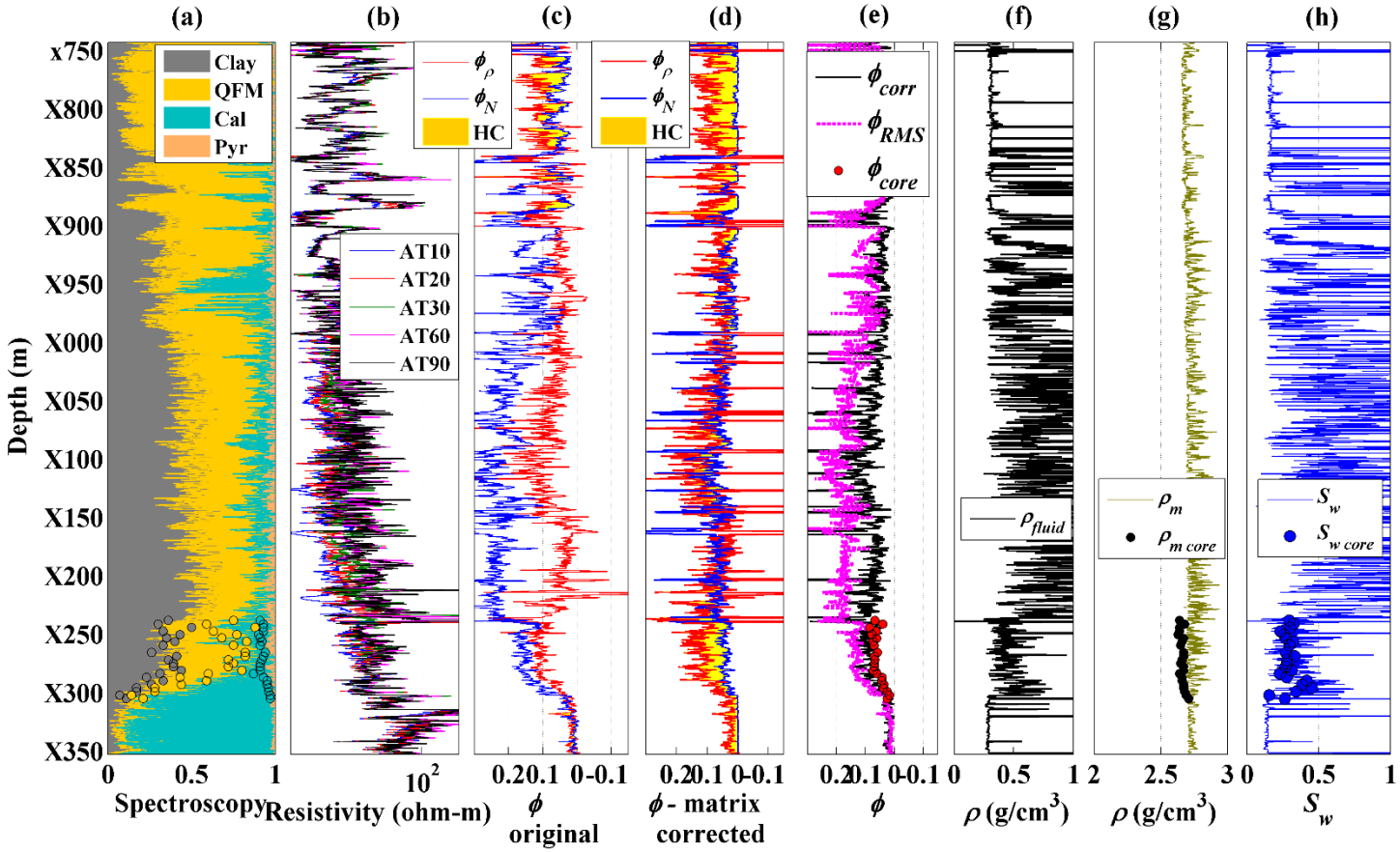

Figure 6.12: Field Case III. (a) Mineral compositions from wireline gamma-ray spectroscopy compared to XRD mineral volume fractions, (b) resistivity logs, (c) neutron and density porosity logs in limestone p.u., (d) matrix-corrected neutron and density logs using the new method, (e) comparison of RMS porosity and matrix- and fluid-corrected total porosity using the new method compared to core measurements, (f) calculated fluid density, (g) calculated matrix density compared to core measurements, and (h) calculated water saturation.

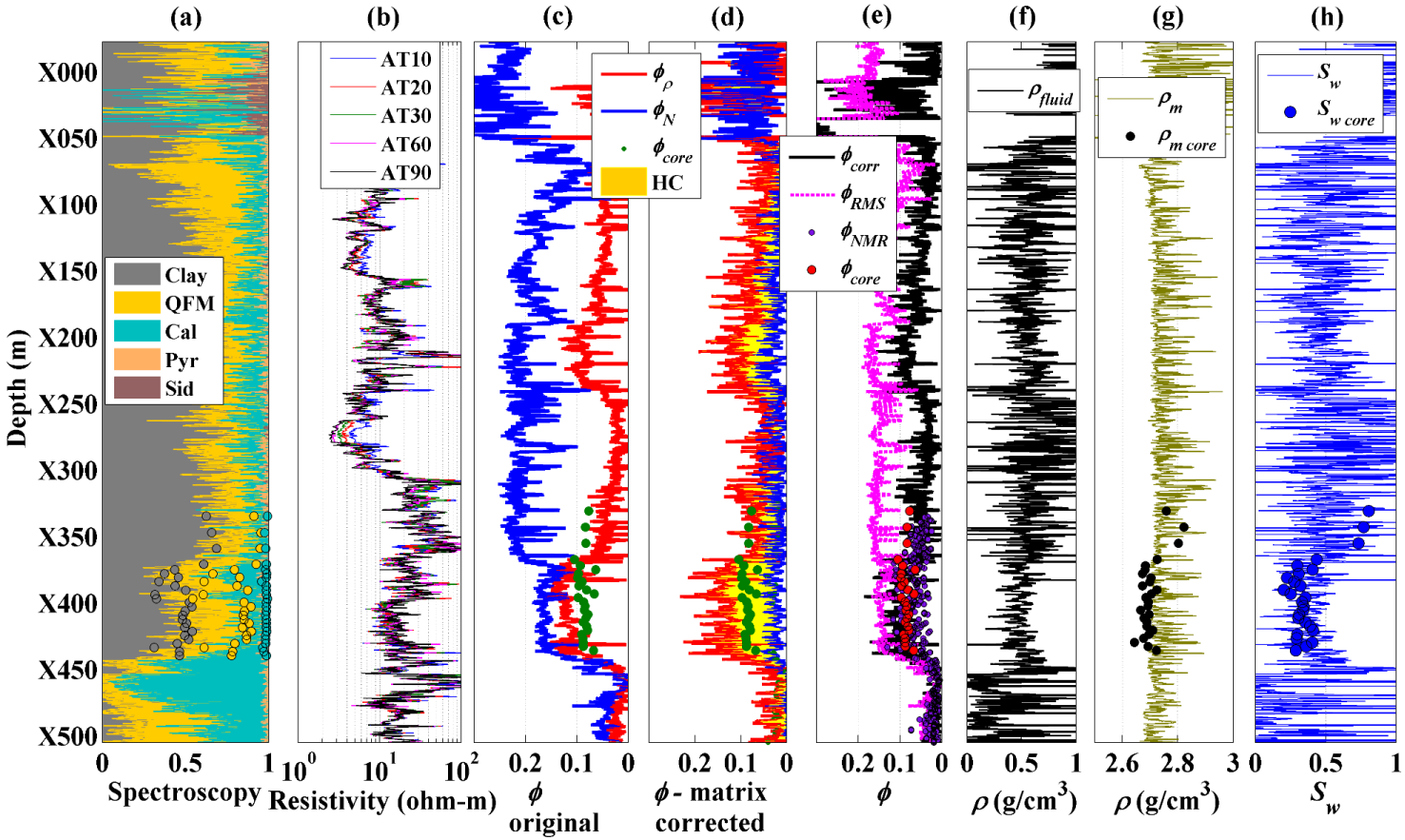

Figure 6.13: Field Case IV. (a) Mineral compositions from wireline gamma-ray spectroscopy compared to XRD mineral volume fractions, (b) resistivity logs, (c) neutron and density porosity logs in limestone p.u., (d) matrix-corrected neutron and density logs using the new method, (e) comparison of RMS porosity and matrix- and fluid-corrected total porosity using the new method compared to core and NMR measurements, (f) calculated fluid density, (g) calculated matrix density compared to core measurements, and (h) calculated water saturation.

Chapter 7: Joint Petrophysical Interpretation of Multi-Detector Nuclear Measurements Corrected for Invasion, Shoulder-Bed, and Well-Deviation Effects

The ultimate application of the multi-detector Sigma measurements is the integration with neutron, density, and spectroscopy logs to perform petrophysical interpretations independently of resistivity measurements. In this chapter, I develop a workflow to perform joint interpretation of multi-detector neutron, density, and Sigma logs to reduce invasion, shoulder-bed, and well-deviation effects in the estimation of porosity, water saturation, and hydrocarbon type whenever invasion is shallow. The procedure begins with the correction for matrix and fluid effects to neutron and density porosity logs to accurately estimate porosity introduced in Chapter 6. Multi-detector time decays are then used to assess radial length of invasion and estimate virgin-zone Sigma while simultaneously correcting for shoulder-bed and well-deviation effects. Density and neutron porosity logs are corrected for invasion and shoulder-bed effects using two-detector density and neutron measurements with the output from the time-decay (Sigma) inversion. The final step invokes a nuclear solver in which corrected Sigma, inverse of migration length, and density in the virgin zone are used to estimate water pore volume and fluid type. Fluid type is assessed with a flash calculation and SNUPAR to account for the nuclear properties of different types of hydrocarbon and water as a function of pressure, temperature, and salinity.

Results suggest that reduction of invasion effects is necessary when using density and neutron logs for petrophysical interpretation beyond the calculation of total porosity. Synthetic and field examples show that the correction for invasion effects becomes important in the case of salty filtrate invading gas-bearing formations. Changes in water saturation in laminated formations, which are averaged by resistivity logs, are better quantified through the proposed procedure. The advantage of the developed interpretation method is its ability to establish a mineral and fluid layer-by-layer model that takes into account tool physics, geometrical, and environmental effects, and also integrates all available information form nuclear measurements in a self-consistent manner.

7.1 INTRODUCTION

Logging-while-drilling (LWD) tools acquire nuclear and propagation measurements that are used in real-time for geosteering and also for quantitative petrophysical characterization. The commercial LWD multi-function tool studied in this dissertation (Weller et al., 2005) performs density measurements using two gamma-ray detectors and a cesium-137 source, neutron porosity measurements using two neutron detectors, and a 14-MeV neutron source, as well as thermal-neutron and gamma-ray time decays (Sigma logs) using three detectors at different spacing from the neutron source. The gamma-ray short-spaced detector is also used for spectroscopy measurements. Ultrasonic measurements are used to calculate azimuthal standoff between tool and borehole. Nuclear measurements can be used with resistivity measurements or independently to perform petrophysical evaluations.

Nuclear measurements have smaller volume of investigation than propagation resistivity, but they are still affected by shoulder-bed and well-deviation effects. This is especially important in the case of thinly bedded formations traversed by high-angle wells where the logs represent averages of actual layered formation properties. The development of rapid approximation methods for nuclear measurements such as neutron and density used with inversion techniques enabled the correction of these effects to find actual layer-by-layer properties (Mendoza et al., 2010b; Shetty et al., 2012; Ijasan et al., 2013a). Density and neutron measurements constituted the first area of attention to correct for these effects since total layer-by-layer porosity combined with resistivity logs has the potential to improve the estimation of hydrocarbon volume whenever resistivity measurements are reliable.

Advanced petrophysical interpretation workflows to reduce environmental and geometrical effects from nuclear logs rely on resistivity measurements to estimate water saturation. Shoulder-bed effects in resistivity logs acquired in deviated wells are difficult to reduce not only because resistivity measurements display artifacts such as horn and anisotropy effects (Anderson et al., 1990; Guzmán-García, 2002), as discussed in previous chapters, but also because there exist no rapid approximation methods of resistivity logs that can be efficiently used for rapid inversion. Ijasan et al. (2013b) proposed a petrophysical solver based on neutron, density, and resistivity measurements corrected for well-deviation and shoulder-bed effects. The forward model for propagation measurements is significantly slower than forward models for nuclear measurements, which increases

considerably the computational time needed to perform the integrated inversion. This problem can be overcome by using a similar approach in which resistivity logs are replaced by Sigma logs to estimate water saturation.

Sigma logs have an advantage over resistivity logs in that they have similar volume of investigation to neutron and density logs and, therefore, are less affected by shoulder-bed and well-deviation effects. **Figure 7.1** displays a set of LWD measurements in a deviated well where a Sigma log is well-correlated to resistivity logs; however, the Sigma log lacks the artifacts that resistivity logs display at bed boundaries and correlates better with azimuthal compensated density images, neutron, gamma-ray, and spectroscopy logs. Phase resistivity measurements, which have the best vertical resolution in the propagation measurement, display horn and anisotropy effects. These effects are more significant in the deep-sensing resistivity logs, but shallow resistivity logs still are affected by anisotropy effects that cause deflections in the log that cause it to disagree with other borehole measurements (observe dashed-circled areas in **Figure 7.1**).

Petrophysical interpretation based solely on nuclear measurements requires correcting all fluid-sensitive nuclear measurements (neutron, density, and Sigma) for the presence of shallow invasion, which is typically present in LWD measurements, due to the shallow-sensing nature of nuclear measurements. Elemental yields from inelastic spectroscopy measurements are only sensitive to the solid components of the rock and, therefore, are not affected by invasion. Invasion occurs when the formation is exposed to

drilling fluid at overbalance pressure for a few hours from rock breakage until the nuclear section collar performs the measurement.

The LWD commercial tool under study was carefully designed to permit the detection of invasion to facilitate petrophysical interpretation of nuclear measurements. In Chapter 2, it was described that the commercial LWD tool under study has three detectors: short-spaced gamma-ray (SSn), long-spaced gamma-ray (LSn), and near thermal-neutron (Near), which measure time decays and have different radial depths of investigation. A rapid approximation model for multi-detector decays was presented in Chapter 3 and was coupled with a 2D inversion scheme in Chapter 5 to estimate radial length of invasion as well as layer-by-layer virgin-zone Sigma devoid of invasion. Full nuclear measurement integration requires correcting neutron and density porosity logs not only for shoulder-bed and well-deviation effects, but also to take into consideration estimated radial length of invasion from multi-detector time decay inversion.

The main purpose of this chapter is to integrate the 2D inversion of multi-detector decays proposed in Chapter 5 with rapid simulation models for neutron and density porosity logs (Ijasan et al., 2013a) to develop a new inversion algorithm that corrects neutron and density porosity logs for simultaneous shoulder-bed, well-deviation, and invasion effects; corrected nuclear properties are used to estimate water saturation and in-situ fluid type. Integration of corrected nuclear properties is performed through a nuclear solver that takes into account the dependency of water and hydrocarbon PVT properties on pressure, temperature, and salinity using a flash calculation program and SNUPAR.

Namely, no hydrocarbon type is assumed; rather, the solver is allowed to determine hydrocarbon type (gas, oil, or intermediate hydrocarbon fractions) that best reconstructs virgin-zone bulk nuclear properties.

This chapter is organized as follows: First, I compare the radial sensitivity functions of the nuclear measurements in the LWD multi-function tool. The 2D inversion for Sigma, neutron, and density logs is then formulated. Next, I present a workflow that includes an initial correction for matrix and fluid effects for neutron and porosity logs to determine total porosity. Subsequently, results of Sigma, neutron, density log inversions are integrated using the nuclear PVT solver mentioned above. Lastly, two synthetic cases and five field cases are presented. One field case demonstrates the direct application of the solver in the instance that multi-detector decays are not available, which is true of cased-hole logs and LWD logs acquired with a tool different that the one described in this dissertation.

7.2 MULTI-DETECTOR LWD NUCLEAR MEASUREMENTS

7.2.1 The Multi-Function LWD Tool

The commercial LWD tool used in this dissertation was introduced in Chapter 2, section 2.3, with emphasis on the Sigma measurement. In this chapter, a complete description of the devices used to perform multi-detector neutron and density measurements is additionally explained. **Figure 7.2** shows the LWD multi-function tool in a typical logging environment with shallow invasion. The figure shows the Pulsed-

Neutron-Generator (PNG) section on top, which includes a 14-MeV neutron source and long-spaced gamma ray (LSn), short-spaced gamma-ray (SSn), and thermal-neutron Near (Near) detectors that measure time decays used to calculate Sigma and to assess the presence of invasion, as previously explained in Chapter 2. The top left of the figure contains the Near and Far thermal-neutron helium-3 detectors used for the thermal neutron porosity measurements. Tool calibration of detector Near/Far count-rate ratio versus water-saturated limestone blocks of different porosities is used to convert field count-rate ratios into equivalent limestone water porosity values. The left side of the middle section of the tool shows the gamma-gamma density section located ahead of the PNG section to prevent activation effects from PNG measurements from impacting density measurements. This section includes a Cesium-137 gamma-ray source and a set of short-spaced (SSg) and long-spaced (LSg) gamma-ray detectors. The density section is located on the stabilizer for improved detector-formation contact and improved measurement statistics. Total gamma-ray count rate decreases logarithmically as a function of formation electron density.

The LWD multi-function tool has two borehole size measurements. A density-derived caliper is calculated from the difference in short-spaced and long-spaced density readings (Labat et al., 2002). This caliper can be affected by the presence of shallow invasion, where invasion can be misinterpreted as tool standoff. Auspiciously, the tool also has two diametrically opposed, ultrasonic standoff sensors that enable it to calculate a 16-sector tool standoff image. The ultrasonic borehole log is important to assess whether or not shallow-sensing nuclear measurements are affected by tool standoff. It is assumed in

the remainder of this chapter that borehole quality is pre-checked using the ultrasonic measurements, and differences in shallow- and deep-sensing measurements are due only to the presence of invasion and/or shoulder-bed effects.

7.2.2 Nuclear Suite Sensitivity Functions

Integration of borehole measurements requires careful understanding of differences in vertical resolution and radial depth of investigation to understand at what level each measurement is affected by the presence of invasion and/or adjacent formations. The volume of investigation of nuclear measurements is a function of source-detector spacing, type of particles measured, the nuclear properties of the logging environment, and time window of the measurement. **Figure 7.3** shows (a) radial geometrical factors for multi-detector density, neutron, and Sigma measurements, and radially and azimuthally integrated multi-detector sensitivity functions for (b) density, (c) neutron, and (d) Sigma measurements for the commercial LWD tool used in this study in a 28-p.u. fresh-water saturated limestone formation. Notice on panel (a) that the density measurement is rather shallow and its maximum depth of investigation is about 5 cm (2 in). The neutron measurement is also shallow, but can sense approximately 10 cm (4 in) into the formation.

The difference in radial depth of investigation between the short-spaced and long-spaced detectors in the density and neutron measurements is not large, but it is sufficient to detect differences in the response due to small tool standoffs that are typical in LWD logging, and compensate for borehole effects. The multiple density and neutron detectors were not designed to assess the presence of invasion. For this reason radial length of

invasion will not be estimated using neutron and density logs, rather, only multi-detector Sigma measurements will be employed. The three Sigma radial sensitivity functions are deeper-sensing (due to the time dependency of the measurement and presence of late-time diffusion effects) and the Sigma detectors have significantly different radial sensitivity functions compared to neutron and density detectors. Multi-detector Sigma measurements were designed to provide significantly different radial sensitivities that enable the assessment of shallow invasion.

Multi-detector decays can be used to estimate the presence of invasion, estimate virgin-zone Sigma, and potentially correct shallow-sensing neutron and density measurements. The correction in neutron, Sigma and density measurements has the potential to enable a more accurate petrophysical interpretation from nuclear properties that otherwise would be masked by invasion effects. In the case of thick formations, only invasion effects have to be reduced from nuclear measurements. In the case of thinly bedded formations, the corrections are more challenging because all the measurements must additionally be corrected for shoulder-bed and well deviation effects.

Panels (b), (c), and (d) in **Figure 7.3** show that the LSn Sigma detector is most affected by adjacent formations, which is because it detects gamma rays from the neutron source and is largely spaced from the source. The Far thermal-neutron porosity detector is also significantly affected by adjacent formations because of its source-detector spacing. Density gamma-ray detectors, on the contrary, have good vertical resolution but are highly affected by invasion, as mentioned in the description of panel (a). In general, always exists

a tradeoff between vertical resolution and depth of investigation. The inversion scheme explained in this chapter is meant to take advantage of the different radial sensitivities of the Sigma measurement to correct all nuclear measurements for invasion, and to then take advantage of the short-spaced detector in all nuclear measurements to estimate layer-by-layer nuclear properties devoid of shoulder-bed, well-deviation, and invasion effects.

7.3 TWO-DIMENSIONAL INVERSION OF MULTI-DETECTOR MEASUREMENTS

7.3.1 Improved Estimation of Reference Invasion-Zone Sigma

Because total porosity in the reference vector is an important component of the multi-detector time decay inversion discussed in Chapter 4 and Chapter 5, I invoke the use of the matrix and fluid correction to neutron-density porosity logs introduced in Chapter 6. The correction is intended to improve both the calculation of total porosity and, therefore, to improve the calculation of the reference vector and the performance of the 2D multi-detector decay inversion. Total porosity is estimated using the following equation

$$a\phi_T^{\eta-1} + b\phi_T^{\eta} + c\left(1-\phi_T\right)^{\eta} - d = 0, \tag{7.1}$$

where

$$a = 0.064\left(\rho_{bulk} - \rho_m\right), \tag{7.2}$$

$$b = 0.064\rho_m + 0.011, \tag{7.3}$$

$$c = \xi_m, \tag{7.4}$$

and

$$d = \xi_{bulk}\,. \tag{7.5}$$

In these equations, ρ_{bulk} and ξ_{bulk} are bulk density and bulk inverse of migration length, respectively, where $\xi = 1/L_m$; ξ_{bulk} can be obtained from a conversion of as-delivered neutron porosity in limestone porosity units to inverse of migration length. The conversion depends on the type of neutron source used and is given by the following equations

$$\xi_{bulk} = -0.134\phi_N^4 + 0.354\phi_N^3 - 0.371\phi_N^2 + 0.191\phi_N + 0.0353, \tag{7.6}$$

for a 14-MeV neutron source, and

$$\xi_{bulk} = -0.124\phi_N^4 + 0.315\phi_N^3 - 0.325\phi_N^2 + 0.223\phi_N + 0.0365, \tag{7.7}$$

for an AmBe neutron source.

7.3.2 Multi-Detector Thermal-Neutron and Density Porosity

The approximation of time-independent nuclear measurements, such as neutron and density, can be written in the following form (Zhou et al., 2009)

$$\alpha(\mathbf{r}) = c_1 \ln N(\mathbf{r}_R) + c_2, \tag{7.8}$$

because the logarithm of the counts, $\ln N(\mathbf{r}_R)$, is approximately linearly related to the interaction cross section, $\alpha(\mathbf{r})$. The first-order approximation of equation 7.8 leads to

$$\alpha(\mathbf{r}) = \alpha_B + \frac{c_1}{N_B(\mathbf{r}_R)} \int d\mathbf{r} \frac{\partial N(\mathbf{r}_R, \mathbf{r}, \alpha_B)}{\partial \alpha(\mathbf{r})} \Delta\alpha(\mathbf{r}), \tag{7.9}$$

where $N_B(\mathbf{r}_R)$ is the a-priori known total number of counts at the detector position $\mathbf{r}_R$ in a material of interaction cross-section α_B, and $N(\mathbf{r}_R)$ is the detector count rate when the material within the detector volume of investigation is replaced by a material of interaction cross-section $\alpha_B + \Delta\alpha(\mathbf{r})$.

The spatially integrated relative change in detector response with respect to interaction cross-section within the volume of investigation of the detector is described by the Flux Sensitivity Function (FSF). Equation 7.9 can be written in terms of the FSF as

$$\alpha(\mathbf{r}) = \alpha_B + \int d\mathbf{r}\mathrm{FSF}(\mathbf{r}_R, \mathbf{r}, \alpha_B)\Delta\alpha(\mathbf{r}). \tag{7.10}$$

The FSF is a function of detector position, type of particles measured, and logging environment, and must obey the following normalization

$$\int d\mathbf{r}\mathrm{FSF}(\mathbf{r}_R, \mathbf{r}, \alpha_B) = 1. \tag{7.11}$$

The interaction cross-section, $\alpha(\mathbf{r})$, is the cross-section that most significantly controls the nuclear measurement to be approximated and that has the closest linear response with respect to detector count rate. In the case of density measurements, the perturbation cross-section is bulk-density, ρ, and in the case of thermal-neutron porosity measurements the perturbation cross-section is the inverse of migration length, ξ. Equation 7.10 can be re-written for the case of density measurements as

$$\rho(\mathbf{r}_R) = \rho_B + \int d\mathbf{r}\mathrm{FSF}(\mathbf{r}_R, \mathbf{r}, \rho_B)\Delta\rho(\mathbf{r}), \tag{7.12}$$

where $\mathrm{FSF}(\mathbf{r}_R, \mathbf{r}, \rho_B)$ is the detector-dependent spatial sensitivity function calculated in a background material of density ρ_B, $\Delta\rho(\mathbf{r})$ is a local perturbation in the density of the background material, and $\rho(\mathbf{r}_R)$ is the linearly approximated bulk density resulting from detector count rates after a local perturbation in formation density is applied. In the case of thinly bedded and invaded formations, measured density resulting from perturbations in the virgin and invaded zone can be approximated as

$$\rho(\mathbf{r}_R, j) = \sum_{i=1}^{m} \gamma^i \cdot \left\{ \left[\int_0^{r_i(i)} \mathrm{FSF}(\mathbf{r}_R, \mathbf{r}_i, \rho_B) d\mathbf{r} \right] \rho_i(i) + \left[\int_{r_i(i)}^{\infty} \mathrm{FSF}(\mathbf{r}_R, \mathbf{r}_i, \rho_B) d\mathbf{r} \right] \rho_v(i) \right\}, \quad (7.13)$$

where the integral in equation 7.13 is the radial geometrical factor of the measurement, *m* is the number of sub-layers in the model, and γ^i is the total sensitivity of detector $\mathbf{r}_R$ to sub-layer *i*, namely

$$\int_0^{r_i(i)} \mathrm{FSF}(\mathbf{r}_R, \mathbf{r}_i, \rho_B) d\mathbf{r} = J(\mathbf{r}_R, r_i(i), \rho_B), \quad (7.14)$$

and

$\rho_v(i)$ and $\rho_i(i)$ are virgin- and invasion-zone densities for model sub-layer *i*, respectively, and $\rho(\mathbf{r}_R, j)$ is the linearly approximated detector-dependent bulk density at measurement depth level *j*.

Equation 7.13 can be re-written as

$$\rho(\mathbf{r}_R, j) = \sum_{i=1}^{m} \gamma^i \cdot \left\{ J(\mathbf{r}_R, r_i(i), \rho_B) \rho_i(i) + \left[1 - J(\mathbf{r}_R, r_i(i), \rho_B) \right] \rho_v(i) \right\}. \quad (7.15)$$

Analogous to bulk density measurements, the count rates in neutron-porosity measurements exhibit a quasi-linear relationship with respect to ξ. Therefore, the bulk inverse of migration length resulting from perturbations in virgin- and invaded-zone inverse of migration length also follows a relationship similar to equation 7.15, i.e.

$$\xi\left(\mathbf{r}_R, j\right) = \sum_{i=1}^{m} \gamma^i \cdot \left\{ J(\mathbf{r}_R, r_i(i), \xi_B)\xi_i\left(i\right) + \left[1 - J(\mathbf{r}_R, r_i(i), \xi_B)\right]\xi_v\left(i\right) \right\}, \tag{7.16}$$

where $\xi_v\left(i\right)$ and $\xi_i\left(i\right)$ are virgin- and invasion-zone inverse of migration lengths, respectively, for model sub-layer i, and $\xi\left(\mathbf{r}_R, j\right)$ is the linearly approximated detector-dependent bulk inverse of migration length at measurement depth level j.

The forward operators for density and neutron measurements are

$$G\left[\begin{pmatrix} \rho_v \\ \rho_i \\ r_i^* \end{pmatrix}_{i=1:m}\right] = \begin{pmatrix} \rho_{SSg} \\ \rho_{LSg} \end{pmatrix}_{j=1:n}, \tag{7.17}$$

and

$$G\left[\begin{pmatrix} \xi_v \\ \xi_i \\ r_i^* \end{pmatrix}_{i=1:m}\right] = \begin{pmatrix} \xi_{Near} \\ \xi_{Far} \end{pmatrix}_{j=1:n}, \tag{7.18}$$

where ρ_v is virgin-zone density, ρ_i is invaded-zone density, r_i^* is radial length of invasion given from the multi-detector decay inversion for model sub-layers i=1:m, ρ_{SSg} and ρ_{LSg} are measured short-spaced and long-spaced densities, respectively, at measured depth levels j=1:n, ξ_v is virgin-zone inverse of migration length, ξ_i is invaded-zone inverse of

migration length, and ξ_{Near} and ξ_{Far} are measured Near and Far water-filled neutron porosities converted to inverse of migration length (ξ), respectively, at measured depth levels j=1:n.

Estimation of virgin zone density and inverse of migration length devoid of invasion effects is performed separately using Occam's method, which was described in Chapter 4, to estimate density and neutron model layer-by-layer properties given in equations 7.17 and 7.18. I rapidly calculate the Jacobian for neutron and density measurements analytically using detector-specific sensitivity functions and fitting a polynomial to detector-specific radial geometrical factors similar to the procedure described in Chapter 5 for multi-detector Sigma measurements. **Appendix A** provides further details about the structure of the Jacobian matrices to be used in the separate 2D multi-detector neutron and density inversion.

The significant difference in the 2D neutron and density inversion when compared to 2D multi-detector decay inversion is the definition of the reference vector. In the case of neutron and density measurements, a reference value for r_i is provided from the output of the Sigma inversion to ensure that the neutron and density inversion corrects for shoulder-bed, well-deviation, and invasion effects at a fixed radial length of invasion imposed by the Sigma inversion. The importance of fixing r_i was described in the comparison of radial sensitivity functions of the nuclear measurements earlier in this chapter. Multi-detector density and neutron responses do not have sufficient differences in radial depth of investigation to provide an accurate estimation of radial length of invasion, whereas LWD

Sigma is better suited to assess invasion so long as there exists enough contrast in virgin- and invasion-zone Sigma, e.g. salty mud filtrate invading a hydrocarbon-bearing formation. The reference vector for the neutron and density inversion can then be written as

$$\mathbf{m}_R\big|_{\rho-N} = \begin{bmatrix} 0 \\ 0 \\ r_i^* \end{bmatrix}, \tag{7.19}$$

where r_i^* is the radial length of invasion for each model sub-layer estimated from 2D inversion of multi-detector decays, and $\mathbf{m}_R\big|_{\rho-N}$ is the reference vector used in the separate inversion of two-detector neutron porosity and density logs.

So far it has been explained how to correct LWD density, neutron, porosity and Sigma measurements performed with multiple detectors for invasion, shoulder-bed, and well-deviation effects. In the following section I introduce a method to integrate all corrected measurements to perform resistivity-independent petrophysical interpretations that are consistent with PVT properties of reservoir fluids.

7.4 Nuclear-Based Estimation of Fluid Type And Water Pore Volume

7.4.1 Nuclear Mixing Laws

In this section layer-by-layer corrected bulk Sigma, inverse of migration length, and density are used to estimate fluid type and water pore volume. To achieve this, the following mixing laws for fluid-sensitive nuclear measurements are considered

$$\Sigma_v = \phi\left[\Sigma_{hc}(1-S_w)+S_w\Sigma_w\right]+(1-\phi)\Sigma_m\,, \tag{7.20}$$

$$\rho_v = \phi\left[\rho_{hc}(1-S_w)+S_w\rho_w\right]+(1-\phi)\rho_m\,, \tag{7.21}$$

and

$$\xi_{bulk} = \phi^{\eta}\left[\xi_{hc}(1-S_w)+S_w\xi_w\right]+\left(1-\phi\right)^{\eta}\xi_m\,, \tag{7.22}$$

for

$$\eta = 0.5\cdot(1\text{-}C_{sh})+0.8\cdot C_{sh}\,, \tag{7.23}$$

where equation 7.22 corresponds to the nonlinear mixing law for inverse of migration length introduced in Chapter 6. Sub-indices hc, w, and m indicate nuclear properties for hydrocarbon, water, and matrix, respectively.

Hydrocarbon properties are a function of pressure, temperature, and the molar fraction of light and heavy hydrocarbon chains (fluid type). The volume fraction of light hydrocarbon in the hydrocarbon phase, V_{light}, describes the lightness of the single-phase hydrocarbon. It is considered that at each depth only one mixed hydrocarbon phase exists e.g. dry gas, black oil, oil with gas in solution, or rich gas. The volumetric mixing laws for the hydrocarbons are

$$\Sigma_{hc} = \Sigma_{light}V_{light}+(1-V_{light})\Sigma_{heavy}\,, \tag{7.24}$$

$$\rho_{hc} = \rho_{light}V_{light}+(1-V_{light})\rho_{heavy}\,, \tag{7.25}$$

and

$$\xi_{hc} = \xi_{light}V_{light}+(1-V_{light})\xi_{heavy}\,. \tag{7.26}$$

The mixing laws for Sigma and density in equations 7.24 and 7.25 are linear because these are volumetric nuclear properties. Equations 7.22 and 7.26 are approximations, as mentioned in Chapter 6.

7.4.2 PVT-Consistent Nuclear Interpretations

Nuclear properties for hydrocarbons are modeled as a function of the volume fractions of a light and a heavy hydrocarbon chain, V_{light}, and V_{heavy}, respectively. In this dissertation methane was chosen to be the light hydrocarbon and decane was chosen to be the heavy hydrocarbon. I wish to take into account the difference in log signatures between oil and gas-bearing formations, but use only two hydrocarbon fractions to simplify the modeling.

The main objective in this section is to establish a relationship between nuclear fluid properties in equations 7.24, 7.25, and 7.26 and fluid type with the intention that inversion of nuclear properties can involve different fluid types instead of a pre-defined fluid type. I express the hydrocarbon properties in terms of V_{light} because at certain conditions of pressure and temperature the volume of light hydrocarbon fraction and fluid type exhibit a specific relationship. This means that V_{light} represents a connection between in-situ fluid nuclear properties and gas-molar fraction in the hydrocarbon, χ_g, referred to as fluid type. **Figure 7.4** displays the variation in light hydrocarbon volume as a function of pressure and temperature for various mixtures, or fluid types, of light and heavy

hydrocarbon with gas-molar fractions, χ_g, in the range of 0 to 1. At specific reservoir pressure and temperature conditions one line in **Figure 7.4** establishes the relationship between light hydrocarbon volume and fluid type.

Nevertheless, the estimation of fluid type is highly sensitive to the presence of invasion. It will be shown in the results section of this chapter that no invasion or shallow invasion enables to differentiate weather the hydrocarbon is gas, oil, or a light hydrocarbon mixture. But the presence of deep invasion makes it difficult to accurately detect fluid type due to the small sensitivity of all nuclear measurements to the virgin formation and considerable uncertainty on nuclear properties corrected for invasion effects.

7.4.3 Nuclear-Based Petrophysical Solver

The forward operator that describes the non-linear system of equations 7.20 through 7.26 can be expressed as

$$G\begin{bmatrix} V_{light} \\ \phi S_w \end{bmatrix} = \mathbf{d}_s = \begin{bmatrix} \Sigma_v \\ \rho_v \\ \xi_v \end{bmatrix}. \tag{7.27}$$

The inverse problem is solved layer by layer using Occam's inversion algorithm in the following form

$$\left[\left(\mathbf{W}_d \cdot \mathbf{J}_s(\mathbf{m}_s^k)\right)^T \cdot \left(\mathbf{W}_d \cdot \mathbf{J}_s(\mathbf{m}_s^k)\right) + \alpha^2 \mathbf{I}\right]\mathbf{m}_s^{k+1} = \mathbf{J}_s(\mathbf{m}_s^k)^T \left[\left(\mathbf{W}_d{}^T \cdot \mathbf{W}_d\right) \cdot \left(\mathbf{d} - G(\mathbf{m}_s^k) + \mathbf{J}_s(\mathbf{m}_s^k)\mathbf{m}_s^k\right)\right] + \alpha^2 \mathbf{m}_{Rs}^T \tag{7.28}$$

where $\mathbf{m}_s^k = \begin{bmatrix} V_{light} \\ \phi S_w \end{bmatrix}$ is the model for a specific layer at iteration *k*, $\mathbf{m}_s^{k+1}$ is the updated model at iteration *k+1*, $\mathbf{J}_s(\mathbf{m}_s^k)$ is the Jacobian matrix containing the derivatives of the nuclear bulk properties with respect to light hydrocarbon volume and water pore volume, $G(\mathbf{m}_s^k)$ is the set of simulated bulk properties using equations 7.20, 7.21, and 7.22 at iteration *k*, α is the updated regularization parameter which is adjusted as a function of the updated cost function, $\mathbf{W}_d = 1/\mathbf{d}_s$ is a data-weight matrix, and $\mathbf{m}_{Rs}$ is a reference vector.

The Jacobian matrix for the nuclear solver is defined as

$$\mathbf{J}_s = \begin{bmatrix} \dfrac{\partial \Sigma_v}{\partial V_{light}} & \dfrac{\partial \Sigma_v}{\partial \phi S_w} \\ \dfrac{\partial \rho_v}{\partial V_{light}} & \dfrac{\partial \rho_v}{\partial \phi S_w} \\ \dfrac{\partial \xi_v}{\partial V_{light}} & \dfrac{\partial \xi_v}{\partial \phi S_w} \end{bmatrix}, \tag{7.29}$$

and the derivatives can be analytically calculated from equations 7.20 through 7.26, namely

$$\frac{\partial \Sigma_v}{\partial V_{light}} = \phi(1-S_w)\left(\Sigma_{light} - \Sigma_{heavy}\right), \tag{7.30}$$

$$\frac{\partial \Sigma_v}{\partial \phi S_w} = \Sigma_w - V_{light}\Sigma_{light} - (1-V_{light})\Sigma_{heavy}, \tag{7.31}$$

$$\frac{\partial \rho_v}{\partial V_{light}} = \phi(1-S_w)\left(\rho_{light} - \rho_{heavy}\right), \tag{7.32}$$

$$\frac{\partial \rho_v}{\partial \phi S_w} = \rho_w - V_{light}\rho_{light} - (1-V_{light})\rho_{heavy}, \tag{7.33}$$

$$\frac{\partial \xi_v}{\partial V_{light}} = \phi^{\eta}\left(1-S_w\right)\left(\xi_{light}-\xi_{heavy}\right), \tag{7.34}$$

and

$$\frac{\partial \xi_v}{\partial \phi S_w} = \phi^{\eta-1}(\xi_w - V_{light}\xi_{light} - (1-V_{light})\xi_{heavy}). \tag{7.35}$$

Corrected nuclear properties cannot always be used for petrophysical inversion because invasion is sometimes deep and sensitivity of all nuclear measurements to the virgin formation is not enough to perform the correction accurately. The inversion scheme is redefined as a function of estimated radial length of invasion because density, neutron porosity, and Sigma are affected by invasion at different degrees, i.e.

- If radial length of invasion, r_i, at certain layer is less than 2.54 cm (1 in), the forward model is defined by equation 7.27 and the reference vector is set to zero $\mathbf{m}_{Rs} = \begin{bmatrix} 0 \\ 0 \end{bmatrix}$.

- If r_i is between 2.54 and 10.2 cm (1 and 4 in), the density measurement is not used in the inversion because it means the responses of the gamma-ray density detectors, SSg and LSg, are completely masked by invasion. In this case I define $G\begin{bmatrix} V_{light} \\ \phi S_w \end{bmatrix} = \begin{bmatrix} \Sigma_v \\ \xi_v \end{bmatrix}$ and $\mathbf{m}_{Rs} = \begin{bmatrix} 0 \\ 0 \end{bmatrix}$.

- If r_i is larger than 10.2 cm, the neutron porosity measurement is masked by invasion and ξ_v is not used in the inversion. In this situation the number of

variables to solve is larger than the size of the measurement vector and the problem is rendered underdetermined. I remedy this by providing a reference value for fluid type. The problem in the case of deep invasion is re-defined as

$$G\begin{bmatrix} V_{light} \\ \phi S_w \end{bmatrix} = \begin{bmatrix} \xi_v \end{bmatrix} \text{ and } \mathbf{m}_{Rs} = \begin{bmatrix} \chi_g^{REF} \\ 0 \end{bmatrix}.$$

7.4.4 Estimation of Uncertainty

Error bars are calculated for all the inversions shown in this chapter using the covariance method previously introduced in Chapter 4, section 4.3.3. The standard deviation of the estimations is calculated as a function of the covariance matrix, $\mathbf{Cov(m)}$, which is a function of the standard deviation of the weighted misfit vector and the data-weighting matrix. Additionally, the Confidence Index (*CI*) for estimated virgin-zone Sigma introduced in Chapter 4 is presented as a means to establish when virgin-zone Sigma, and consequently water saturation, are uncertain. The index acts as a red flag in cases where virgin- and invasion-zone Sigma contrast is not significant and results from multi-detector decay inversion are subject to considerable uncertainty.

7.5 MULTI-NUCLEAR INTERPRETATION WORKFLOW

This section introduces the workflow to estimate fluid type and water pore volume exclusively from multi-detector density, neutron, and Sigma measurements independently from resistivity (observe **Figure 7.5**). I begin with the matrix and fluid correction for compensated neutron and density logs introduced in Chapter 6 to obtain an accurate

estimation of total porosity that is used in the reference value for Σ_i required by the multi-detector decay inversion. From the multi-detector decay inversion I obtain virgin-zone Sigma corrected for shoulder-bed, well-deviation, and invasion effects and an estimation of radial length of invasion. r_i is used as an input for the 2D inversion of short-spaced (SSg) and long-spaced (LSg) gamma density logs, and 2D inversion of Near and Far thermal-neutron porosity logs. From these inversions, corrected values of ρ and ξ in the virgin formation are obtained.

Next, a flash calculation is performed to define the densities of light and heavy hydrocarbon fractions at reservoir pressure and temperature conditions (Abdollahpour, 2011). These densities are used as an input to SNUPAR to calculate Sigma and inverse of migration length of the hydrocarbon fractions. Nuclear properties of water are calculated as a function of salinity, pressure, and temperature also using SNUPAR. This step establishes the range of possible nuclear properties in the hydrocarbon at reservoir conditions that will enable to calculate the proportion of light and heavy hydrocarbon fractions that best reconstructs corrected nuclear properties.

Finally, the solver measurement vector, $\mathbf{d}_s$, is defined with corrected nuclear properties, Σ_v, ρ_v, and ξ_v, depending on the extent of radial length of invasion, as explained in the previous section. The solver estimates light hydrocarbon volume, V_{light}, in the hydrocarbon mixture, and pore water volume, ϕS_w. Mud filtrate salinity is required to

estimate radial length of invasion, and connate water salinity is required to estimate water pore volume. The nuclear solver can be run independently to estimate ϕS_w and V_{light} in cases where multi-detector time decays are not available (assuming no invasion), and/or whenever shoulder-bed effects are not corrected. Results from uncorrected nuclear properties are subject to the validity of the assumptions of negligible invasion and geometrical effects on the measurements.

The following sections depict applications of petrophysical interpretation of synthetic and field cases using only nuclear measurements and following the workflow shown in **Figure 7.5**. Two synthetic and four field cases correspond to measurements of the LWD multi-function tool under consideration. Additionally, the last field case is an application where uncorrected cased-hole Σ, ρ, and ξ are integrated in the nuclear solver to estimate fluid type and water pore volume.

7.6 SYNTHETIC RESULTS

7.6.1 Synthetic Case I

This synthetic example describes the interpretation of multi-detector LWD density, neutron and Sigma measurements simulated in an 80º deviated well penetrating laminated formations 0.48-m (1.5 ft) thick. I assume a capillary transition from a top gas-bearing zone to a bottom 80-kppm [NaCl] water leg. Mud filtrate salinity is 200 kppm [NaCl]. This case is challenging to interpret because of simultaneous invasion, well-deviation, and shoulder-bed effects present in all the measurements. I will prove that large virgin- and invasion-

zone Sigma contrasts help to accurately estimate radial length of invasion and perform corrections on all fluid-sensitive nuclear measurements. **Figure 7.6** shows (a) actual and reconstructed multi-detector decays, (b) borehole- and diffusion-corrected Sigma logs, (c) actual and reconstructed Near and Far inverse of migration length logs, (d) actual and reconstructed short-spaced (SSg) and long-spaced (LSg) density logs, (e) a sketch of the borehole, invasion profile, and virgin formation with error bars on radial length of invasion, (f) estimated virgin- and invasion-zone layer-by-layer Sigma, (g) inverse of migration length, and (h) density with error bars, (i) estimated layer-by-layer volumetric model, and (j) a comparison of actual model versus estimated water saturation. **Table 7.1** describes assumed petrophysical properties for this example.

Analysis of results in **Figure 7.6** indicates that while three-detector Sigma logs display differences due to shallow invasion, multi-detector neutron and density logs display only small differences primarily due to shoulder-bed effects. Short-spaced and long spaced gamma-ray density values overlap, and Near and Far neutron values overlap through all invaded zones because both measurements are mostly sensing the invaded zone as seen on tracks (c) and (d). However, after estimating radial length of invasion and correcting for invasion effects, tracks (f), (g), and (h) show that the algorithm enables the calculation of actual corrected values of virgin- and invaded-zone nuclear properties. Differences in corrected density and inverse of migration length for both zones on tracks (g), and (h), compared to all detectors reading the same value on (c) and (d) indicates that multi-detector nuclear inversion enabled the correction of shallow-sensing neutron and density

measurements for invasion effects. The correction is reflected in satisfactory estimations of water saturation and fluid type on tracks (i) and (j).

Hydrocarbon type is described by the color bar on track (i) in **Figure 7.6**. Green indicates a heavy fluid with nuclear properties close to the properties of decane and red indicates a light fluid with nuclear properties similar to the properties of methane at reservoir pressure and temperature conditions. The algorithm accurately predicted fluid type even in the presence of invasion (compare hydrocarbon type in **Figure 7.6** and **Table 7.1**). An exceptional advantage of the method is the flexibility that exists in the nuclear solver to estimate the fluid type that best describes nuclear corrected bulk properties, rather than assuming a single fluid type. This has a direct impact on the estimation of water saturation. Notice on track (j) that the estimation of water saturation is better in the upper section where the hydrocarbon (gas) displays the largest contrast in nuclear properties compared to connate water. Also, error bars on virgin-zone density are large whenever invasion is present, and tend to be larger than error bars in virgin-zone inverse of migration length because density logs are shallower sensing than neutron logs.

7.6.2 Synthetic Case II

In this second synthetic example I test the multi-detector nuclear inversion in the case of alternations of gas-bearing sand and shale formations where the combined effect of shoulder strong absorbing shale and invasion of salty filtrate are difficult to decouple and typically result in overestimation of water saturation if not corrected. Permeable formations are invaded at different extensions by 230 kppm [NaCl] mud filtrate. Reservoir fluid

properties are calculated at 150 ^{o}F and 24131.7 kPa (3500 psia), and connate water salinity is 80 kppm [NaCl]. Assumed well deviation is 45^{o}. **Figure 7.7** shows (a) actual and reconstructed multi-detector decays, (b) borehole- and diffusion-corrected Sigma logs, (c) actual and reconstructed Near and Far inverse of migration length logs, (d) actual and reconstructed short-spaced (SSg) and long-spaced (LSg) density logs, (e) a sketch of borehole, invasion profile, and virgin formation with error bars on radial length of invasion, estimated virgin- and invasion-zone layer-by-layer (f) Sigma, (g) inverse of migration length, and (h) density with error bars, (i) estimated layer-by-layer virgin-zone volumetric model, and (j) a comparison of actual model versus estimated water saturation. **Table 7.2** presents assumed petrophysical properties for this synthetic example.

Coupled effects of adjacent shale formations, which are strong absorbers of thermal neutrons, and salty filtrate in the measurements are the greatest challenge in this synthetic example. It is shown on track (a) the high variability of the time decays with depth, and on track (b) that the separation between borehole- and diffusion-corrected Sigma logs is not a clear indication of invasion. Nonetheless, a-priori knowledge of matrix composition and an educated estimate of invasion-zone Sigma lead to a satisfactory estimation of the invasion profile on track (e), even though radial length of invasion was overestimated in sand formations at 4 and 10 m. The significant correction on all nuclear logs is seen on tracks (f), (g), and (h). Low Sigma, high inverse-of-migration-length, and low density values indicate the presence of gas in the virgin zone, even though original multi-detector neutron and density measurements, on tracks (c) and (d), respectively, display similar

values that are non-indicative of gas in gas-bearing zones due to the presence of invasion. The correction permits a good approximation of water saturation on track (j).

Despite there being disparities in estimations with respect to the actual model values, this example takes nuclear measurements to the edge, correcting them in a case where the actual formation response is completely masked by invasion and geometrical effects, and making them usable for quantitative petrophysical interpretations. I see that in permeable layers at 4 and 10 m the algorithm was not able to detect the presence of gas in the virgin zone and instead estimated the presence of oil. An explanation for this misinterpretation is that radial length of invasion was overestimated due to the degree of non-uniqueness in the multi-detector inversion imposed by the simultaneous presence of invasion and adjacent shale formations. At this estimated radial length of invasion neutron and density logs are not sensitive to the virgin zone, and Sigma is slightly sensitive to it. Overall, the performance of the multi-detector inversion is fairly satisfactory, given the limitations of the measurement and the extreme environment of application.

7.7 FIELD RESULTS

7.7.1 Field Case I

This field case presents the inversion of multi-detector density, neutron, and Sigma time decays in an offshore well in West Africa. The section of interest is a siliciclastic laminated anticline with presence of carbonates that was perforated above the oil-water contact by a 45^{o} deviated well. The hydrocarbon is light and gas has been produced from

top formations which are below bubble pressure. The presence of a compositional gradient or gas-oil contact is suspected but has not been confirmed from interpretation of LWD logs. The well was drilled with synthetic based mud (SBM) and mud-filtrate salinity is 136 kppm [NaCl]. **Figure 7.8** shows (a) measured and reconstructed multi-detector decays, (b) borehole- and diffusion-corrected Sigma logs, (c) measured and reconstructed Near and Far inverse of migration length logs, and (d) short-spaced and long-spaced density logs, (e) a sketch of the borehole, invasion profile, and virgin formation, estimated virgin- and invaded-zone layer-by-layer (f) Sigma, (g) inverse of migration length, and (h) density with error bars, and (i) estimated mineral and fluid volumetric model in the virgin formation.

The accurate reconstruction of time decays along with Near and Far neutron logs are shown on tracks (a) and (c). Reconstructed density logs on track (d) show dissimilarity at the deep-invaded formation located at X44 m. Careful inspection of time decays at X44 and X51 m indicates that the measurements at these depths are noisy, especially the Near detector time decay. This is why radial length of invasion was overestimated, which then resulted in uncertainty and difficulty in matching corrected neutron and density logs at those depths. I recommend the statistical quality of time decays be evaluated before attempting to estimate radial length of invasion with the aim of carefully inspecting inversion results at depths where the multi-detector decay measurement lacks quality.

Multi-detector nuclear logs are highly affected at the top gas section by the presence of salty mud filtrate invasion (see tracks (g) and (h)). The difference in corrected virgin-

zone and invasion-zone nuclear properties occurs mainly at the top section where the volumetric model on track (i) indicates the presence of a light fluid. At the middle and bottom section exists a small contrast in invaded-virgin zone Sigma and the estimation of radial length of invasion is subject to greater uncertainty. Whenever invasion is deeper than approximately 4 cm, the error bars on corrected virgin-zone density become large because the density measurement is no longer sensitive to the virgin zone. Virgin-zone density in invaded formations seems higher than invasion-zone Sigma, opposite to what would be expected in the case of SBM invading light hydrocarbon-bearing formations. Corrected virgin-zone densities in formation where invasion is deeper than 4 cm are not representative of the actual properties of the virgin-zone formation. Similarly, error bars on corrected inverse of migration length expand when invasion is deeper than 7 cm because the neutron measurement is mostly affected by the high-salinity filtrate in the near wellbore zone at this invasion depth.

Figure 7.9 summarizes inversion results for Field Case I. I present (a) estimated radial length of invasion with error bars, (b) borehole- and diffusion-corrected field Sigma logs, (c) matrix- corrected neutron and density logs and total porosity estimated using equation 7.1, (d) water saturation derived using the introduced method (solid line) compared to water saturation derived using phase resistivity, (e) estimated layer-by-layer fluid and mineral volumetric model, and (f) comparison of simulated (dashed lines) versus field (solid lines) phase resistivity logs and calculated layer-by-layer resistivities (green solid line), and confidence index (*CI*) on estimated virgin-zone Sigma.

There are three features of importance to observe in **Figure 7.9**. First, the nuclear solver can accurately detect the presence of gas that coincides with the neutron-density crossover at the top and detects a heavier fluid at the bottom, where the crossover disappears (compare tracks (c) and (e)). Some intervals in the gas section show oil, but I hypothesize this is due to the large radial length of invasion in these layers affecting neutron and density measurements. Invasion is relatively deep and the measurements cannot be accurately corrected for invasion effects. Second, observe how the improved vertical resolution of the nuclear inversion enables the changes in water saturation in this laminated sequence, that are averaged by resistivity logs on track (d), to be discerned. The reason for this being that resistivity logs have a larger volume of investigation and small amounts of clay can dominate the measurement response in the case of highly laminated formations. Lastly, note that (f) shows simulated and field resistivities to agree fairly well, except for the formations where invasion is deep and *CI* marks a red color indicating that corrected virgin Sigma and estimations that stem from it have considerable uncertainty.

7.7.2 Field Case II

In this field example I take advantage of the small volume of investigation of all nuclear measurements to estimate water saturation in a highly laminated siliciclastic sequence in the North Sea. The commercial LWD tool under study was run in a 70^{o} deviated well. Invasion effects are expected to be small due to low mud filtrate salinity, 46 [NaCl] kppm. Nonetheless, the laminated nature of the formations suggests that correction for shoulder-bed effects is necessary in order to estimate actual layer-by-layer

properties that can be integrated in the nuclear solver to evaluate fluid type and water saturation. **Figure 7.10** shows (a) measured and reconstructed multi-detector decays, (b) borehole- and diffusion-corrected Sigma logs, (c) measured and reconstructed Near and Far inverse of migration length logs, and (d) short-spaced and long-spaced density logs, (e) a sketch of the borehole, invasion profile, and virgin formation, estimated virgin- and invaded-zone layer-by-layer (f) Sigma, (g) inverse of migration length, and (h) density with error bars, and (i) estimated mineral and fluid volumetric model in the virgin formation.. Layer boundaries were defined using the sinusoids in the compensated density image.

The high statistical quality of multi-detector decays acquired in this well is reflected in an excellent match between measured and reconstructed decays on track (a) in **Figure 7.10**. The output of the multi-detector inversion on track (e) suggests that invasion is minimal throughout the sequence. Depths where the algorithm detected invasion have significant uncertainty because of the low contrast between virgin- and invasion-zone Sigma (Ortega et al., 2013). Since connate water is saltier than mud filtrate, at depths were r_i is nonzero, nuclear properties are larger in the virgin than in the invaded zone (see tracks (f), (g), and (h) where invasion is nonzero). The algorithm inaccurately increases salinity in the virgin zone to account for the low-salinity mud filtrate placed in the near-wellbore zone by the output of the multi-detector decay inversion. In these thinly bedded formations, Sigma logs on track (b) correlate well with volumetric concentration of shale estimated from gamma-ray spectroscopy logs on track (i).

Figure 7.11 describes on track (d) the advantage of the nuclear based petrophysical interpretation to estimate layer-by-layer water saturation in laminated formations. Observe how water saturation from resistivity logs averages saturation in the hydrocarbon-bearing and the water-bearing formations. The inversion method enables important changes in water saturation with depth to be seen. These changes coincide with the hydrocarbon crossover in matrix-corrected neutron and density measurements on track (c). Additionally, I calculate layer-by-layer resistivity and compare simulated and measured high-frequency phase resistivity logs on track (f). Again, the method enables seeing variations in resistivity typical of layered systems. Disparities at the top and bottom formations might be due to changes in well azimuth and/or formation anisotropy not considered in the modeling. Both simulated and field resistivity logs average the properties of all the layers into one value, which can lead to inaccurate evaluation of reservoir performance. Knowledge about the actual distribution of fluids in the reservoir can improve the design of perforations and directly impact production performance. The confidence index on corrected virgin Sigma on the rightmost track indicates in red colors formations where the estimations are uncertain because the logging environment does not exhibit the conditions under which the multi-detector Sigma measurement is functional.

Results in **Figure 7.11** can be improved by decoupling shoulder-bed and well-deviation effects from gamma-ray spectroscopy logs. The spectroscopy log averages the minerals in the rocks and what appears to be an even distribution of shale in all the layers on track (e) is in fact alternations of high and low shale concentrations. The correction in

spectroscopy logs can improve layer-by-layer mineral properties used in the inversion and has the potential to maximize the deflections in water saturation and resistivity on tracks (d) and (f). However, such correction is beyond the scope of this dissertation.

7.7.3 Field Case III

This field case examines a laminated sequence of siliciclastic formations with significant amounts of carbonate minerals traversed by a 35^{o} deviated well. Well-deviation effects are not significant in this field case, but shoulder-bed and invasion effects are of importance because of the thinly bedded nature of the formations and approximately 1 hr of exposure to mud filtrate prior to measurement acquisition. Connate water salinity from laboratory analysis is approximately 130 kppm [NaCl] in several wells in the region. Mud-filtrate salinity is approximately 136 kppm [NaCl]. The high salinity of formation water make this environment and ideal case for the application of Sigma to estimate water saturation independently of resistivity. This field was drilled in the same offshore West Africa anticlinal described in Field Case I. It is desired to confirm whether or not gas is present in the section traversed by the well and what could be its relative position in the anticlinal with respect to the well in the first field case.

The presence of intermittent neutron density crossovers in this field example suggest the presence of gas, but it is still unknown at what extent nuclear measurements are affected by invasion. One of the objectives is to estimate radial length of invasion to correct nuclear measurements for invasion, if necessary, and understand the effects of in-situ fluid type and invasion on all nuclear measurements. **Figure 7.12** shows (a) measured

and reconstructed multi-detector decays, (b) borehole- and diffusion-corrected Sigma logs, (c) measured and reconstructed Near and Far inverse of migration length logs, and (d) short-spaced and long-spaced density logs, (e) a sketch of the borehole, invasion profile, and virgin formation, estimated virgin- and invaded-zone layer-by-layer (f) Sigma, (g) inverse of migration length, and (h) density with error bars, and (i) estimated mineral and fluid volumetric model in the virgin formation.

The match between measured and simulated multi-detector decays is excellent because of the high statistical quality of measured time decays, track (a) in **Figure 7.12**. The strong match and large contrast in virgin-invaded Sigmas resulting from salty filtrate and large porosities validate the estimated invasion profile on track (e). Deflections in shallow-sensing density logs on track (d) agree well with estimated invasion profile and water saturation. Neutron logs show fewer deflections and display small inverse of migration length values in the middle section, which is typical of gas-bearing formations because they sense deeper into the virgin zone than density logs. This further confirms the presence of shallow invasion, in which the density logs are highly affected and neutron logs are partially affected by invasion, but still enable to detect the presence of light hydrocarbons.

Tracks (f), (g), and (h) in **Figure 7.12** show that the corrections on Sigma, inverse of migration length, and density in the virgin formation are especially important in the middle of the sequence where results on track (i) indicate the presence of gas. Note that most of the middle section is gas saturated, but the algorithm indicates the presence of some

apparent oil-bearing layers whenever invasion is deep. All formation in this section are most-likely gas-saturated, but the presence of invasion makes it difficult to recognize actual in-situ fluid in some of the invaded formations. The effect of invasion is evidenced in large error bars in virgin-zone density and inverse of migration lengths on tracks (g) and (h). Corrected density logs when invasion is approximately deeper than 4 cm are not representative of the actual properties of the virgin formation.

Figure 7.13 shows matrix-corrected neutron and density logs and matrix- and fluid-corrected total porosity on track (c), estimated water saturation using the workflow compared to water saturation from resistivity logs (d), estimated mineral and fluid volumetric model (e), a comparison of measured and simulated high-frequency phase resistivity logs, calculated layer-by-layer resistivity (f), and the confidence index (*CI*) for corrected virgin-zone Sigma. The inversion workflow allows to observe more variation of water saturation between layers, and overall shows larger water saturations compared to using resistivity logs. Estimated presence of gas in the middle section of track (e) agrees with corrected neutron-density crossover on track (c). Simulated and measured resistivities on track (f) agree satisfactorily; small differences could be due to using a simulation model for another propagation tool different from the one used in the field and/or anisotropy effects on the resistivity measurement.

Comparison of results from field cases I and III indicates that the well in Field Case III penetrates the anticlinal at shallower depths and traverses the structure most-likely at the top where the gas section is thicker. The well in Field case I is probably located at a

flank traversing a thinner gas section because deeper zones of the reservoir might not be below bubble pressure yet, and goes deeper into the oil leg without reaching the oil-water contact. Large porosities are fairly constant throughout the structure in both wells. In siliclastic formations high porosity is associated with high permeability. This further suggests that LWD measurements acquired in these West Africa wells are highly affected by invasion, and validates results on estimated radial length of invasion.

7.7.4 Field Case IV

This field case consists of laterally continuous siliciclastic formations in offshore Australia penetrated by a 60^{o} deviated well. Previous petrophysical evaluations indicate that reservoir sands have low porosities, between 8 and 15 p.u., high permeabilities, up to 2000 md, and the section under study was perforated above the water contact. The application of the workflow introduced in this chapter is aimed to decouple shoulder-bed, and well-deviation effects, rather than to assess invasion effects. The reason is that the contrast between virgin- and invasion-zone Sigma precludes the accurate evaluation of invasion. The contrast is low because the well was perforated with low-salinity, 40 kppm [NaCl], WBM, and porosities are relatively low in the section under consideration. Connate water salinity is 31 kppm [NaCl] as estimated from laboratory measurements on produced water. Resistivity measurements acquired in this well lack of horns and anisotropy effects, and their correlation to Sigma measurements is excellent.

Figure 7.14 and **Figure 7.15** show inversion results for this field case. In **Figure 7.14**, (a) measured (blue) and reconstructed (red) multi-detector time decays, and (b)

borehole- and diffusion-corrected Sigma logs are displayed. Careful inspection of LSn time decays in the shale sections, where significant absorption occurs, at X575m-X595m and X635m-X650m shows that low readings of LSn Sigma are due to a poor background gamma-ray correction. Low count rates in these sections additionally generate noisy time decays. The low LSn-Sigma value at X635m is clearly a consequence of noise in the measurement. The pulsing protocol of the LWD tool under study includes a late-time window to detect natural gamma radiation, as well as radiation resulting from neutron activation. Nonetheless, if the statistical quality of acquired signals is not good, the background correction can fail to accurately subtract background radiation that affects mostly the late-time components of time decays, and can result in anomalous Sigma logs.

MDOI Sigma logs on track (b) in **Figure 7.14** display separation that is typical of salty-filtrate invasion in low-Sigma hydrocarbon-bearing formations. Interpretation of other borehole measurements led to the recognition that invasion cannot explain the separation in MDOI Sigma logs because these sections are shaly, low-permeability formations. Despite miscorrected gamma-ray background and presence of noise, I used these original measured field-decays in the 2D multi-detector time decay inversion to test whether or not the algorithm can bypass the presence of noise and address petrophysical estimations that are consistent with qualitative interpretation of other borehole measurements.

Track (e) in **Figure 7.14** shows that no invasion is present in the drilled section, or the inversion algorithm cannot detect invasion because invasion-virgin zone Sigma

contrast is too low, as previously mentioned. Reconstructed multi-detector neutron and density measurements are shown on tracks (c) and (d), respectively. Differences in SSg and LSg density logs at the top are due to the enlarged borehole, as suggested from density-derived caliper and ultrasonic borehole measurements. Nuclear properties corrected for shoulder-bed and well-deviation effects are presented on tracks (f), (g), and (h), and estimated petrophysical model is presented on track (i).

Figure 7.15 shows the main petrophysical interpretations for this field example. Density-derived caliper on track (a) shows a tool-standoff about 2.54 cm (1 in) at the top that agrees with the difference in SSg and LSg densities see on track (d) in **Figure 7.14**. I additionally show on track (b) a comparison of the original background-miscorrected LSn Sigma log to a re-calculated LSn Sigma improving the background correction. As expected, the correction shows that now all three Sigma logs overlap throughout the shale formations. The low Sigma at X635m is present after the correction because it is a consequence of noise in the measurement. Track (c) shows an azimuthal gamma-ray image used to define bed-boundary locations. Track (d) shows matrix-corrected neutron and density porosity logs. Large separation in corrected neutron and density logs agrees well with the estimation of hydrocarbon type, i.e. gas, on track (f) (indicated by the color bar at the bottom). The estimation of a light hydrocarbon in the porous sands agrees well with initial reservoir evaluations of a gas-condensate reservoir normally pressured above dew point, as well as with production fluids.

Estimation of a light hydrocarbon permits to accurately calculate the nuclear properties of the fluid (Sigma, inverse of migration length, and density) using the flash calculation and SNUPAR. This results in a good estimation of layer-by-layer water saturation that agrees with resistivity-derived water saturation on track (e). Observe that the mineral and fluid model on track (f) agrees significantly well with qualitative analysis in all nuclear measurements. Track (g) shows a good comparison between measured (solid lines) and simulated (dashed lines) phase resistivity logs, and calculated layer-by-layer formation resistivity. Differences in simulated and measured resistivity logs are due to using a forward model for resistivity not corresponding to the actual LWD resistivity tool used in the field measurement. The Confidence Index (*CI*) on virgin-zone Sigma shows intermediate confidence due to the low invasion-virgin zone Sigma contrasts in this logging setting. Shallow invasion might be present but due to the similarity in nuclear properties between mud filtrate and in-situ fluids, the impact of invasion, if existent, is rendered negligible, as explained in Chapter 4.

7.7.5 Field Case V

The four previous field cases depict actual applications of the workflow presented in this chapter in which LWD nuclear measurements are corrected for invasion and geometrical effects and fully integrated for petrophysical evaluations. I now wish to show an application in the case where multi-detector decays are not available, but a Sigma log is available to perform petrophysical interpretations, e.g. cased-hole logs. A Sigma log, a compensated neutron porosity log converted to inverse of migration length, and a bulk

compensated density log, are integrated using the mixing laws in equation 7.20, 7.21, and 7.22 and the nuclear-based solver. Water saturation and fluid type are assessed using only cased-hole logs. The effect of invasion and adjacent beds is neglected.

Figure 7.16 shows (a) mineral concentrations from gamma-ray spectroscopy logs, (b) natural gamma-ray log, (c) matrix-corrected neutron and density porosity logs, and matrix- and fluid-corrected total porosity, (d) comparison of water saturation estimated using an open-hole resistivity log and estimated using our nuclear-based petrophysical solver, (e) a map of fluids in the pore space, (f) open-hole resistivity logs, and a comparison of measured versus reconstructed (g) Sigma, (h) compensated density, and (i) compensated neutron porosity converted to inverse of migration length. The high quality of the gamma-ray spectroscopy log (a), which agrees with the gamma ray log (b), results in a good correction for matrix effects in neutron-density logs on track (c). Compensated neutron and density porosity overlay in shaly zones and large hydrocarbon crossovers are seen in clean zones.

Estimation of water saturation on track (d) agrees well with the estimations from open-hole resistivity logs with the advantage that estimations from the nuclear-based solver have better vertical resolution, and show deflections that are more consistent with laminations seen in the spectroscopy logs on track (a). It is also seen that the nuclear solver accurately detected the fluid type, gas, which is indeed the case, as this sequence comprises tight gas sands. The reconstruction of Sigma, density, and neutron porosity converted to inverse of migration length on tracks (g), (h), and (i), respectively, is also quite satisfactory.

7.8 CONCLUSIONS

Petrophysical interpretation can be performed independently of resistivity using only nuclear logs with the advantage that nuclear logs have smaller volume of investigation than resistivity logs and are not affected by nonlinear effects, such as horns and anisotropy in the case of thinly bedded formations, presence of shale, and deviated wells. I introduced a workflow in which matrix properties are calculated using gamma-ray spectroscopy logs and fluid-sensitive nuclear measurements are used to estimate water saturation and hydrocarbon type. Multi-detector time decay measurements are used to correct invasion effects from formation Sigma, inverse of migration length, and density, while reducing shoulder-bed and well-deviation effects from all measurements. Synthetic and field cases indicate that in the case of salty filtrate invading hydrocarbon formations, the multi-detector time-decay inversion accurately estimates radial length of invasion and is useful to correct neutron and density measurements for invasion effects. The effect of the correction is especially important in the case of gas-bearing formations where gas properties can be masked by the presence of invasion in the near-wellbore zone. The nuclear inversion workflow also allows for variations in water saturation, which are averaged by resistivity measurements to be seen, making the method ideal to evaluate laminated formations.

Results suggest that the estimation of water saturation and fluid type can be highly affected by radial length of invasion. In the instance where invasion is approximately deeper than 15 cm, only the deep-sensing Sigma detector (LSn) is sensitive to the virgin

formation and the inversion problem is rendered non-unique. Additionally, presence of noise in the Near detector time decays or miscorrected background gamma radiation in SSn or LSn time decays can result in large uncertainty in solved radial length of invasion and, therefore, large uncertainty in invasion-corrected nuclear properties. It is recommended the quality of the multi-detector decays be evaluated before attempting to use inversion. If time decays are noisy, the interpretation should be performed both with and without invasion to verify that results in uninvaded formations agree using both methods and also with qualitative interpretation of all borehole measurements.

Table 7.1: Summary of assumed thickness, porosity, mineral volumetric fractions, in-situ fluid type, water saturation (S_w), invasion- and virgin-zone densities (ρ_i and ρ_v), inverse of migration lengths (ξ_i and ξ_v), Sigmas (Σ_i and Σ_v), and radial lengths of invasion (r_i) for Synthetic Case I. Filtrate salinity is 200 kppm [NaCl], Σ_{mf} = 96.6 c.u., and connate water salinity is 80 kppm [NaCl], Σ_w = 50.3 c.u.

			Mineral volumetric fractions (v/v)					**ρ (g/cm3)**		**ξ (cm^{-1})**		**Σ (c.u.)**		
Layer	**Thickness (m)**	**Porosity (p.u.)**	**Quartz**	**Calcite**	**Clay**	**In-situ fluid**	**S_w**	**ρ_v**	**ρ_i**	**ξ_v**	**ξ_i**	**Σ_v**	**Σ_i**	**r_i (cm)**
1	0.48	25	0.58	0.4	0.02	Gas	0.1	2.05	2.05	0.038	0.038	7.01	7.01	0
2	0.48	35	0.4	0.58	0.02	Gas	0.1	1.81	2.14	0.039	0.072	7.68	38.57	5.08
3	0.48	20	0.68	0.3	0.02	Gas	0.1	2.17	2.17	0.037	0.037	6.62	6.62	0
4	0.48	25	0.4	0.58	0.02	Oil	0.15	2.07	2.30	0.041	0.067	8.12	29.42	10.16
5	0.48	20	0.58	0.4	0.02	Oil	0.2	2.29	2.37	0.060	0.063	10.93	24.48	5.08
6	0.48	30	0.4	0.58	0.02	Oil	0.3	2.12	2.22	0.067	0.069	14.98	33.99	15.24
7	0.48	35	0.58	0.4	0.02	Oil	0.5	2.05	2.13	0.070	0.071	19.14	38.27	5.08
8	0.48	25	0.38	0.4	0.22	Oil	0.5	2.24	2.24	0.068	0.068	19.33	19.33	0
9	0.48	30	0.48	0.4	0.12	Oil	0.8	2.18	2.22	0.069	0.070	23.03	35.50	10.16
10	0.48	30	0.58	0.4	0.02	Oil	0.8	2.17	2.17	0.068	0.068	21.20	21.20	0

Table 7.2: Summary of assumed thickness, porosity, mineral volumetric fractions, in-situ fluid type, water saturation (S_w), invasion- and virgin-zone densities (ρ_i and ρ_v), inverse of migration lengths (ξ_i and ξ_v), Sigmas (Σ_i and Σ_v), and radial lengths of invasion (r_i) for Synthetic Case II. Filtrate salinity is 230 kppm [NaCl], Σ_{mf} = 112 c.u., and connate water salinity is 80 kppm [NaCl], Σ_w = 50.3 c.u.

			Mineral volumetric fractions (v/v)					**ρ (g/cm3)**		**ξ (cm^{-1})**		**Σ (c.u.)**		
Layer	**Thickness (m)**	**Porosity (p.u.)**	**Quartz**	**Calcite**	**Clay**	**In-situ fluid**	**S_w**	**ρ_v**	**ρ_i**	**ξ_v**	**ξ_i**	**Σ_v**	**Σ_i**	**r_i (cm)**
1	0.65	15	0	0	1	Gas	1	2.50	2.50	0.072	0.072	33.62	33.62	0
2	1.29	30	0.71	0.29	0	Gas	0.23	1.98	2.21	0.050	0.069	9.18	37.32	7.62
3	0.97	15	0	0	1	Gas	1	2.50	2.50	0.072	0.072	33.62	33.62	0
4	0.81	40	0.75	0.25	0	Gas	0.25	1.76	2.06	0.052	0.073	10.76	47.95	7.62
5	1.29	15	0	0	1	Gas	1	2.50	2.50	0.072	0.072	33.62	33.62	0
6	0.81	25	0.73	0.27	0	Gas	0.3	2.11	2.29	0.050	0.066	9.22	31.94	7.62
7	0.97	15	0	0	1	Gas	1	2.50	2.50	0.072	0.072	33.62	33.62	0
8	0.97	25	0.76	0.24	0	Gas	0.33	2.11	2.29	0.050	0.065	9.47	31.89	7.62
9	1.45	15	0	0	1	Gas	1	2.50	2.50	0.072	0.072	33.62	33.62	0
10	0.48	28	0.85	0.15	0	Gas	0.35	2.05	2.24	0.052	0.067	10.06	34.93	7.62
11	0.97	15	0	0	1	Gas	1	2.50	2.50	0.072	0.072	33.62	33.62	0
12	0.81	39	0.89	0.11	0	Gas	0.35	1.81	2.07	0.054	0.072	12.03	46.67	7.62

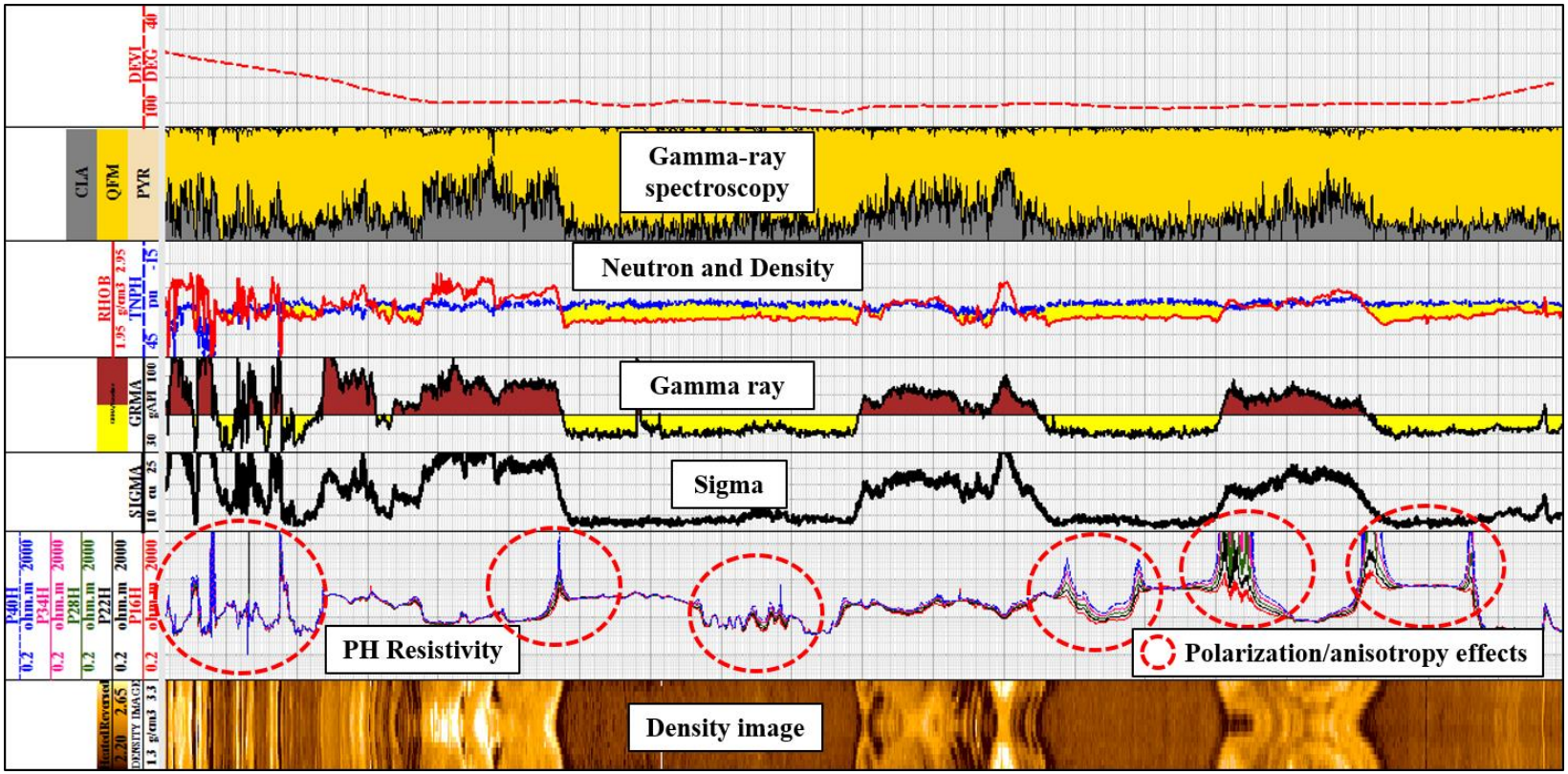

Figure 7.1: LWD measurement suite in a highly deviated North Sea well. Sigma logs correlate with resistivity measurements but lack of artificial effects such as horns and separation at bed boundaries. Sigma logs show very good agreement with neutron, density porosity, gamma-ray, and gamma-ray spectroscopy logs.

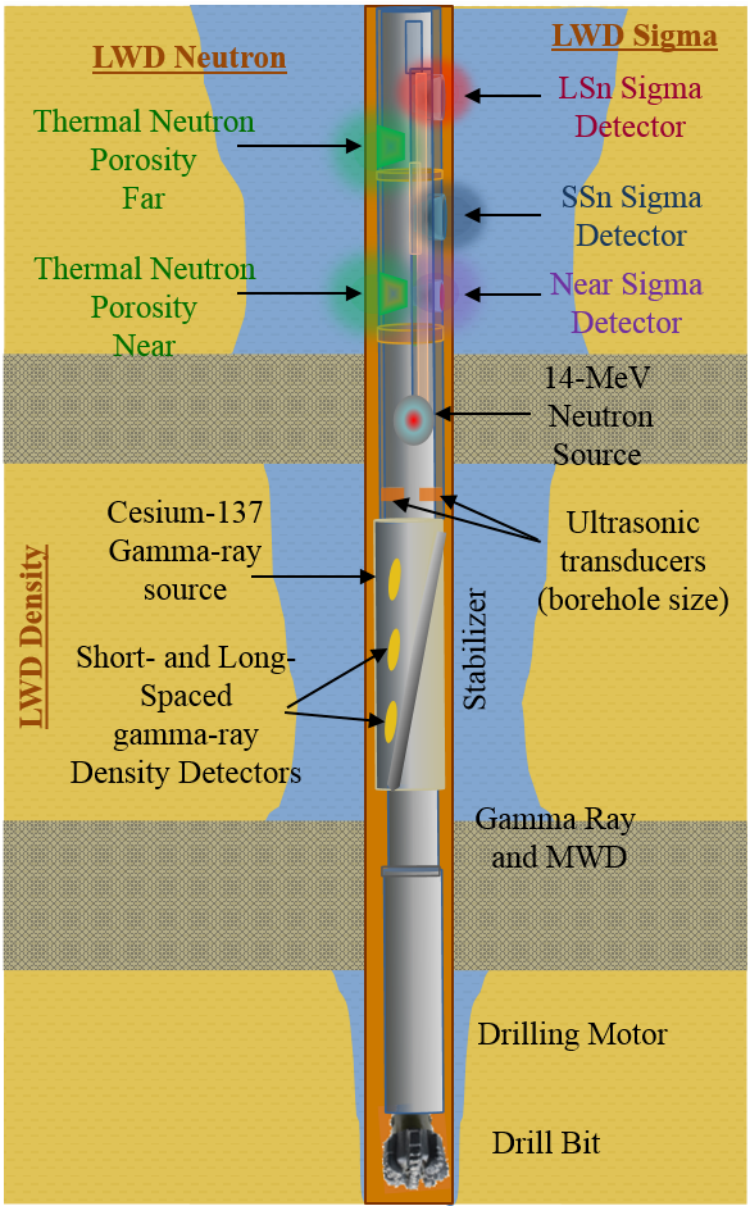

Figure 7.2: Sketch of commercial LWD multi-function tool with emphasis on the nuclear measurement suite (Sigma, neutron, and density).

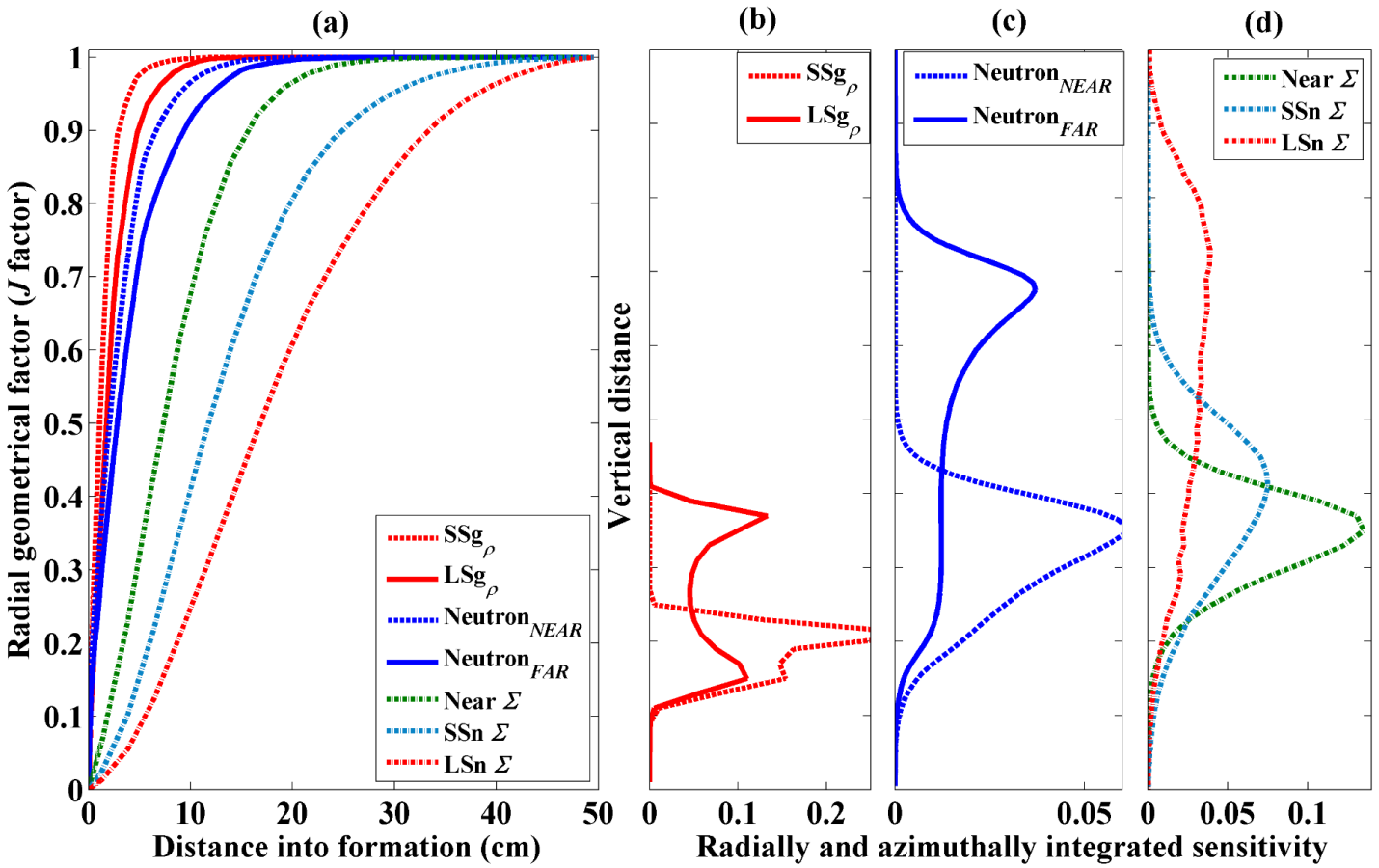

Figure 7.3: Comparison of radial and vertical sensitivity functions for multi-detector density, neutron, and Sigma measurements for the LWD tool under study in a 28 p.u. fresh water-saturated limestone formation.

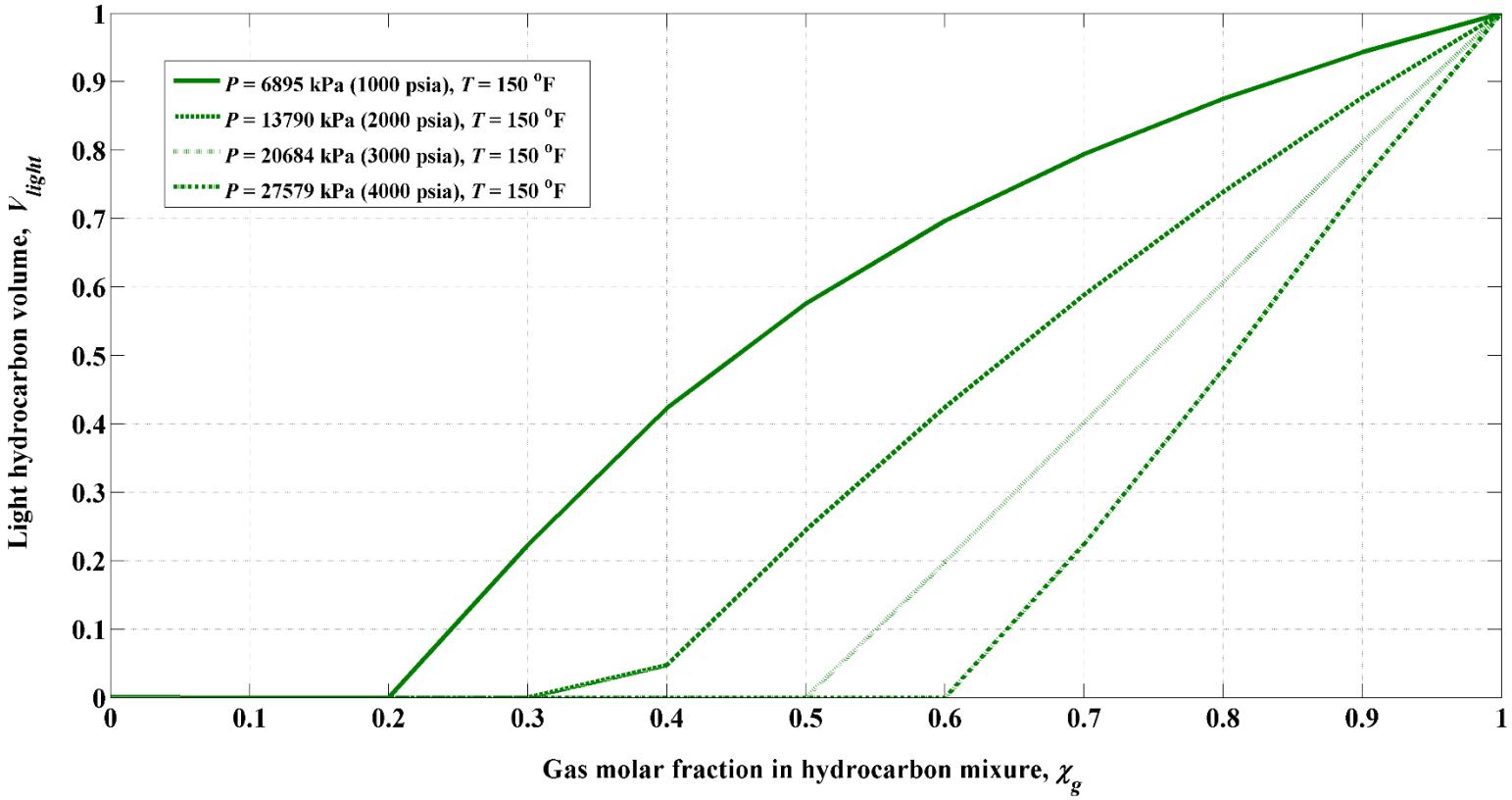

Figure 7.4: Light hydrocarbon compound volume for various fluid types, χ_g, as a function of pressure and temperature. Results calculated from a simulated flash calculation considering mixtures of methane and decane of gas molar fractions in the range of 0 to 1.

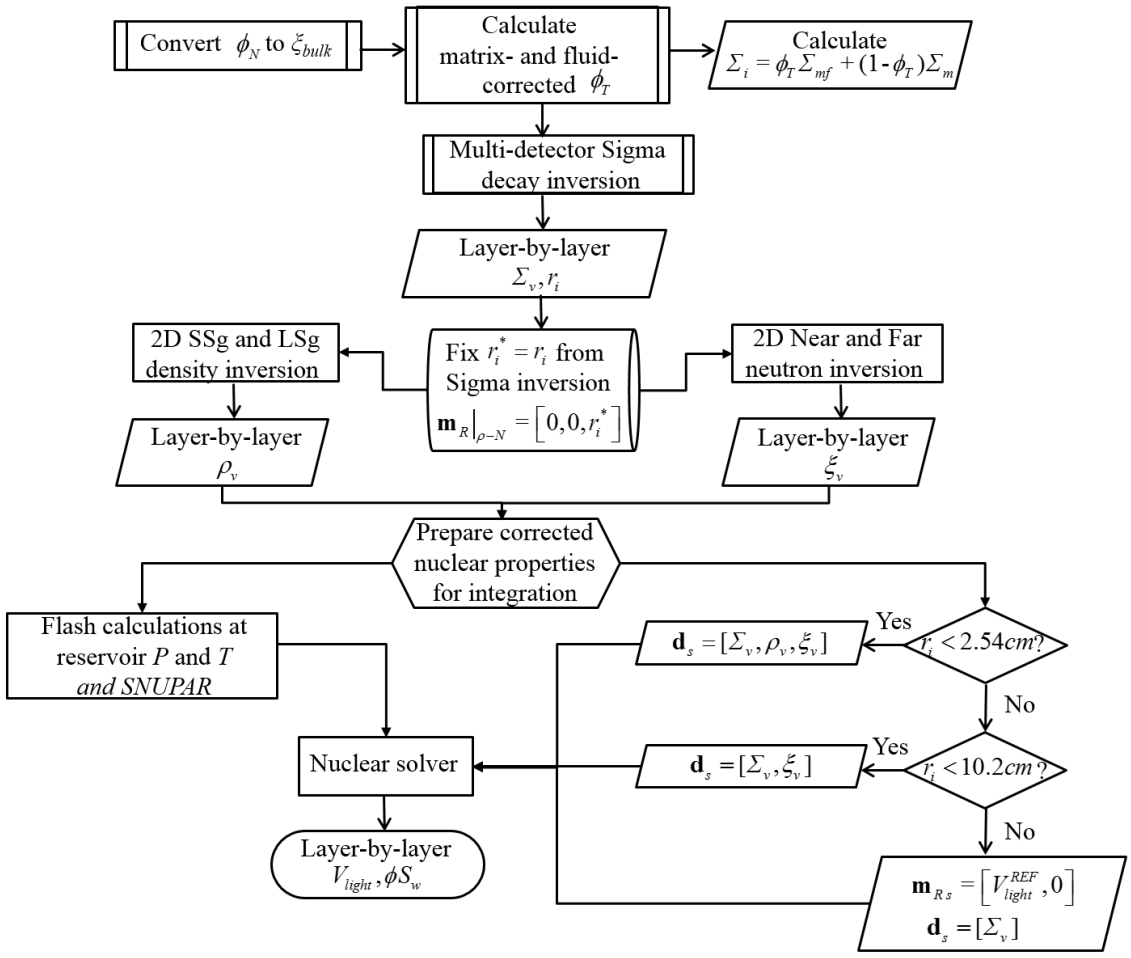

Figure 7.5: Workflow to perform invasion, shoulder-bed, and well-deviation effect correction on multi-detector Sigma, density, and thermal neutron porosity measurements, and post-integration using a nuclear solver to estimate fluid type and water pore volume.

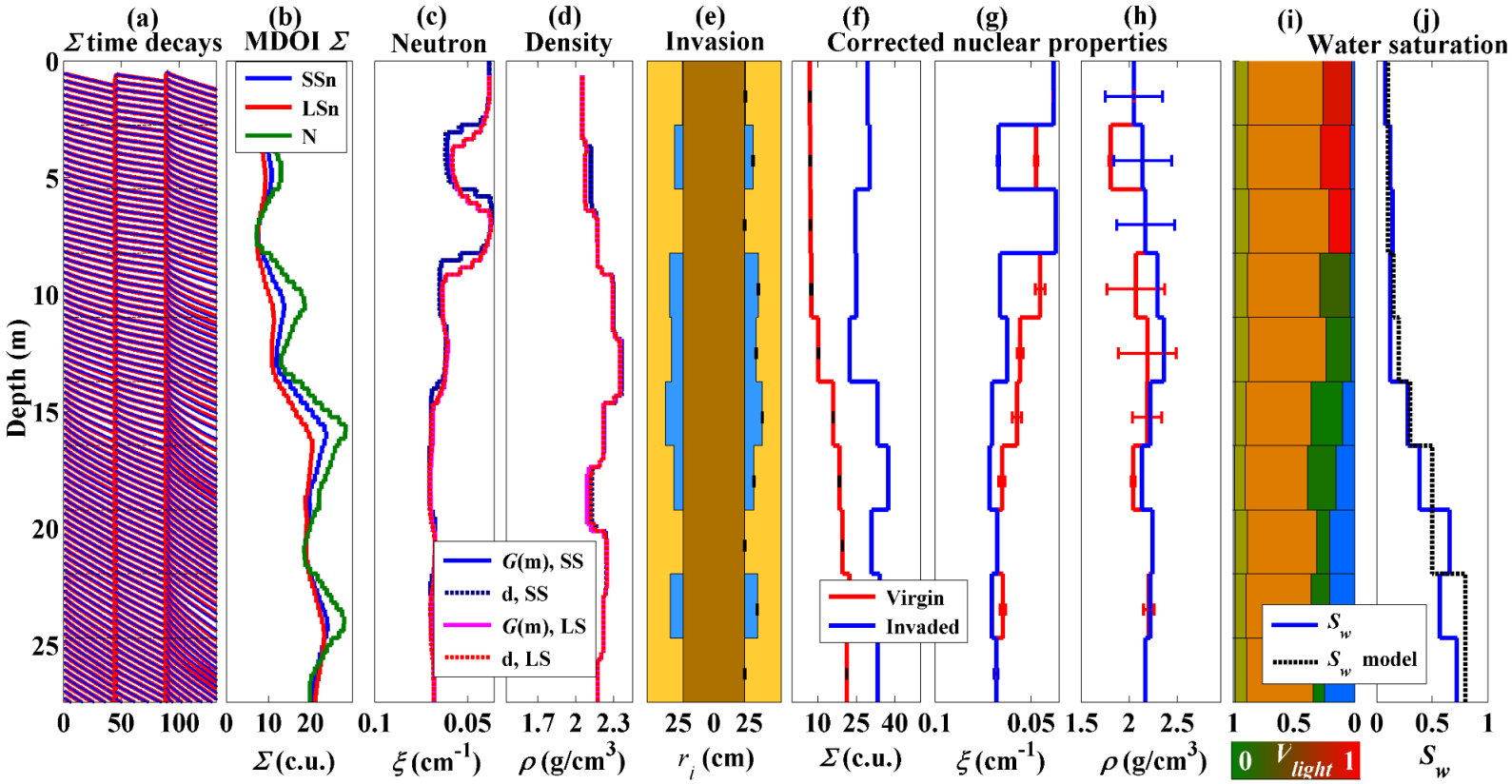

Figure 7.6: Inversion results for Synthetic Case I. (a) Simulated (blue) and reconstructed (red) multi-detector time decays, (b) borehole- and diffusion-corrected Sigma logs, (c) simulated and reconstructed Near and Far neutron inverse of migration length logs, (d) simulated and reconstructed short-spaced (SSg) and long-spaced (LSg) gamma density logs, (e) sketch of borehole, invasion profile, and virgin formation, corrected virgin- and invaded-zone (f) Sigma, (g) neutron, and (h) density logs, (i) virgin-zone volumetric model, and (j) comparison of model and estimated water saturation. On track (i): the color scale on bottom represents hydrocarbon type. Blue color represents water. Matrix minerals are chlorite (gray), limestone (light green), and quartz (orange). Well deviation is 80°.

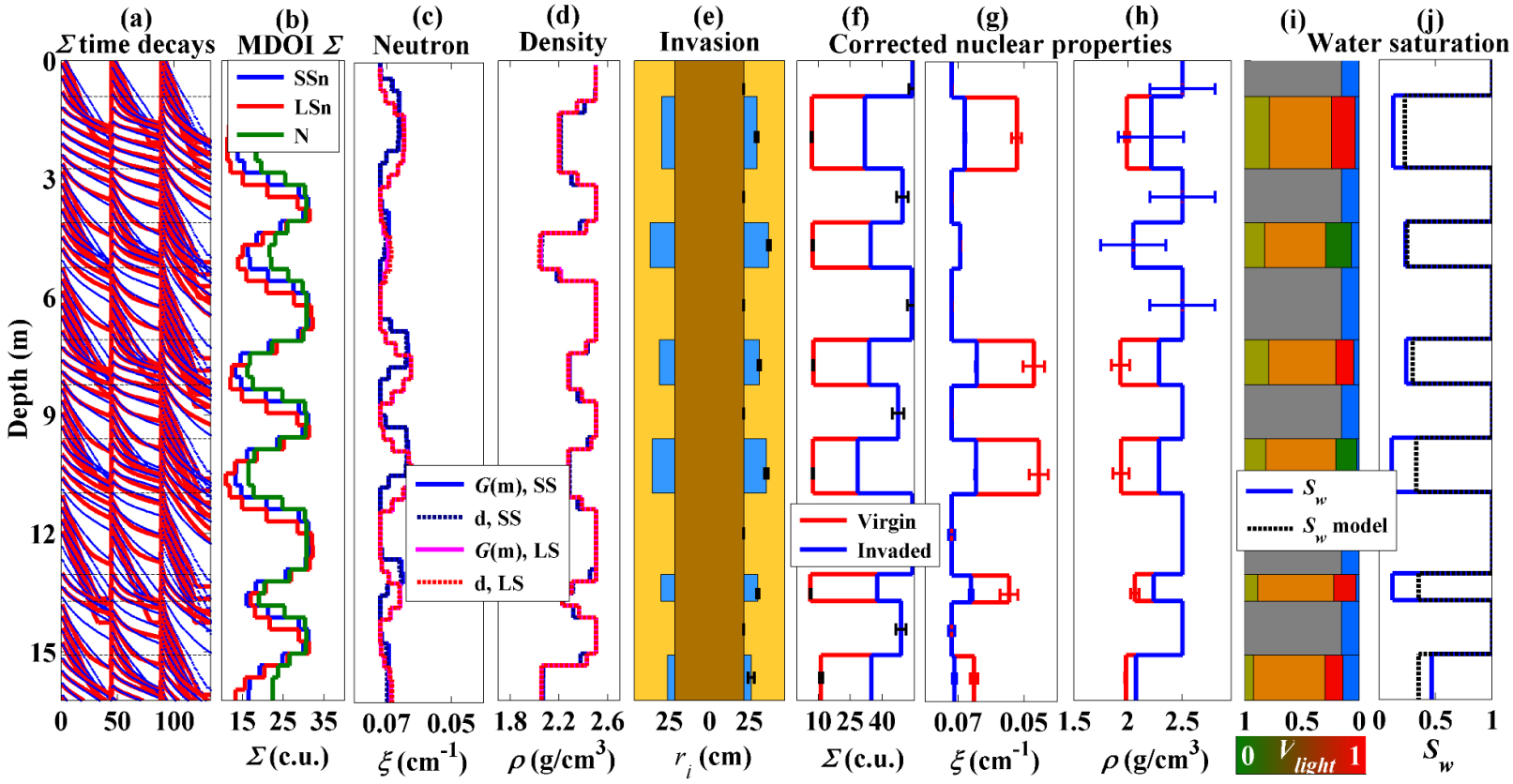

Figure 7.7: Inversion results for Synthetic Case II. (a) Simulated (blue) and reconstructed (red) multi-detector time decays, (b) borehole- and diffusion-corrected Sigma logs, (c) simulated and reconstructed Near and Far neutron inverse of migration length logs, (d) simulated and reconstructed short-spaced (SSg) and long-spaced (LSg) gamma density logs, (e) sketch of borehole, invasion profile, and virgin formation, corrected virgin- and invaded-zone (f) Sigma, (g) neutron, and (h) density logs, (i) virgin-zone volumetric model, and (j) comparison of model and estimated water saturation. On track (i): the color scale on bottom represents hydrocarbon type. Blue color represents water. Matrix minerals are chlorite (gray), limestone (light green), and quartz (orange). Well deviation is 0^{o}.

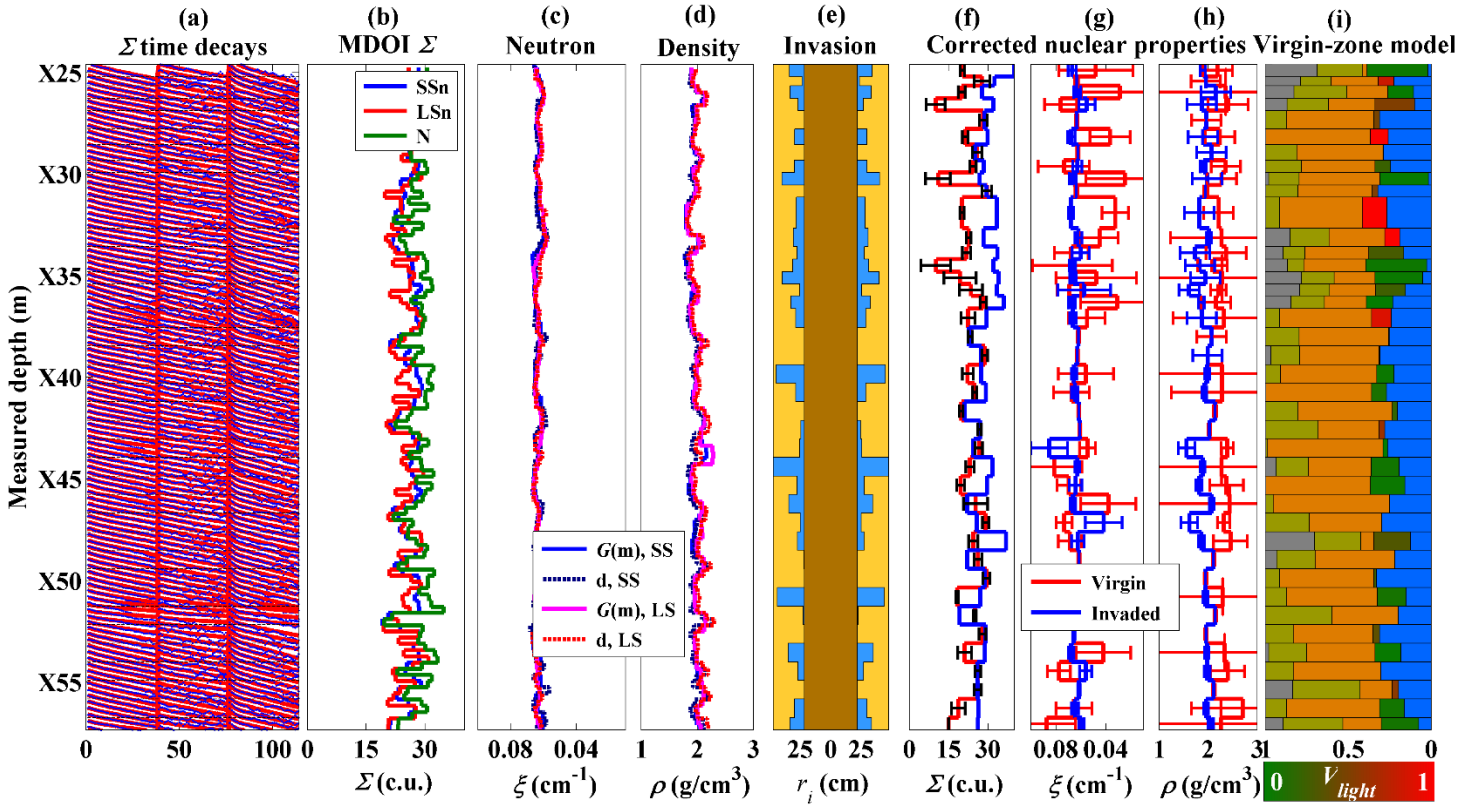

Figure 7.8: Reconstructed field measurements and corrected layer-by-layer nuclear properties for Field Case I. (a) Measured (blue) and reconstructed (red) multi-detector time decays, (b) borehole- and diffusion-corrected Sigma logs, (c) measured and reconstructed Near and Far neutron inverse of migration length logs, (d) measured and reconstructed short-spaced (SSg) and long-spaced (LSg) gamma density logs, (e) sketch of borehole, invasion profile, and virgin formation, corrected virgin- and invaded-zone (f) Sigma, (g) neutron, and (h) density logs, respectively, and (i) virgin-zone volumetric model. On track (i): the color scale on bottom represents hydrocarbon type. Blue color represents water. Matrix minerals are clay (gray), limestone (light green), and quartz (orange).

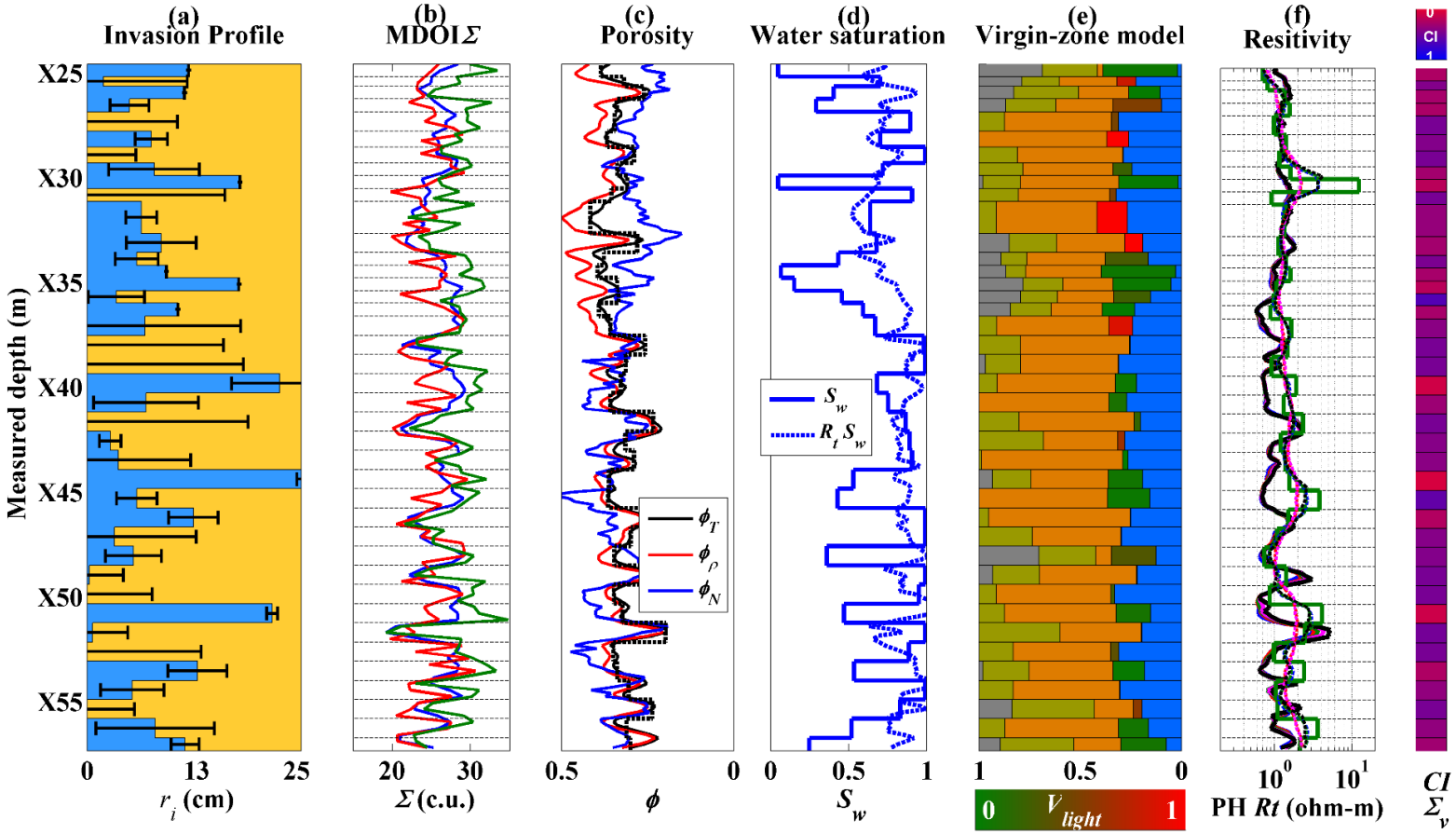

Figure 7.9: Inversion results for Field Case I. (a) Estimated radial length of invasion with error bars, (b) borehole- and diffusion-corrected measured Sigma logs, (c) matrix-corrected neutron and density porosity logs, and matrix- and fluid-corrected estimated total porosity, (d) comparison of water saturation estimated form resistivity logs and using the introduced workflow, (e) virgin-zone volumetric model, (f) field and simulated high-frequency resistivity logs and layer-by-layer resistivity, and confidence index on virgin-zone Sigma.

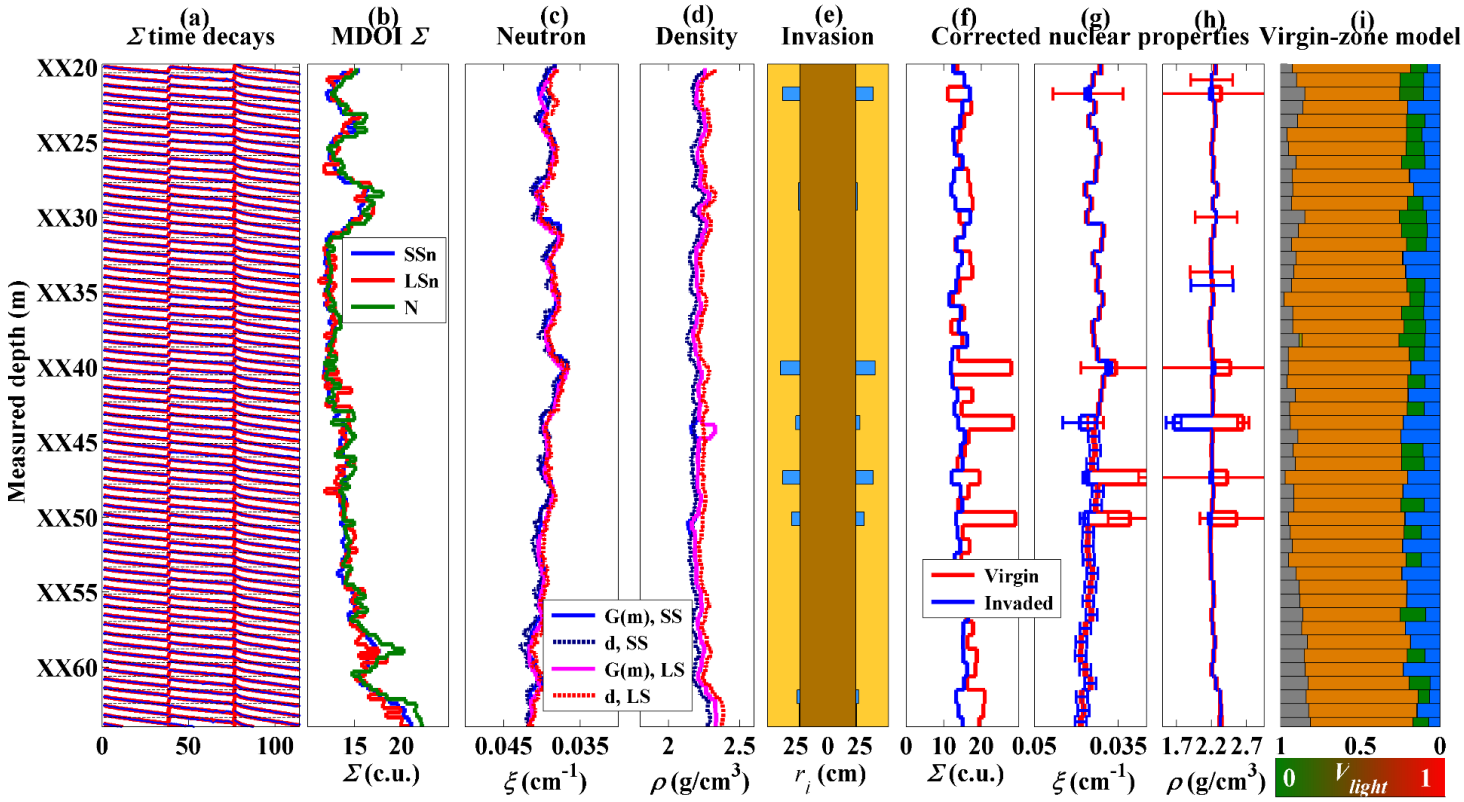

Figure 7.10: Reconstructed field measurements and corrected layer-by-layer nuclear properties for Field Case II. (a) Measured (blue) and reconstructed (red) multi-detector time decays, (b) borehole- and diffusion-corrected Sigma logs, (c) measured and reconstructed Near and Far neutron inverse of migration length logs, (d) measured and reconstructed short-spaced (SSg) and long-spaced (LSg) gamma density logs, (e) sketch of borehole, invasion profile, and virgin formation, corrected virgin- and invaded-zone (f) Sigma, (g) neutron, and (h) density logs, respectively, and (i) virgin-zone volumetric model. On track (i): the color scale on bottom represents hydrocarbon type. Blue color represents water. Matrix minerals are clay (gray), limestone (light green), and quartz (orange).

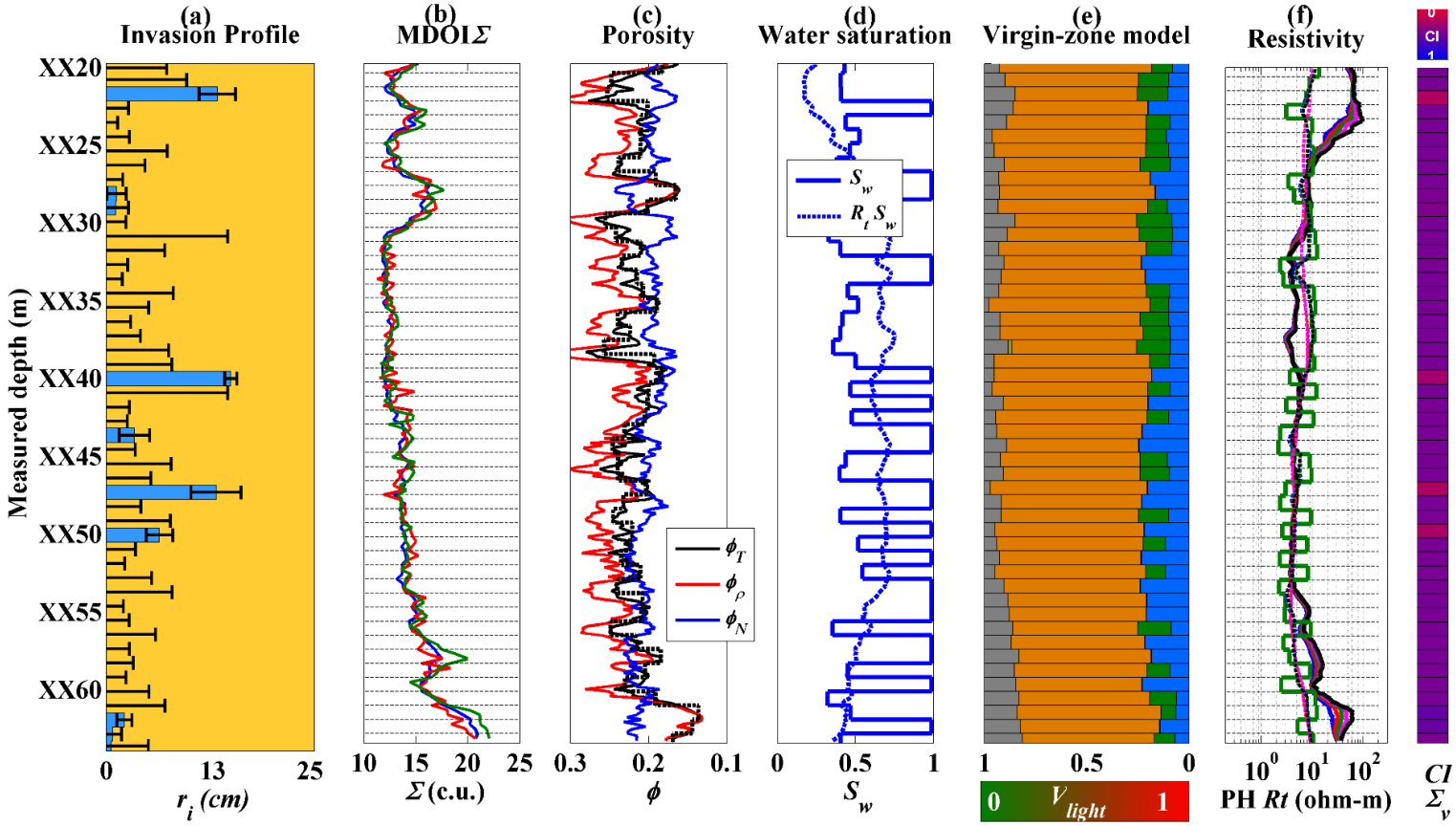

Figure 7.11: Inversion results for Field Case II. (a) Estimated radial length of invasion with error bars, (b) borehole- and diffusion-corrected measured Sigma logs, (c) matrix-corrected neutron and density porosity logs, and matrix- and fluid-corrected estimated total porosity, (d) comparison of water saturation estimated form resistivity logs and using the introduced workflow, (e) virgin-zone volumetric model, (f) field and simulated high-frequency resistivity logs and layer-by-layer resistivity, and confidence index on virgin-zone Sigma.

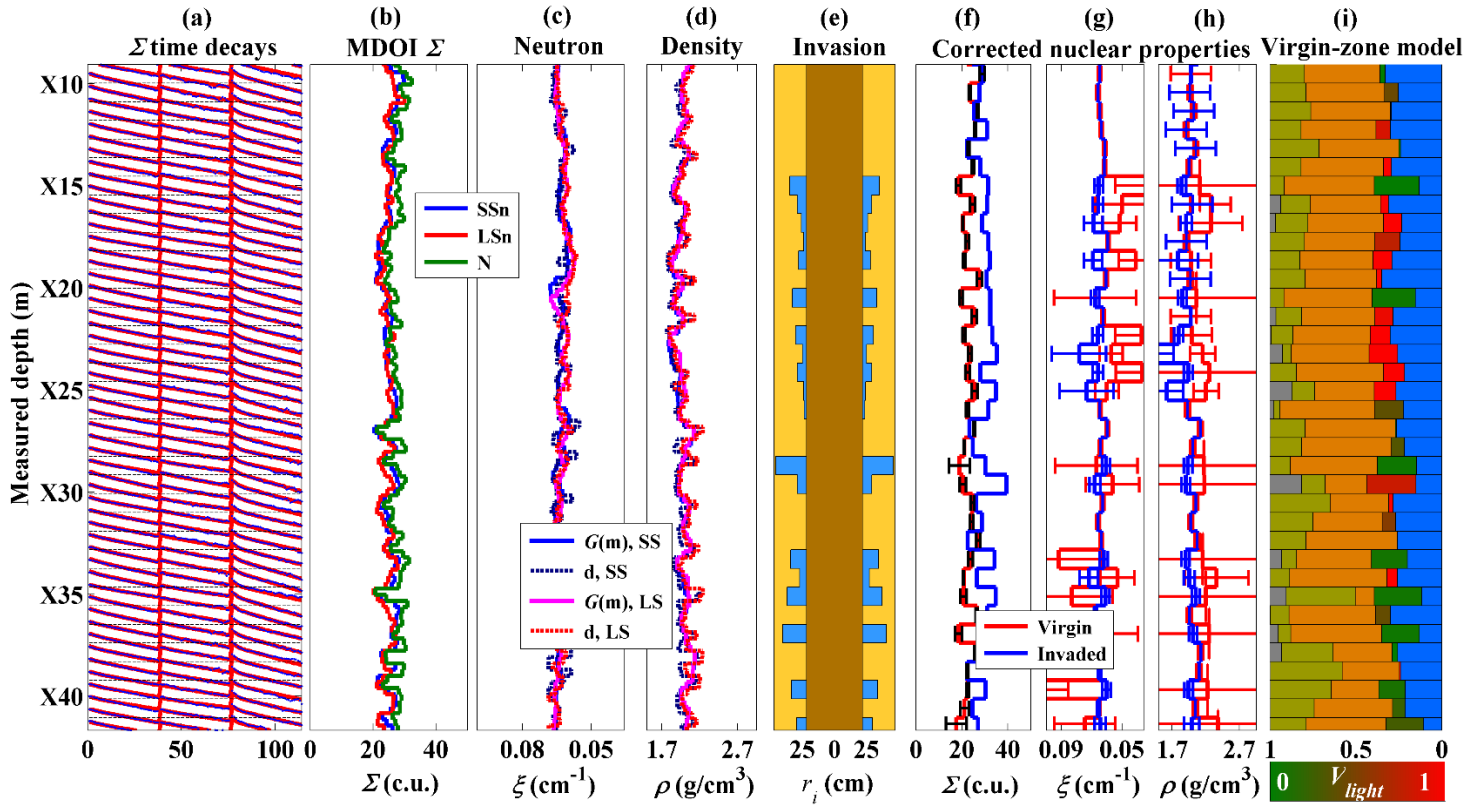

Figure 7.12: Reconstructed field measurements and corrected layer-by-layer nuclear properties for Field Case III. (a) Measured (blue) and reconstructed (red) multi-detector time decays, (b) borehole- and diffusion-corrected Sigma logs, (c) measured and reconstructed Near and Far neutron inverse of migration length logs, (d) measured and reconstructed short-spaced (SSg) and long-spaced (LSg) gamma density logs, (e) sketch of borehole, invasion profile, and virgin formation, corrected virgin- and invaded-zone (f) Sigma, (g) neutron, and (h) density logs, respectively, and (i) virgin-zone volumetric model. On track (i): the color scale on bottom represents hydrocarbon type. Blue color represents water. Matrix minerals are clay (gray), limestone (light green), and quartz (orange).

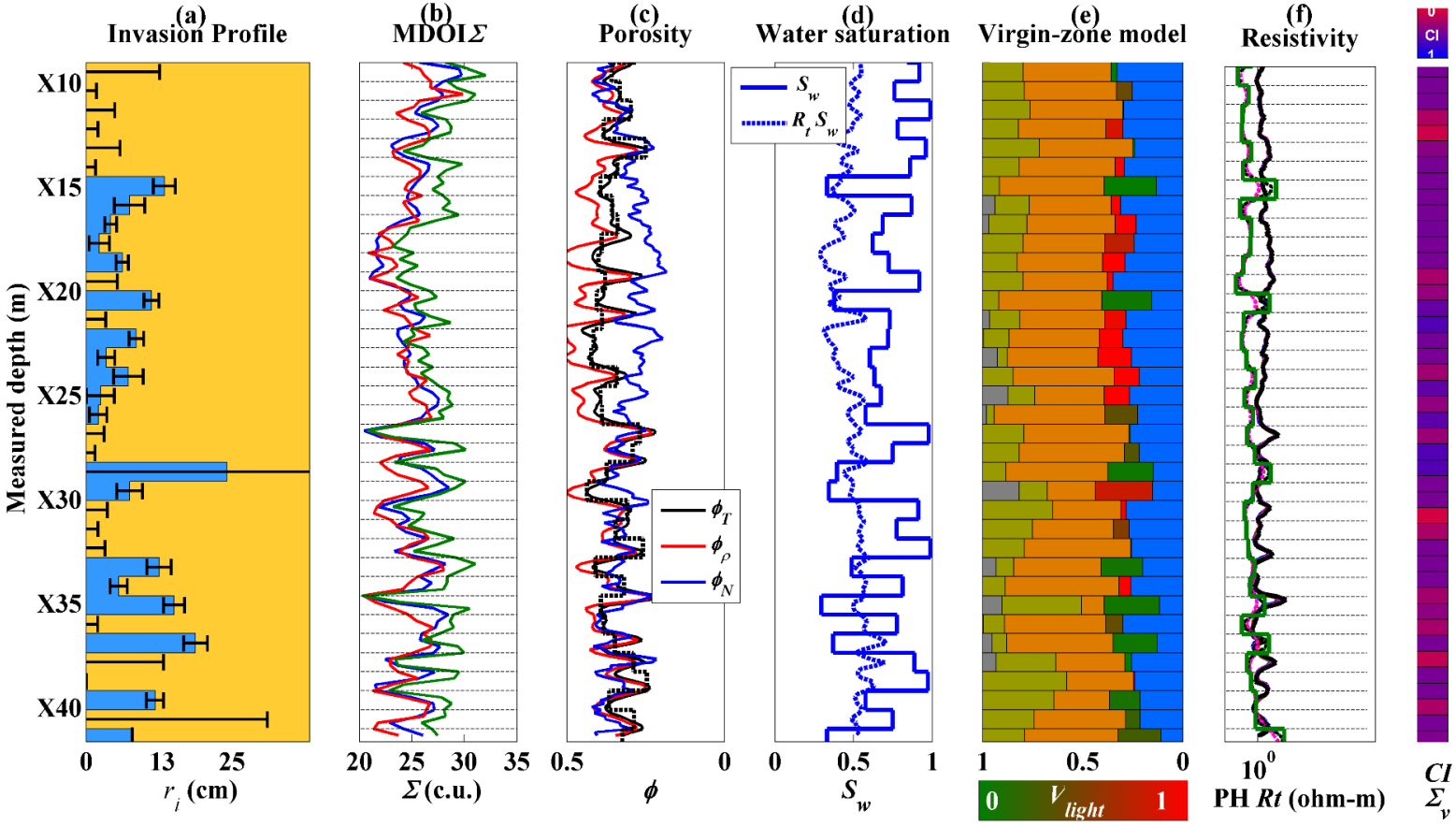

Figure 7.13: Inversion results for Field Case III. (a) Estimated radial length of invasion with error bars, (b) borehole- and diffusion-corrected measured Sigma logs, (c) matrix-corrected neutron and density porosity logs, and matrix- and fluid-corrected estimated total porosity, (d) comparison of water saturation estimated form resistivity logs and using the introduced workflow, (e) virgin-zone volumetric model, (f) field and simulated high-frequency resistivity logs and layer-by-layer resistivity, and confidence index on virgin-zone Sigma.

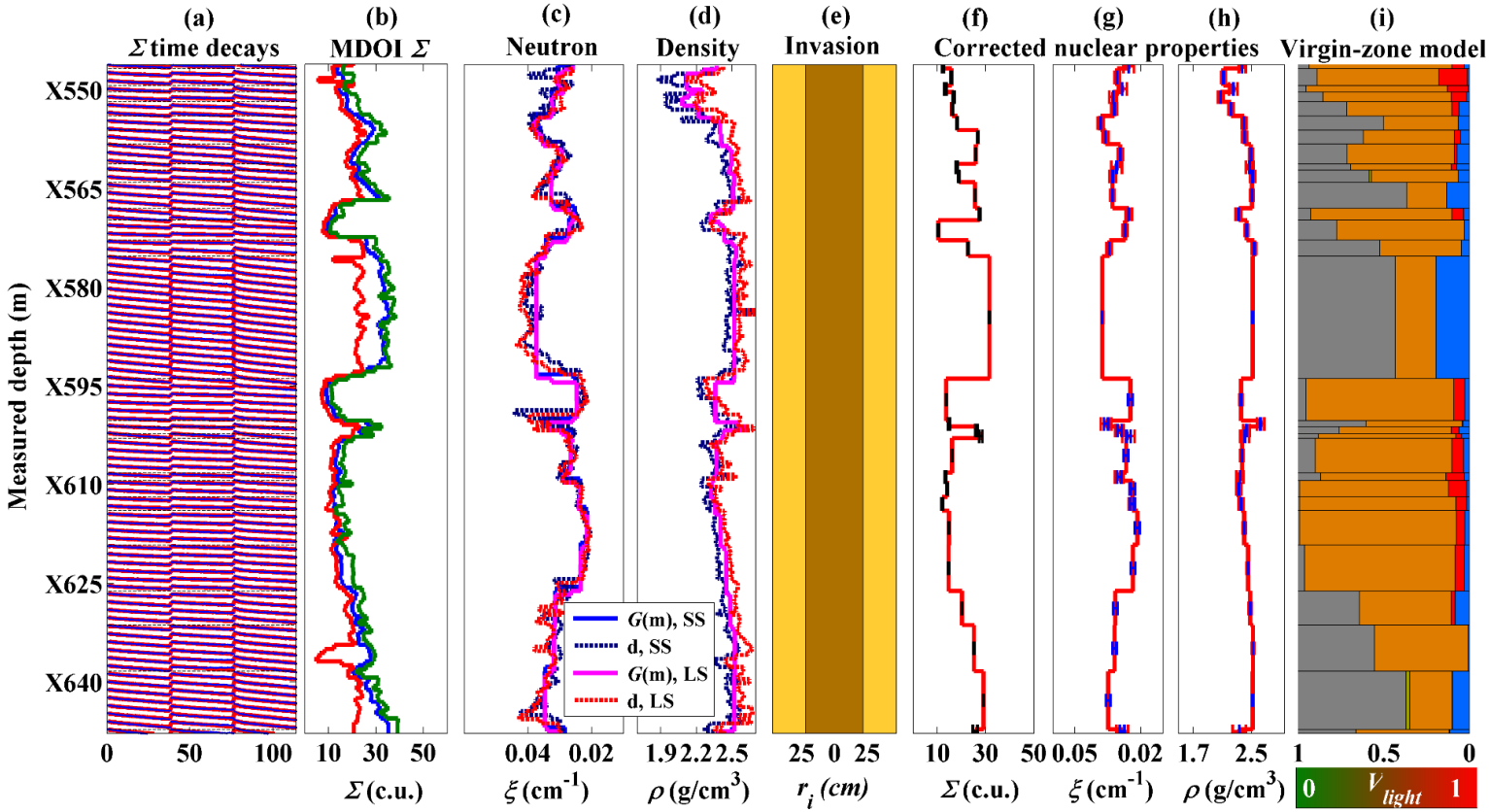

Figure 7.14: Reconstructed field measurements and corrected layer-by-layer nuclear properties for Field Case IV. (a) Measured (blue) and reconstructed (red) multi-detector time decays, (b) borehole- and diffusion-corrected Sigma logs, (c) measured and reconstructed Near and Far neutron inverse of migration length logs, (d) measured and reconstructed short-spaced (SSg) and long-spaced (LSg) gamma density logs, (e) sketch of borehole, invasion profile, and virgin formation, corrected virgin- and invaded-zone (f) Sigma, (g) neutron, and (h) density logs, respectively, and (i) virgin-zone volumetric model. On track (i): the color scale on bottom represents hydrocarbon type. Blue color represents water. Matrix minerals are clay (gray), limestone (light green), and quartz (orange).

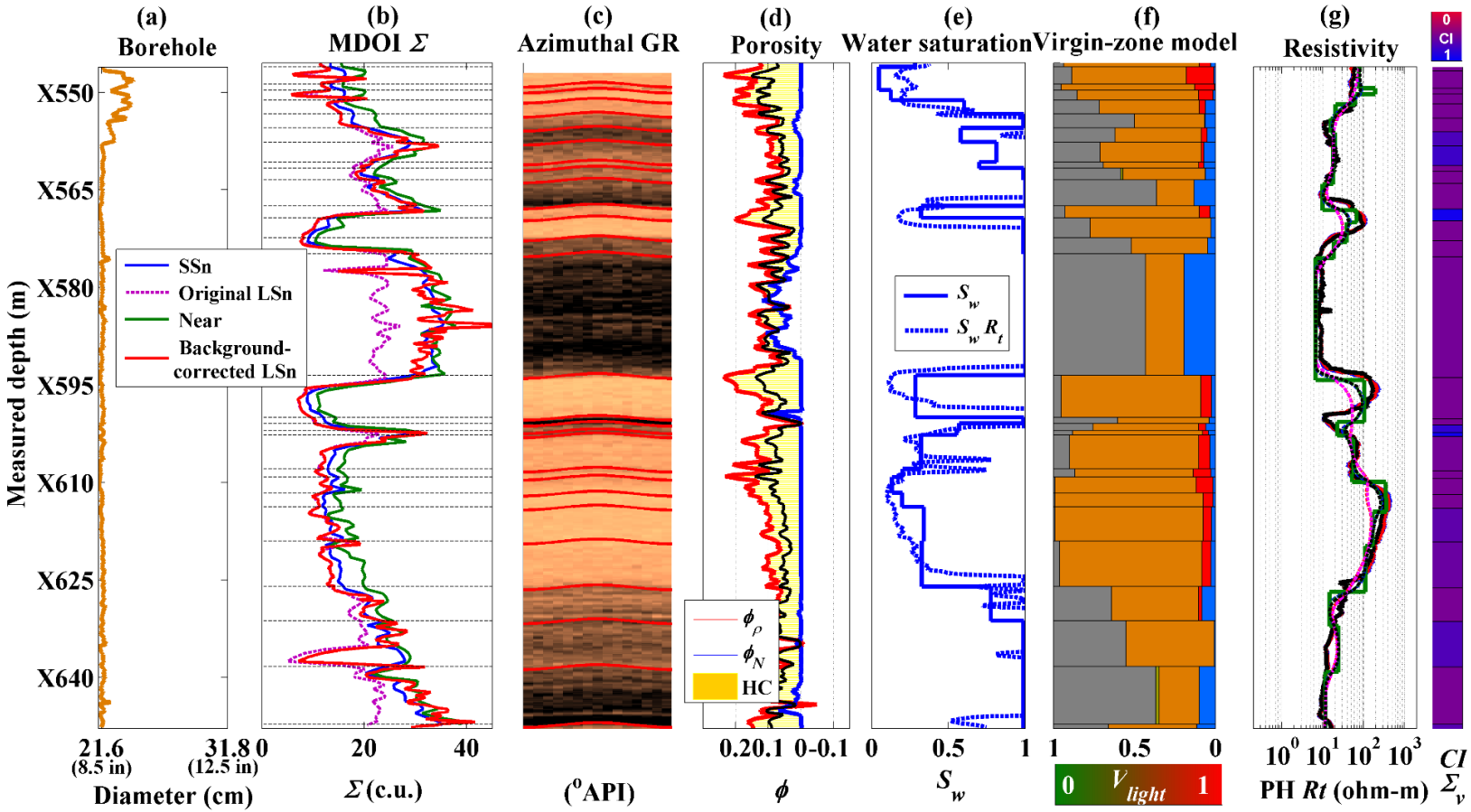

Figure 7.15: Inversion results for Field Case IV. (a) Density-derived caliper, (b) borehole- and diffusion-corrected measured Sigma logs, (c) azimuthal gamma-ray image and bed boundary locations, (d) matrix-corrected neutron and density porosity logs, and matrix- and fluid-corrected estimated total porosity, (e) comparison of water saturation estimated form resistivity logs and using our workflow, (f) virgin-zone volumetric model, (g) field and simulated high-frequency resistivity logs and layer-by-layer resistivity, and confidence index on virgin-zone Sigma.

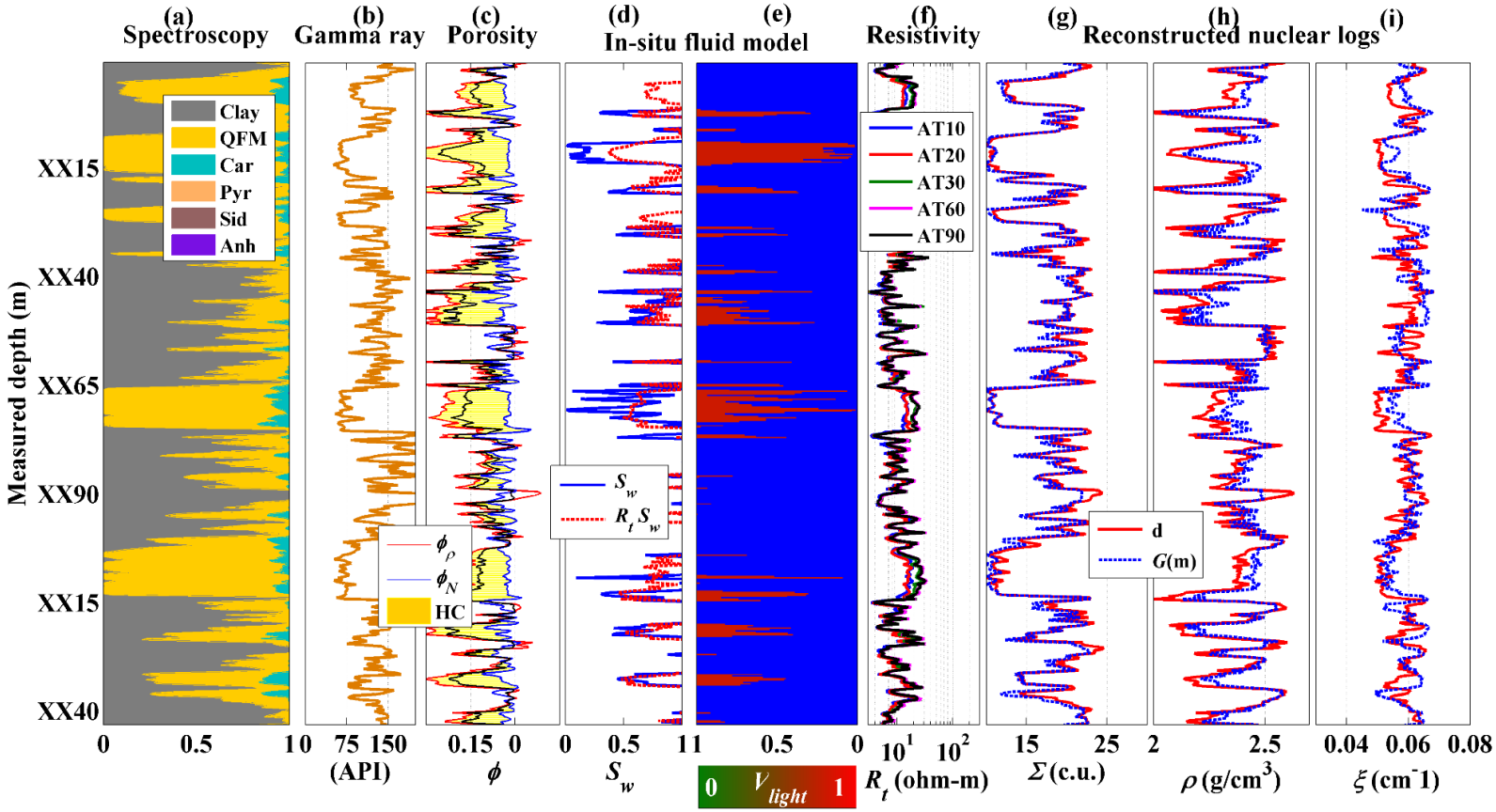

Figure 7.16: Inversion results for cased-hole Field Case V. (a) Mineral volumetric concentrations from gamma-ray spectroscopy logs, (b) natural gamma-ray log, (c) matrix-corrected neutron and density porosity logs, and matrix- and fluid-corrected estimated total porosity, (d) water saturation calculated form resistivity logs and using our nuclear solver, (e) a sketch of in-situ fluid distributions and fluid type; the color scale on bottom represents hydrocarbon type and blue represents water, (f) induction resistivity logs, and measured and reconstructed (g) Sigma, (h) compensated density, and (i) compensated neutron logs.

Chapter 8: Summary, Conclusions, and Recommendations

8.1 SUMMARY

The purpose of this dissertation is to advance the field of Sigma logging by assessing the qualitative and quantitative potential of multi-detector Sigma measurements, which were only recently introduced to the oil and gas industry. Prior to this study, multi-detector nuclear measurements were acquired using a commercial multi-function LWD tool, but fewer knowledge existed about how these measurements should be interpreted, and the capabilities and limitations they possessed. The motivation behind this project was the following: First, to qualitatively understand the physical basis of LWD Sigma measurements, environmental effects, and ideal logging environments using laboratory measurements and Monte Carlo simulations. Second, to develop a method that enabled the integration of all the factors that control detector response to perform inversion-based petrophysical interpretation of multi-detector Sigma measurements. The latter motivation was aimed to improve petrophysical interpretations based on resistivity logs or environmentally affected Sigma logs. This dissertation begins with an introduction in Chapter 1 that documents previous work on Sigma logging and advances in LWD nuclear measurement interpretation.

Chapter 2 presented the thermal-neutron and gamma-ray transport equations and assumptions used to estimate Sigma from time decays. I explained the operation of the commercial tool under study and how its three detectors, at different spacings from a fast-

neutron source, enable the detection of invasion in the near-wellbore zone while simultaneously improving petrophysical calculations in thinly bedded formations, due to the small spacing between the thermal neutron detector and the source. I described the processing of thermal-neutron time decays using the 2-exponential method and the processing of gamma-ray time decays using the moments method. The impact of environmental effects, such as borehole/diffusion and tool standoff, was described. Additionally, I showed simulation of mud filtrate invasion, which proved that under regular drilling conditions filtrate invasion exists and all nuclear LWD measurements are affected by invasion. I finalized the introductory chapter with comparisons of multi-detector LWD resistivity and Sigma to define the logging conditions under which each measurement has the greatest potential to assess radial length of invasion.

In Chapter 3, I introduced a first-order approximation to time-dependent nuclear measurements, which is the main technical contribution of this dissertation. The method relies on a library of detector-specific 3D sensitivity functions and a library of detector-specific time decays that were calculated using MCNP as a function of Sigma. The library of time decays considers the actual pulsing-scheme of the LWD tool under study. Thermal-neutron and gamma-ray detector response approximations were performed using thermal-neutron sensitivity functions and thermal-neutron absorption sensitivity functions, respectively. Measurements acquired in a laboratory facility that includes homogeneous water-saturated blocks as well as piston-like invasion, were used for benchmarking purposes. The model was additionally benchmarked against MCNP simulations in multiple

cases that combine homogeneous formations, invasion, thinly bedded formations, and highly deviated wells.

Chapters 4 and 5 described the application of the forward-model together with non-linear inversion to perform petrophysical interpretations. In Chapter 4, I calculate virgin-zone Sigma and radial length of invasion from three-detector time decays acquired in thick formations. I assumed that formations are thick enough to neglect shoulder-bed and well-deviation effects. A multiple-realization study in synthetic signals with realistic noise as a function of the logging-environment Sigma and rate of penetration, was used to ascertain the stability of the model under different invasion-virgin zone Sigma contrasts. I introduced an index, called *CI*, which represents the confidence on the estimations according to the degree of uniqueness of the inversion problem. Laboratory measurements and time-decay simulations were used to test the inversion algorithm. The algorithm was additionally applied in a field case. Chapter 5 extended the inversion algorithm to the more challenging situation of invaded formations that are thinner than the vertical resolution of the detectors. The extension allowed the inversion algorithm to be used for interpretation of field measurements acquired in high-angle wells traversing thinly bedded formations where the presence of invasion was speculated. The 2D algorithm was tested on synthetic and field measurements. Both chapters 4 and 5 documented estimations of water saturation and comparisons against similar estimations obtained for resistivity measurements.

Lastly, Chapters 6 and 7 documented the integration of multi-detector Sigma logging with other borehole measurements. In Chapter 6, I introduced a new approximation

for the mixing law of inverse of migration length that was coupled with the mixing law for bulk density to calculate matrix- and fluid-corrected total porosity. The approximation was also used to correct neutron-density crossovers masked by the presence of shale. In Chapter 7, I proposed a workflow to integrate Sigma inversion results with other nuclear measurements. The corrected porosity was used to improve the reference for invasion-zone Sigma that the multi-detector Sigma inversion needs to reduce non-uniqueness. I estimated radial length of invasion and virgin-zone Sigma using the 2D inversion algorithm for multi-detector decays. A new 2D inversion algorithm was introduced to estimate layer-by-layer inverse of migration length and density in virgin and invasion zones using two-detector neutron and density logs. The correction relies on estimated radial length of invasion from the multi-detector decay inversion. A petrophysical nuclear-based solver that uses corrected nuclear properties and a flash calculation was employed to ultimately calculate layer-by-layer pore water volume and hydrocarbon type, while accounting for the temperature, pressure, and salinity dependency of fluid nuclear properties.

8.2 CONCLUSIONS

Significant conclusions resulting from the studies presented in this dissertation are highlighted below.

8.2.1 Part One: Study of the Potential and Limitations of Multi-Detector LWD Sigma Measurements

i. The three detectors of the commercial LWD Sigma tool under study, located at different spacings from the source, provide different radial lengths of investigation and are affected by environmental effects at distinct levels due to differences in spatial sensitivities.

ii. The thermal-neutron Sigma (Near) measurement of the LWD tool is suited to distinguish thin layers. However, the caliper log should be monitored for washouts because the Near detector is greatly affected by tool standoff.

iii. Calculation of Sigma from time-decay curves produces an apparent Sigma which must be corrected for detector-specific diffusion and borehole effects. The environmental correction is larger in the thermal-neutron detector than in the long-spaced gamma-ray detector due to differences in spatial diffusion gradients.

iv. The effect of the fluid in the borehole is negligible because the large Sigma of the tool steel housing and stabilizer dominates the early-time detector response. However, the effect of fluid in the borehole may be important if there is standoff at the detector side of the tool.

v. LWD Sigma measurements are affected by the presence of invasion because they are shallow-sensing and the detectors are not placed adjacent to the drill bit.

vi. Filtrate invasion takes place because permeable formations are exposed to overbalanced drilling fluid for a period of time, normally between a few minutes to a few hours, using the LWD tool under study.

vii. Simulations of mud-filtrate invasion in hydrocarbon-bearing formations under typical LWD conditions indicate that invasion can range from a few inches to several feet into the formation. Therefore, LWD nuclear measurements are slightly affected or even completely masked by filtrate invasion.

viii. The different radial lengths of investigation of the three Sigma measurements permit the assessment of invasion in the shallow near-wellbore zone. In the case of thick formations and accurate conversion from apparent to intrinsic Sigma, separation of the three Sigma logs indicates presence of invasion in the zone within 35 cm from the borehole wall.

ix. In the case of brine invading a high porosity rock, multi-detector Sigma is useful to assess invasion in the shallow near-wellbore zone and outperforms the resistivity measurement. Resistivity measurements are better suited to assess invasion deeper than the depth of investigation of LWD Sigma measurements.

x. If there exists a small difference between the salinity of the drilling fluid and formation fluid, and/or if the rock has low porosity, the contrast in Sigma between virgin and invaded zones is not sufficient to assess invasion.

xi. The multi-detector Sigma method is particularly suitable to the evaluation of hydrocarbon-bearing, high-porosity formations invaded by high-salinity filtrate.

xii. Accurate calculation of water saturation form formation Sigma requires the presence of salt [NaCl] in connate water to generate sufficient contrast between water and hydrocarbon Sigma.

8.2.2 Part Two: Rapid Forward Modeling of Multi-Detector Logging-While-Drilling Sigma Measurements

i. Accurate rapid simulation of LWD Sigma measurements can be performed using first-order perturbation theory and pre-calculated time decays, rather than Sigma itself. Simulation of time decays, instead of Sigma, is desirable because time decays are fundamental measurements, while Sigma is affected by introduced borehole/diffusion corrections.

ii. Thermal-neutron time-dependent responses can be accurately modeled using Monte Carlo calculated, thermal-neutron sensitivity maps. These maps consists of tracking the spatial importance of thermal neutrons that produce counts in the thermal neutron detector. Similarly, gamma-ray time-dependent responses can be accurately modeled using Monte Carlo calculated, thermal-neutron absorption sensitivity maps. These maps consists of tracking the spatial importance of thermal-neutrons that are absorbed, and whose generated gamma rays produce counts in the gamma-ray detectors.

iii. Simulated time decays include all pertinent detector-dependent borehole and diffusion effects. No conventional conversions from apparent Sigma to intrinsic

Sigma are necessary for inversion-based petrophysical interpretation of time decays.

iv. I benchmarked the rapid simulation algorithm against MCNP simulated time decays, and against laboratory measurements. Results show that the fast-forward algorithm accurately reproduces all the environmental and geometrical effects observed in MCNP calculated time decays under complex measurement conditions, with average absolute disparities within 2 c.u. and in a hundred thousandth of the computer time required by MCNP.

v. Differences between MCNP time decays and rapidly simulated time decays are expected to be larger than the average of 2 c.u. when simulating measurements acquired in environments with uncommonly high Sigma values. This is especially true for the Near detector time decays, as more absorption results in low thermal-neutron counts and more noise in the Near detector measurement. In highly absorbing logging environments, statistical quality of Near-detector time decays is not ideal for both MCNP simulations and actual measurements.

vi. Although slight differences between MCNP and fast-forward simulated time decays exist, the simulation algorithm provides the level of reliability and speed necessary to interpret field measurements, which in reality are acquired in conditions that depart from the assumed geometry of sharp transition boundaries, piston-like invasion, and constant-angle well sections.

8.2.3 Part Three: Inversion-Based Interpretation of Multi-Detector LWD Sigma Measurements

i. A nonlinear gradient-based algorithm can be coupled with the fast-forward simulation method to invert multi-detector LWD thermal-neutron and gamma-ray time decays. I showed that a 1D radial inversion algorithm was sufficient to accurately estimate formation Sigma, free of invasion effects, as well as radial length of invasion in thick formations.

ii. Noise in LWD Sigma measurements is a function of the logging-environment Sigma and rate of penetration.

iii. A Confidence Index (*CI*), calculated from a multiple realization study on synthetic time decays with noise, proved successful in complementing covariance-based error bars to estimate the uncertainty of model estimations. Synthetic and field results indicate that the index is useful in recognizing uncertainty in the estimations when the inversion problem is non-unique. Error bars calculated by the covariance method do not allow recognizing these situations.

iv. The 1D radial inversion algorithm is especially useful to assess radial length of invasion, to correct formation Sigma for invasion effects, and to accurately calculate resistivity-independent water saturation from LWD Sigma logs in shallow-invaded formations.

v. The multiple realization study confirmed qualitative observations: If there is only a small difference between the salinity of drilling mud and formation fluid, and/or if

the rock has low porosity, the contrast in Sigma between virgin and invaded zones is not sufficient to assess invasion. Fortunately, in these cases the inversion to correct Sigma for invasion effects is not essential because the error on formation Sigma due to the presence of invasion is not significantly large.

vi. The 1D radial inversion algorithm is to be utilized to isolate invasion effects in thick formations, because the 1D implementation of the inversion cannot account for shoulder-bed and well-deviation effects.

vii. The multi-detector Sigma inversion showed the greatest potential to improve petrophysical evaluations in the case of high-porosity, hydrocarbon-bearing formations invaded by salty mud filtrate.

viii. Benchmarking results of the 1D radial inversion algorithm in a synthetic example indicates that calculating water saturation using the conventional approach with a single gamma-ray detector (SSn) leads to overestimation of water saturation in a gas zone (as much as 33 percent), and underestimation of water saturation in a water zone (as much as 27 percent) if Sigma is not corrected for shallow salty-filtrate invasion effects.

ix. A 2D inversion algorithm coupled with the rapid 3D multi-detector time decay simulation model enables to concurrently reduce shoulder-bed, shallow invasion, well-deviation, and borehole and diffusion effects from multi-detector time decays. The 2D inversion is useful to interpret time decays acquired in challenging environments such as thinly bedded formations traversed by high-angle wells.

x. Interpretation of LWD field measurements indicates that Sigma measurements are often better suited for petrophysical evaluation of thinly bedded formations than resistivity measurements because of the smaller volume of investigation of Sigma measurements. This is especially true in the case of deviated wells traversing thinly bedded formations, where resistivity logs average the properties of various layered formations and generally display horns and anisotropy effects.

xi. The overestimation of water saturation in formations invaded by salty mud filtrate is more noteworthy if there are shoulder high-Sigma layers, such as shales, affecting the measurement in hydrocarbon zones. Combined shoulder-bed and invasion effects can lead to oversight of thin hydrocarbon-bearing formations.

xii. Application of the 2D inversion in field cases allowed for estimating lower water saturations in hydrocarbon-bearing formations interspaced between shales than was suggested by one-detector uncorrected Sigma or resistivity log analyses. Water saturation was as much as 50 percent lower in the case of oil-bearing formations affected mostly by shoulder-bed and well-deviation effects, and as much as 100 percent lower in the case of gas-bearing thinly bedded formations additionally affected by high-salinity filtrate invasion.

xiii. The estimation of radial length of invasion improves the understanding of neutron-density crossovers. Suppression of neutron-density crossovers in hydrocarbon zones is the combined effect of shaliness, water saturation, and radial length of invasion.

xiv. Results of the 2D inversion should be carefully analyzed and estimations of water saturation are to be trusted only when invasion remains shallow (within 20 cm approximately) and when there exists enough Sigma contrasts between virgin- and invasion-zone Sigmas.

xv. Interpretation of field LWD Sigma and propagation measurements showed that the improved vertical resolution of the Sigma log compared to the resistivity log enables the local variations in water saturation, which are averaged by resistivity measurements, to be identified.

8.2.4 Part Four: Integration of Multi-Detector LWD Sigma Measurements with Other Borehole Nuclear Measurements

i. A new approximation for the mixing law of migration length proved satisfactorily comparable to SNUPAR-calculated inverse of migration length. The approximation is analogous to the linear mixing law for density, but takes into account nonlinear effects in the measurement induced by the presence of gas and shale in the formation.

ii. Analytical expressions of migration length and density mixing laws can be coupled to obtain a new analytical expression for total porosity. Estimated total porosity using the coupled expression does not require any assumption regarding matrix or fluid composition of the rock.

iii. Matrix correction of neutron and density logs requires matrix density and inverse of migration length, ρ_m and ξ_m, respectively. Assuming linear mixing of the

minerals in the matrix generates minor deviations from SNUPAR-calculated matrix properties.

iv. Synthetic and field results indicate that matrix corrections to neutron and porosity logs can be accurately performed using single-mineral nuclear properties and gamma-ray spectroscopy logs, or calculated C_{sh} when only triple-combo logs are available.

v. Synthetic and field results show that the new method to perform matrix corrections on neutron and density logs can effectively isolate shale effects and expose hydrocarbon crossovers that agree with core measurements and resistivity logs.

vi. The new expression for total porosity can be used to calculate total porosity without taking an average between neutron and density, nor assuming a specific fluid saturation.

vii. The improvement of the new method to calculate total porosity from the conventional root-mean-square (RMS) method is particularly valid in the case of low-porosity, gas-bearing formations with large concentrations of shale, such as shale-gas formations. The RMS average porosity method led to the overestimation of porosity up to 15 p.u. in one field case.

viii. Field results indicate that the new calculation of total porosity is more accurate than the traditional RMS average, which overestimates porosity in shaly rocks, and compares well to core total porosity and NMR porosity.

ix. Calculated matrix density can be used concurrently with the new matrix- and fluid-corrected porosity to estimate water saturation in strong agreement with core water saturation.

x. Calculation of water saturation from density logs generates more reliable results in gas-bearing environments where the nuclear properties of water and hydrocarbon display large contrasts and enable clear differentiation.

xi. The LWD nuclear measurement suite (Sigma, neutron, density, and spectroscopy) of the commercial multi-function tool under study enables to perform petrophysical interpretations independently of resistivity. The advantage of using solely nuclear logs is that they have a smaller volume of investigation than resistivity logs and are not affected by nonlinear effects, such as horns and anisotropy effects. Additionally, the similar volume of investigation for all nuclear measurements facilitates integration.

xii. A new workflow for petrophysical interpretation independently of resistivity measurements enabled to successfully integrate all nuclear measurements, while correcting them for environmental and geometrical effects. Matrix nuclear properties were calculated using gamma-ray spectroscopy logs, and fluid-sensitive nuclear measurements were used to accurately estimate water saturation and hydrocarbon type.

xiii. Flash calculations and SNUPAR can be used to calculate the nuclear properties of the fluids as a function of pressure, temperature, and salinity.

xiv. The workflow to interpret multi-detector time decays (Sigma), neutron porosity, and density measurements exploits the different vertical resolutions and depths of investigation of the detectors to reduce invasion, shoulder-bed and well-deviation effects.

xv. Synthetic and field cases indicate that, in the instance of salty filtrate invading hydrocarbon formations, the multi-detector time decay inversion accurately estimates radial length of invasion and is useful to correct neutron and density measurements for invasion effects. The effect of the correction is especially significant in the instance of gas-bearing formations, where gas properties can be masked by the presence of invasion in the near-wellbore zone.

xvi. The nuclear inversion workflow additionally allows for variations in water saturation, which are averaged by resistivity measurements, to be seen.

xvii. The estimation of water saturation and fluid type can be greatly affected by radial length of invasion. In the event of invasion being deeper than approximately 15 cm, only the deep-sensing Sigma detector (LSn) is sensitive to the virgin formation, and the inversion problem is rendered non-unique.

xviii. The presence of noise in measured time decays can result in large uncertainty for the estimated radial length of invasion and, therefore, large uncertainty in the invasion-corrected nuclear properties. Qualitative interpretation and observations of field measurements suggest that the Near and LSn detectors are more prone to exhibiting noise and should be inspected before attempting inversion.

xix. Gamma-ray background corrections on SSn and LSn gamma-ray time decays are of enormous importance in petrophysical interpretation. Failing to correct for background effects can yield values in the SSn and LSn Sigma logs significantly smaller than Near Sigma (not affected by background radiation), which mimics the effect of salty-filtrate invasion on Sigma logs. Miscorrecting background radiation also affects the separation of multi-detector Sigma logs. This is an example of why the interpretation of time decays, rather than Sigma logs, is a clever choice.

xx. Nuclear properties corrected for invasion effects cannot always be used for petrophysical interpretation because invasion is sometimes deep and sensitivity of all nuclear measurements to the virgin formation is not enough to perform the correction accurately. Error bars and the confidence index on virgin-zone Sigma should be checked to detect intervals in which estimated petrophysical properties are subject to substantial uncertainty.

8.3 CONTRIBUTIONS

i. The main technical contribution of this dissertation is the development of a method to numerically simulate the fundamental pulsed neutron capture measurement, i.e. time decays, as opposed to Sigma. Simulation of time decays provides several advantages such as (a) the use of all the information contained in the time decay instead of a portion of it, (b) the reproduction of all the detector-specific diffusion and borehole effects, and (c) the elimination of correction factors stemming from tool calibration and used to convert apparent Sigma to intrinsic Sigma.

ii. A significant feature of the forward simulation model is its versatility. The model can be used in association with any pre-calculated FSF and time decay library for any tool using any pulsing scheme, and can also be employed to calculate Sigma logs using any method of choice (two-exponentials, moments, NMR-like, etc.).

iii. This dissertation presents the first holistic study on Sigma measurements that accounts for all the factors involved in the measurement, such as its physical basis, assumptions in the interpretation of time decays, quantitative studies of borehole effects and tool standoff, filtrate-invasion, and shoulder-bed and well deviation effects. Furthermore, I present the first comprehensive method to quantify radial length of invasion from nuclear measurements, while simultaneously considering all factors that affect multi-detector tool responses.

iv. This dissertation introduced a new method to calculate total porosity devoid of matrix and fluid effects. The method proved to be advantageous in the evaluation of shale-gas formations.

v. The significance of the combined interpretation of multi-detector Sigma, neutron, and density measurements presented in this dissertation is that the method establishes a petrophysical model that agrees with the physics of all nuclear measurements, PVT properties of reservoir fluids, and a-priori knowledge, such as mud-filtrate salinity, connate water salinity, and layer boundary locations. The method integrates information from all nuclear measurements in the most holistic manner to decouple any artifacts in the measurements and reveal actual formation

properties, while simultaneously maximizing the resolution of nuclear measurements.

8.4 RECOMMENDATIONS FOR BEST PRACTICES

i. Interpretation of Sigma logs should always be accompanied by a borehole quality check. Inversion results can be greatly affected by the presence of tool standoff. Nonzero radial length of invasion may be estimated in non-invaded formations if tool standoff exists, because of the small volume of investigation of the thermal-neutron Near detector. It is advisable to check borehole quality using azimuthal ultrasonic measurements, rather than density-derived caliper logs, because density-derived caliper logs are highly affected by shallow invasion. Shallow invasion can generate differences between density SSg and LSg measurements that may be inaccurately interpreted as an enlarged borehole.

ii. Gamma-ray time decays should always be corrected for background gamma-ray radiation before attempting any petrophysical interpretation. Not correcting for background gamma-ray radiation results in lower than actual Sigma values and anomalous upward tails in time decays. Background gamma-ray counts arise from induced neutron activation and natural radioactivity

iii. Salt should be added to drilling fluid whenever multi-detector LWD Sigma is intended to allow assessment of shallow invasion. Ideally, the amount of salt in the filtrate should ensure that the contrast between virgin-invasion zone Sigma is at least 10 c.u. Larger contrast in virgin-invasion zone Sigma increases the stability of

the inversion and accuracy of estimated radial length of invasion and virgin-zone Sigma.

iv. I advise the use of Sigma logs for geosteering applications based on my observations of LWD nuclear and resistivity logs in deviated wells. Sigma logs correlate notably well with neutron, density, and spectroscopy measurements because of their similar volumes of investigation as opposed to propagation resistivity measurements. The differences in volume of investigation are especially important in the case of deviated wells. For such case, nuclear measurements are better suited to identify and evaluate thinly bedded formations. Even though quantitative applications require high statistical quality of the time decays, fast processing of the late-time components of the SSn detector signal has the potential to be used in real time to complement the use of deep resistivities, or even for standalone geosteering applications if the Sigma measurement devices were to be assembled closer to the drill bit.

v. One of the most important aspects of the matrix and fluid correction proposed in this dissertation is the assumed nuclear properties, ξ and ρ, for the minerals. Matrix nuclear properties can be calculated using single-mineral nuclear properties, which are combined using volumetric mineral fractions from spectroscopy logs or calculated C_{sh}. The determination of which minerals constitute the matrix can be difficult, especially since spectroscopy measurements group multiple clay minerals into one single clay group, and quartz, feldspars, and micas into another group

called QFM. Constituents of such groups can display different ξ and ρ, but one average value must be selected for the whole group. Clay typing is, therefore, critical to establish the dominant properties for wet clay. I advise that the correction be started with nuclear properties for the most dominant clay type and quartz, and assessing whether neutron and density logs overlay in low-resistivity zones. If this is not the case, I advise the calibration of the properties for the shale and sand components, especially ξ, until both porosities read the same value in a water zone or in a water-saturated shale formation, i.e., low-resistivity formations.

vi. I recommend the quality of the multi-detector decays be evaluated before attempting to apply inversion. If time decays are noisy, the inversion-based interpretation should be performed both with and without invasion to verify that results in uninvaded formations agree using both methods, and also agree with qualitative interpretation of all borehole measurements.

vii. Rate of penetration should be considered when planning to use multi-detector time decays for petrophysical interpretation. Large penetration rates result in low detector count rates and large statistical noise in the signals, which could result in misinterpretations of radial length of invasion that affect the correction for invasion effects to all other nuclear borehole measurements. Based on my experience with field data, one factor that currently makes the interpretation of multi-detector decays acquired with the LWD tool under study challenging is the statistical quality of thermal-neutron (Near) and long-spaced gamma-ray (LSn) detector time decays.

viii. In the absence of thinly bedded formations, the quality of multi-detector Sigma logs acquisition and environmental corrections performed by a service company can be checked by visually inspecting that the SSn Sigma log reads values between Near and LSn Sigma values. SSn Sigma logs not affected by shoulder-bed effects should display intermediate values because the volume of investigation of the SSn detectors is intermediate between the volume of investigation of the Near and LSn detectors.

8.5 Recommendations for Future Work

i. Laboratory time decays used in this dissertation were highly affected by the presence of steel liners, which are strong absorbers, that were used to physically separate virgin and invasion zones. For future laboratory measurements, I recommend to replace the steel cylinders for cylinders made out of low-absorption cross section materials.

ii. The forward modeling work presented in this dissertation was benchmarked against laboratory measurements for the case of piston-like invasion. Unfortunately, there existed no laboratory measurements across thinly bedded formations. I suggest additional validation of the model and Monte Carlo simulations in a laboratory setting that includes layers of contrasting Sigma separated by a low-Sigma material. Additionally, the relative angle between the well and layers dipping plane should be varied to verify the effect of shoulder beds and well deviation on multi-detector Sigma measurements.

iii. The multi-detector Sigma logging technique can be further improved by using strong absorbers as additives to the drilling fluid. This would maximize the contrast in multi-detector Sigma response whenever filtrate invasion takes place. However, studies on the use of strong absorbers as additives should consider the trade-off in time-decay statistical quality. Large absorption cross section in the invasion zone can cause a significant decrease in detector counts, and therefore, a decrease in statistical quality of the measurement. Strong absorbing environments require low logging speeds to compensate for the increased absorption in the formation. Additionally, the use of strong absorbers as fluid additives decreases the contrast in borehole and formation Sigma, and may result in increased borehole effects at al late times.

iv. I recommend to improve the calculation of water saturation from the 2D inversion algorithm by isolating shoulder-bed and well-deviation effects from spectroscopy and porosity logs. The estimation of water saturation from Sigma logs requires knowledge of matrix Sigma, derived from the volumetric mineral concentrations given by the spectroscopy log, in addition to knowledge of the total porosity derived from neutron and density logs. In this dissertation I calculated matrix properties using spectroscopy logs read at the center of each assumed layered formation. Errors are introduced to the calculation of water saturation from Sigma logs in the case of thinly bedded formations where the logs average the properties of multiple formations.

v. Gamma-ray background corrections, from activation and natural gamma radiation, should be improved to guarantee that gamma-ray time decays (SSn and LSn) display an exponential decay at late times. Often, I observed count rates flatting off at late times, especially in long-spaced gamma-ray time decays (LSn). Miscorrected gamma-ray background can be visually evidenced in the form of "tails" at late times that do not agree with the behavior predicted by the Boltzmann equation, i.e., a plot of the logarithm of count rates versus time should follow a straight line at late times. Water saturation from Sigma logs may be underestimated if background gamma radiation is not properly subtracted from measured time decays.

vi. Multiple studies have addressed the effects of invasion on propagation measurements. Published radial sensitivity functions for phase and amplitude resistivity measurements show no sensitivity to invasion within approximately 15 cm from the borehole wall, which was confirmed by simulations of resistivity logs in shallow-invaded formations traversed by a vertical well that were documented in this dissertation. Nonetheless, I recommend to study the effect of shallow invasion in LWD resistivity measurements acquired in deviated wells. Possible resistivity anisotropy in such a geometrical configuration can create particular effects that deserve attention since they might impact petrophysical interpretations of propagation measurements.

Appendix A

The Jacobian matrices to be used for the 2D inversion of density and neutron measurements are defined as follows:

$$\mathbf{J}_{\rho} = \begin{Bmatrix} \begin{bmatrix} \frac{\partial \rho_{SSg}}{\partial \rho_v} & \frac{\partial \rho_{SSg}}{\partial \rho_i} & \frac{\partial \rho_{SSg}}{\partial r_i} \\ \frac{\partial \rho_{LSg}}{\partial \rho_v} & \frac{\partial \rho_{LSg}}{\partial \rho_i} & \frac{\partial \rho_{LSg}}{\partial r_i} \end{bmatrix}_1^1 & \cdots & \begin{bmatrix} \frac{\partial \rho_{SSg}}{\partial \rho_v} & \frac{\partial \rho_{SSg}}{\partial \rho_i} & \frac{\partial \rho_{SSg}}{\partial r_i} \\ \frac{\partial \rho_{LSg}}{\partial \rho_v} & \frac{\partial \rho_{LSg}}{\partial \rho_i} & \frac{\partial \rho_{LSg}}{\partial r_i} \end{bmatrix}_m^1 \\ \vdots & \ddots & \vdots \\ \begin{bmatrix} \frac{\partial \rho_{SSg}}{\partial \rho_v} & \frac{\partial \rho_{SSg}}{\partial \rho_i} & \frac{\partial \rho_{SSg}}{\partial r_i} \\ \frac{\partial \rho_{LSg}}{\partial \rho_v} & \frac{\partial \rho_{LSg}}{\partial \rho_i} & \frac{\partial \rho_{LSg}}{\partial r_i} \end{bmatrix}_1^n & \cdots & \begin{bmatrix} \frac{\partial \rho_{SSg}}{\partial \rho_v} & \frac{\partial \rho_{SSg}}{\partial \rho_i} & \frac{\partial \rho_{SSg}}{\partial r_i} \\ \frac{\partial \rho_{LSg}}{\partial \rho_v} & \frac{\partial \rho_{LSg}}{\partial \rho_i} & \frac{\partial \rho_{LSg}}{\partial r_i} \end{bmatrix}_m^n \end{Bmatrix}_{2 \cdot n \;\; x \;\; 3 \cdot m}, \quad \text{(A-1)}$$

for the 2D inversion of multi-detector density measurements, and

$$\mathbf{J}_N = \left\{ \begin{array}{ccc} \left[\begin{array}{ccc} \frac{\partial \xi_{Near}}{\partial \xi_v} & \frac{\partial \xi_{Near}}{\partial \xi_i} & \frac{\partial \xi_{Near}}{\partial r_i} \\ \frac{\partial \xi_{Far}}{\partial \xi_v} & \frac{\partial \xi_{Far}}{\partial \xi_i} & \frac{\partial \xi_{Far}}{\partial r_i} \end{array} \right]_1^1 & \cdots & \left[\begin{array}{ccc} \frac{\partial \xi_{Near}}{\partial \xi_v} & \frac{\partial \xi_{Near}}{\partial \xi_i} & \frac{\partial \xi_{Near}}{\partial r_i} \\ \frac{\partial \xi_{Far}}{\partial \xi_v} & \frac{\partial \xi_{Far}}{\partial \xi_i} & \frac{\partial \xi_{Far}}{\partial r_i} \end{array} \right]_m^1 \\ \vdots & \ddots & \vdots \\ \left[\begin{array}{ccc} \frac{\partial \xi_{Near}}{\partial \xi_v} & \frac{\partial \xi_{Near}}{\partial \xi_i} & \frac{\partial \xi_{Near}}{\partial r_i} \\ \frac{\partial \xi_{Far}}{\partial \xi_v} & \frac{\partial \xi_{Far}}{\partial \xi_i} & \frac{\partial \xi_{Far}}{\partial r_i} \end{array} \right]_1^n & \cdots & \left[\begin{array}{ccc} \frac{\partial \xi_{Near}}{\partial \xi_v} & \frac{\partial \xi_{Near}}{\partial \xi_i} & \frac{\partial \xi_{Near}}{\partial r_i} \\ \frac{\partial \xi_{Far}}{\partial \xi_v} & \frac{\partial \xi_{Far}}{\partial \xi_i} & \frac{\partial \xi_{Far}}{\partial r_i} \end{array} \right]_m^n \end{array} \right\}_{2 \cdot n \;\; x \;\; 3 \cdot m} \quad ,(A\text{-}2)$$

for the 2D inversion of multi-detector neutron measurements. Subscripts represent model sub-layers i=1:m, and superscripts represent measurement depth levels j=1:n. The size of the Jacobian sensitivity matrices is $2 \cdot n$ rows, which correspond to two-detector measurements at n depth locations, and $3 \cdot m$ columns, which correspond to three formation properties for m number of model sublayers.

List of Symbols

$a(\mathbf{r}_R)$	Detector-specific constant derived from *J*-factor polynomial fitting.
A	Amplitude of particle decay signal (cps).
AmBe	Americium-beryllium neutron source.
Anh	Anhydrite.
AT	Acquisition time (s).
B	Bottom azimuthal sector.
$b(\mathbf{r}_R)$	Detector-specific constant derived from *J*-factor polynomial fitting.
BH	Borehole.
C	Concentration.
$c(\mathbf{r}_R)$	Detector-specific constant derived from *J*-factor polynomial fitting.
Cal	Calcite.
Car	Carbonate.
CDR	Compensated dual resistivity.
CI	Confidence index.
Clay	Wet clay mineral group in spectroscopy logs.
$\mathbf{Cov(m)}$	Covariance matrix.
cps	Counts per second.
CR	Count rate (cps).
CR^0	Count rate in synthetic decay without noise (cps).
c.u.	Capture unit.
$d(\mathbf{r}_R)$	Detector-specific constant derived from *J*-factor polynomial fitting.
$\mathbf{d}$	Measurement vector.
DF	Duty factor.
DL	Dolomite.

E	Particle energy.
eV	Electron volt.
$\mathbf{f}$	Fractional uncertainty.
F	Cost function.
Far	Thermal-neuron far detector.
FF	Fast-forward numerical simulation model.
fph	Feet per hour.
FSF	Flux sensitivity function.
G	Nonlinear fast-forward simulator.
GR	Gamma-ray log.
HA/HZ	High-angle/horizontal.
h_{bit}	Spacing between bit and measurement point (m).
HC	Hydrocarbon crossover in neutron- and density-porosity logs.
HI	Hydrogen index.
$\mathbf{I}$	Identity matrix.
i	Model layer sub-i.
in	Inches.
Inv.	Invasion zone.
Inver.	Inverted model properties.
j	Model measurement point sub-j.
$\mathbf{J}$	Jacobian matrix.
J	Normalized radial geometrical factor.
K_v	Vertical permeability (md).
K_h	Horizontal permeability (md).
K_{ro}	Oil relative permeability.
kPa	Kilo Pascal.
kppm	Kilo part per million.

L	Left azimuthal sector.
L_d	Neutron diffusion length (cm).
L_m	Neutron migration length (cm).
L_s	Neutron slowing-down length (cm).
LRLC	Low-contrast low-resistivity.
LS	Long-spaced detector measurement.
LSg	Long-spaced gamma-ray density.
LSn	Long-spaced gamma-ray detector.
LWD	Logging while drilling.
m	Number of model sublayers.
$\mathbf{m}$	Model property vector.
$\mathbf{m}_R\big\|_{\rho-N}$	Reference vector in neutron and density inversion.
MC	Monte Carlo.
MCNP®	Monte Carlo N-Particle code.
MDOI	Multi depth of investigation.
MeV	Mega electron volt.
MWD	Measurement while drilling.
n	Number of measurement points.
N	Detector counts.
N_{filter}	Number of averaged depth level measurements.
$\mathbf{n}(t)$	Time-dependent detector response (particle decay).
$\mathbf{n}(t)_1$	Short-spaced gamma-ray (SSn) detector time decay.
$\mathbf{n}(t)_2$	Short-spaced gamma-ray (LSn) detector time decay.
$\mathbf{n}(t)_3$	Thermal-neutron (Near) detector time decay.
$\mathbf{n}(\mathbf{r}_R, t)$	Time decay measured at detector position $\mathbf{r}_R$.

$\mathbf{n}_B(\mathbf{r}_R,t)$	Detector-specific background material decay.
$\mathbf{n}_i(\mathbf{r}_R,t)$	Invaded-zone detector-specific decay.
$\mathbf{n}_v(\mathbf{r}_R,t)$	Virgin-zone detector-specific decay.
$\mathbf{n}(\mathbf{r}_R,t,i)$	Partial detector-specific response for sublayer *i*.
$\mathbf{n}(\mathbf{r}_R,t,j)$	Detector-specific integrated response at measurement point *j*.
$\mathbf{n}_i(\mathbf{r}_R,t,i)$	Partial detector-specific response for invaded zone in sublayer *i*.
$\mathbf{n}_v(\mathbf{r}_R,t,i)$	Partial detector-specific response for virgin zone in sublayer *i*.
Near	Near thermal-neutron detector.
NMR	Nuclear magnetic resonance.
OBM	Oil-based mud.
P	Pressure (kPa).
P_c	Capillary pressure (kPa).
PEF	Photoelectric factor (barn/e^-).
PH	High-frequency phase resistivity.
PNC	Pulsed neutron capture.
PNG	Pulsed neutron generator.
psia	Force pounds per square inch.
p.u.	Porosity unit.
PVT	Pressure-volume-temperature.
Pyr	Pyrite.
QFM	Quartz-feldspar-mica mineral group in spectroscopy logs.
Qtz	Quartz.
$\mathbf{r}$	Position vector.
$\mathbf{r}_i$	Position vector corresponding to sublayer *i*.
r_i	Radial length of invasion measured from the borehole wall (cm).

$r_i(i)$	Radial length of invasion at sublayer *i*.
r_i^*	Fixed radial length of invasion in neutron and density inversion.
$\mathbf{r}_R$	Detector position vector.
R	Right azimuthal sector.
ROP	Rate of penetration (cm/s).
R_t	Formation resistivity (ohm-m).
s	Standard deviation of weighted noise.
S	Particle source (particles/cm^3-s-eV-ster).
SBM	Synthetic-based mud.
SD	Sampling interval (cm).
Sid	Siderite.
SNUPAR	Schlumberger nuclear parameter calculation program.
$S.O.$	Standoff (cm).
SS	Short-spaced detector measurement.
SSg	Short-spaced gamma-ray density.
SSn	Short-spaced gamma-ray detector.
S_w	Water saturation.
S_{wirr}	Irreducible water saturation.
t	Time (μs).
T	Temperature (°F).
tb	Total number of time bins in a nuclear time decay.
TAB	Time after bit (s).
TN	Thermal neutron.
TST	True stratigraphic thickness (cm).
U	Upper azimuthal sector.
UTAPWeLS	Integrated petrophysics and well-log modeling platform.
V	Volume fraction.

V_A	Volume fraction of mineral component *A*.
V_B	Volume fraction of mineral component *B*.
v/v	Volumetric fraction.
Vir.	Virgin zone.
ν	Number of degrees of freedom.
v_N	Average thermal-neutron velocity (cm/s).
w	Test statistics in the Shapiro-Wilk normality test.
WBM	Water based mud.
$\mathbf{W}_d$	Modified relative data-weighting matrix.
XRD	X-ray diffraction.
α	Regularization parameter.
$\alpha(\mathbf{r})$	Interaction cross-section (barns).
α_B	Background interaction cross-section.
β	Coefficients in data-weighting matrix.
γ^i	Sensitivity of detector $\mathbf{r}_R$ to sublayer *i*.
δCR_i	Decay signal noise.
ζ	Weighted misfit vector.
η	Exponent in inverse of migration length mixing law.
λ	Random number from a standard normal distribution.
μ	Mean value of Poisson distribution.
μs	Micro second.
ξ	Inverse of migration length (cm^{-1}).
ρ	Density (g/cm^3).
σ	Standard deviation of estimations.
$\sigma_{realizations}$	Standard deviation of random nuclear events.

Σ_a	Macroscopic thermal-neutron absorption cross section (c.u.).
Σ_s	Macroscopic scattering cross section (cm^2/cm^3).
Σ_t	Macroscopic total interaction cross section (cm^2/cm^3).
τ	Thermal-neutron decay time (μs).
ϕ	Porosity (p.u.).
χ_g	Gas molar fraction in hydrocarbon.
$\boldsymbol{\Psi}$	Angular flux (particles/cm^2-s-eV-ster).
$\hat{\boldsymbol{\Omega}}$	Angular direction (ster).

Subscripts

a	Absorption.
app	Apparent.
B	Background.
bulk	Bulk formation property.
BH	Borehole.
clay	Wet clay property.
corr	Corrected.
est	Estimated.
F	Formation.
f	Fluid.
Far	Far thermal neutron.
filt	Filtrate.
g	Gas.
hc	Hydrocarbon.
heavy	Heavy hydrocarbon component.
i	Invasion.

int	Intrinsic.
light	Light hydrocarbon component.
LSg	Long-spaced gamma-ray density.
LSn	Long-spaced gamma ray.
m	Matrix.
mf	Mud filtrate.
min	Mineral.
N	Neutron.
Near	Near thermal neutron.
N-G	Neutron-gamma density measurement.
o	Oil.
R	Reference.
RMS	Root mean square.
s	Nuclear-based solver.
sh	Shale.
ss	Sandstone.
SSg	Short-spaced gamma-ray density.
SSn	Short-spaced gamma ray.
T	Total.
Tr	True model properties.
v	Virgin.
w	Water.
γ	Gamma ray.
ρ	Density.

Superscripts

i	Layer sub-*i*.
j	Measurement point sub-*j*.

k	Iteration number.
m	m-th order Taylor's series term.
N	Neutron.
n	Number of mineral components in rock matrix.
T	Transpose.
v	Virgin zone.
γ	Gamma ray.
η	Coefficient in inverse of migration length mixing law.

References

Abdollah-Pour, R., 2011, Development and application of a 3D equation-of-state compositional fluid-flow simulator in cylindrical coordinates for near-wellbore phenomena: Dissertation, The University of Texas at Austin.

Alger, R. P., L.L. Raymer, W. R., Hoyle, and M. P. Tixier, 1963, Formation density log applications in liquid-filled holes: Society of Petroleum Engineers Annual Fall Meeting Proceedings, SPE 435.

Alger, R. P., S. Locke, W.A. Nagel, and H. Sherman, 1972, The dual-spacing neuron log – CNL: Journal of Petroleum Technology, **24**, 1073-1083.

Allen, L.S., W.R. Mills, and R.W. Caldwell, 1965, The effects of fluid invasion in pulsed neutron logging: Geophysics, **30**, no. 3, 389-395.

Allen, L.S., C. W. Tittle, W. R. Mills, and R. L. Caldwell, 1967, Dual-spaced neutron logging for porosity: Geophysics, **32**, no. 1, 60-68.

Anderson, B., S. Banner, M. Luling, and R. Rosthal, 1990, Response of 2-MHz resistivity and wireline induction tools in dipping beds and laminated formations: Transactions of the Society of Petrophysicists and Well Log Analysts, 31st Annual Logging Symposium.

Anderson, B., 2001, Modeling and inversion methods for the interpretation of resistivity logging tool response: Dissertation, Delft University of Technology.

Aster, R., B. Barchers, and C. Thurber, 2013, Parameter estimation and inverse problems: Elsevier Inc.

Aqivlera, R., 1979, 1979, A new approach for log analysis of the pulsed neutron and resistivity log combination: Journal of Petroleum Technology, **31**, no. 4, 415-418.

Bardsley, S.R., and S.T. Algermissen, 1963, Evaluating oil shale by log analysis: Journal of Petroleum Technology, **15**, 81-84.

Case, C., C. C. Watson, and R. Lawrence, 1994, Sensitivity function technique for modeling nuclear tools: U.S. Patent 5,334,833.

Chemali, R., S. Gianzero, and R. Strickland, 1983, The shoulder bed effect on the dual laterolog and its variation with resistivity of the borehole fluid: Transactions of the Society of Petrophysicists and Well Log Analysts, 24th Annual Logging Symposium, paper UU.

Cramér, H., 1946, Mathematical methods of statistics. Princeton University Press.

El-Din, S., C. Minh, D. Murray, and J. Brahmakulam, 2012, Water saturation from Logging-While-Drilling resistivity, capture Sigma and core analysis for ROS determination in a giant middle east carbonate reservoir: Society of Petroleum Engineers Annual Technical Conference and Exhibition Proceedings, SPE 161463.

Ellis, D.V., C. Flaum, J.E. Galford, and H.D. Scott, 1987, The effect of formation absorption on the thermal neutron porosity measurement: Society of Petroleum Engineers Annual Technical Conference and Exhibition Proceedings, SPE 16814.

Ellis, D., C. R. Case, and J. Chiaramonte, 2004, Porosity from neutron logs II: interpretation: Petrophysics, **45**, 1529-9074.

Ellis, D.V. and J.M. Singer, 2007, Well logging for earth scientists: Springer.

Frenkel, M.A., A.G. Mezzatesta, and K.-M. Strack, 1997, Improved estimation of high-resolution formation resistivities for thin-bed analysis: Transactions of the Society of Petrophysicists and Well Log Analysts, 38th Annual Logging Symposium, paper CC.

Gaymard, R., and A. Poupon, 1968, Response of neutron and formation density logs in hydrocarbon bearing formations: The Log Analyst, **9**, 3-11.

Greenspan, E., 1976, Developments in perturbation theory: Academic Press, Advances in Nuclear Science and Technology, 9.

Griffiths, R., 2010, EcoScope user's guide: Schlumberger.

Guzman-Garcia, A., 2002, Analysis of LWD and wireline logs in highly deviated boreholes penetrating deepwater turbidites: anisotropy, polarization horns, and net sand derivation: Transactions of the Society of Petrophysicists and Well Log Analysts, 43rd Annual Logging Symposium, paper UU.

Gyllensten, A., A. Saif, A. Mohamed, A. Khadid, A. Madjidi, M. Mauborgne, and G. Weller, 2009, Advances in LWD Sigma measurements and applications to real-time formation evaluation in carbonate reservoirs: Transactions of the Society of Petrophysicists and Well Log Analysts: 35th Annual Logging Symposium, paper Q.

Haley, R.A., 1995, Pulsed-neutron capture log interpretation in laminated formations: a dual-exponential-decay model: Society of Petroleum Engineers Formation Evaluation, **10**, no. 1, 20-25.

Hansen, B., 2009, Evaluating tertiary water based EOR methods on the Veslefrikk field, with emphasis on analyzing sodium silicate injection by numerical simulation: M.S. thesis, University of Bergen.

Hardman, R.H., and L.C. Shen, 1987, Charts for correcting effects of formation dip and hole deviation on induction logs: The Log Analyst, **28**, no. 4, 349-356, issn: 0024-581X.

Henderson, D.L., and C.W. Maynard, 1989, Time-dependent single-collision kernels for integral transport theory: Nuclear Science and Engineering, **102**, 172-182.

Hilchie, D.W., W.R. Mills, C.L. Dennis, and W.W. Givens, 1969, Some aspects of pulsed neutron logging: The Log Analyst, **10**, no. 2, 7-17.

Ijasan, O., C. Torres-Verdín, and W. E. Preeg, 2013a, Fast modeling of borehole neutron porosity measurements with a new spatial transport-diffusion approximation: Geophysics, **78**, no. 3, D151-D168.

Ijasan, O., C. Torres-Verdín, and W. E. Preeg, 2013b, Inversion-based petrophysical interpretation of logging-while-drilling nuclear and resistivity measurements: Geophysics, **78**, no. 6, D473-D489.

Ijasan, O., C. Torres-Verdín, and W. E. Preeg, 2013c, Integration of porosity and fluid constituents from logs using an interactive neutron-density matrix scale: Interpretation, **1**, no. 2, T143-T155.

Jennings, R.L., and G.A. Weber, 1995, Towards fast quantitative modeling of pulsed neutron logging tools: Transactions of the Society of Petrophysicists and Well Log Analysts: 36th Annual Logging Symposium, paper A.

Lamarsh, J.R., and A.J. Baratta, 2001, Introduction to nuclear engineering: Prentice Hall.

Labat, C., S. Brady, M. Everett, E. Ellis, M. Doghmi, J. Tomlinson, and G. Shebab, 2002, 3D azimuthal LWD caliper: Society of Petroleum Engineers Annual Technical Conference and Exhibition Proceedings, SPE 77526.

La Vigne, J., M. Herron, and R. Hertzog, 1994, Density-neutron interpretation in shaly sands: Transactions of the Society of Petrophysicists and Well Log Analysts: 35th Annual Logging Symposium, paper EEE.

Lin, Y., S. Gianzero, and R. Strickland, 1984, Inversion of induction logging data using the least squares technique: Transactions of the Society of Petrophysicists and Well Log Analysts: 25th Annual Logging Symposium, paper AA.

Locke, S., and R. Smith, 1975, Computed departure curves for the thermal neutron decay time log: Transactions of the Society of Petrophysicists and Well Log Analysts: 16th Annual Logging Symposium, paper S.

Lyons, L., 1986, Statistics for nuclear and particle physicists: Cambridge University Press.

Mauborgne, M., F. Allioli, C. Minh, R. Griffihs, C. Maeso, N. Reichel, C. Stoller, D. Murray, H. Prabawa, M. Haggag, and A. AlKhoori, 2013, Advances in LWD multiple depth of investigation array Sigma measurements: Transactions of the Society of Petrophysicists and Well Log Analysts: 54th Annual Logging Symposium, paper III.

McKeon, D. C., and H. D. Scott, 1989, SNUPAR – A nuclear parameter code for nuclear geophysics applications: IEEE Transactions on Nuclear Science, **36**, 1215–1219.

Mendoza, A., C. Torres-Verdín, and W. E. Preeg, 2007, Rapid simulation of borehole nuclear measurements based on spatial flux-scattering functions: Transactions of the Society of Petrophysicists and Well Log Analysts, 48th Annual Logging Symposium, paper O.

Mendoza, A., C. Torres-Verdín, and W. E. Preeg, 2010a, Linear iterative refinement method for the rapid simulation of borehole nuclear measurements: Part 1 – Vertical wells: Geophysics, **75**, no. 1, E9-E29.

Mendoza, A., C. Torres-Verdín,, and W.E. Preeg, 2010c, Linear iterative refinement method for the rapid simulation of borehole nuclear measurements: Part 2 – High angle and horizontal wells: Geophysics, **75**, no.2 , E79 – E90.

Mickael, M.W., 1992, Importance estimation in Monte Carlo modeling of neutron and photon transport: Nuclear Geophysics, **6** , no. 3, 341-350.

Mickael, M.W., 1999, A new algorithm for correcting neutron decay logs for borehole and diffusion effects: The Log Analyst, **40**, no. 6, 471-478.

Mimoun, J.G., C. Torres-Verdín, and W.E. Preeg, 2011, Quantitative interpretation of pulsed neutron capture logs: Part 1 – Fast numerical simulation: Geophysics, **76**, no.3, E81 – E93.

Morris, F., and T. Quinlan, 2005, Applications of pulsed neutron capture logs in reservoir management: Society of Petroleum Engineers Annual Technical Conference and Exhibition Proceedings, SPE 93889.

Murdoch, B.T., C.J. Hunter, R.R. Randall, and C.W. Towsley, 1990, Diffusion corrections to pulsed neutron capture logs: methodology: Transactions of the Society of Petrophysicists and Well Log Analysts: 31st Annual Logging Symposium, paper Q.

Ortega, E., C. Torres-Verdín, W.E. Preeg, and J. Miles, 2013, Multi-detector LWD Sigma logging principles, petrophysical applications, and environmental effects: Transactions of the Society of Petrophysicists and Well Log Analysts, 54th Annual Logging Symposium, paper NNN.

Passey, Q.R., H. Yin, C.M. Rendeiro, and D.E. Fitz, 2005, Overview of high-angle and horizontal well formation evaluation – Issues, learnings, and future directions: Transactions of the Society of Petrophysicists and Well Log Analysts, 46th Annual Logging Symposium, paper A.

Preeg, W.E., and H.D. Scott, 1986, Computing thermal neutron decay time environmental effects using Monte Carlo techniques: SPE Formation Evaluation, **1**, no. 1, 35-42.

Rasmus, J., R. Altman, T. Barber, M. Javalagi, 2009, Workflow for determining true formation resistivity in HAHZ wells: Transactions of the Society of Petrophysicists and Well Log Analysts, 50th Annual Logging Symposium.

Savre, W. C., 1963, Determination of a more accurate porosity and mineral composition in complex lithologies with the use of the sonic, neutron and density surveys: Journal of Petroleum Technology, **15**, 945-959.

Shapiro, S., and M. Wilk, 1965, An analysis of variance test for normality (complete samples): Biometrika, **52**, no. 3-4, 591-611.

Shetty, S., D. Omeragic, T. Habashy, J. Miles, J. Rasmus, R. Griffiths, and C. Morriss, 2012, Inversion-based workflows for interpretation of nuclear density images in high-angle and horizontal wells: Transactions of the Society of Petrophysicists and Well Log Analysts, 53rd Annual Logging Symposium.

Simpson, G., and J. Menke, 2010, Identifying low contrast – low resistivity pay zones with pulsed neutron capture logs in shaly sand Miocene formations in South Louisiana: Transactions of the Society of Petrophysicists and Well Log Analysts, 51st Annual Logging Symposium.

Stacey, W.M., 2007, Nuclear reactor physics: Wiley-VCH.

Suau, J., P. Grimaldi, A. Paupon, and P. Souhaite, 1972, The dual laterolog-Rxo tool: Fall Meeting of the Society of Petroleum Engineers of American Institute of Mining, Society of Petroleum Engineers, SPE 4018.

Tittle, C.W., 1961, Theory of neutron logging I: Geophysics, **26**, no 1, 27-39.

Vail, W.B., S.T. Momii, and J.T. Dewan, 1996, Through casing resistivity measurements and their interpretation for hydrocarbon saturations: Society of Petroleum Engineers Annual Technical Conference and Exhibition Proceedings, SPE 30582.

Wahl, J. S., J. Tittman, C. W. Johnstone, and R.P., Alger, 1964, The dual spacing formation density log: Journal of Petroleum Technology, **16**, 1411-1416.

Warrilow, I.M., R. Ibrahim, H. T. Chin, and D. Forsyth, 1995, Applications of resistivity inversion software to thin-bed evaluation: Society of Petroleum Engineers Asia, Pacific, Oil & Gas Conference Proceedings, SPE 29263.

Watson, C.C., 1984, Monte Carlo computation of differential sensitivity functions: Transactions of American Nuclear Society, **46**, 655-657.

Watson, C.C., 1992, A spatial sensitivity analysis technique for neutron and gamma-ray measurements: Transactions of American Nuclear Society, **65**, 3-4.

Weller, G., R. Griffiths, C. Stoller, F. Allioli, M. Berheide, M. Evans, L. Labous, D. Dion, and P. Perciot, 2005, A new integrated LWD platform brings next-generation

formation evaluation services: Transactions of the Society of Petrophysicists and Well Log Analysts: 46th Annual Logging Symposium, paper H.

Wu, C., and J. Krug, Density-neutron crossplot analysis for shaly gas sands using hand-carried calculators: The Log Analyst, **19**, 3-10.

X-5 Monte Carlo Team, 2003, MCNP – A general Monte Carlo N-particle transport code, version 5, developer's guide: University of California, Los Alamos National Laboratory.

X-5 Monte Carlo Team, 2005, MCNP – A general Monte Carlo N-particle transport code, version 5, vol 1: Overview and theory: University of California, Los Alamos National Laboratory.

Xiao, J., M.S. Bittar, and G. Hu, 2003, Asymptotic dipping and nonlinear shoulder correction of resistivity logs: Society of Petroleum Engineers Annual Technical Conference and Exhibition Proceedings, SPE 84601.

Yang, J., D. Omeragic, C. Liu, Q. Li, J. Smits, and M. Wilson, 2005, Bed-boundary effect removal to aid formation resistivity interpretation from LWD propagation measurements at all dip angles: Transactions of the Society of Petrophysicists and Well Log Analysts: 46th Annual Logging Symposium, paper F.

Zaslavsky, M., S. Davydycheva, V. Druskin, A. Abubakar, T. Habashy, and L. Knizhnerman, 2006, Finite-difference solution of 3D EM problem with divergence-free preconditioners: Transactions of the Society of Exploration Geophysicists: 76th Annual Meeting.

Zhou, T., J. Miles, C. Case, J. Chiaramonte, and D. Ellis, 2009, A second-order fast-forward model for a gamma-gamma density logging tool: Society of Petroleum Engineers Annual Technical Conference and Exhibition Proceedings, SPE 124193.

Vita

Edwin Ortega was born and raised in Bogotá, Colombia. There he attended Universidad de América and graduated with honors in Petroleum Engineering in 2009. In Colombia, Edwin interned for BP Exploration Colombia in the production technology team working on formation damage and developed his undergraduate thesis on reservoir modeling of gas condensate reservoirs. He then worked as a company man assistant in well operations during 2009. In 2010, he joined the Department of Petroleum and Geosystems Engineering at The University of Texas at Austin as a graduate research assistant in the Formation Evaluation group and obtained his M.Sc. degree in 2013. Edwin interned for Schlumberger-Doll Research during the summer of 2010 and spring of 2013 in Sugarland, Texas, and Cambridge, Massachusetts, respectively. His work for Schlumberger focused on modeling and interpretation of nuclear measurements. Edwin also interned for ConocoPhillips in Houston, Texas, working on interpretation of dielectric measurements in shale-gas formations during the summer of 2011, and on nuclear modeling during the summers of 2012 and 2013. Edwin will join ConocoPhillips as a petrophysicist in the Petrophysical Technology group in the division of Geoscience and Reservoir Engineering of the company based in Houston, Texas.

Permanent e-mail address: ortega.edwin@hotmail.com

This dissertation was typed by the author.